UNIVERSITY OF SOUTHAMPTON

APPLICATIONS OF SUPERSTRUCTURE FIBRE BRAGG GRATINGS FOR

OPTICAL CODE DIVISION MULTIPLE ACCESS
&
PACKET SWITCHED NETWORKS

by Peh Chiong TEH

A thesis submitted for the degree of
Doctor of Philosophy

FACULTY OF ENGINEERING AND APPLIED SCIENCE

OPTOELECTRONICS RESEARCH CENTRE

DEPARTMENT OF ELECTRONICS AND COMPUTER SCIENCE

April 2003

UNIVERSITY OF SOUTHAMPTON

ABSTRACT

FACULTY OF ENGINEERING AND APPLIED SCIENCE
OPTOELECTRONICS RESEARHC CENTRE
DEPARTMENT OF ELECTRONICS AND COMPUTER SCIENCE

Doctors of Philosophy

Applications of Superstructure Fibre Bragg Gratings for Optical Code Division Multiple Access and Packet Switched Networks

By Peh Chiong TEH

This thesis describes the research on the implementation of all-optical code generation and recognition based on superstructure fibre Bragg grating (SSFBG) for use in Optical Code Division Multiple Access (OCDMA) systems and also in high-speed all-optical packet switched networks.

Initially, the relative merits of bipolar coding/decoding schemes compared to the unipolar equivalent are investigated experimentally for 7-chip and 63-chip SSFBGs. Error free performance can be obtained even in the presence of an interfering user. The SSFBGs can also be used for recoding functions. Next, 255-chip quaternary phase coded SSFBGs are fabricated to demonstrate that the current grating writing technique has the resolution to fabricate longer code sequences gratings. These SSFBGs are used in an OCDMA/WDM system incorporating different coding schemes, repetition rates and wavelengths. The use of optical nonlinear thresholder based on either a NOLM or a highly nonlinear holey fibre followed by long pass spectral filtering to improved the code recognition performance are demonstrated. A practical 16-channel OCDMA/WDM system based on simple, conventional DFB fibre lasers with associated Electro-Absorption modulator as pulse transmitters is described. The system demonstrates the attraction of using the wavelength selectivity of the gratings to simultaneously perform the wavelength 'drop' function and optical decoding of 'in-band' channel, eliminating the requirements for additional WDM filtering components. 8- and 16-chip, multi-level phase code-tunable devices based on uniform fibre Bragg gratings are also described. These compact and simple devices offer excellent code recognition signatures with error free operation achieved in the BER measurements. A novel spectrally interleaved bi-directional OCDMA system and clock distribution bi-directional architecture are proposed and experimentally demonstrated. Such architectures combine the functionality of OCDMA approach with WDM architectures, without creating complicated topologies.

The thesis also describes the use of SSFBG encoders/decoders to generate and subsequently recognise optical headers within optical packet switched networks. The approach can be combined with WDM multiplexing in a 400 Gbit/s multi-wavelength optical packet router demonstration. A simple self-routing edge-to-edge optical packet switched network based on all-optical recognition of a 20 Gchip/s cascaded header using fibre Bragg gratings is presented. Self-routing of optical packets through two network switching nodes is demonstrated.

These results highlight the precision and flexibility of the continuous grating writing process and show that the SSFBG technology represents a promising technology not just for OCDMA but an extended range of other pulse shaping, and associated optical processing applications such as required within optical packet switched networks.

List of Contents

List of Contents iii

List of Tables and figures vi

Acknowledgements xix

Principle Abbreviations xxi

Overview 1
References 8

Chapter One: A Review on Optical Code Division Multiple Access (OCDMA) 11
1.1 Introduction 11
1.2 Review on various coherent OCDMA coding/decoding schemes 18
References 25

Chapter Two: Theory and Principle of Operation 29
2.1 Principle of Pulse Encoding and Decoding 30
2.2 SSFBG Fabrication 44
2.3 Coherent OCDMA System Simulation 48
2.3.1 System Model 48
2.3.2 Simulation Results 50
2.4 Summary 53
References 54

Chapter Three: Assessment on the quality of the Superstructure Fibre Bragg Gratings encoders/decoders 56
3.1 Characterisation of the gratings fabricated 57
3.2 Performance of 7-chip unipolar and bipolar M-sequence SSFBGs 63
3.3 Performance of 63-chip bipolar Gold sequence SSFBGs 69
3.3.1 Single channel experiment 69
3.3.2 Two-channel experiment (multi-user operation) 75
3.3.3 Generation, recognition and re-coding of 63-chip bipolar optical code sequences 79
3.4 Performance of 255-chip quaternary Family A sequence SSFBGs 82
3.4.1 Assessment of the quality of the 255-chip SSFBGs for coding/decoding operation 82
3.4.2 OCDMA/WDM System Experimental Results 86

3.5 Hybrid combination of fibre delay lines and SSFBG for a 7-chip optical codes generation/recognition 90
3.6 Conclusions 94
References 95

Chapter Four: Mutiple Access Interference (MAI) reduction based on nonlinear optical thresholidng 96
4.1 Multiple Access Interference (MAI) noise reduction 97
4.2 High performance 63-chip OCDMA receiver incorporating a nonlinear optical loop mirror 101
4.2.1 Single channel performance 102
4.2.2 Two-channel performance 108
4.3 Holey fiber based nonlinear optical thresholder 111
4.3.1 Experimental results 112
4.4 Conclusions 117
References 118

Chapter Five: 16-chip, 50ps, Four-level Phase coding Superstructure Fiber Bragg Gratings 121
5.1 Multi-wavelength pulse generation 122
5.2 16-chip, 50ps quaternary SSFBGs 124
5.3 16-channel OCDMA/DWDM experimental results 131
5.4 Performance enhancement using NOLM 138
5.5 Conclusions 140
References 141

Chapter Six: Reconfigurable OCDMA Phase Coders 143
6.1 Introduction 143
6.2 Principle of Operation 145
6.3 Device Description 148
6.4 8-chip, bipolar code-tunable OCDMA encoders/decoders 152
6.5 16-chip, multi-level reconfigurable OCDMA phase encoder 155
6.6 Summary 159
References 160

Chapter Seven: OCDMA Architectures 161
7.1 Bi-directional spectrally interleaved OCDMA/WDM 162
7.1.1 Proposed bi-directional architecture 162
7.1.2 Experimental results 164
7.2 Clock Distribution OCDMA Architecture 169
7.2.1 Proposed clock distribution architecture 169
7.2.2 Experimental results 170
7.3 Conclusions 176
References 177

Chapter Eight: Header Generation and Recognition for Optical Packet Switched Networks 178
- 8.1 Introduction to optical packet switching 179
- 8.2 255-chip multi-hop experiment 185
- 8.3 Multi-wavelength add/drop node 190
  - 8.3.1 Proposed multi-wavelength packet switched architecture 190
  - 8.3.2 Multi-wavelength packet transmitter 191
  - 8.3.3 Multi-wavelength packet switching node 193
- 8.4 Self Routed Edge-to-Edge Packet Switched Network 197
  - 8.4.1 Proposed self-routing architecture 197
  - 8.4.2 Experimental demonstration and results 198
- 8.5 Summary 203
- References 204

Conclusions and Future Directions 206

Appendix A 210

Appendix B 218

List of Publications 223

List of Tables and Figures

Overview

Figure 1: *Characteristics of the fibre Bragg grating (FBG) which can operate either in the transmission mode or reflective mode. The centre frequency of the reflected narrowband spectrum depends on the effective refractive index of the fibre core (n_{eff}) and the grating pitch (Λ).* 3

Chapter One: A Review on Optical Code Division Multiple Access (OCDMA)

Figure 1.1: *Schematic showing a typical radio CDMA network based on spread spectrum technique. Information bits to be transmitted are 'spread' by means of a digital code. At the receiver, the intended spread spectrum signal is recovered using a receiver having a correct code and bandpass filtered to remove the interfering signals from other users. Note: f_c denotes the carrier frequency.* 12

Figure 1.2: *Schematic showing a typical OCDMA network based on time-spreading and matched filtering process. Information bits are encoded all-optically with a unique code before transmission into fibre optic network. At the receiving end, the intended information can be recovered using a matched filter having the correct code. Time domain optical gating can be used to improve the recovered signal contrast.* 14

Figure 1.3: *Coherent FH-OCDMA technique. The 'frequency hopped' encoded signal contains a train of pulses in which their carrier frequencies is changed according to the frequency- hopped code.* 15

Figure 1.4: *FE-OCDMA technique. An input broadband signal is sliced into individual frequency components according to an amplitude/phase modulated spectral code. As a result, a short, high intensity input pulse is transformed into a long duration, low intensity frequency encoded signal in the time domain.* 16

Figure 1.5: *DS-OCDMA technique. The encoded 'time-spread' signal comprises of a sequence of pulses according to the code sequence defined at the direct sequence encoder.* 16

Figure 1.6: *Fibre delay lines based optical encoder and decoder for DS-OCDMA approach.* 18

Figure 1.7: *Optical encoder/decoder based on PLC technology to implement DS-OCDMA approach.* 19

Figure 1.8: *FE-OCDMA implementation using bulk optics. The decoder has the same configuration as the encoder but with the input signal replaced by the frequency encoded signal from the network and the output detected via a photodetector.* 20

Figure 1.9: *Frequency hopped OCDMA implementation using arrays of narrowband fibre Bragg gratings.* 22

Figure 1.10: *Outline of the physical approach of pulse encoding and decoding using SSFBG's. When short optical pulses are reflected from the encoder grating, they are reshaped into coded pulse sequences according to the superstructure profile (OCDMA code) imprinted into the grating. At the receiver, a matched filter of the encoder is required for the decoding process. This is formed by using a decoder grating identical to the encoder but illuminated from the opposite end. Sharp correlation peak can be obtained at the output when the encoded signal matches the decoder grating (see matched case), otherwise, no peak correlation can be seen if incorrect coded signal (or otherwise an incorrect decoder) is used (see unmatched case).* 23

Chapter Two: Theory and Principle of Operation

Figure 2.1: *Schematic examples of temporal codes (upper traces) and the corresponding refractive index modulation profiles along the SSFBG structures (lower traces); (a) shows a 7-chip unipolar code, (b) a 7-chip bipolar code, and (c) the matched filter to the unipolar code outlined in (a).* Δn *is the change in the refractive index modulation of the grating.* T_{chip} *is the duration of one chip.* 32

Figure 2.2: *(a) Calculated reflectivity spectrum (solid line) and optical power spectrum obtained after reflection from the unipolar grating using 2.5ps input soliton pulses; (b) calculated impulse response (solid line) and temporal response to 2.5ps soliton pulses (dashed lines) for the unipolar grating; (c) and (d), same as in (a) and (b) respectively, but for the 7-chip, bipolar grating.* 33

Figure 2.3: *Calculated (a) autocorrelation and (b) crosscorrelation (when the encoder orthogonal code is '1011000') traces of the decoded signals for 2.5ps soliton input pulses for 7-chip unipolar coding encoder/decoder gratings pair. (c- d) Equivalent resultant waveforms when 7-chip bipolar coding encoder/decoder gratings are used. The orthogonal code used for determining the bipolar crosscorrelation traces is* '$\pi 0 \pi \pi 000$'. 37

Figure 2.4: *Superstructure profiles (upper traces) and the corresponding calculated reflectivity spectra (lower traces) for (a) G63B-1 and (b) G63B-2. Note that the notation G63B-1 indicates* ***Gold*** *family codes,* ***63****-chip code lengths,* ***Bipolar*** *phase coding and Code* ***1****.* 38

Figure 2.5: *Calculated traces of the signals after the code:decode process for 2.5ps soliton input pulses, for the grating combinations: (a) G63B-1:G63B-1*, (b) G63B-2:G63B-2*, (c) G63B-2:G63B-1* and (d) G63B-1:G63B-2*. In the autocorrelation signals, most of the energy is concentrated at the center of the signal, giving rise to a sharp high intensity spike. In contrast, the low-level crosscorrelation signals have the energy spread over the waveform (the crosscorrelation signal has a full duration of twice the duration of the encoded signal).* 39

***Figure 2.6**: Calculated normalised intensity (a) autocorrelation and (b) crosscorrelation traces obtained when using 255-chip quaternary Family A. (c) and (d) Similar correlation traces when 255-chip bipolar Gold code sequence is used. The input pulse duration is 2.5ps for all four cases.* 41

***Figure 2.7:** Calculated autocorrelation response after the decoding grating, G63B-1*, when the encoded signal, G63B-1 is transmitted over some distance of SMF-28 before decoding.* 42

***Figure 2.8:** Calculated autocorrelation response after the decoding grating, Q1*, when the encoded signal, Q1 is transmitted over some distance of SMF-28.* 42

***Figure 2.9**: Continuous grating writing setup.* 45

***Figure 2.10**: BER performance calculated against number of active users in the network using (a) bipolar Gold codes and (b) quaternary Family A codes for code lengths L=15 to L=255.* 51

***Figure 2.11**: BER performance against number of active users in the network using 1023-chip, quaternary phase Family A code sequences with each channel operating at 1 Gbit/s data rate. The FEC error free limit shown in the graph considers a general case of the performance improvement expected when a typical FEC code is used.* 52

Chapter Three: Assessment on the quality of the Superstructure Fibre Bragg Gratings encoders/decoders

***Table 3.1**: Different types of SSFBGs fabricated for use in the experiment.* 57

***Figure 3.1**: Reflectivity spectra for (a) the M7U-1 and (b) the M7B-1 grating (solid lines: experimental measurements, dashed lines: theoretical plots). The period of the refractive index modulation used to write these gratings was set to Λ=~520nm.* 59

***Figure 3.2**: Superstructure profiles (upper traces) and the corresponding measured reflectivity spectra (lower traces) for (a) G63B-1, (b) G63B-1*, (c) G63B-2, and (d) G63B-2*. These gratings was written with a refractive index modulation period of Λ=~520nm. The dashed horizontal lines indicate the noise floor in the reflectivity measurements.* 60

***Figure 3.3**: 255-chip four-level phase modulation profile of (a) code A255Q-1 and (b) code A255Q-2 to be imprinted onto the photosensitive fibre during the grating writing process.* 61

***Figure 3.4**: Spectral reflectivity profiles (theory and experiment) for 255-chip, 320 Gchip/s quadrature sequences SSFBGs (a) encoder A255Q-1 and (b) encoder A255Q-2. These gratings have peak reflectivity of ~25 % and they are 8.415cm long. The dashed horizontal lines indicate the noise floor in the reflectivity measurements.* 62

***Figure 3.5**: Experimental set-up (EDFA: Erbium-doped fibre amplifier, LCFBG: linearly chirped fibre Bragg grating).* 63

Figure 3.6:*Measured responses after reflection off grating M7U-1 (a) with the calculated waveforms in (b). Corresponding measured (c) and calculated (d) phase-encoded waveforms after reflection off grating M7B-1. Note that the measured responses have a limited bandwidth of 20 GHz. (e) and (f) Predicted time response considering the detector bandwidth of 20 GHz for M7U-1 and M7B-1 respectively.* 64

Figure 3.7: *(a) Intensity SHG autocorrelation traces of the encoded waveforms for the M7U-1 grating, for 2.5ps soliton input pulses; (b) spectral response of the encoded waveforms for the M7U-1 grating; (c) and (d), same as in (a) and (b) respectively, but for the M7B-1 grating (solid lines: experimental measurements, dashed lines: theoretical plots). The 10GHz periodic structure on the spectral envelope of the experimental measurements results from the 10Gbit/s modulation of the signal.* 65

Figure 3.8: *Intensity SHG autocorrelation traces of the signals after the code:decode process for 2.5ps soliton input pulses, for the grating combinations: (a) M7U-1:M7U-1*, and (b) M7B-1:M7B-1* (solid lines: experimental measurements, dashed lines: theoretical plots). $\Delta\tau$ is the decoded pulse width obtained from the SHG intensity measurement. The phase coding autocorrelation pulse width depends on the chip duration because maximum peak intensity is obtained when all contributing elementary chip-pulses add up in phase. This occurs when the encoded signal overlaps exactly at the center of the decoder grating. At other positions, out-of-phase interferometric cancellation occurs yielding low-level autocorrelation sidelobes. For unipolar coding, the decoded pulse width is much broader than the chip duration because power summation occurs and no coherent correlation taking place.* 66

Figure 3.9: *Reflectivity spectrum of the dispersion compensating grating. The time delay diagram is shown in the inset.* 67

Figure 3.10: *BER curves for the M7B-1:M7B-1* combination (open circles: laser back-to-back, closed circles: decoded signal without transmission, triangles: decoded signal after transmission). Inset shows eye diagrams of the decoded signals without (upper trace) and after 25km transmission (lower trace). The data rate was 10 Gbit/s. (Note that the intensity noise observed in the '1' bits in the eye diagram of decoded signals after 25km transmission is due to the drift in the laser pulse source when the measurement was made).* 68

Figure 3.11: *Experimental set-up (EDFA: Erbium-doped fibre amplifier, LCFBG: linearly chirped fibre Bragg grating).* 69

Figure 3.12: *Traces of the encoded waveforms for (a) the G63B-1, and (b) the G63B-2 grating, for 2.5ps soliton input pulses (solid lines: experimental measurements, dashed lines: theoretical plots). The detection bandwidth of the experimental measurement (~20GHz) was not taken into account for the theoretical calculation.* 70

Figure 3.13: *Traces of the signals after the code:decode process for 2.5ps soliton input pulses, for the grating combinations: (a) G63B-1:G63B-1*, (b) G63B-2:G63B-2*, (c) G63B-2:G63B-1*, and (d) G63B-1:G63B-2*. The detection bandwidth was 20GHz. All the traces were taken at the same received optical power.* 71

Figure 3.14: *Eye diagrams obtained at a data rate of 1.25 Gbit/s. (a) laser back-to-back, (b) matched case (correct code used), (c) unmatched case (incorrect code used).* 72

Figure 3.15: *Intensity SHG autocorrelation traces of the signals after code:decode process for 2.5ps soliton input pulses for the 63-bit grating combinations: (a) G63B-1:G63B-1* and (b) G63B-2:G63B-2*. (solid lines: experimental measurements, dashed lines: theoretical plots). $\Delta\tau$ is the decoded pulse width obtained from the SHG intensity measurement.* 73

Figure 3.16: *Figure 3.16: BER curves for the G63B-1:G63B-1* combinations (closed circles: laser back to-back, open squares: no transmission, closed triangles: after transmission). The data rate was 1.25 Gbit/s.* 74

Figure 3.17: *Experimental set-up for two-channel experiment (EDFA: Erbium-doped fibre amplifier).* 75

Figure 3.18: *Pulseforms at data rate of 1.25 Gbit/s showing the encoding signals after reflection off the gratings: (a) G63B-1, (b) G63B-2 and (c) the combined signals of G63B-1 and G63B-2 with full temporal overlap. A – Combined signal when both channels have '1' data bits, B – Combined signal when only one of the channels has a '1' data bit, while the data bit on the other channel is '0'. C – Combined signal when both channels have '0' data bits.* 76

Figure 3.19: *BER results for two-channel experiment (closed circles: laser back-to-back, closed diamonds: two-channel operation and open squares: single-channel operation). Inset: Corresponding eye diagram for two-channel experiment. The data rate is 1.25 Gbit/s.* 78

Figure 3.20: *Experiment set up for investigation of the cascading of functions.* 79

Figure 3.21: *The measured (solid) and theoretical (dashed) pulse shapes at points: A - input pulse shape (a), B – G63B-1 code sequences (b), C – G63B-1:G63B-1* correlation (c) and D – G63B-1:G63B-1*:G63B-2:G63B-2* correlation (d) within the system (refer to Figure 20). The theoretical curves are not corrected for the electronic measurement system resolution (20ps), i.e. they represent the true optical signals. The measured (solid) and theoretical (dashed) traces from the SHG intensity autocorrelation measurements for G63B-1:G63B-1* correlation and G63B-1:G63B-1*:G63B-2:G63B-2* correlation are shown in Figures (e) and (f) respectively.* 81

Figure 3.22: *Experimental set up to assess the performance of the 255-chip gratings.* 82

Figure 3.23: *Calculated time domain response for (a) 2.5ps transform limited input pulse, (b) encoded waveform from A255Q-1 after convolving with the input response, (c) similar encoded waveform obtained from A255Q-2, (d) autocorrelation signatures using grating combinations A255Q-1:A255Q-1*, (e) autocorrelation signatures using grating combinations A255Q-2:A255Q-2*, (f) cross-correlation signatures using grating combinations A255Q-2:A255Q-1*.* 83

Figure 3.24: *Oscilloscope traces of (a) 2.5ps transform limited input pulse, (b) encoded waveform after reflection from SSFBG A255Q-1, (c) encoded waveform after reflection from SSFBG A255Q-2, (d) after matched filtering for the grating combinations A255Q-1:A255Q-1*, (e) after matched filtering for the grating combinations A255Q-2:A255Q-1*.*

The measured resolution was ~20ps. Note that the ringing observed in the traces is due to the effects of the photodiode. 84

Figure 3.25: Theoretical (dashed line) and experimental (solid line) SHG intensity autocorrelation traces for the Q1:Q1* process. Note that the low level pedestal indicates a high quality code recognition signature. The correctly decoded pulsewidth was ~3.2ps. 85

Figure 3.26: Experimental setup to demonstrate the OCDMA/WDM system. QPSK: Quaternary phase shift keying SSFBGs, BPSK: bipolar phase shift keying SSFBGs. 86

Figure 3.27: Optical spectra for the combined 4-channel (1552nm: A255Q-1, A255Q-2 and 1556.2nm: G63B-1, G63B-2) OCDMA/WDM signals. Note that the different peak power spectrum for both wavelengths is due to the different repetition rates used (1552.5nm: 1.25 Gbit/s and 1556.2nm: 10 GHz). The measured resolution is ~20pm. 87

Figure 3.28: Optical spectra after matched filtering with (a) decode grating A255Q-1* and (b) decode grating A255Q-2*. The measured resolution is ~20pm. 88

Figure 3.29: BER results for various combinations of interfering channels measured against received power:
At 1.25 Gbit/s
Laser back-to-back (open circles),
A255Q-1:A255Q-1* (closed triangles),
A255Q-1+A255Q-2:A255Q-1* (open triangles),
A255Q-1+G63B-1+G63B-2:A255Q-1* (open squares)
and A255Q-1+A255Q-2+G63B-1+G63B-2:A255Q-1* (closed squares).
At 622 Mbit/s
Laser back-to-back (closed circles),
and A255Q-1:A255Q-1* (open diamonds) 89

Figure 3.30: Experimental setup and SSFBG decoder reflectivity profile; where EFRL: erbium doped fibre ring laser, PC: polarization controller, PM isolator: polarization maintaining isolator, SSFBG: superstructure fibre Bragg grating. 91

Figure 3.31: (a) Delay line encoder (b) SSFBG encoder M7U-1. Intensity SHG autocorrelation traces of the encoded sequence at the output of the particular encoder (solid line: experiment, dashed line: theory). Inset: Theoretical and experimental traces of the encoded waveform at 10 Gbit/s with 20GHz bandwidth limitation included. (Note: the SSFBG encoder used in (b) is being reflected from the opposite side and hence the time inversed nature of the encoded waveform). The delay line encoder has a chip duration of 2.5ps while the SSFBG encoder has a chip duration of 6.4ps. This explains why the intensity SHG autocorrelation traces for both cases are different. 92

Figure 3.32: A fibre delay line encoder - SSFBG decoder system. Left: Intensity SHG autocorrelation traces of the decoded signal (solid line: experiment, dashed line: theory). Right: Numerically calculated and measured experimental results of the oscilloscope traces of the decoded signal taking into account the 20GHz bandwidth limitation of the detector at 10 Gbit/s. 93

Chapter Four: Multiple Access Interference (MAI) reduction based on nonlinear optical thresholding

Figure 4.1: *Experimental set up (EDFA: Erbium-doped fibre amplifier, LCFBG: linearly chirped fibre Bragg grating).* 102

Figure 4.2: *SHG intensity autocorrelation traces of the pulse forms after matched filtering at data rates of 1.25 Gbit/s and 2.5 Gbit/s.* 103

Figure 4.3: *BER results without using NOLM at data rates of 1.25 Gbit/s and 2.5 Gbit/s.* 103

Figure 4.4: *SHG intensity autocorrelation traces of the pattern recognition pulse forms after matched filtering and subsequent nonlinear switching by the NOLM at data rates of 1.25 Gbit/s and 2.5 Gbit/s.* 104

Figure 4.5: *Eye diagrams showing (a) laser input 2.5ps pulses (b) the pulses after matched filtering and (c) the correlated pulses after nonlinear switching by the NOLM. The data rate used is 2.5 Gbit/s.* 105

Figure 4.6: *BER performances for 1.25 Gbit/s and 2.5 Gbit/s systems.* 106

Figure 4.7: *10 Gbit/s single channel OCDMA operation: (a) eye diagrams (b) BER results.* 107

Figure 4.8: *Two-channel experimental set up (EDFA: Erbium-doped fibre amplifier).* 108

Figure 4.9: *SHG intensity autocorrelation traces of the decoded signal central autocorrelation spike (solid line: after matched filtering technique G63B-1:G63B-1* and dashed line: after subsequent nonlinear switching by the NOLM). The data rate is 2.5 Gbit/s.* 109

Figure 4.10: *Eye diagrams at 2.5 Gbit/s showing (a) laser input pulses (b) after matched filtering alone and (c) after self-switching by the NOLM.* 109

Figure 4.11: *BER versus received optical power for two-channel operation at 1.25 Gbit/s and 2.5 Gbit/s.* 110

Figure 4.12: *Experimental setup to demonstrate the holey fiber nonlinear thresholder.* 112

Figure 4.13: *Measured SPM-induced nonlinear phase shift versus launched optical power in the HF. Inset: Cross-sectional SEM image of the HF used.* 113

Figure 4.14: *(a) Signal spectrum both before and after the HF. (b) Experimentally obtained power transmission characteristic of the HF switch as a function of the input peak power.* 114

Figure 4.15: *SHG intensity auto-correlation traces showing that the switched output pulses had roughly the same temporal width as the 2.5ps input pulses.* 115

Figure 4.16: *Eye diagrams for the 1.25 Gbit/s OCDMA system. The measured resolution is ~20ps.* 116

Figure 4.17: *Measured BER versus received optical power for the 1.25 Gbit/s OCDMA system.* 116

Chapter Five: 16-chip, 50ps, Four-level Phase coding Superstructure Fiber Bragg Gratings

Figure 5.1: *Principle of operation of an electro-absorption (EA) modulator. By increasing the reverse bias voltage, shorter duration pulse trains (solid lines) can be obtained.* 122

Figure 5.2: *Multi-wavelength pulse generation using EA modulator.* 123

Figure 5.3: *Typical configuration of a distributed feedback (DFB) fibre laser.* 123

Figure 5.4: *(a) Calculated optical spectra of the 20ps pulse source (dashed lines) and the reflectivity spectrum of the 16-chip, quaternary phase coding grating (solid lines). (b) Calculated resulting reflected optical power spectrum after excitation with 20ps pulses. (c) Calculated temporal response after reflection from the SSFBG when 20ps pulses were launched into the grating. The 16-chip code used is 'π, π, π, 0.5π, 0.5π, 1.5π, 0.5π, 1.5π, π, 0, 0.5π, 1.5π, π, 1.5π, 0, 0'.* 124

Figure 5.5: *Calculated optical spectra of the (a) 2ps pulse source (dashed lines) and the reflectivity spectrum of the 16-chip, quaternary phase coding grating (solid lines). (b) Calculated resulting reflected optical power spectrum after excitation with 2ps pulses. (c) Calculated temporal response after reflection from the SSFBG when ultrashort 2ps pulses were launched into the grating.* 125

Figure 5.6: *Calculated decoded autocorrelation traces when input pulse duration used to excite the gratings is (a) 20ps and (b) 2ps.* 125

Figure 5.7: *(a)-(d) Phase modulation profile of the four 16-chip quaternary codes and the respective measured (solid line) and calculated (dashed line) reflectivity spectra of the gratings fabricated using the continuous grating writing technique. These gratings have a peak reflectivity of ~25% and are 8.22cm long.* 127

Figure 5.8: *(a)-(d: Oscilloscope traces (measured – solid line and theory – dashed line) after reflection off the respective gratings. These measurements have a resolution of ~20ps.* 128

Figure 5.9: *(a) Measured decoded autocorrelation signature after reflecting encoded signal Q1 off the decoder grating Q1*. (b)-(d): Measured crosscorrelation signatures obtained after reflecting encoded signal Q2, Q3 and Q4 respectively off the decoder grating Q1*. The extinction between auto-correlation signature and cross-correlation waveforms is ~ 8dB. All the decoded output signals have a full duration of 1.6ns corresponding to twice the encoded duration as a result of matched filtering process.* 129

Figure 5.10: *(a)-(d) Measured (solid lines) and calculated (dashed lines) of the correctly decoded autocorrelation traces for all four different quaternary codes to be used in the experiment. The decoded pulsewidths are ~50ps.* 130

Figure 5.11: *Schematic diagram of the OCDMA/DWDM experimental set up.* 131

Figure 5.12: *Optical spectra obtained at various points along the system: (a) The multiplexed four WDM sources, separated in frequency by 100 GHz. (b) Encoded 16-channel OCDMA/DWDM. (c) After matched filtering using decoder grating Q1* centred at* λ_2 *= 1548.11nm. The measured resolution is 60pm.* 132

Figure 5.13: *Eye diagrams and the histogram data showing the distribution of zeros and ones of the decoded signals after reflection from decode grating Q1* when all four OCDMA coded channels (Q1, Q2, Q3 and Q4) are active in the system. The measurements were taken using a 10 GHz detector.* 133

Figure 5.14: *Eye diagrams obtained after matched filtering process using decode grating Q2* for all four wavelengths in the presence of all 16 coded channels at data rate of 311 Mbit/s.* 134

Figure 5.15: *BER measurements obtained against received optical power for all 311 Mbit/s, 16-coded channels including after transmission over 50km of SMF-28.* 135

Figure 5.16: *(a) Optical spectrum showing the multiplexed 16-channel OCDMA/DWDM when the WDM laser sources have the frequency spacing reduced to 50 GHz. (b) After matched filtering using decode grating Q1*. The measured resolution is 10pm.* 136

Figure 5.17: *Eye diagrams of the decoded signals after reflection from the decode gratings Q1** λ_1*, Q2** λ_2*, Q3** λ_3 *and Q4** λ_4 *respectively at data rate of 311 Mbit/s.* 137

Figure 5.18: *BER measurements made against received optical power at data rate of 311 Mbit/s using decode gratings Q1** λ_1*, Q2** λ_2*, Q3** λ_3 *and Q4** λ_4 *in the presence other 15 interfering channels after transmission through the 44km of NZDSF.* 137

Figure 5.19: *Eye diagrams obtained at data rate of 622 Mbit/s for the (a) 20ps DWDM input pulse trains (b) after matched filtering using the decode gratings Q1* (c) improved eye diagrams after NOLM.* 138

Figure 5.20: *BER measurements obtained at data rate of 622 Mbit/s after nonlinear thresholding using the NOLM for all four decode gratings (Q1*, Q2*, Q3* and Q4*) strain-tuned to* λ_2*,* λ_3 *in the presence of other 15 interfering OCDMA/DWDM channels.* 139

Chapter Six: Reconfigurable OCDMA Phase Coders

Figure 6.1: *Schematic structure of the reconfigurable encoder/decoder. The grating is mounted on a fibre stretcher to allow flexible tuning of the overall grating central wavelength.* 149

***Figure 6.2**: 4cm Uniform fibre Bragg grating spectral reflectivity profile. (measured – solid line and calculated – dashed line). The peak reflectivity of the grating, R is ~75%.* 149

***Figure 6.3**: Phase shift obtained when various amount of electrical current is applied to the thin heating wire placed at the centre of the 4cm uniform grating. Inset shows the spectral reflectivity response obtained when a π-phase shift is induced at the centre of the uniform fibre Bragg grating.* 150

***Figure 6.4**: Induced phase shift as a function of the applied current obtained for 8cm uniform fibre Bragg grating. The dotted lines show the required amount of current to induce four different phase shifts.* 150

***Figure 6.5**: Experimental set up using 8-chip code-tunable encoder and decoder. EAM – Electro-Absorption modulator, MOD – Electro-optic modulator.* 152

***Figure 6.6**: Oscilloscope traces (measured: solid line and calculated: dashed line) after reflection off the code tunable grating, (a) encoder (b) decoder, when configured to the bipolar phase code shown in the inset.* 153

***Figure 6.7**: Measured (solid lines) and calculated (dashed lines) oscilloscope traces of the matched filtered output after encoding:decoding process for (a) correctly matched code (0π00πππ0:0πππ00π0) (b) incorrectly matched code (00ππ00ππ:0πππ00π0).The measured extinction between the peak autocorrelation pulse with the crosscorrelation sidelobes is 6.6 dB.* 154

***Figure 6.8**: Experimental set up. Q1* and Q2* are fixed-code SSFBGs.* 156

***Figure 6.9**: Phase modulation profile imprinted onto the grating during the writing process for decoders Q1* and Q2*.* 156

***Figure 6.10**: Oscilloscope traces of the decoded autocorrelation (left) and the crosscorrelation (right) outputs when the quaternary phase code-tunable encoder is programmed to generate Code Q1 (0, 0, 0, 1.5π, 1.5π, 0.5π, 1.5π, 0.5π, 0, π, 1.5π, 0.5π, 0, 0.5π, π, π). Code Q1 is the matched filtered code to Q1*. The measured extinction between the peak autocorrelation pulse with the crosscorrelation sidelobes is 5.4dB.* 157

***Figure 6.11**: Oscilloscope traces of the decoded autocorrelation (left) and the crosscorrelation (right) outputs when the quaternary phase code-tunable encoder is programmed to generate Code Q2 (0, 0, 0.5π, π, 0.5π, 1.5π, π, 0, π, 0.5π, 0, 0.5π, 1.5π, 0, π, 0). Code Q2 is the matched filtered code to Q2*. The measured extinction between the peak autocorrelation pulse with the crosscorrelation sidelobes is 5.5 dB.* 157

***Figure 6.12**: Eye diagrams obtained at a data rate of 622 Mbit/s when the code-tunable encoder is set to match the SSFBG decoder (a) Q1* and (b) Q2*.* 158

***Figure 6.13**: Bit-error-rate measurements under the influence of the reconfigurable encoder in comparison to that using a superstructured grating encoder and also for the back-to-back laser.* 158

Chapter Seven: OCDMA Architectures

Figure 7.1: *Block diagram showing the bi-directional spectrally interleaved OCDMA system on WDM architecture.* 162

Figure 7.2: *Full-duplex bi-directional spectrally interleaved OCDMA/DWDM experimental set-up. Q1-Q4: SSFBGs matched to the DWDM wavelengths. The schematics show the DWDM wavelength filtering using SSFBGs at various points along the system.* 165

Figure 7.3: *(a) Combined eight DWDM wavelengths separated in frequency by 50 GHz. (b) Downstream optical spectra obtained after matched filtering with decode grating Q2*. (c) Similar upstream results after matched filtering with grating Q3*.* 166

Figure 7.4: *(a) Downstream decoded eye diagram after matched filtering with grating Q2* at the data rate of 622 Mbit/s. (c) Similar upstream eye diagram after matched filtering with grating Q3*. The correctly decoded pulseforms have duration of 50ps.* 167

Figure 7.5: *BER measurements for bi-directional OCDMA/DWDM experiment at a data rate of 622 Mbit/s.* 168

Figure 7.6: *Schematic showing the proposed clock distribution OCDMA architecture.* 169

Figure 7.7: *Experimental setup to demonstrate the bi-directional, clock distributed OCDMA architecture. PPG – Pseudorandom Pattern Generator, ED – Error Detector, EOM – Electro-optic Modulator, ATT – optical attenuator.* 170

Figure 7.8: *Optical spectra showing (a) the combined 622 Mbit/s OCDMA coded channel and 622 MHz clock pulses, (b) the downlink decoded response using decoder SSFBG C1*, (c) the uplink decoded response using SSFBG B1*.* 172

Figure 7.9: *Oscilloscope traces after matched filtering for (a) code-tunable C1:SSFBG C1*, (b) code-tunable C2:SSFBG C2* and (c) SSFBGs B1:B1*. The measured resolution is 20ps for all three cases.* 173

Figure 7.10: *622 Mbit/s decoded eye diagrams for both downlink and uplink OCDMA channels.* 174

Figure 7.11: *BER results when both uplink and downlink channels are transmitting simultaneously at a data rate of 622 Mbit/s.* 175

Chapter Eight: Header Generation and Recognition for Optical Packet Switched Networks

Figure 8.1: *An optical packet structure, including both payload and header. (a) The optical header is transmitted in parallel by subcarrier multiplexing or on another optical channel. (b) The optical header is tagged in series with the data payload, separated by a guard band.* 180

Figure 8.2: *Architecture of an optical packet routing node. Dashed lines show electrical connections. Add (drop) ports allow packets to be added into (removed from) the optical networks.* 181

Figure 8.3: *Schematic showing the principle of optical header generation and recognition using SSFBGs.* 183

Figure 8.4: *Parallel decoder SSFBGs configuration.* 184

Figure 8.5: *Block diagrams showing the optical packet switching experiment. The architecture of the packet add/drop and re-label node is shown inset. Input packets enter the node at Rx and appropriate packets being switched out at Tx.* 185

Figure 8.6: *Experimental optical packet switching system configuration and associated optical outputs. The packet structure is shown inset.* 186

Figure 8.7: *Phase modulation profile, measured and calculated spectral reflectivity plots of SSFBG (a) H1 and (b) H2.* 187

Figure 8.8: *SHG Intensity autocorrelation measurements of the header pulse before encoding (solid line), after matched filtering (dashed line) and after reshaping in the NOLM (circles).* 188

Figure 8.9: *BER measurements on dropped Packet 3 after one-hop operation.* 189

Figure 8.10: *Multi-wavelength optical packet structure based on serial encoding.* 190

Figure 8.11: *An NxN multi-wavelength optical packet routing node.* 191

Figure 8.12: *Experimental configuration of the multi-wavelength packet transmitter.* 191

Figure 8.13: *Multi-wavelength packet structure used in the experiment. H1 and H2 are the coded pulse sequences generated by reflection from the SSFBGs.* 192

Figure 8.14: *Experimental configuration of the multi-wavelength optical packet router.* 193

Figure 8.15: *(a) Optical spectrum incident to the demultiplexing AWG. (b) Optical spectrum of a dropped wavelength channel. The measured resolution was 10pm.* 194

Figure 8.16: *A: Packet structure at a particular wavelength showing two headers and the associated packets.*
B: Corresponding decode signal after matched filtering using decoder grating H1.*
C&D: Dropped packets at output ports 1 and 2 respectively. 195

Figure 8.17: *(a) BER of header recognition in the absence of the attached payloads and WDM MUX:DEMUX. (b) BER of the packet recognition for the full system in the presence of multiple WDM wavelengths.* 196

Figure 8.18: *Self-routing optically packet switched mesh network architecture. The packet structure and self-routing principle is illustrated. Matched filtering of the cascaded header using an array of decoder gratings allows self-routing of the packet at each node. The schematic shows a cascaded header and payload being self-routed across the core network from the source edge node to the destination edge node.* 198

Figure 8.19: *Schematics showing the two-node self-routing demonstration. The notation* $Q_{1,2}$ *refers to optical header that will be decoded at* $OPSN_1$ *and will exit the node at output 2.* 199

Figure 8.20: *Self-routing optical packet switching experimental setup. The packet routes and associated outputs are shown. The packets P1, P2 and P3 were labelled with optically coded cascaded headers denoted by* $Q_{1,1}$ $Q_{2,1}$, $Q_{1,2}$ $Q_{2,2}$ *and* $Q_{1,1}$ $Q_{2,2}$ *respectively.* 199

Figure 8.21: *Schematics showing a packet labelled containing four unique routing codes being routed through four OPSNs before arriving at its destination.* 201

Figure 8.22: *(a)-(e) Oscilloscope traces showing the cascaded header before and after the decoding operation on each of the four codes.* 201

Figure 8.23: *BER measurements obtained for each of the four codes in the cascaded header after the decoding operation.* 202

Conclusions and Future Directions

Figure 1: *Proposed asynchronous DS-OCDMA test bed.* 208

Acknowledgements

It has been a tremendous three years of learning experience at the Optoelectronics Research Centre that I will always remember. The ORC provides me with countless opportunities working with experience people who have, on many occasions, provided me with invaluable advice and guidance. I would like to take this opportunity to express my sincere gratitude to all of them.

First and foremost, many thanks to my supervisor Prof. David Richardson for his constant support, guidance and patience throughout my PhD years. It has been an exciting three-year working under his supervision.

I am indebted to Dr. Periklis Petropoulos for his assistance and guidance in the early stages of my PhD projects.

I would like to express my sincere thanks a good friend of mine, Mr. Morten Ibsen, who fabricated all the superstructure fibre Bragg gratings described throughout this thesis. Thank you for your constant support and help throughout my PhD years.

I would also like to thank all the people in the Advanced Fibre Technologies and Applications group, for being my close friends and co-workers in various experiments. Especially, I would like to thank Mr. Ju Han Lee for providing his assistance and expertise in undertaking the nonlinear thresholding experiments, Dr. Benn Thomsen for his advise in the optical packet switching experiments, Dr. Li Bin Fu for his help in constructing the DFB fibre lasers to be used in various OCDMA experiments, described in Chapter Five and Dr. Neil Broderick for useful discussions. It has also been a great pleasure to work with Mr. Zulfadzli Yusoff, Mr. Mohd. Ridzuan Mokhtar, Mr. Fabio Ghiringhelli, Mrs. Anoma McCoy, Mr. Paulo Almeida, Miss Francesca Parmigiani. Your contributions have made my PhD years at the ORC the most meaningful and enjoyable experience I will never forget.

My sincere thank you also goes to Mr. Simon Butler and Mr. Tim McIntyre for various helps in the mechanical workshop.

I gratefully acknowledge the Overseas Research Studentships (ORS) committee for supporting my PhD tuition fees and the ORC for providing the necessary stipends during the course of my PhD. Many thanks also to the IEEE Laser and Electro-Optic Society (LEOS) for awarding me with the prestigious 2001 IEEE/LEOS Graduate Student Fellowships Award. I would also like to acknowledge Southampton Photonics Inc. (SPI) for funding the OCDMA activities.

Finally, I would also like to acknowledge the useful past discussions and inputs from Prof. Anatoly Grudinin, Dr. Saif-ul Alam, Dr. Johan Nilsson, Mr. Alexander Fu, Dr. Harald Geiger, Prof. Mikhail Zervas and Dr. Richard Laming.

Principle Abbreviations

ASE	Amplified Spontaneous Emission
BER	Bit-Error-Rate
CDMA	Code Division Multiple Access
CW	Continuous-wave
DFB	Distributed feedback
DSF	Dispersion shifted fibre
DS-OCDMA	Direct Sequence Optical Code Division Multiple Access
DWDM	Dense Wavelength Division Multiplexing
EDFA	Erbium doped fiber amplifier
EFRL	Erbium Fibre Ring Laser
FBG	Fibre Bragg Grating
FE-OCDMA	Frequency Encoded Optical Code Division Multiple Access
FH-OCDMA	Frequency Hopped Optical Code Division Multiple Access
FWHM	Full Width Half Maximum
GVD	Group Velocity Dispersion
LED	Light Emitting Diode
LFSR	Linear Feedback Shift Register
MAN	Metropolitan area network
NRZ	Non Return to Zero
OCDMA	Optical Code Division Multiple Access
OTDM	Optical Time division multiplexing
RF	radio frequency
RZ	Return to Zero
SC	Supercontinuum
SHG	Second Harmonic Generation
SPM	Self Phase Modulation
SSFBG	SuperStructure Fibre Bragg Grating
TDM	Time Division Multiplexing
UV	Ultra Violet
WDM	Wavelength division multiplexing

Chapter 1

A Review on Optical Code Division Multiple Access (OCDMA)

Overview

This chapter introduces the topic of OCDMA and reviews the various technological approaches that have been suggested to perform the key function of optical code generation and recognition. The first OCDMA demonstration based on SSFBGs encoder and decoder is also described in the review.

1.1 Introduction

The explosive growth of the Internet over recent years has placed increasing demands on both the capacity and the functionality of optical transmission systems and networks. Internet traffic has been doubling every four to six months and this trend has created a tremendous requirement for the development of future optical networks capable of delivering broadband and multi-protocol data services in a flexible manner where and when needed. Apart from offering the Quality of Service (QoS)[1] required, the optical network should also be capable of supporting enormous capacities, up to several Tbit/s in total network throughput. Most works reported to date have focused on the use of wavelength division multiplexing (WDM), time division multiplexing (TDM) or a hybrid approach, to achieve the Tbit/s aggregate channel capacity required. Now that data rates up to tens of Tbit/s have been demonstrated in the laboratory [1-5], interest is beginning to grow in investigating alternative multiplexing schemes such as optical code division multiple access (OCDMA) that can further enhance the functionality of future optical networks.

---

[1] **Quality of Service (QoS)** refers to certain guarantees on the maximum packet delay as well as the variation in the delay, and guarantees on providing a minimum average bandwidth for each connection.

The Optical Code Division Multiple Access (OCDMA) technique is based on the CDMA spread spectrum technique that has been implemented with success in the wireless domain [6]. Spread spectrum technology was developed in the mid 1950s as an alternative form of transmission technique, which promised a means to overcome the rigid restrictions in radio bandwidth allocation. It is based on the idea of spreading the spectrum of a narrowband message over a much wider frequency spectrum according to some digital codes. Due to the spreading action, the transmitted signal arrives at the receiver as a noise-like signal, and the message recovery is impossible unless the original code is known, as will be the case for an authorized user. In this case the received signal is correlated by the authorized receiver with a local code, which is a replica of the one used by the transmitter, and in this case de-spreading (code recognition) and signal recovery in the presence of interference from other sources can be accomplished (see Figure 1.1 for a wireless typical spread spectrum network). The spread spectrum technique has found immediate application in military communications as a method for transmitting signals in very noisy environments with very high security.

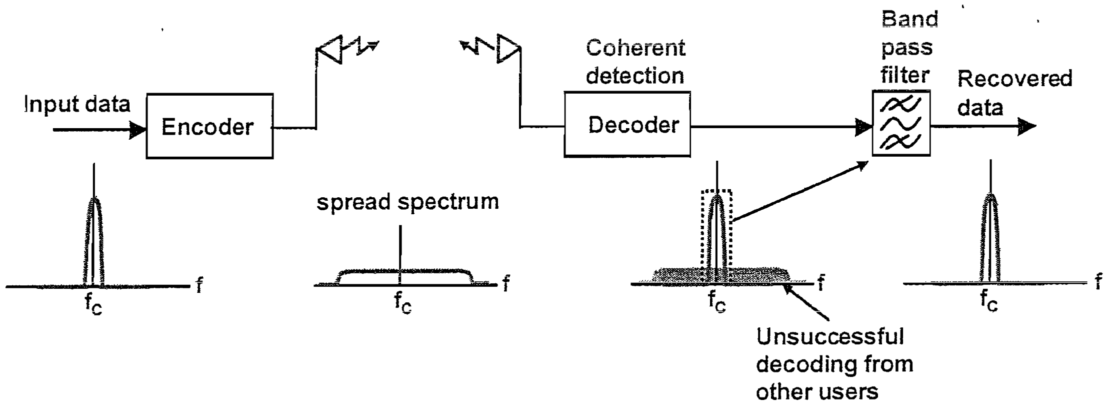

Figure 1.1: Schematic showing a typical radio CDMA network based on spread spectrum technique. Information bits to be transmitted are 'spread' by means of a digital code. At the receiver, the intended spread spectrum signal is recovered using a receiver having a correct code and bandpass filtered to remove the interfering signals from other users. Note: f_c denotes the carrier frequency.

Following the emergence of satellite technology and the vast advancement and worldwide deployment of mobile communications networks, the spread spectrum technique has begun to be widely adopted as a new multiple access technique, known as CDMA, replacing the more conventional PCN and GSM[2] networks. This is achieved by allocating a unique code to each individual user and distinguishing them from other users by code division multiplexing and demultiplexing. The new technique has proved to be extremely effective, and currently several satellite systems operate under the CDMA format [7]. Almost immediately, this scheme was adopted by the mobile communications community and proved to offer greater capacity and potential in an environment, which is under very tight frequency allocation control. The next generation of cellular networks in North America, United Kingdom, Japan and indeed all other major parts of the world, have begun using or are at least planning to use CDMA.

The primary difference between radio CDMA and optical CDMA (OCDMA) is the manner in which the signal is detected. OCDMA reception is based on optical light (intensity) converted to an electrical signal in a photodetector rather than amplitude (electric field) detection as in radio CDMA. A radio CDMA receiver is based on the homodyne detection technique in which a local copy of the code used to spread the transmitted signal is mixed with the spread spectrum signal and the resulting signal integrated over a bit/code period. The output of the receiver greatly depends on the correct alignment of the local code to the received signal. Such an approach can be easily adopted in radio CDMA since it is possible to implement complicated control loops in the receiver to synchronise and track the received signal. However, such an approach is not readily applicable in the optical domain. The matched filtering technique is hence the preferred method for detection in optical CDMA. A matched filter is defined by the relationship between its impulse response and a particular received pulse shape that it has been designed to filter. Convolution of the correct received code with the impulse response of the filter results in a readily recognised output pulse (this is also known as the autocorrelation signature). Conversely the convolution of the incorrect code with the filter results in a low-level, noise-like output (this is known as the crosscorrelation signature). Figure 1.2 illustrates a basic OCDMA network.

---

[2] **Personal Communication Networks (PCN)** and **Global System for Mobile Communication (GSM)** refer to two globally accepted standard for digital cellular communication.

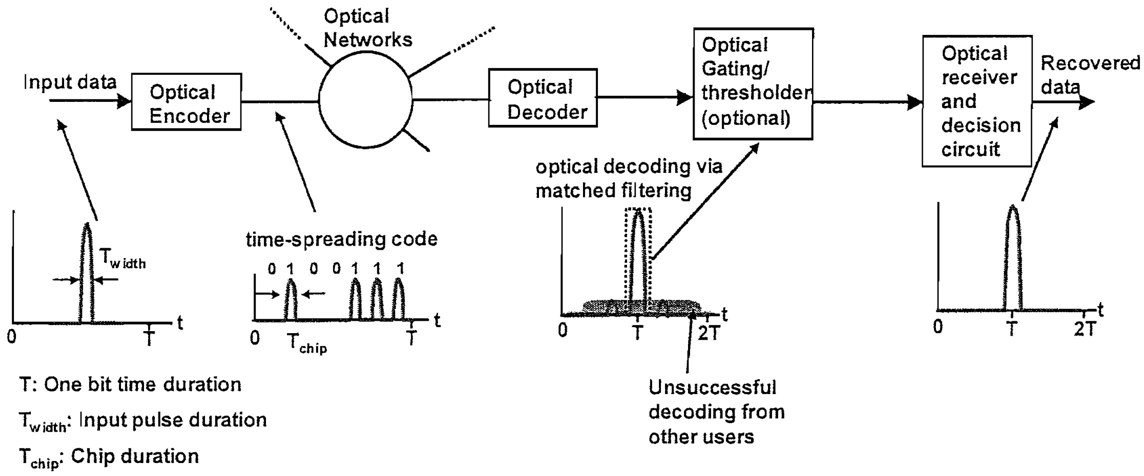

Figure 1.2: Schematic showing a typical OCDMA network based on time-spreading and matched filtering process. Information bits are encoded all-optically with a unique code before transmission into fibre optic network. At the receiving end, the intended information can be recovered using a matched filter having the correct code. Time domain optical gating can be used to improve the recovered signal contrast.

In general, OCDMA techniques can be grouped into two major categories (based on the type of optical sources and the detection techniques employed): coherent or incoherent. Coherent OCDMA techniques are based on using interference of the incoming optical signals to convert electric field values into intensity variations that can then be detected by a photoreceiver [8]. Thus it enables cancellation of undesired user channels through destructive interference. Coherent detection allows bipolar phase codes (-1/1 code sequences) to be used as in radio CDMA, but optical implementations have until now required either expensive or complicated systems [9]. More recently, several approaches have been suggested and demonstrated that allow the optical phase of the light to be manipulated. This opens the possibility of using phase coding adopted from the radio CDMA to be implemented in coherent OCDMA networks.

By contrast, incoherent detection OCDMA systems detect the optical signal directly without the use of coherent interference, thus the detected signal is simply the superposition of the incoming optical signals. As optical intensity is a non-negative value, this makes it impossible to achieve perfect cancellation between interfering channels. Coding is limited to unipolar schemes (0/1 code sequences), which by their very nature do not allow for perfect orthogonality between users. However, schemes using balanced detection have been proposed to overcome this limitation of unipolar codes [10]. Also, the incoherent nature of the processing enables the use of inexpensive broadband sources such as light emitting diodes (LEDs) and amplified spontaneous noise (ASE) sources, which is an attractive option for cost sensitive metropolitan/access networks. Other benefits of using an incoherent source include reduced sensitivity to both environmental changes and polarization problems. Nonetheless, the excess photon noise due to the incoherent nature of the source remains to date, a major limiting factor in OCDMA techniques employing incoherent sources.

Within the coherent OCDMA approach, the optical encoding/decoding process can be performed in the frequency domain (frequency-encoded FE-OCDMA and frequency-hopping FH-OCDMA) and time domain (direct sequence DS-OCDMA). The first technique, known as the frequency-hopping FH-OCDMA, is performed in the frequency domain. The information signal is modulated onto a carrier whose frequency is changed over a wide set of discrete frequencies according to a well-defined pseudo random code sequence. The transmitted signal contains a stream of carrier bursts, which hop around the frequency spectrum at a rate greatly in excess of the data rate. In order to receive the frequency-hopped signal, a narrowband frequency filter is incorporated within the receiver whose tuning sequence is synchronised to that of the transmitter. Figure 1.3 shows a schematic of the FH-OCDMA approach.

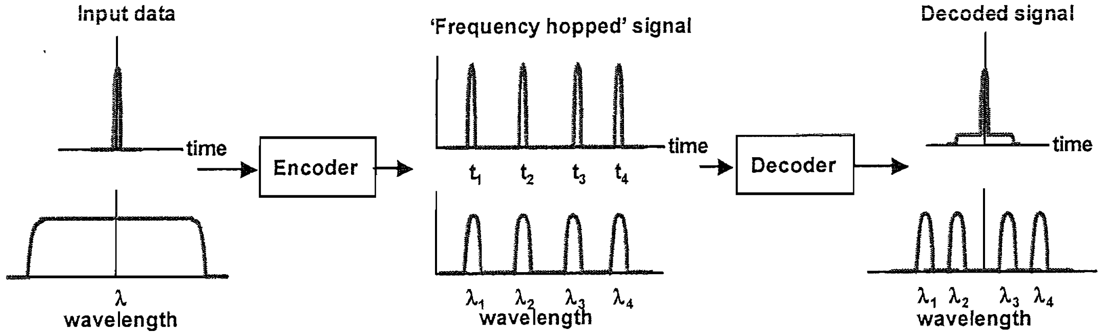

Figure 1.3: Coherent FH-OCDMA technique. The 'frequency hopped' encoded signal contains a train of pulses in which their carrier frequencies is changed according to the frequency- hopped code.

This is in contrast to the frequency encoded FE-OCDMA technique in which the broad spectral bandwidth of the information signal is encoded into a code consisting of a number of discrete spectral components. This approach is also known as the spectral encoding OCDMA and the schematics of an FE-OCDMA system is shown in Figure 1.4.

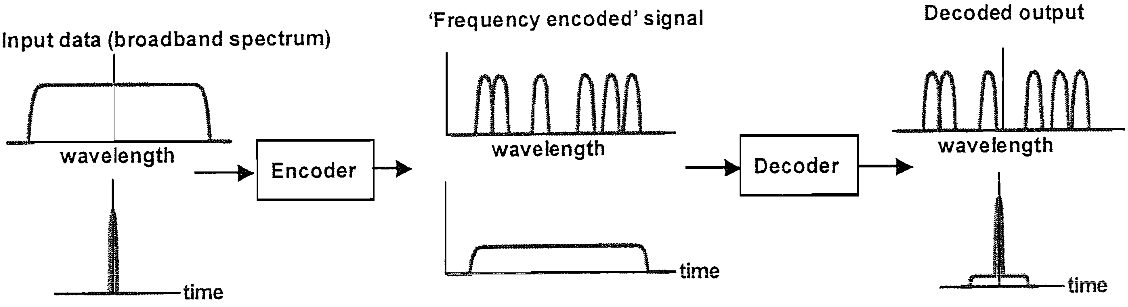

Figure 1.4: FE-OCDMA technique. An input broadband signal is sliced into individual frequency components according to an amplitude/phase modulated spectral code. As a result, a short, high intensity input pulse is transformed into a long duration, low intensity frequency encoded signal in the time domain.

An alternative to the FH-OCDMA and FE-CDMA techniques is the direct sequence DS-OCDMA performed in the time domain (see Figure 1.5). In DS-OCDMA each data bit to be transmitted is defined by a code composed of a sequence of pulses. The individual pulses comprising the coded bit are commonly referred to as chips. The coded bits are then broadcast onto the network /but are only received by users with a receiver designed to unambiguously recognize data bits of the given specific address code.

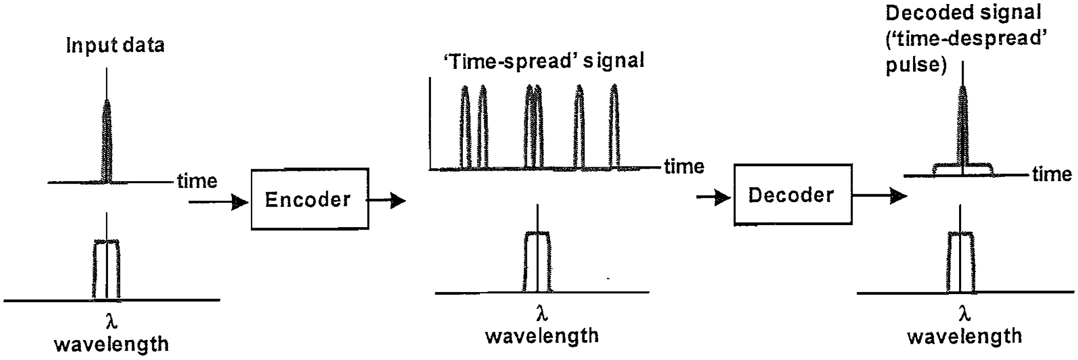

Figure 1.5: DS-OCDMA technique. The encoded 'time-spread' signal comprises of a sequence of pulses according to the code sequence defined at the direct sequence encoder.

OCDMA approach offers the advantage of being a totally asynchronous system requiring no clock signals for synchronisation in the networks. Hence the OCDMA network topology is simpler and offers the potential for scalability to higher levels of connectivity. The inherent security in transmission offered by the OCDMA encoding/decoding process also provides a level of security directly implemented in the physical layer [11, 12]. These advantages make OCDMA attractive for use in optical networks compared to the conventional time domain multiplexing (TDM), frequency division multiplexing (FDM) or wavelength division multiplexing (WDM) which are based on time, frequency and wavelength allocation respectively. OCDMA approach also enables high spectral efficiency to be achieved [13], enabling such optical networks to achieve throughputs in excess of Tbit/s by making efficient use of the available fibre bandwidth.

1.2 Review on various coherent OCDMA coding/decoding schemes

Since OCDMA is still in the very earliest stages of technological development, a fundamental issue relates to how to reliably generate and recognize appropriate code sequences. (The issue of what constitutes an appropriate code sequence is described in Chapter 2 of this thesis). The first work in OCDMA dated back to the late 1970s in the area of fibre delay lines for optical processing [14]. This work formed the basis for a range of modern OCDMA approaches based on incoherent and coherent OCDMA using matched filtering process. This section will focus on providing a brief summary of the various all-optical encoding/decoding schemes that use coherent optical light sources.

To date the most common approach is to use arrays of discrete optical waveguide based delay lines to temporally, or sometimes spectrally, manipulate the individual data bits in order to perform the coding and decoding process. In the earliest implementations the delay lines used were simple optical fibres of different lengths appropriately coupled together using fibre couplers as shown in Figure 1.6 [15-18].

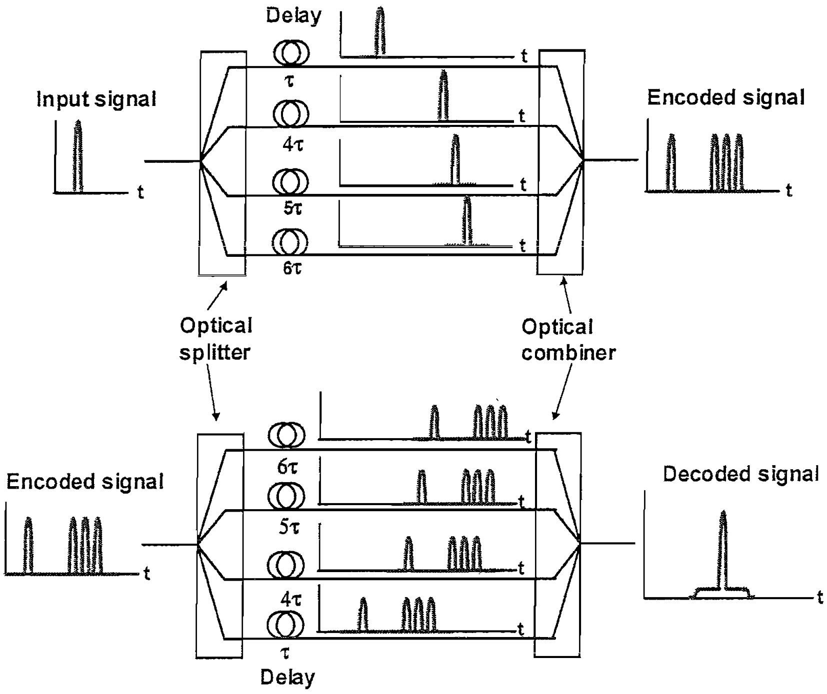

Figure 1.6: Fibre delay lines based optical encoder and decoder for DS-OCDMA approach.

Here the main issues that arise concern the difficulty in maintaining the accurate delays that constitutes the code sequence and compensation of the changes in fibre lengths due to environmental conditions. Lam et. al. proposed a multistage Mach-Zender interferometer chain fabricated on a silica planar waveguide to overcome these issues and the receiver used balanced detection scheme to enhance the code recognition recovery [19]. Alternative optical waveguide technology have also been proposed and demonstrated for use in OCDMA system: Tsuda et. al. reported on the use of arrayed waveguide gratings with a phase filter to perform the spectral encoding and decoding [20]. More recently, Wada et. al. demonstrated an integrated planar lightwave circuit (PLC) that contained the tunable taps, optical phase shifters, delay lines and optical splitters/combiners [21, 22]. The structure of the PLC based encoder/decoder is shown in Figure 1.7. The PLC is installed in a temperature-controlled box to provide good stability against environmental fluctuations. Such PLC-based optical encoders/decoders were capable of producing bipolar codes (where the chip encoding is 0 and π rather than 0 and 1 in unipolar signalling). Whilst these approaches (waveguide based devices) indeed represent a more practical approach that using discrete optical fibre delay lines, PLCs (and other waveguide based devices) are difficult and expensive to fabricate and are therefore a far from ideal technical solution. Such devices also have limited scalability with up to only 32-chip code sequences generated using the PLCs technology [23].

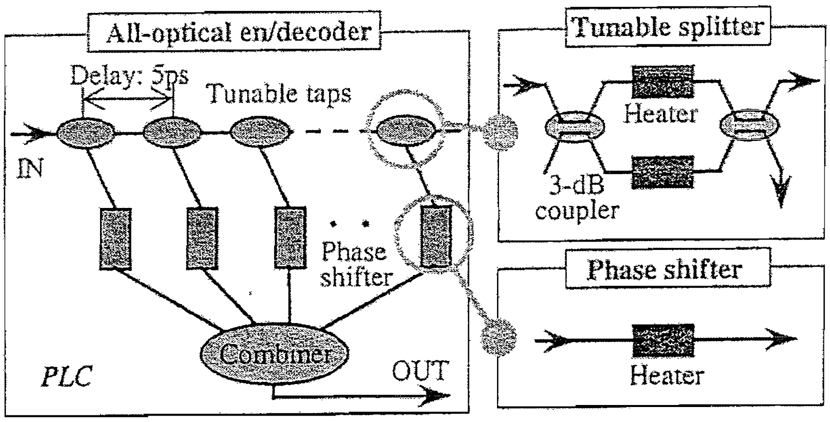

Figure 1.7: Optical encoder/decoder based on PLC technology to implement DS-OCDMA approach.

An alternative approach, and one that does not rely upon individual discrete waveguides to provide different paths through the system in order to perform the necessary pulse spreading and shaping is to use diffractive free space optics, configured in a Fourier optical 4F set-up as shown in Figure 1.8 [24]. The standard approach is to employ a bulk grating pair to spatially separate, and then recombine, the individual frequency components of a short pulse. A spatial phase mask can then be used to perform the necessary filtering functions and to reshape the pulse [9, 25]. The source consists of a broadband, sub-picosecond pulse laser, which is electro-optically modulated with a data stream. Spatial decomposition of the spectral components of the modulated pulses is obtained using a diffraction grating, and the phase encoding is achieved by the insertion of a specially patterned phase mask. A second diffraction grating is used to recombine the encoded spectral components, prior to transmission. At the receiver, de-spreading is achieved through an identical process, except that the phase mask used is the complex conjugate of that in the transmitter. Again, this bulk-optics approach is again of somewhat limited practical value due to lack of compactness, spectral/temporal resolution and cost.

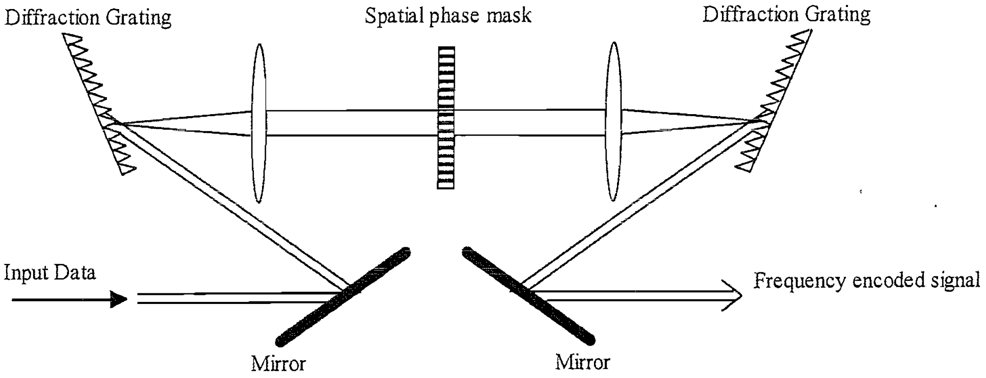

Figure 1.8: FE-OCDMA implementation using bulk optics. The decoder has the same configuration as the encoder but with the input signal replaced by the frequency encoded signal from the network and the output detected via a photodetector.

Karafolas et. al. suggested the use of electro-optic phase modulators to perform the optical encoding and decoding [26, 27]. The information signal is first electronically encoded with a digital code before being applied to the encoder phase modulator. The encoder phase modulator modulates the phase of a narrow linewidth optical carrier according to the digital code to produce bipolar code sequences. At the receiver, a similar electro-optic phase modulator driven by a local synchronised digital code is used to retrieve the information signal. Such approach suffers from the disadvantage that the individual chip duration of the code sequence tends to be very long, hence limiting the overall bit rate achievable.

More recently, passive 'single beam' encoding and decoding schemes based on fibre Bragg grating (FBG) technology have been proposed and demonstrated. The most straightforward approach is to use an array of FBGs written/or spliced in a sequence along a single fibre length [28, 29] to implement the FH-OCDMA approach. The spatial position of the gratings and their associated reflection profile can then be used to encode both temporal and spectral information onto an incident data pulse. Fathallah et. al. proposed that multiple gratings of different central wavelengths could be written/spliced into a single piece of fibre, thereby slicing the wide spectrum of an ultrashort optical pulse into different time slots so as to define the individual chips within the code (see Figure 1.9 for the physical implementation) [28]. The frequency hopped pulse sequence could then be recomposed at the receiver simply by using an identical array of gratings illuminated from the opposite end. Both the encoding and decoding gratings could be strain tuned to ensure a perfect match between the discrete wavelengths. Such approach has also been demonstrated by Wada et. al. using a coherent supercontinuum[3] optical source [30]. The use of chirped Moiré fibre gratings to perform simultaneous encoding in both wavelength and time domain was proposed by Chen et. al. in [31]. A chirped Moiré grating is made from the superposition of two linearly chirped Bragg gratings of different but closely spaced Bragg wavelengths. This enabled the grating pattern to develop fringes, where the phase of the grating changes by π, thereby producing narrow stop bands when the grating is used in the reflection mode. Thus, the spectral response of the grating is divided into segments (the number of which depends on the choice of the beating Bragg wavelengths) and each segment constitutes a chip of the spectral code. The encoding grating performs two functions: spectral slicing and temporally arranging these spectral components in a linear fashion, i.e. temporal spreading. If the decoder is the physically reversed structure of the encoder, then the filtering operations are identical and the temporal arrangements of the wavelength components are complementary so that the decoder grating can recover all of the wavelengths of the encoded signal into the same time slot, i.e de-spread the signal. Such frequency-hopped approaches either require wide bandwidth optical sources or a fast tunable

---

[3] **Supercontinuum (SC)** source is capable of generating hundreds of highly coherent optical carriers with uniform channel spacing. The SC is a spectral broadening phenomenon and is obtained when a nonlinear fibre is optically pumped by a picosecond pulse source. It occurs due to the combined effects of self-phase modulation, cross-phase modulation and parametric four-wave mixing.

lasers with fast switches to generate the multiple frequencies, which places significant disadvantages both in terms of cost and feasibility.

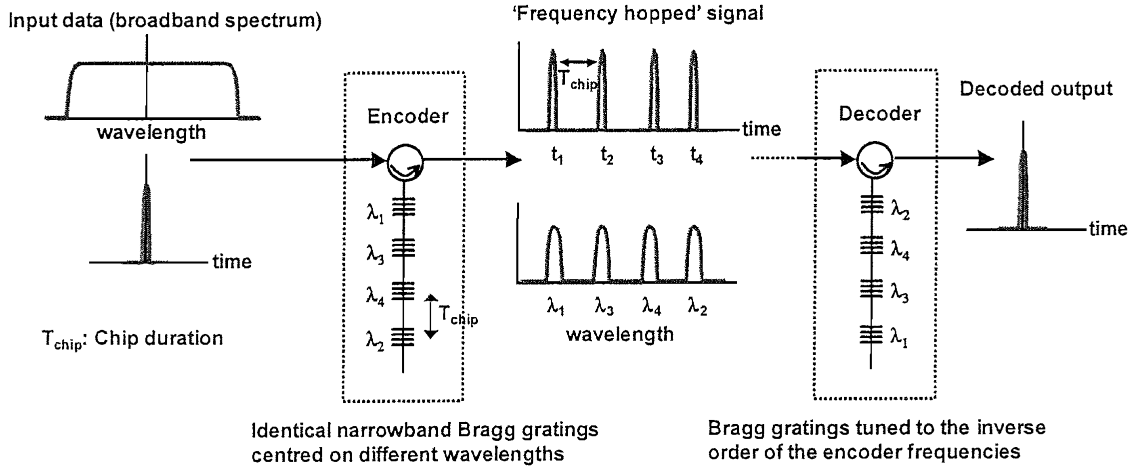

Figure 1.9: Frequency hopped OCDMA implementation using arrays of narrowband fibre Bragg gratings.

More recently, grating technology has progressed to the point that the optical phase of light reflected from 'individual' gratings can also be exploited and accurately controlled, allowing the use of optical phase as a coding parameter in the DS-OCDMA environment (note that this is already possible using PLC technology [21]). Use of phase coding is significant since it is well known that bipolar codes exhibit far better cross-correlation/cross-talk characteristics than amplitude only unipolar codes. This key aspects of phase encoding allows lower interchannel interference, and thus more simultaneous users for a given code length (and associated optical bandwidth) than unipolar coding. This ultimately permits a higher overall system spectral efficiency relative to unipolar coding and can be combined with the WDM scheme to support a large user in a DS-OCDMA/WDM network.

The use of bipolar codes with FBG technology was first demonstrated using a segmented FBG array, which comprised of uniform period gratings with an accurately controlled phase (pathlength) between individual gratings [32]. The phase mask used to 'imprint' the grating into the fibre defined the precision of the grating structure in this experiment, which places significant practical limits to the length and accuracy with which such an array could be written, as well as the flexibility in writing many gratings with different codes.

Another alternative approach to the discrete FBG array based pulse encoders and decoders discussed above is to use Superstructured fibre Bragg gratings (SSFBGs). Figure 1.10 shows a schematic outlining the use of SSFBG to perform pulse encoding/decoding function.

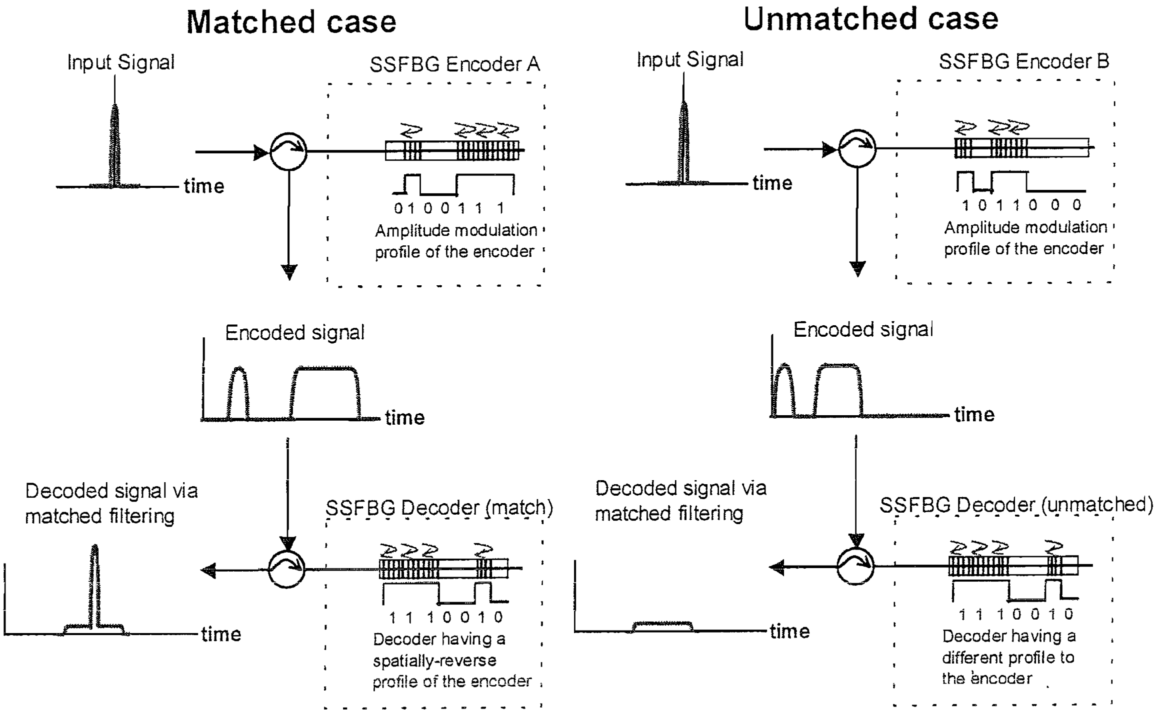

Figure 1.10: Outline of the physical approach of pulse encoding and decoding using SSFBG's. When short optical pulses are reflected from the encoder grating, they are reshaped into coded pulse sequences according to the superstructure profile (OCDMA code) imprinted into the grating. At the receiver, a matched filter of the encoder is required for the decoding process. This is formed by using a decoder grating identical to the encoder but illuminated from the opposite end. Sharp correlation peak can be obtained at the output when the encoded signal matches the decoder grating (see matched case), otherwise, no peak correlation can be seen if incorrect coded signal (or otherwise an incorrect decoder) is used (see unmatched case).

The SSFBG fabrication technique is based on the 'continuous grating writing' approach developed at the University of Southampton that allows the possibility of essentially continuous amplitude and phase control along an individual grating structure [33]. This particular technique is attractive in that it is far more flexible from a fabrication perspective than other techniques so far demonstrated and therefore allows for a far broader range of codes, and potential coding schemes. Most significantly it is also not bounded by the current resolution limits and device lengths imposed by phase mask technology and offers a great scope for the production of low cost filtering devices.

The first demonstration of pulse encoding/decoding using SSFBG was reported by Geiger et. al. in 1998 [34]. The aim of the experiment was to explore the feasibility of using the SSFBG approach to perform coherent, passive direct sequence pulse encoding/decoding functions suitable for applications in DS-OCDMA systems. The single-user experiment employed 7-chip unipolar SSFBGs to perform the elementary optical encoding and decoding functions at a repetition rate of 125 MHz. The success of this initial experiment paves way for further investigations into the potentials of this promising technology for OCDMA systems and a wide range of associated pulse processing applications.

References

[1] G. Vareille, B. Julien, F. Pitel, and J. F. Marcerou, "3.65 Tbit/s (365x11.6 Gbit/s) transmission experiment over 6850km using 22.2 GHz channel spacing in NRZ format," presented at European Conference on Optical Communication (ECOC2002), paper PD.M.1.7 (postdeadline), 2001.

[2] S. Bigo, W. Idler, J.-C. Antona, G. Charlet, C. Simonneau, M. Gorlier, M. Molina, S. Borne, C. d. Brarros, P. Sillard, P. Tran, R. Dischler, W. Poehlamn, P. Nouchi, and Y. Frignac, "Transmission of 125 WDM channels at 42.7 Gbit/s (5 Tbit/s capacity) over 12x100km of TeraLight TM Ultra fibre," presented at European Conference on Optical Communication (ECOC2001), paper PD.M.1.1 (postdeadline), 2001.

[3] D. G. Foursa, C. R. Davidson, M. Nissov, M. A. Mills, L. Xu, J. X. Cai, A. N. Pilipetskii, Y. Cai, C. Breverman, R. R. Cordell, T. J. Carvelli, P. C. Corbett, H. D. Kidorf, and N. S. Bergano, "2.56 Tb/s (256x10 Gb/s) transmission over 11,000km using hybrid Raman/EDFAs with 80nm of continuous bandwidth," presented at Optical Fibre Communication Conference (OFC2002), paper FC3 (postdeadline), 2002.

[4] B. Zhu, L. Leng, L. E. Nelson, L. Gruner-Nielsen, Y. Qian, J. Bromage, S. Stulz, P. Gaarde, A. Judy, B. Palsdottir, R. L. Lingle, S. Kado, Y. Emori, and S. Namiki, "3.2 Tb/s (80 x 42.7 Gb/s) transmission over 20x100km of non-zero dispersion fiber with simultaneous C+L-band dispersion compensation," presented at Optical Fiber Communication Conference (OFC2002), paper FC8 (postdeadline), 2002.

[5] Y. Frignac, G. Charlet, W. Idler, R. Dischler, P. Tran, S. Lanne, S. Borne, C. Martinelli, G. Veith, A. Jourdan, J.-P. Hamaide, and S. Bigo, "Transmission of 256 wavelength-division and polarisation-division-multiplexed channels at 42.7 Gb/s (10.2 Tb/s capacity) over 3x100km of TeraLight fiber," presented at Optical Fiber Communication Conference (OFC2002), paper FC5 (postdeadline), 2002.

[6] R. Dixon, *Spread Spectrum Systems.* New York: Wiley-Interscience.

[7] D. Grosbie, "The new space race satellite mobile communications," *IEE Review*, 1993.

[8] H. P. Sardesai, C.-C. Chang, and A. M. Weiner, "A femtosecond code-division multiple access communication system test bed," *IEEE Journal of Lightwave Technology*, vol. 16, pp. 1953-1964, 1998.

[9] T. Dennis and J. F. Young, "Optical implementation of bipolar codes," *IEEE Journal of Quantum Electronics*, vol. 35, pp. 287-291, 1999.

[10] D. Zaccarin and M. Kavehrad, "An optical CDMA system based on spectral encoding of LED," *IEEE Photonic Technology Letters*, vol. 5, pp. 479-482, 1993.

[11] L. Tancevski and I. Andonovic, "Hybrid wavelength hopping/time spreading schemes for use in massive optical networks with increased security," *IEEE Journal of Lightwave Technology*, vol. 14, pp. 2636-2647, 1996.

[12] L. Tancevski, I. Andonovic, and J. Budin, "Secure optical network architectures utilizing wavelength hopping/time spreading codes," *IEEE Photonic Technology Letters*, vol. 7, pp. 573-575, 1995.

[13] H. Sotobayashi, W. Chujo, and K. Kitayama, "1.6 bit/s/Hz, 6.4 Tbit/s OCDM/WDM (4 OCDM x 40 WDM x 40 Gbit/s) transmission experiment," presented at 27th European Conference on Optical Communication (ECOC2001), Amsterdam, Holland, 2001.

[14] E. Marom and O. G. Ramer, "Encoding-decoding optical fibre network," *IEE Electronics Letters*, vol. 14, pp. 48, 1978.

[15] P. R. Prucnal, M. A. Santoro, and T. R. Fan, "Spread spectrum fiber-optic local area network using optical processing," *IEEE Journal of Lightwave Technology*, vol. 4, pp. 547-554, 1986.

[16] R. M. Gagliardi, A. J. Mendez, M. R. Dale, and E. Park, "Fiber-optic digital video multiplexing using optical CDMA," *IEEE Journal of Lightwave Technology*, vol. 11, pp. 20-26, 1993.

[17] D. A. Chapman, P. A. Davies, and J. Monk, "Code-Division Multiple-Access in an optical fiber LAN with amplified bus topology: the SLIM bus," *IEEE Transaction on Communications*, vol. 50, pp. 1405-1408, 2002.

[18] D. D. Sampson, R. A. Griffin, and D. A. Jackson, "Photonic CDMA by coherent matched filtering using time-addressed coding in optical ladder networks," *IEEE Journal of Lightwave Technology*, vol. 12, pp. 2001-2010, 1994.

[19] C. F. Lam, D. T. K. Tong, M. C. Wu, and E. Yablonovitch, "Experimental demonstration of bipolar optical CDMA system using a balanced transmitter and complementary spectral encoding," *IEEE Photonic Technology Letters*, vol. 10, pp. 1504-1506, 1998.

[20] H. Tsuda, H. Takenouchi, T. Ishii, K. Okamoto, T. Goh, K. Sato, A. Hirano, T. Kurokawa, and C. Amano, "Spectral encoding and decoding of 10 Gbit/s femtosecond pulses using high resolution arrayed-waveguide grating," *IEE Electronics Letters*, vol. 35, pp. 1186-1187, 1999.

[21] N. Wada and K. Kitayama, "A 10Gb/s optical code division multiplexing using 8-chip optical bipolar code and coherent detection," *IEEE Journal of Lightwave Technology*, vol. 17, pp. 1758-1765, 1999.

[22] K. Kitayama, H. Sotobayashi, and N. Wada, "Optical Code Division Multiplexing (OCDM) and its applications to photonic networks," *IEICE Transaction on Fundamentals (Special Section on Spread Spectrum Techniques and Applications)*, vol. E82-A, pp. 2616-2626, 1999.

[23] K. Kitayama and N. Wada, "Photonic IP routing," *IEEE Photonic Technology Letters*, vol. 11, pp. 1689-1691, 1999.

[24] A. M. Weiner, D. E. Leaird, J. S. Patel, and J. R. Wullert, "Programmable shaping of femtosecond pulses by use of a 128-element liquid crystal phase modulator," *IEEE Journal of Quantum Electronics*, vol. 28, pp. 908-920, 1992.

[25] C.-C. Chang, H. P. Sardesai, and A. M. Weiner, "Code-division multiple-access encoding and decoding of femtosecond optical pulses over a 2.5-km fiber link," *IEEE Photonic Technology Letters*, vol. 10, pp. 171-173, 1998.

[26] N. Karafolas and D. Uttamchandani, "Optical CDMA System using Bipolar Codes and based on narrow passband optical filtering and Direct Detection," *IEEE Photonic Technology Letters*, vol. 7, pp. 1072-1074, 1995.

[27] N. Karafolas and D. Uttamchandani, "Optical Fiber Code Division Multiple Access Netowrks: A Review," *Optical Fiber Technology*, vol. 2, pp. 149-168, 1996.

[28] H. Fathallah, L. A. Rusch, and S. LaRochelle, "Passive Optical Fast Frequency-Hop CDMA Communications System," *IEEE Journal of Lightwave Technology*, vol. 17, pp. 397-405, 1999.

[29] D. B. Hunter and R. A. Minasian, "Programmable high-speed optical code recognition using fiber Bragg grating arrays," *IEE Electronics Letters*, vol. 35, pp. 412-414, 1999.

[30] N. Wada, H. Sotobayashi, and K. Kitayama, "2.5Gbit/s time-spread/wavelength-hop optical code division multiplexing using fibre Bragg grating with supercontinuum light source," *IEE Electronics Letters*, vol. 36, pp. 815-817, 2000.

[31] L. R. Chen and P. W. E. Smith, "Demonstration of incoherent wavelength-encoding/time-spreading optical CDMA using chirped Moire gratings," *IEEE Photonic Technology Letters*, vol. 12, pp. 1281-1283, 2000.

[32] A. Grunnet-Jepsen, A. E. Johnson, E. S. Maniloff, T. W. Mossberg, M. J. Munroe, and J. N. Sweetser, "Demonstration of All-Fiber Sparse Lightwave CDMA based on Temporal Phase Encoding," *IEEE Photonic Technology Letters*, vol. 11, pp. 1283-1285, 1999.

[33] M. Ibsen, M. K. Durkin, M. J. Cole, M. N. Zervas, and R. I. Laming, "Recent advances in long dispersion compensating fiber Bragg gratings," *IEE Publications*, vol. 0963-3308-ref.no. 1999/023, 1999.

[34] H. Geiger, A. Fu, P. Petropoulos, M. Ibsen, D. J. Richardson, and R. I. Laming, "Demonstration of a simple CDMA transmitter and receiver using sampled fiber gratings," presented at European Conference on Optical Communication, 1998.

Chapter 2

Theory and Principle of Operation

Overview

The principle of pulse encoding and matched filtering (decoding) using SSFBGs is described in this chapter. Using the equations outlined, the simulations of the pulse encoding and code correlation based on the matched filtering process are obtained and quantified. These simulations allow for the relative merits of bipolar (and higher levels of phase) coding to unipolar (on-off keying) coding to be confirmed. The advantage of extending this approach to longer code sequences is evident from the simulation results and clearly yields better code recognition contrast. A brief description on the SSFBG writing technique to fabricate both unipolar and phase coding gratings is presented. The chapter also includes the results on the assessment of the OCDMA system based on the SSFBG coders/decoders in terms of the number of possible asynchronous users that can be supported. This developed statistical model also shows that performance improvement can be achieved when Forward Error Correlation (FEC) scheme is adopted in conjunction with the SSFBG coding/decoding approach.

2.1 Principle of Pulse Encoding and Decoding

In the OCDMA approach, each individual user (or group of users) is assigned an address code that is unique within the network. At the receiving end, only receivers configured with the correct code will be able to recover the information data encoded with this code. The code allocation and recognition can be performed using a pulse encoding and decoding approach based on the superstructured fibre Bragg grating (SSFBG) technology.

A superstructured fibre Bragg grating is defined as a standard fibre grating, i.e. a fibre having a rapidly varying refractive index modulation of uniform amplitude and pitch, onto which an additional, slowly varying refractive index modulation profile has 7been imposed along its length (see Figure 1). In the weak SSFBG grating limit, (well within the Fourier design limit such that the reflectivity of the grating R<20%), i.e. where the grating strength is such that light penetrates the full grating length and the individual elements of the grating contribute more or less equally to the reflected response, the wavevector response $F(\kappa)$ can be shown to be given simply by the Fourier transform of the spatial superstructure refractive index modulation profile $A(x)$ used to write the grating [1] i.e.

$$F(\kappa) = \frac{1}{2\pi} \int_{-\infty}^{+\infty} A(x) e^{j\kappa x} dx \tag{2.1}$$

The uniform rapid refractive index modulation simply defines the central frequency/wavelength of the grating's reflection band. Similarly, the impulse response of a fibre grating $h(t)$ is given by the inverse Fourier transform of its frequency response $H(\omega)$

$$h(t) = \int_{-\infty}^{+\infty} H(\omega) e^{-j\omega t} d\omega \tag{2.2}$$

From the above equations and the fact that κ the wavevector is proportional to the optical frequency ω it is clear that the impulse response of a weak grating has a temporal profile given by the complex form of the refractive index superstructure modulation profile of the grating. For example, in the instance that the grating superstructure is simply amplitude modulated, i.e. the grating phase is uniform (such gratings are referred to as unipolar coded herein), the impulse response follows precisely the amplitude modulation profile used to write the grating [2]. (The scaling factor $t=2nx/c$ is used to convert from the spatial to temporal domain where n is the refractive index and c is the speed of light).

When a short but finite bandwidth pulse, (i.e. not an impulse pulse) is reflected from a SSFBG it is transformed into a pulse with a temporal shape given by the convolution between the input pulse and the impulse response of the grating i.e.

$$y(t)=x(t)*h(t) \tag{2.3}$$

the process is described in the frequency domain by the product of the Fourier transform of the incident signal $X(\omega)$ with the frequency response of the grating $H(\omega)$

$$Y(\omega)=X(\omega)H(\omega) \tag{2.4}$$

Figures 2.1(a) and 2.1(b) show two example gratings in terms of their refractive index modulation $A(x)$. Above each graph of the refractive index modulation, the corresponding chip signature is also plotted. As a specific example, we consider theoretically pulse reflection from the two gratings depicted above. These correspond to two particular gratings (denoted by M7U-1 and M7B-1) used within the experiments described in Chapter Three.

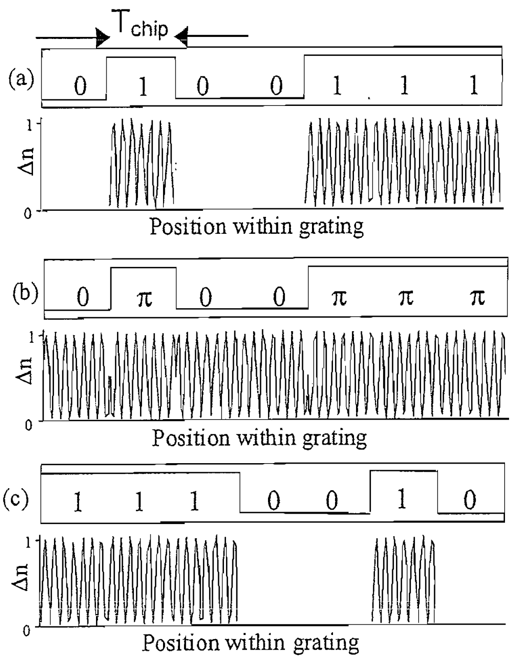

Figure 2.1: Schematic examples of temporal codes (upper traces) and the corresponding refractive index modulation profiles along the SSFBG structures (lower traces); (a) shows a 7-chip unipolar code, (b) a 7-chip bipolar code, and (c) the matched filter to the unipolar code outlined in (a). Δn is the change in the refractive index modulation of the grating. T_{chip} is the duration of one chip.

The grating in Figure 2.1(a), is a pure amplitude-modulated, (unipolar coded), grating containing 7 discrete sections defining respective zeroes and ones of the 'spatial' OCDMA chips (each chip has a duration of T_{chip} as shown in Figure 2.1(a)). Each grating section exhibits either full, or zero refractive index modulation. Figure 2.1(b) illustrates another grating that has a uniform amplitude refractive index level along its length but discrete (+/- π) jumps in phase are written into the grating at the boundaries of adjacent spatial chips, subject to the same chip pattern (code) used in Figure 2.1(a). This specific form of SSFBG modulation is referred herein as bipolar coding. In both gratings (Figures 2.1(a) and 2.1(b)) the spatial chip lengths are set to be 0.66mm corresponding to temporal chip duration of 6.4ps. These SSFBGs are used in the initial experiment described in Chapter Three to confirm the potential of using phase coding compared to the amplitude-modulated codes.

Figures 2.2(a) and 2.2(b) plot the theoretical impulse response and optical power reflectivity spectrum of the unipolar grating shown earlier in Figure 2.1(a), and the resulting reflected optical power spectrum and temporal response after excitation with 2.5ps soliton pulses (dashed lines). Figures 2.2(c) and 2.2(d) are the corresponding plots for the bipolar grating shown in Figure 2.1(b).

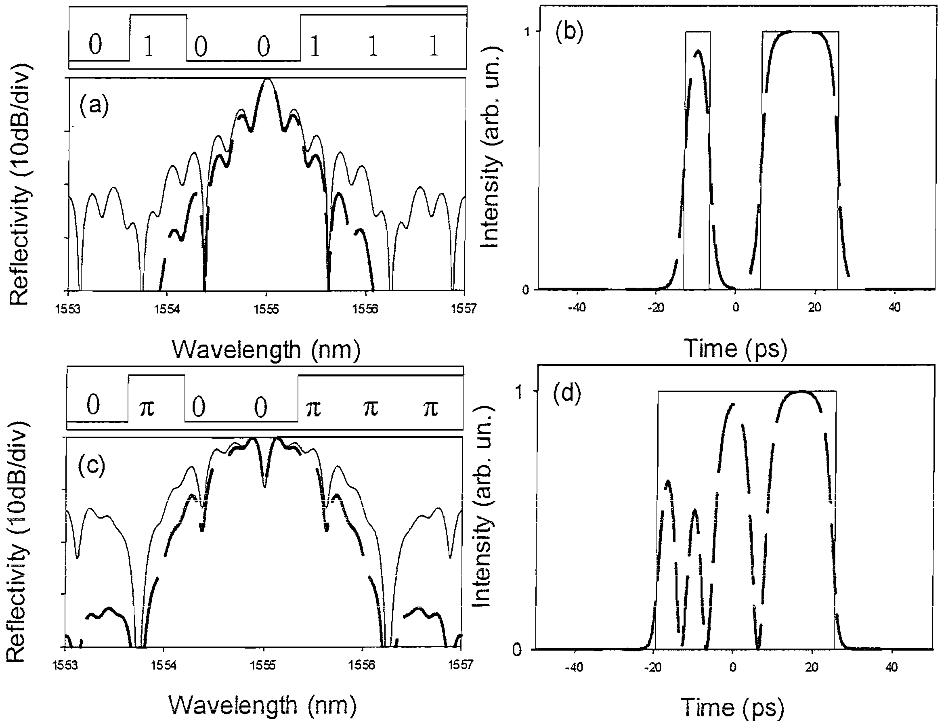

Figure 2.2: (a) Calculated reflectivity spectrum (solid line) and optical power spectrum obtained after reflection from the unipolar grating using 2.5ps input soliton pulses; (b) calculated impulse response (solid line) and temporal response to 2.5ps soliton pulses (dashed lines) for the unipolar grating; (c) and (d), same as in (a) and (b) respectively, but for the 7-chip, bipolar grating.

The relations between the superstructure refractive index modulation profiles and the gratings temporal response are clear for both grating modulation formats. The reduced temporal feature resolution, and additional code-sequence amplitude profiling, due to the use of finite bandwidth optical pulses to excite the gratings is also apparent within Figure 2.2. By using shorter pulses, more abrupt changes can be obtained at the chip boundaries of the encoded waveforms after reflection from the gratings.

In order to perform all-optical pattern recognition of the temporal code sequences the encoded waveform is reflected from a second SSFBG (the decoder) with a frequency response $G(\omega)$ and associated impulse response $g(t)$. In the frequency domain the overall response of the system is given by

$$R(\omega)=Y(\omega)G(\omega) \tag{2.5}$$

from which it is clear that if an impulse response excitation of the encoder grating is used and $G(\omega)=Y^*(\omega)=H^*(\omega)$ then $r(t)$ (can be calculated by performing the inverse Fourier transform of $R(\omega)$) is the autocorrelation function of the superstructure profile used to write the encoder grating with the impulse response of the decoder grating, $g(t)=h(-t)$.

Physically, this requirement dictates that the superstructure function of the decoder grating is the spatially reversed form used to write the encoder grating (see Figures 2.1(a) and 2.1(c)). This principle of pattern recognition is thus nothing more than a simple matched filtering. Note that if $G(\omega)$ is different from $H^*(\omega)$ then the resultant waveform represents the crosscorrelation function of the two different grating superstructure profiles (codes). Note also that $r(t)$ has a total temporal length of two times the code length. The full duration of $r(t)$ dictates the maximum bit period (and hence the bit rate) that has to be used in order to avoid the decoded correlation signals to overlap into adjacent data bits causing additional interference noise. This means that using a longer code sequence will reduce the maximum bit rate achievable unless a shorter chip duration is employed.

In order to achieve good high contrast code recognition one needs to restrict the use of codes within the system to those which have both distinct autocorrelation features with a single dominant, well-defined autocorrelation peak, and low peak level mutual cross-correlation functions. In unipolar coding, the chips within the codes are based on the presence or complete absense of optical power (on-off keying). Such code sequences limit the performance of the correlation operation both in terms of the autocorrelation peak contrast (lower than bipolar codes) and crosscorrelation signatures (higher levels of crosstalk) because only power summation takes place at the decoder. Several new amplitude-modulated (unipolar) codes have been proposed for use within OCDMA systems to overcome these issues and can use incoherent light sources. Examples of these new codes are the Optical Orthogonal Codes (OOCs) first proposed by Salehi et. al. [3, 4] and the Prime Codes suggested by several groups [5, 6]. The design concept behind these new codes is based on the appropriate distribution of a small number of '1's within a very large code period. In this way, when many users access the network simultaneously, the pulses from all the coded signals are uniformly distributed within the bit period, filling the available positions of '0's. Therefore the codes employed for these systems are very sparse and long, limiting the maximum allowable transmitted data rate. For example, it has been calculated that for the 6000-chip OOC code period where each code in the sequence contains only eight '1's, there are only unique 100 OOC codes having suitable autocorrelation and crosscorrelation properties that are available [7].

This is in contrast to the use of phase coding (bipolar and higher phase-shift-keyed levels) that allows for coherent correlation to take place at the decoder. In the coherent matched filtering process, interferometric cancellation of the correlation peak background (coherent correlation) can take place thereby offering significant improvements in the contrast of the decoded autocorrelation waveform and lower level crosscorrelation signatures. The height of the peak autocorrelation spike increases with N^2 where N is the code length, corresponding to all contributing elementary chip-pulses adding up in phase (this gives rise to the decoded autocorrelation pulse having a width of the chip duration). In unipolar coding, the peak autocorrelation spike scales with N. This represents an increase by a factor of N in terms of the autocorrelation contrast when using phase coding.

The bipolar coding scheme has been adopted within radio based direct sequence CDMA and the bipolar code sequences used are usually the well known M-sequences[1], or are based on combinations of M-sequences such as Gold codes, Kassami codes or Walsh-Hadamard codes, which are known to have such excellent correlation properties [8, 9]. Such bipolar codes are also applicable to the coherent DS-OCDMA approach based on SSFBGs. The quality of the code recognition and the number of code sequences available for a given code length is a strong function of the code length [10], and 'degree of polarity' (i.e. the number of possible coding levels) of the implementation. Both the recognition quality and number of users improve significantly with the use of longer codes and increasing degrees of polarity.

---

[1] **M-sequence (Maximal) codes** can be generated by a given shift register or a delay element of given length. In binary shift register sequence generators, the maximum length sequence is (2^n -1) chips where n is the number of stages in the shift register. A M-sequence shift register generator consists of a shift register in conjunction with the appropriate logic, which feeds back a logical combination of the state of two or more of its stages to its input. Further details can be found in Appendix A.

Figure 2.3(a) and 2.3(c) explicitly illustrate these features by plotting the response of the decode gratings to the pulse patterns generated from the relevant encoder grating after they have been excited with 2.5ps pulses (see Figures 2.2(b) and 2.2(d) respectively and the autocorrelation traces are calculated by performing an inverse Fourier transform on Equation (2.5)). In both instances a well-defined pulseform is obtained with a single distinct autocorrelation feature. Even with this relatively short code length the benefits of bipolar coding are self evident in terms of contrast between the correlation peak and the autocorrelation sidelobes. The bipolar autocorrelation trace has a pulse width of the order of chip duration (6.4ps). However, both codes exhibit a high level of crosscorrelation when an incorrect 'orthogonal' code is used as the encoder grating (see Figure 2.3(b) and 2.3(d) respectively). Such undesirable high level crosscorrelation waveforms can be reduced with the use of longer codes.

In unipolar code sequences, perfect orthogonality between different interfering users can be achieved by using codes that are based on the appropriate distribution of a small number of '1's within a very large code period. All the interfering codes will have their '1' chips filling the available positions of '0's. The codes (optical orthogonal code and Prime code) employed are very sparse and long, limiting the maximum transmitted data rate. For example, consider a 7-chip M-sequence unipolar code. An orthogonal code for 0,1,0,0,1,1,1 would only be 1,0,1,1,0,0,0. In phase coding, 'quasi-orthogonal' codes are used since for a given code combination, there can only be one code that is a 'perfect orthogonal' (for example, an orthogonal code to –1,1,-1,-1,1,1,1 would only be 1,-1,1,1,-1,-1,-1). Quasi-orthogonal in the text refers to a group of code sequences that are almost 'orthogonal' and still exhibit excellent single peak autocorrelation and low-level crosscorrelation profiles.

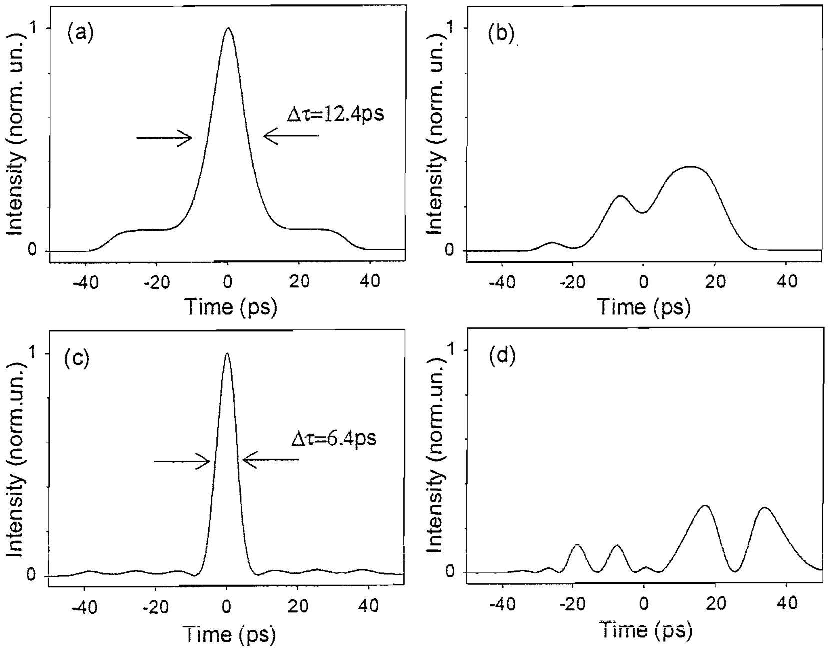

Figure 2.3: Calculated (a) autocorrelation and (b) crosscorrelation (when the encoder orthogonal code is '1011000') traces of the decoded signals for 2.5ps soliton input pulses for 7-chip unipolar coding encoder/decoder gratings pair. (c- d) Equivalent resultant waveforms when 7-chip bipolar coding encoder/decoder gratings are used. The orthogonal code used for determining the bipolar crosscorrelation traces is '$\pi 0 \pi \pi 000$'.

For a 7-bit M-sequence there are only two orthogonal codes, which is clearly impractical for most real system applications. However the number of orthogonal codes increases rapidly with code length. Figures 2.4(a) and 2.4(b) show the theoretical superstructure profile and optical power reflectivity profiles of two 'quasi-orthogonal' 63-bit Gold code bipolar sequences respectively, denoted by G63B-1 and G63B-2. These codes are chosen to exhibit the highest autocorrelation contrast and low crosscorrelation properties between them. The description and the derivations of the Gold codes can be found in Appendix A. Note that the complex, many-peaked reflectivity profiles which result from the numerous discrete phase jumps. For an L-chip Gold sequence there are L+2 such 'orthogonal' codes [11]. For example, in a 63-chip Gold sequence family, there are 65 possible combinations of codes available.

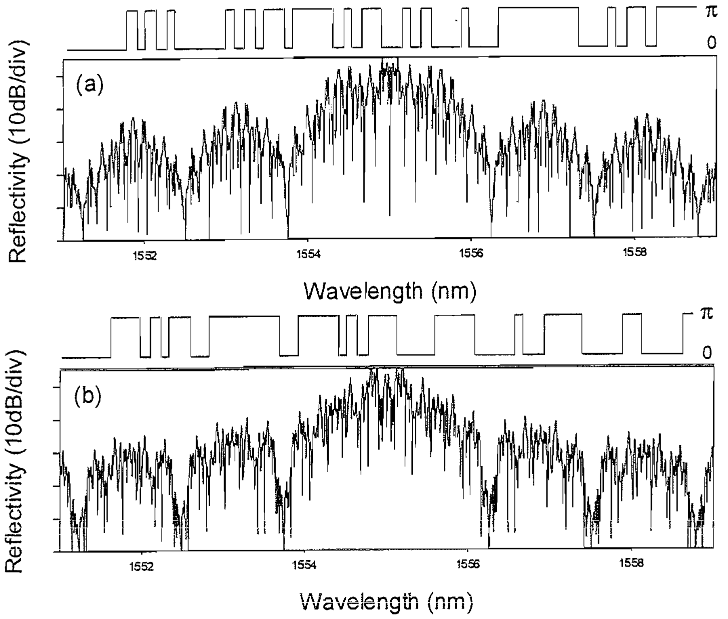

*Figure 2.4: Superstructure profiles (upper traces) and the corresponding calculated reflectivity spectra (lower traces) for (a) G63B-1 and (b) G63B-2. Note that the notation G63B-1 indicates **Gold** family codes, **63**-chip code lengths, **Bipolar** phase coding and Code **1**.*

Figures 2.5(a)-(d) show the theoretically predicted responses resulting from the code:decode process for 2.5ps input pulses for the following combinations of coding and decoding gratings: G63B-1:G63B-1*, G63B-2:G63B-2*, G63B-2:G63B-1* and G63B-1:G63B-2*.The form of labelling A:B* indicates grating A is used for the encoder, and the conjugate grating of grating B as the decoder. This labelling convention is used throughout this thesis.

Comparing Figure 2.5(a) and Figure 2.3(b), it can be seen that the use of the longer 63-chip code sequences provides much better and higher peak autocorrelations than are achievable with 7-chip code sequences. Moreover, the absence of any significant peak on the crosscorrelation profile also shows that much higher pulse code discrimination can be achieved using longer code sequences when comparing Figure 2.5(c) and Figure 2.3(d). While using longer code sequences provide higher peak autocorrelations, the bit period needs to be increased (and hence lower bit rate is used) to keep the total encoded signal within the bit period. This effectively degrades the spectral efficiency of the system. To maintain the same bit period (and spectral efficiency), shorter chip duration for a given code length will be required.

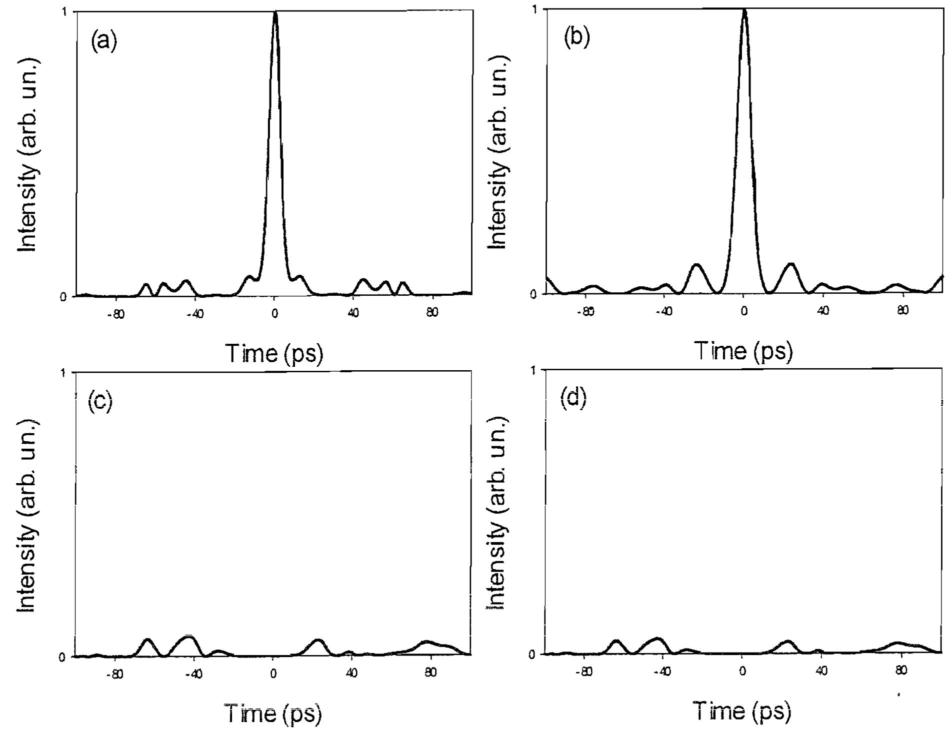

Figure 2.5: Calculated traces of the signals after the code:decode process for 2.5ps soliton input pulses, for the grating combinations: (a) G63B-1:G63B-1, (b) G63B-2:G63B-2*, (c) G63B-2:G63B-1* and (d) G63B-1:G63B-2*. In the autocorrelation signals, most of the energy is concentrated at the center of the signal, giving rise to a sharp high intensity spike. In contrast, the low-level crosscorrelation signals have the energy spread over the waveform (the crosscorrelation signal has a full duration of twice the duration of the encoded signal).*

Another method to obtain better code correlation characteristics instead of increasing the code lengths is to use codes with a higher 'degree of polarity'. For example, quaternary phase codes (codes containing four distinct phase-shifts given by 0, $\pi/2$, π and $3\pi/2$ compared to bipolar codes having only two phase-shifts, 0 and π) [12]. Quaternary codes can be generated from the Family A code sequences adapted for mobile CDMA communications [13]. From the literatures [13-15], Family A quaternary coding is known to provide codes with more desirable cross-correlation characteristics (for the same code length) than can be achieved with lower level coding such as unipolar and bipolar codes. The derivation and attributes of Family A sequences can be found in Appendix A. (Note that the Family A quaternary codes are a subset of the possible 4^L-1 code combinations available, where L is the sequence length). Family A quaternary phase sequences contain the same number of distinguishable code combinations as the bipolar Gold code family (i.e. N=L+2, where N is the number of code combinations available). For example, a Family A quaternary code of length 255 will have up to 257 unique code combinations, that are distinguishable from each other. The large code family, combined with the fact that better correlation contrasts means that quaternary coding is preferable compared to lower level coding schemes in an OCDMA network.

Figure 2.6 illustrates the comparison between the autocorrelation signatures obtained when using quaternary Family A and bipolar Gold code sequences for a code length of 255-chip. It can be seen that the Family A quaternary phase code generally yields a better signal contrast when compared to the bipolar Gold code of the same code length. Also, when comparing the crosscorrelation traces obtained when another 'orthogonal' code is used, it is evident that lower levels of cross correlation signatures can be obtained using the quaternary phase coding approach, compared to the bipolar coding scheme. Figure 2.6 also shows that the extinction ratio between the autocorrelation and crosscorrelation profiles of the quaternary Family A phase code shows ~2.5 dB improvement when compared to the bipolar Gold code traces.

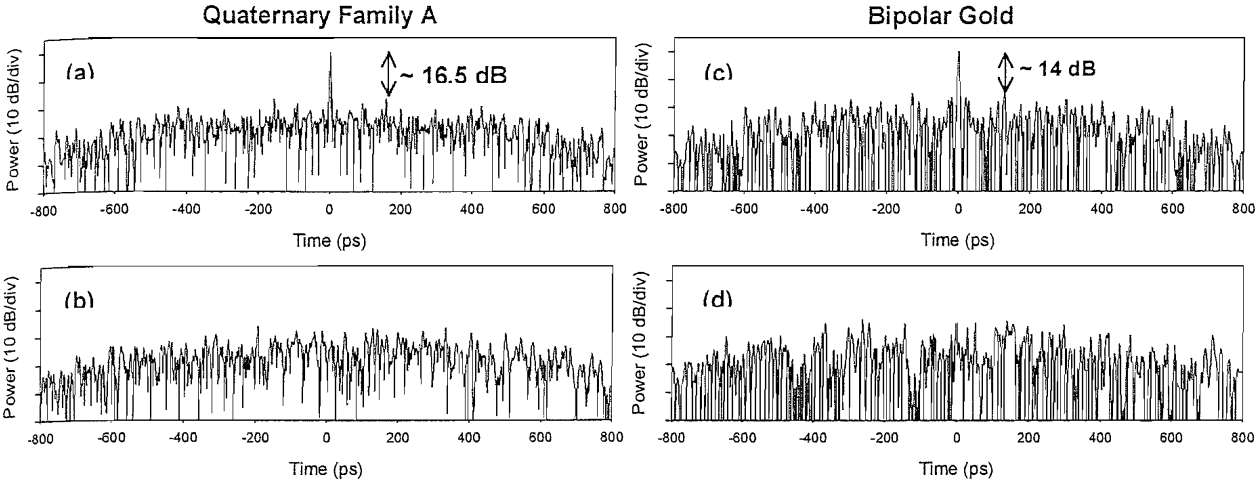

Figure 2.6: Calculated normalised intensity (a) autocorrelation and (b) crosscorrelation traces obtained when using 255-chip quaternary Family A. (c) and (d) Similar correlation traces when 255-chip bipolar Gold code sequence is used. The input pulse duration is 2.5ps for all four cases.

Next the effect of dispersion on the code transmission is investigated. The encoded signal after transmission over a distance *z* can be represented in the frequency domain by [16]

$$Y_{transmission}(z,\omega) = Y(\omega)e^{\frac{i}{2}\beta_2\omega^2 z} \tag{2.6}$$

where $Y(\omega)$ is defined earlier in Equation (2.4) and β_2 is group velocity dispersion (GVD) parameter and has a value of β_2=-20 ps^2/km for a standard single mode fibre (SMF-28). Similarly the decoded autocorrelation (and crosscorrelation) signal can be determined by considering Equation (2.6) and performing an inverse Fourier transform to obtain the temporal response. Figure 2.7 shows the autocorrelation peak intensity when a 63-bit bipolar Gold code sequence (G63B-1), having a chip duration of 6.4ps (160 Gchip/s) is transmitted over a distance of 10km in a standard telecom single mode fibre (SMF-28). It can be seen that the peak autocorrelation contrast degrades significantly even after transmission over 1km of standard fibre because the encoded signal is effectively being transmitted at a chip rate of 160 Gchip/s, corresponding to a dispersion length, $L_D=T_{chip}^2/|\beta_2|$ of only ~2km (for distortion free transmission, $z \ll L_D$). This drop in the autocorrelation contrast will affect the number of interfering users that can be reliably supported within the system.

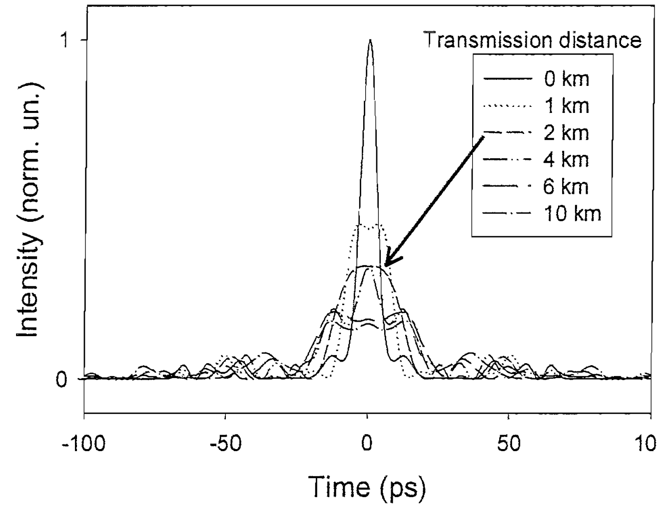

Figure 2.7: Calculated autocorrelation response after the decoding grating, G63B-1, when the encoded signal, G63B-1 is transmitted over some distance of SMF-28 before decoding.*

The above results show that some means of dispersion compensation elements (based on dispersion compensating fibre or chirped fibre Bragg grating) are required after the transmission (see Chapter Three experiments). However, when the chip duration is increased to 50ps (20 Gchip/s) as demonstrated in the experiments reported in Chapter Five, good code recognition can still be obtained for transmission up to 50km of SMF-28 (the effective dispersion length in this case is $L_D=T_{chip}^2/|\beta_2|$~*125km*). Figure 2.8 shows the calculated autocorrelation trace for a 16-chip, Family A code Q1 (see Chapter Five, Figure 5.7 for the code) when a transmission fibre up to 100km in length is inserted between the encoder and decoder gratings.

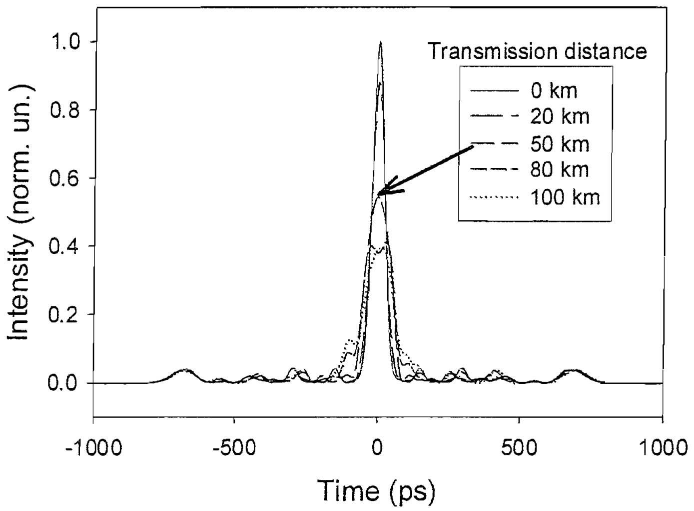

Figure 2.8: Calculated autocorrelation response after the decoding grating, Q1, when the encoded signal, Q1 is transmitted over some distance of SMF-28.*

The ASE noise from the optical amplifier (EDFA) is known to degrade the signal to noise ratio of the amplified signal. In the experiments described in Chapter Three, the EDFAs are placed before the encoder/decoder gratings. The gratings will effectively suppress the ASE noise generated outside the bandwidth of the intended signal, since the reflecting gratings also act as narrowband filters.

H.X.C. Feng et. al. has reported that the non-uniform gain of the EDFA has deleterious effects on degrading the peak autocorrelation spike [21]. The optical spectrum of the encoded signal will be modified and caused the autocorrelation peak that are composed of low power wavelength components to be masked by the crosscorrelation signals that have wavelengths with higher power. Furthermore, the authors also show that nonzero dispersion slope will cause different wavelength components in the signal to propagate at slightly different speed. This variation in propagation speed (if uncompensated) will reduce the autocorrelation contrast. Such effects are likely to be important if very short chip duration is employed. For example, for a code having a chip duration of 1ps, it will have a 10dB-bandwidth of ~6nm using an input pulse of 0.5ps. Such broad bandwidth signal is likely to be affected by the non-uniform gain of the EDFA and the effects of higher-order dispersion. In these current experiments, such effects should not be significant.

Having theoretically demonstrated the principle and potential of using SSFBG technology for coding:decoding applications, the following section provides a brief description on the SSFBG fabrication technology based on the 'continuous grating writing' technique developed at the University of Southampton. Firstly, I would like to acknowledge the contributions from Mr. Morten Ibsen, the Senior Research Fellow in charge of the Advanced Fibre Grating group, who carried out the fabrication of the high quality gratings used in the entire range of experiments reported in this thesis.

2.2 SSFBG fabrication

The continuous grating writing technique, developed at the University of Southampton effectively writes gratings on a grating plane by grating plane basis and allows for the fabrication of gratings with truly complex (having varying amplitude and phase jumps) refractive index profiles [17]. This technique uses a simple phase mask with uniform pitch and relies upon precise control of the positioning of the fibre relative to the phase mask and controlled exposure to the index modifying UV light used to write the grating. A single phase mask can thus be used to write a wide range of complex grating structures. Indeed all of the gratings described herein, including the dispersion compensating grating used for the transmission experiments, were written using a single uniform-pitch phase mask. This is to be contrasted with traditional grating fabrication techniques where the induced refractive index pattern is written into the phase mask itself, and then simply imprinted into the fibre [18]. The conventional approach limits both the quality and the length of the gratings that can be written to what can be achieved for current phase-mask production itself, which is considerably inferior to what can be achieved using our fibre Bragg grating writing technique. The practical benefits of this SSFBG approach regarding flexibility, manufacturability and grating quality should be self-evident.

Figure 2.9 shows the continuous grating writing apparatus. The laser used is a continuous wave (CW) laser producing ultraviolet (UV) beam with a power of up to 100mW at a lasing wavelength of 244nm. It delivers a UV-beam to a photosensitive fibre through a phase mask (via a mirror and an accusto-optic modulator (AOM)). The photosensitive fibre is mounted on a translation stage, which is used to move the fibre relative to the phase mask under computer control (with sub-nanometre precision). The control is implemented through a decision logic unit and an interferometer that is used to provide position measurements from the moving part of the translation stage.

By placing the photosensitive fibre in the interference pattern consisting of regions of high and low UV intensity generated by the phase mask, a grating will be formed with a period given by the periodicity of the interference pattern. The fibre-waveguide is then translated continuously at a constant velocity along the axis perpendicular to the interference fringes. To avoid obliterating the grating structure, the writing beam (interference pattern) is digitally modulated on and off at least once within one grating period using the AOM. The on/off position will determine the phase-coherence between adjacent grating periods. The actual on/off positions are determined by feedback from the interferometer. Therefore, this technique allows the accurate positioning of phase-shifts and the magnitude of the phase-shifts between adjacent chips in the grating can be accurately defined. Furthermore, the length of the grating formed is no longer limited by the length of the phase-mask but by the length of the translation equipment holding the fibre. This allows for fabrication of fibre Bragg gratings up to 1000mm in length.

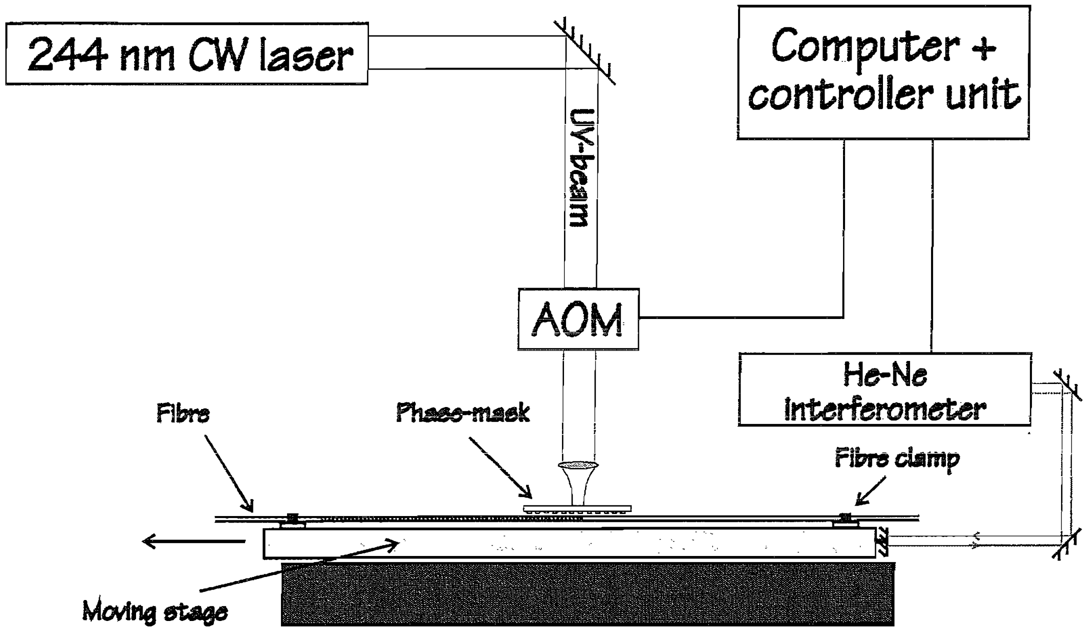

Figure 2.9: Continuous grating writing setup.

By exposing the photosensitive fibre on a plane-by-plane basis, the UV exposure on the fibre always occurs under the same part of the phase mask (the incident UV beam and the phase mask are stationary while only the fibre is translated accurately across the phase mask), while any amplitude or phase modulation are imposed by reducing the incident UV flux or dephasing the fibre relative to the phase mask [19].

In the case of the 7-chip unipolar SSFBGs as shown in Figure 2.1(a), the chips consist of either a region of uniform grating of the same duration as the chip-duration or a region of un-modulated refractive index of the same duration as the chip-duration, i.e. no Bragg grating exists. The individual chips all are in phase (i.e. are separated by an integer number of 2π in phase terms, that is an integer number of grating periods in spatial terms) and all have the same Bragg wavelength.

In the case of the 7-chip bipolar SSFBGs as illustrated previously in Figure 2.1(b), the chips all consist of a region of uniform Bragg grating of the same duration as the chip-duration and with the same Bragg wavelength. The individual chips are separated by a phase-shift of either 0π (equivalent to no phase-shift) or π. A π-phase-shift (both positive and negative) corresponds to a discrete step in the position of adjacent grating periods of half the period of the interference pattern at the position of the start of the adjacent chip (the phase of each chip is relative to the previous chip, where the first chip in the grating is taken as the reference chip).

In fabricating quaternary phase coded SSFBGs where the individual chips are separated by either one of the four phase-shifts, 0π, π/2, π or 3π/2, the π/2 and 3π/2 phase shifts correspond to shifts of quarter and three-quarter period of the interference pattern of the adjacent chip respectively. Similarly the - π/2 and -3π/2 phase shifts correspond to shifts of three-quarter and quarter period of the interference pattern of the adjacent chip. This phase transition at the chip boundary of the grating has a physical width of ~40-50um (corresponds to ~80-100 grating periods).

The data set of pre-calculated beam modulation positions defining the individual OCDMA chips to be fabricated is first loaded into the control computer. This information is then used to control the exposures via the AOM at positions defined by the linear translation stage. To write the NRZ modulated unipolar/bipolar SSFBG, the control computer first generates a first set of N exposures to write the first chip, where N is an integer equal to or greater than 2, separated by an integer multiple of the fringe period.

To write the next chip (assuming that there is a transition in the code data between the first and second chips) a second set of N exposures is made, also separated by the integer multiple of the fringe period and offset from the first set of N exposures by a distance equal to a predetermined fraction of the fringe period in the bipolar SSFBG (for example ½ for a π phase shift). The AOM will be fully switched off in the unipolar case for the un-modulated region (since no exposures will be required). If there is no transition in the code data between the first and second chips, the exposures carry on continuously from the first chip exposures with no offset. The profile of subsequent chips is then written in the same way.

The example profiles discussed above are for non-return to zero (NRZ) type modulation. The procedure for writing OCDMA coder/decoder gratings with return to zero (RZ) modulation is the same between chips where there is a transition in the code data, but different in the case when there is no transition in the code data. More specifically, in the case of a RZ-type unipolar modulation, i.e. a chip-profile that alters from full contrast (one) (uniform Bragg grating) to no contrast (zero) (no Bragg grating) once within the chip-duration, the chip-duration would then be the sum of the durations of the (one) and (zero) portions. Typically, the duty-cycle of this RZ modulation then will be given by the duration of the (one)-part to the total chip duration. For bipolar RZ SSFBG, two π phase shifts could be implemented at every chip boundary. Where there is no transition, the two π phase shifts can be separated by one or more periods of normal modulation.

2.3 Coherent OCDMA System Simulation

Having described the principle of pulse encoding and decoding based on SSFBG technology, the use of phase coding to improve the correlation contrast and the continuous grating writing technique to fabricate the SSFBGs, this section focuses on the theoretical calculation of the DS-OCDMA system based on the SSFBGs coders/decoders. The potential of the approach both in terms of number of asynchronous users and the aggregate channel bit rate is investigated. The system simulation is based on the statistical analysis of the effect of multiple access interference (MAI) (i.e. effects of interference from other users transmitting on the same bandwidth) on the number of active users in an asynchronous network. Mr. Fabio Ghiringhelli, a PhD research student from the Advanced Fibre Grating group, wrote this simulation software.

The simulation is computed based on bipolar (Gold [8]) and quaternary (Family A [13]) phase codes. The results are plotted as the bit-error-rate (BER) obtained against the number of users N and the code length L. This is followed by the comparison between the MAI-limited BER and the total network, including the effects of using Forward Error Correction (FEC)[2] over the OCDMA channels.

2.3.1 System Model

A simplified system model is considered. The OCDMA system is characterised by discrete correlation sequences, and the only source of performance degradation considered is MAI. The characteristics of the optical channel (optical source, SSFBG encoding/decoding imperfections, propagation, amplification) are neglected since the main contribution of noise in an OCDMA system will be MAI as has been reported in several literatures to date [10, 20, 21]. The model also neglected the effects of optical shot and thermal noise at the receiver. Polarisation effects in the system are neglected to simplify the calculation. N users are assumed to transmit statistically independent bit sequences with identical bit rate R, power and symbol probability (probability that a ‘zero’ is transmitted, P(0) = probability that a ‘one’ is transmitted, P(1)=0.5). Each bit is phase-encoded using an L-long, bipolar (Gold code) or quaternary (4 phase levels Family A code) codeword (implemented using encoder

---

[2] The **Forward Error Correction (FEC)** approach involves transmitting additional bits, called redundancy, along with the data bits in the electrical domain. These additional bits (FEC codes) carry redundant information and are used by the receiver to correct most of the errors in the data bits via a FEC decoding module. In general, FEC codes are capable of correcting errors up to BER of 10^{-4}.

grating), and the resulting encoded sequence is eventually zero-padded to twice the length of the longest code considered, i.e. L=255 so that the correlation sequences of successive data bits do not overlap after the decoder and no self-interference between adjacent data bit '1' occurs. N different correlation signals interfere coherently at the receiver (modelled by an infinite bandwidth intensity photodetector) after the matched filtering (with a decode grating), followed by an electrical thresholder and a decision circuit.

The asynchronous OCDMA operation is modelled by considering the time lags $\tau_{h,k}$ between the correlation signals of different users *h* and *k* as random variables, uniformly distributed over the bit period, T=1/R. Since each transmitter broadcasts its encoded signal to all the receivers in the network, an absolute (carrier) phase difference $\Phi_{h,k}$ of the crosscorrelation signal to the decoded autocorrelation signal, incident on the receiver is assumed and uniformly distributed between '0' to '2π'. At the receiver, coherent interference takes place for each possible value of phase and time lag. At the peak autocorrelation position (t=0), the photocurrent *i* generated at the detector is given by

$$i \propto \left| b[1].A + \sum_{k=2}^{N} b[k].\left|C_k(t+\tau_k)\right| e^{j\phi_k} \right|^2 \tag{2.7}$$

where *b[1]* and *b[k]* are the transmitted bits for user *1* and $k \in [2,N]$ respectively. *A* is the autocorrelation peak value (which absolute phase has been set to 0).

Let I_1 and I_0 denote the mean photocurrent sampled by the receiver during a 'one' bit and a 'zero' bit respectively and let σ_1^2 and σ_0^2 represent the corresponding noise variances [22]. The noise signals are assumed to be Gaussian. The probability density function if a 'one' bit is transmitted can be obtained (similarly for the probability density function if a 'zero' bit is transmitted) by measuring the photocurrent over a large number of samples. For the case when *P(1)* and *P(0)* bits are equally likely, the threshold photocurrent is given by

$$I_{th} = \frac{\sigma_0 I_1 + \sigma_1 I_0}{\sigma_0 + \sigma_1} \tag{2.8}$$

The probability of error when a 'one' is transmitted is the probability that $I<I_{th}$ and is denoted by $P[0|1]$ and is given by

$$P[0|1]=Q(\frac{I_1-I_{\mathrm{th}}}{\sigma_1}) \qquad (2.9)$$

Likewise, $P[1|0]$ is the probability of deciding that a 'one' is transmitted when actually a 'zero' is transmitted and is the probability that $I \geq I_{th}$ as shown below.

$$P[1|0]=Q(\frac{I_{th}-I_0}{\sigma_0}) \qquad (2.10)$$

where $Q(x)$ is give by $Q(x)=\frac{1}{2\pi}\int_x^\infty e^{-\frac{y^2}{2}}dy$ (2.11)

The BER is given by

$$BER=Q(\frac{I_1-I_0}{\sigma_0+\sigma_1}) \qquad (2.11)$$

The system performance in terms of the bit-error–rate (BER) against the number of users in the presence of various code lengths can be calculated.

2.3.2 Simulation Results

Initially, the performance of two classes of codes (bipolar Gold sequences and family A quadriphase sequences) used in DS-OCDMA (the experiments are described in Chapter Three) is obtained by calculating the BER against the number of asynchronous users for code lengths varying from

$$L=2^n-1,\ n\in[4,..8]\ (Lmax=255) \qquad (2.12)$$

In order to obtain a statistical average, six different sets of code combination decoders are considered for each code family and code length. These codes are selected to give the highest autocorrelation peak contrast. The results are shown in Figure 2.10. Each user in the network is assumed to be transmitting at a data rate of 1 Gbit/s. The results show that the quaternary phase codes show better performance compared to the bipolar equivalents. Also, the use of longer code sequences will allow for more users to be accommodated into the network while still operating below the error free level (BER<10^{-9}). Longer phase codes have the benefit of increasing the autocorrelation contrast while reducing the crosscorrelation interference. In the model, more than 10 asynchronous active users with each operating at 1 Gbit/s with BER performance~10^{-10} can be obtained when quaternary phase coding SSFBG encoders/decoders are used. The improvement in terms of system performance when using quaternary phase codes suggests the analysis of other higher phase-level (8-16 phase levels) codes to allow for more users to be included in the system for a given code length. The model also shows the performance improvement when Forward Error Correction (FEC) code is used in conjunction with the SSFBG encoders/decoders in the system. In the case above (L=255, T_{chip}~4ps, data rate 1 Gbit/s), the number of users that can be allocated in the DS-OCDMA network increase to more than 30 users when a typical FEC code such as the Reed-Solomon RS (255,239)[3] code is used.

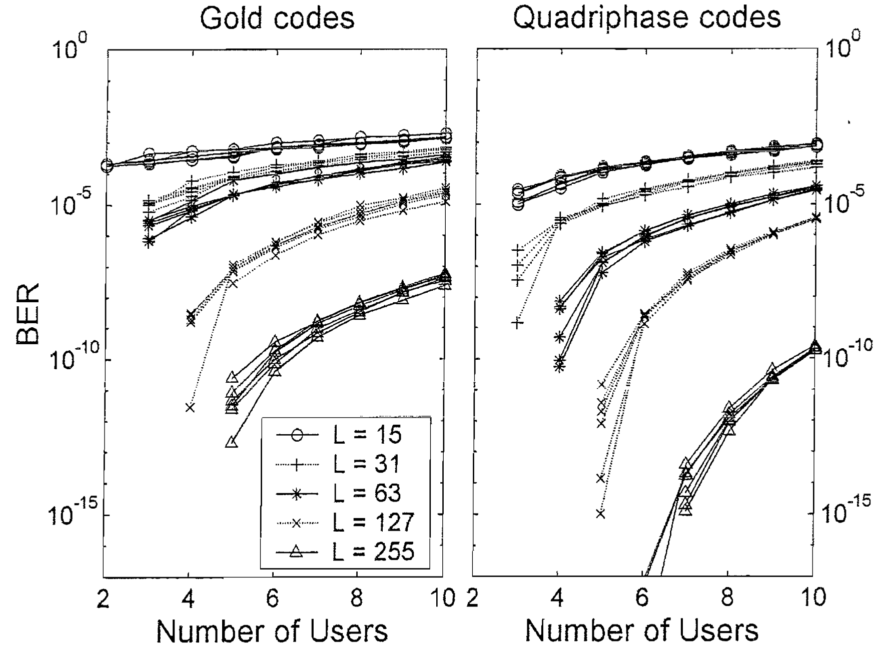

Figure 2.10: BER performance calculated against number of active users in the network using (a) bipolar Gold codes and (b) quaternary Family A codes for code lengths L=15 to L=255.

---

[3] **Reed-Solomon (RS) (255,239) code** is one type of FEC code currently used in communication systems. A (255,239) code is capable of correcting up to 8 error bytes in a block of 239 bytes (less than 7% of redundancy).

Further calculations showed that by increasing the code length to L=1023 while retaining the OCDMA channel data rate at 1 Gbit/s (this would require T_{chip}~1ps and hence shorter pulses need to be obtained from the pulsed source), more than 40 users can be accommodated in the DS-OCDMA network with each channel operating with BER<10^{-10} without the need for FEC code. Combining such long code sequences with FEC will allow more than 100 users to operate at data rates of 1 Gbit/s in an asynchronous, secured network. Figure 2.11 shows the BER performance when the code length, L=1023.

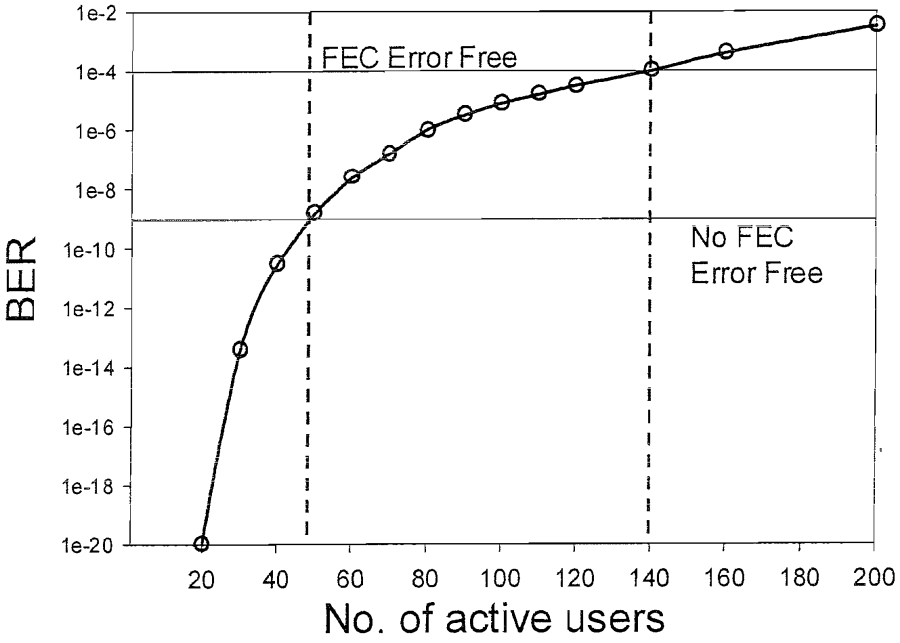

Figure 2.11: BER performance against number of active users in the network using 1023-chip, quaternary phase Family A code sequences with each channel operating at 1 Gbit/s data rate. The FEC error free limit shown in the graph considers a general case of the performance improvement expected when a typical FEC code is used.

There has been great interest recently to combine OCDMA multiplexing functionality with WDM in order to make efficient use of the spectral bandwidth [23] and to achieve an even larger user base. It has been experimentally proven that WDM channels can be multiplexed with very little power penalty if the channel spacing $\Delta\lambda$ is made comparable/larger than the spectral width of the main lobe of the encoded sequence. Consider the case of L=1023, T_{chip}~1ps and OCDMA channel data rate of 1 Gbit/s, up to three WDM wavelengths can be used within a standard erbium doped fibre amplifier (EDFA) bandwidth of 30nm. The WDM channel spacing is set to $\Delta\lambda$~10nm. Each WDM wavelength will support ~100 OCDMA channels using FEC and the total throughput of the OCDMA/WDM system is ~300 Gbit/s. The spectral efficiency of the system calculated to be 300 Gbit/s/1.25 THz~0.24 bit/s/Hz.

Note that the OCDMA system modelled so far does not incorporate the use of nonlinear thresholding. Nonlinear optical thresholders can be used after the decoding operation to reduce/remove the interference noise arising from MAI, in effect allowing more channels to be included in the system (the experiments highlighting the use of nonlinear optical thresholders to reduce the effects of MAI are described in Chapter Four).

2.4 Summary

This chapter had provided the theoretical backgrounds required to understand the principle of pulse encoding and decoding based on superstructure fibre Bragg gratings. From the calculations, it can be observed that phase coding schemes provide better autocorrelation contrast than using unipolar codes. The chapter also briefly described the SSFBG fabrication technique based on the continuous grating writing technique. The OCDMA system simulation showed that up to 100 active, asynchronous users can be accommodated in the network, each channel operating at a data rate of 1 Gbit/s, using the SSFBG coding/decoding devices in conjunction with FEC code. When combined with the WDM technology, up to 300 users can be allowed in the network. The critical question remains however, as to whether the current SSFBG fabrication technology is capable of fabricating sufficiently precise gratings to make the SSFBG approach both viable and applicable to chip rates, bit rates and code lengths of practical interest within OCDMA systems. The next chapter shows that the fabrication technology does have the precision and flexibility required to fabricate suitable SSFBGs for use within OCDMA systems. Chapter Three also presents a range of experiments employing the fabricated SSFBG coders/decoders.

References

[1] B. J. Eggleton, P. A. Krug, L. Poladian, and F. Ouellette, "Long periodic superstructure Bragg gratings in optical fibres," *IEE Electronics Letters*, vol. 30, pp. 1620-1622, 1994.

[2] H. Geiger, A. Fu, P. Petropoulos, M. Ibsen, D. J. Richardson, and R. I. Laming, "Demonstration of a simple CDMA transmitter and receiver using sampled fiber gratings," presented at European Conference on Optical Communication, 1998.

[3] J. A. Salehi, "Code Division Multiple-Access Techniques in Optical Fiber Networks-Part I: Fundamental principles," *IEEE Transaction on Communications*, vol. 37, pp. 824-833, 1989.

[4] F. Chung, J. A. Salehi, and V. Wei, "Optical Orthogonal codes: Design, analysis and applications," *IEEE Transaction of Information Theory*, vol. 35, pp. 595, 1989.

[5] J. Zhang, "Shortened Prime Codes and their cost-effective encoders for use in all-optical CDMA networks," *IEICE Transaction on Communications*, vol. E79-B, pp. 198-201, 1996.

[6] A. Holmes and R. Syms, "All-optical CDMA using 'quasiprime' code," *IEEE Journal of Lightwave Technology*, vol. 10, pp. 279-286, 1992.

[7] J. A. Salehi, "Emerging optical code-division multiple access communications systems," *IEEE Network*, vol. 31, 1989.

[8] R. Gold, "Optical Binary Sequences for Spread Spectrum Multiplexing," *IEEE Transaction on Information Theory*, vol. IT-B, pp. 619-621, 1967.

[9] E. H. Dinan and B. Jabbari, "Spreading Codes for Direct Sequence CDMA and Wideband CDMA Cellular Networks," *IEEE Communications Magazine*, vol. 36, pp. 48-54, 1998.

[10] J. A. Salehi, A. M. Weiner, and J. P. Heritage, "Coherent ultrashort light pulse code-division multiple access communication systems," *IEEE Journal of Lightwave Technology*, vol. 8, pp. 478-491, 1990.

[11] N. Wada and K. Kitayama, "A 10Gb/s optical code division multiplexing using 8-chip optical bipolar code and coherent detection," *IEEE Journal of Lightwave Technology*, vol. 17, pp. 1758-1765, 1999.

[12] P. V. Kumar and O. Moreno, "Polyphase sequences with periodic correlation properties better than binary sequences," *IEEE Transaction of Information Theory*, vol. 37, pp. 603-616, 1991.

[13] S. Boztas, R. Hammons, and P. V. Kumar, "4-phase sequences with near-optimum correlation properties," *IEEE Transaction of Information Theory*, vol. 38, pp. 1101-1113, 1992.

[14] F.-W. Sun and H. Leib, "Optimal phases for a family of quadriphase CDMA sequences," *IEEE Transaction of Information Theory*, vol. 43, pp. 1205-1217, 1997.

[15] K. Yang, Y. Kim, and P. V. Kumar, "Quasi-orthogonal sequences for code-division multiple-access systems," *IEEE Transaction of Information Theory*, vol. 46, pp. 982-993, 2000.

[16] G. P. Agrawal, *Nonlinear fiber optics*, 2nd ed: Academic Press Inc, 1995.

[17] M. Ibsen, M. K. Durkin, M. J. Cole, and R. I. Laming, "Sinc-Sampled Fiber Bragg Gratings for Identical Multiple Wavelength Operation," *IEEE Photonics Technology Letters*, vol. 10, pp. 842-844, 1998.

[18] A. Grunnet-Jepsen, A. E. Johnson, E. S. Maniloff, T. W. Mossberg, M. J. Munroe, and J. N. Sweetser, "Demonstration of All-Fiber Sparse Lightwave CDMA based on Temporal Phase Encoding," *IEEE Photonic Technology Letters*, vol. 11, pp. 1283-1285, 1999.

[19] M. Ibsen, M. K. Durkin, M. J. Cole, M. N. Zervas, and R. I. Laming, "Recent advances in long dispersion compensating fiber Bragg gratings," *IEE Publications*, vol. 0963-3308-ref.no. 1999/023, 1999.

[20] D. D. Sampson, M. Calleja, and R. A. Griffin, "Crosstalk performance of coherent time-addressed photonic CDMA networks," *IEEE Transaction on Communications*, vol. 46, pp. 338-348, 1998.

[21] H. X. C. Feng, A. J. Mendez, J. P. Heritage, and W. J. Lennon, "Effects of Optical Layer Impairments on 2.5 Gb/s Optical CDMA Transmission," *OSA Optics Express*, vol. 7, pp. 2-9, 2000.

[22] R. Ramaswami and K. N. Sivarajan, *Optical Networks: A practical perspective*, 2nd ed: Academic Press Inc, 2002.

[23] K. Kitayama, "OCDM/WDM networks for gigabit access: 1.24 Gbit/s, 2xOCDM by 2xWDM experiment," presented at Europepan Conference on Optical Communication, 1999.

Chapter 3

Assessment on the quality of the Superstructure Fibre Bragg Gratings encoders/decoders

Overview

Having explained the principle and the theoretical background to the SSFBG coding/decoding approach including the grating writing technique, this chapter describes a range of elementary optical coding and decoding experiments employing the SSFBG components. Firstly, the SSFBGs required were fabricated and characterised by measuring their spectral reflectivity profiles and comparing the results with theoretical calculations. In Section 3.2, a comparison of the relative merits of 7-chip, 160 Gchip/s unipolar and bipolar M-sequence coding:decoding schemes is made experimentally. The results show that the SSFBG approach allows for high quality unipolar and bipolar coding and that the performance obtained was close to that theoretically predicted. Next, the experimental performance of the 63-chip, 160 Gchip/s, bipolar Gold sequence gratings is investigated including the performance of the system under multi-user operation (two simultaneous users). A cascaded coding/decoding and recoding functions is then described. The scalability of the SSFBG fabrication technique to fabricate longer grating and more complicated structure was demonstrated by fabricating gratings with longer codes (255-chip), higher chip rates (320 Gchip/s) and multiple phase shift levels. These 255-chip gratings were used in a four-channel OCDMA/WDM system demonstration incorporating different coding schemes, repetition rates and wavelengths. The last section describes the use of a fibre delay lines encoder and an SSFBG decoder for code generation and recognition and which shows that SSFBG technology is compatible with other coding/decoding approaches.

3.1 Characterisation of the gratings fabricated

Table 1 lists the range of different gratings fabricated for use within the experiments discussed in this chapter. Firstly, to enable us to establish experimentally the feasibility and benefits of using bipolar (phase) codes relative to unipolar (amplitude) codes, the 7-chip structures shown earlier in Chapter Two (Figures 2.1(a) and 2.1(b)), along with their matched filter pairs were fabricated. This was followed by the fabrication of 63-chip, bipolar code gratings to demonstrate the improved code recognition contrast using longer code sequences. Finally, 255-chip quaternary gratings are fabricated in order to access the scalability and the precision of the grating writing technique to fabricate longer codes with higher chip rates and containing up to four discrete phase shifts.

Grating	Type	Code Sequence	Code Length	Chip Length (cm)	Grating Length (cm)	Peak Reflectivity
M7U-1	Unipolar	M-Sequence	7	0.066	0.462	3%
M7U-1*	Unipolar	M-Sequence	7	0.066	0.462	3%
M7B-1	Bipolar	M-Sequence	7	0.066	0.462	50%
M7B-1*	Bipolar	M-Sequence	7	0.066	0.462	50%
G63B-1	Bipolar	Gold Sequence	63	0.066	4.158	20%
G63B-1*	Bipolar	Gold Sequence	63	0.066	4.158	20%
G64B-2	Bipolar	Gold Sequence	63	0.066	4.158	20%
G63B-2*	Bipolar	Gold Sequence	63	0.066	4.158	20%
A255Q-1	Quaternary	Family A	255	0.033	8.415	25%
A255Q-1*	Quaternary	Family A	255	0.033	8.415	25%
A255Q-2	Quaternary	Family A	255	0.033	8.415	25%
A255Q-2*	Quaternary	Family A	255	0.033	8.415	25%

Table 3.1: Different types of SSFBGs fabricated for use in the experiments.

The unipolar gratings (M7U-1, M7U-1*) were similar in design to those used in the earlier experiments [1], only physically shorter in length. The total grating length in each instance was 4.63mm (corresponding to a temporal code duration of 44.8ps) and the individual chip width was 0.66mm (corresponding to a temporal chip length of 6.4ps versus ~200ps in the earlier experiments). The amplitude modulated superstructure profiles used to write the unipolar code gratings (M7U-1, M7U-1*) are shown inset with the corresponding theoretical and experimental power reflectivity profiles in Figure 3.1(a).

The corresponding bipolar grating (M7B-1, M7B-1*) designs are shown in Figure 3.1(b). They are pure phase encoded structures with discrete π phase shifts at the (NRZ) chip transition boundaries. The agreement between the theoretical and experimental spectral responses of both sets of 7-bit SSFBG types are seen to be excellent, highlighting the precision of our grating writing process. Note that the absolute reflectivity of the M7B gratings is ~50% (due to the use of a higher photosensitive fibre) and which is significantly higher than the quoted upper limit generally considered for the weak-grating Fourier design approach to be reliable (the theoretical calculations of the reflectivity shown in Figure 3.1 are computed based on the weak-grating Fourier design). However, even at this higher level of reflectivity the gratings are still found to perform well, with the reflectivity plots showing good agreement with the theoretical calculations. Note that for longer gratings (4.158cm and 8.415cm), the use of higher reflectivity will have a significant effect on the reflected temporal response of the grating because the contributions of the total reflected light from the grating will be uneven across the entire grating length (more light will be reflected from the front of the grating, gradually diminishing as it travels down the grating).

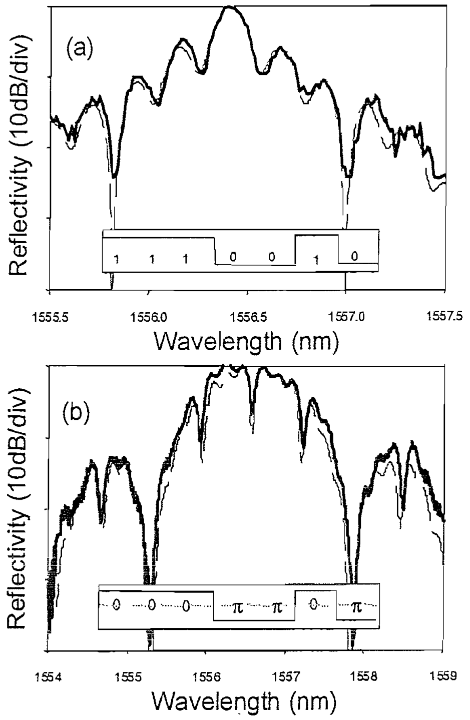

Figure 3.1: Reflectivity spectra for (a) the M7U-1 and (b) the M7B-1 grating (solid lines: experimental measurements, dashed lines: theoretical plots). The period of the refractive index modulation used to write these gratings was set to Λ=~520nm.

The second set of encoding:decoding gratings to be produced were nominally identical to the 7-bit bipolar encoded gratings of Figure 3.1(b) in terms of chip length (0.66mm=6.4ps) and wavelength, only much longer both in terms of number of chips (63) and correspondingly physical length (~42mm). The gratings were made to the theoretical designs shown in Chapter Two (Figure 2.4). Four specific gratings were made G63B-1, G63B-1*, G63B-2 and G63B-2* as shown in Figure 3.2.

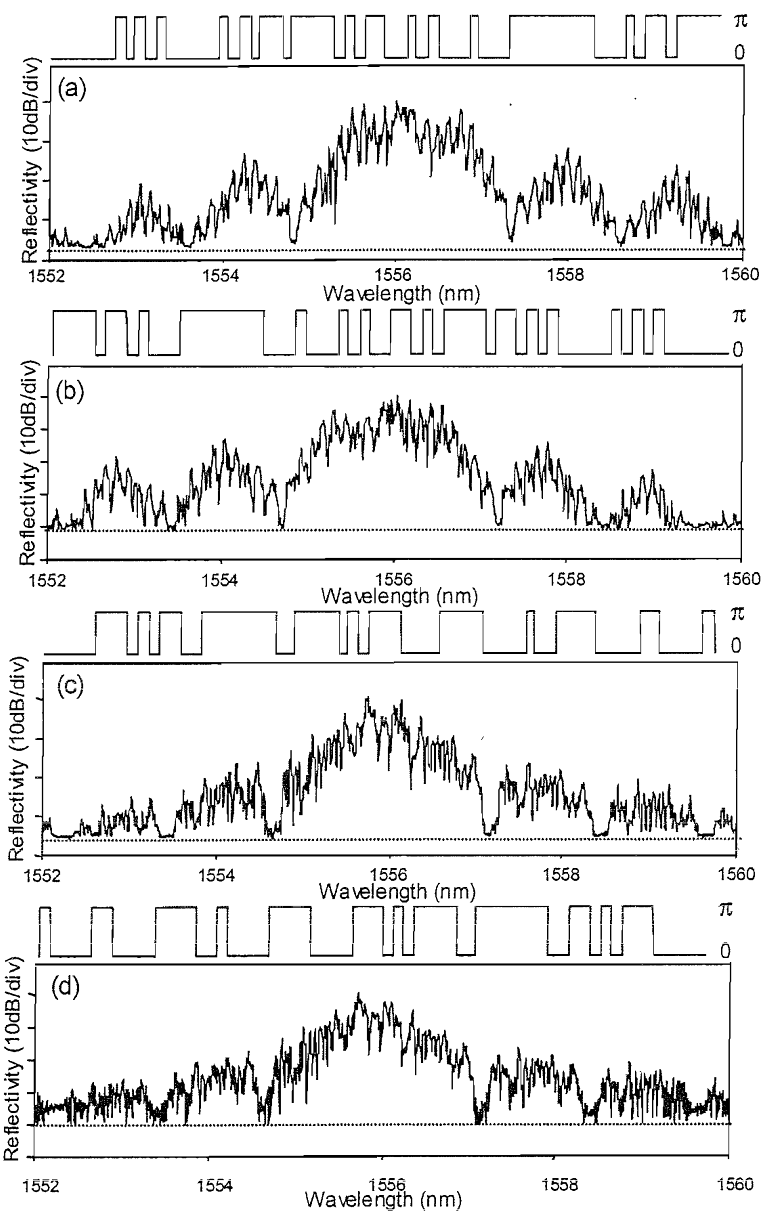

Figure 3.2: Superstructure profiles (upper traces) and the corresponding measured reflectivity spectra (lower traces) for (a) G63B-1, (b) G63B-1, (c) G63B-2, and (d) G63B-2*. These gratings was written with a refractive index modulation period of Λ=~520nm. The dashed horizontal lines indicate the noise floor in the reflectivity measurements.*

The success in producing long SSFBGs of this quality proved that the coherence of the grating process can be maintained for the greatly increased grating lengths (for example 63 chips and above). This is required to provide codes with a sufficient number of OCDMA chips to support a practical number of users in an OCDMA system (not just two users as for the shorter 7-bit codes). It has also been possible to make a more sensible assessment of the achievable minimum levels of code cross-correlation, and to assess the system penalties associated with multi-user operation.

The third set of gratings fabricated allowed further assessment into the scalability of the grating writing technology to write longer-length gratings. Two 'quasi-orthogonal' 255-chip quaternary codes were selected from Family A code sequences to be imprinted onto the photosensitive fibre. The chip duration was set to 3.2ps, corresponding to a chip rate of 320 Gchip/s. A total of four 255-chip quaternary phase coding gratings were fabricated, denoted by A255Q-1, A255Q-1*, A255Q-2 and A255Q-2*. The gratings have a peak reflectivity of ~ 25%. The total length of the gratings is 8.415cm. Figure 3.3 shows the four-level phase modulation profiles of both codes, denoted by A255Q-1 and A255Q-2.

(a) A255Q-1

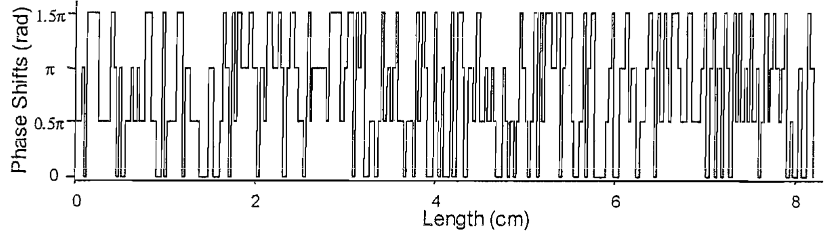

(b) A255Q-2

Figure 3.3: 255-chip four-level phase modulation profile of (a) code A255Q-1 and (b) code A255Q-2 to be imprinted onto the photosensitive fibre during the grating writing process.

Figure 3.4 shows the corresponding theoretical and experimental plots of the reflectivity spectrum of two of the gratings fabricated, A255Q-1 and A255Q-2. The quality of the gratings is evident when comparing the experimental and theoretical reflectivity of grating A255Q-1. Similar comparison is also obtained with grating A255Q-2. Again, the reflectivity responses of both gratings show that long length and higher complexity SSFBGs can be reliably fabricated using the continuous grating writing technology.

(a) A255Q-1

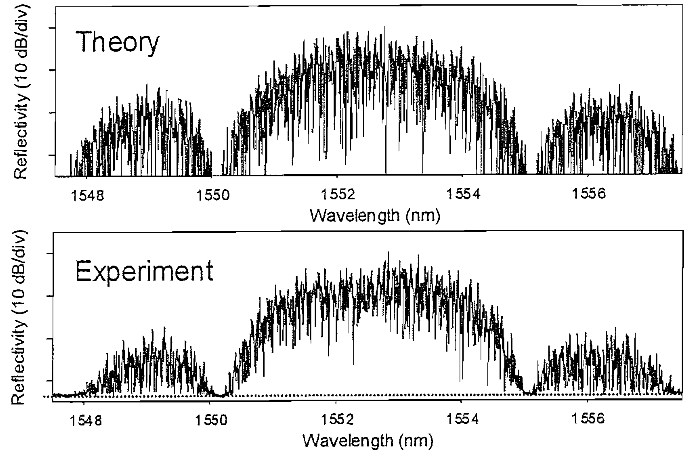

(b) A255Q-2

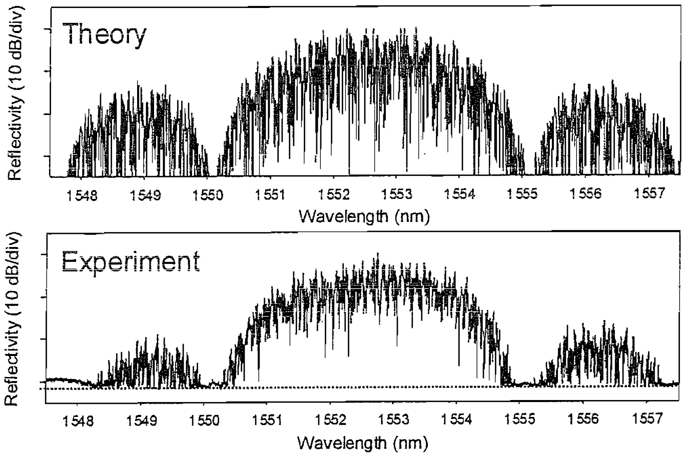

Figure 3.4: Reflectivity profiles (theory and experiment) for 255-chip, 320 Gchip/s quadrature sequences SSFBGs (a) encoder A255Q-1 and (b) encoder A255Q-2. These gratings have peak reflectivity of ~25 % and they are 8.415cm long. The dashed horizontal lines indicate the noise floor in the reflectivity measurements.

Having experimentally characterised the quality of the various SSFBGs coders/decoders fabricated, the following section discusses the range of OCDMA experiments performed using the SSFBGs fabricated earlier.

3.2 Performance of 7-chip unipolar and bipolar M-sequence SSFBG

The basic experimental set up is shown in Figure 3.5, and comprises: an externally modulated, mode-locked soliton fibre laser; circulators for coupling light on to and off the coding and decoding gratings; a transmission line with associated dispersion compensation and finally a decoder grating to perform the code recognition. The principle and descriptions of the actively mode-locked fibre ring laser pulse source are described in Appendix B and also can be found in Ref [2]. Amplifiers were incorporated within the system at appropriate positions to compensate for the various sources of optical power loss such as the transmission line loss, optical circulator insertion loss and coupler splitting ratios. The transmitter (soliton laser + external modulator) could be used to generate either continuous pulse trains of 2.0-2.5 ps, transform limited soliton pulses at predetermined frequencies in the range 0.5 to 10 GHz, or pseudorandom data at predetermined data rates in the range 1 to 10 Gbit/s. This data stream was then coded using an SSFBG, and either decoded immediately using a matched grating, or transmitted over some distance, and then decoded. The pulse shaping properties (temporal and spectral), and bit-error rate performance at various points throughout the system were characterized using: a fast pin-diode and sampling scope of ~20 GHz combined measurement bandwidth, a Second Harmonic Generation (SHG) autocorrelator[1] (<100fs resolution), an optical spectrum analyzer and, where appropriate, a 10 Gbit/s receiver and Bit-Error Rate Test set (BERT).

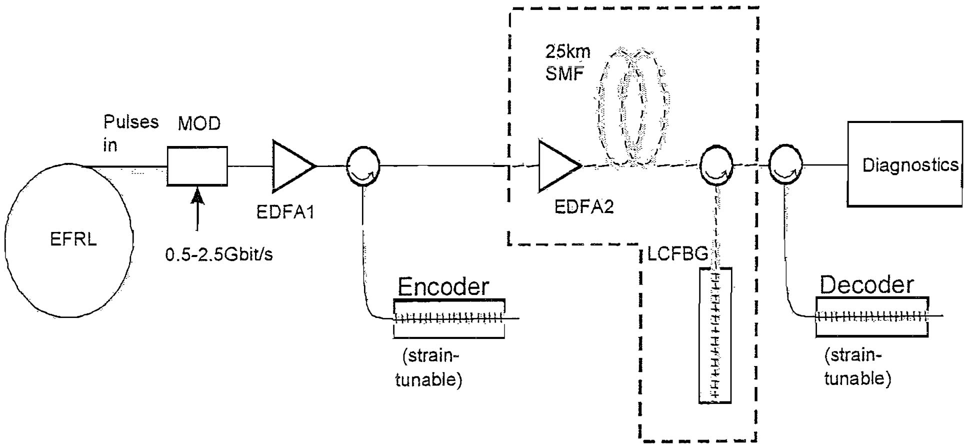

Figure 3.5: Experimental set-up (EDFA: Erbium-doped fibre amplifier, LCFBG: linearly chirped fibre Bragg grating).

---

[1] The **SHG autocorrelator** is a high resolution instrument based on the conventional Michelson Interferometer set-up for continuous monitoring and display of femtosecond and picosecond laser pulses. It utilizes background free (noncollinear) second harmonic generation method for the measurement of the autocorrelation function of repetitive ultrashort pulses.

In order to assess the quality of the individual gratings, a series of code generation experiments were performed and the temporal and spectral characteristics of pulse forms generated on reflection from the individual code gratings were examined. Firstly the temporal measurements were obtained for encoded pulseforms after reflecting 2.5ps pulses generated from the mode-locked fibre ring laser, off gratings M7U-1 and M7B-1 using a fast photodiode and a sampling oscilloscope. The measured and calculated responses for both encoded signals are shown in Figure 3.6.

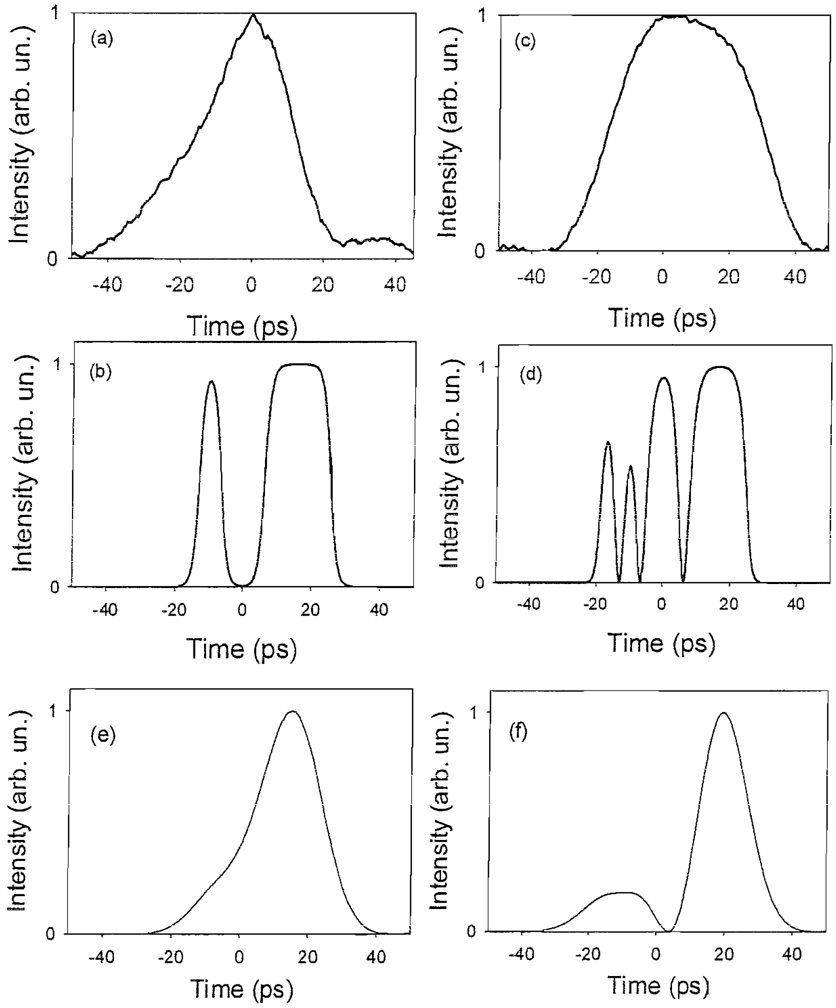

Figure 3.6: Measured responses after reflection off grating M7U-1 (a) with the calculated waveforms in (b). Corresponding measured (c) and calculated (d) phase-encoded waveforms after reflection off grating M7B-1. Note that the measured responses have a limited bandwidth of 20 GHz. (e) and (f) Predicted time response considering the detector bandwidth of 20 GHz for M7U-1 and M7B-1 respectively.

Note that due to the limited bandwidth of the photodiode and sampling oscilloscope, the amplitude variations associated with the phase jumps in the encoded waveform cannot be clearly resolved (it would require a detection bandwidth of 160GHz to resolve each individual chip since each chip has a duration of 6.4ps, corresponding to a chip rate of 160 Gchip/s). The variation in the chip amplitude in the theoretical calculations of the phase-encoded waveform shown in Figure 3.6(d) is due to the use of finite bandwidth 2.5ps pulses to calculate the temporal response after reflection off the M7B-1 grating. Figure 3.6(e) and Figure 3.6(f) show the predicted unipolar and bipolar encoded signal for a detector bandwidth of 20 GHz.

Figure 3.7 plots the temporal response of gratings M7U-1 and M7B-1 as measured using the SHG autocorrelator along with the corresponding optical spectra obtained from the optical spectrum analyser. The measured autocorrelations and spectral forms are found to be in excellent agreement with the theoretical predictions within the resolution limits of the respective measurements, confirming the formation of the correct code patterns and the desired chip duration of 6.4ps.

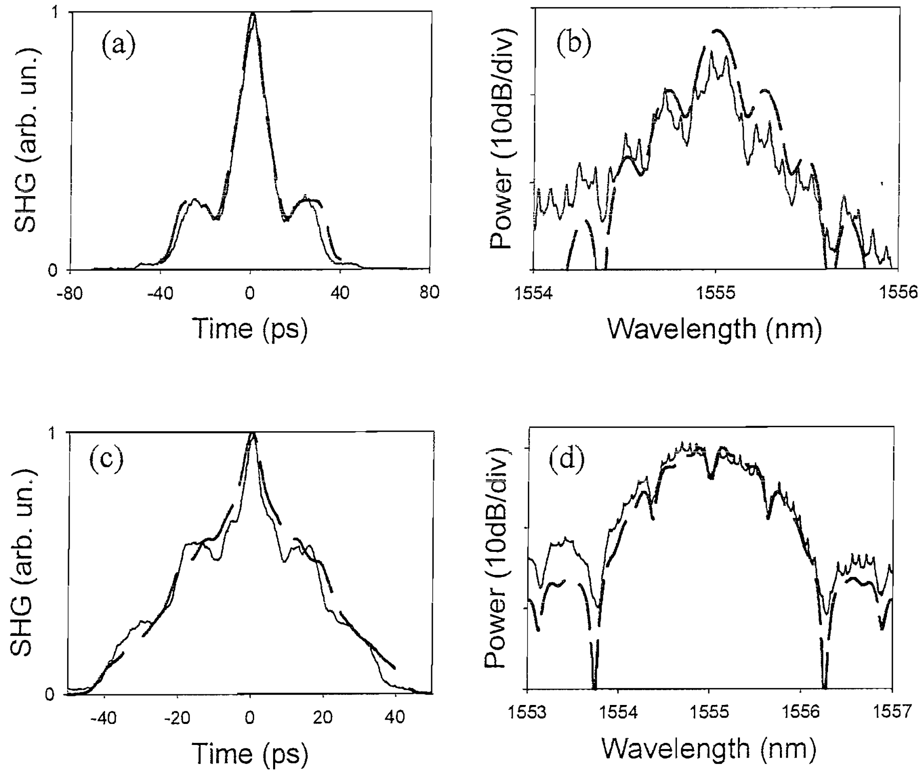

Figure 3.7: (a) Intensity SHG autocorrelation traces of the encoded waveforms for the M7U-1 grating, for 2.5ps soliton input pulses; (b) spectral response of the encoded waveforms for the M7U-1 grating; (c) and (d), same as in (a) and (b) respectively, but for the M7B-1 grating (solid lines: experimental measurements, dashed lines: theoretical plots). The 10GHz periodic structure on the spectral envelope of the experimental measurements results from the 10Gbit/s modulation of the signal.

Having established the high quality of the individual coding and decoding gratings, their self-code recognition properties were examined. Figure 3.8 directly compares the SHG autocorrelator measurements of the code recognition signature of the 7-bit unipolar and bipolar gratings with each other and against the theoretical predictions. The SHG autocorrelator (<100 fs resolution) allows the precise determination of the decoded pulse width. Close to the ideal theoretical performance is achieved in both cases. Our measurements confirm the expected benefits of using the bipolar form of coding since in this case an extremely well defined code recognition peak of 6.4ps pulse width is obtained.

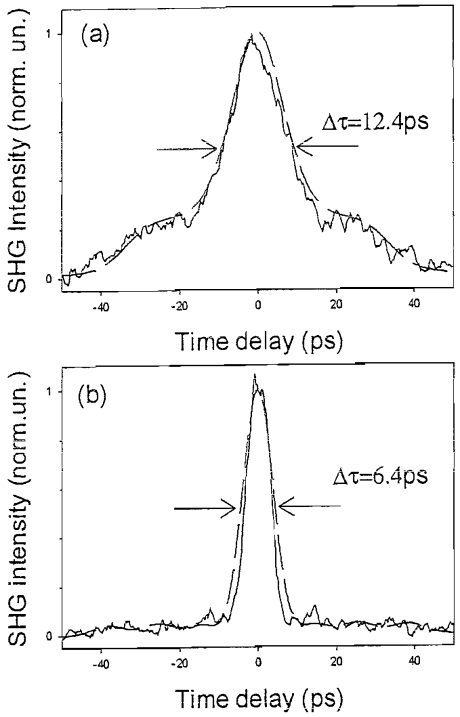

Figure 3.8: Intensity SHG autocorrelation traces of the signals after the code:decode process for 2.5ps soliton input pulses, for the grating combinations: (a) M7U-1:M7U-1, and (b) M7B-1:M7B-1* (solid lines: experimental measurements, dashed lines: theoretical plots). $\Delta\tau$ is the decoded pulse width obtained from the SHG intensity measurement. The phase coding autocorrelation pulse width depends on the chip duration because maximum peak intensity is obtained when all contributing elementary chip-pulses add up in phase. This occurs when the encoded signal overlaps exactly at the center of the decoder grating. At other positions, out-of-phase interferometric cancellation occurs yielding low-level autocorrelation sidelobes. For unipolar coding, the decoded pulse width is much broader than the chip duration because power summation occurs and no coherent correlation taking place.*

In order to quantify the quality of these SSFBG coding/decoding processes from a system perspective, Bit Error Rate (BER) measurements were made on a number of coding:decoding grating pairs. Both back-to-back coding:decoding and coding:decoding after transmission were investigated. Bipolar coding:decoding grating pairs are used in this system measurement since they exhibit a well-defined decode pulsewidth compared to the unipolar gratings. The transmission line used within these experiments was composed of 25km of standard SMF-28 grade fibre, with ~0.2 dB/km loss. The high dispersion of this fibre (~20 ps/nm/km) was compensated for using a chirped fibre grating of opposite and nominally equal dispersion at the system operating wavelength of 1557.5nm. This grating had a full 3dB bandwidth of 5nm. A plot of the dispersion compensating grating response is shown in Figure 3.9. Note that the dispersion compensating grating was also fabricated using the same continuous grating writing technique and with the same phase mask used to fabricate the coding/decoding SSFBGs.

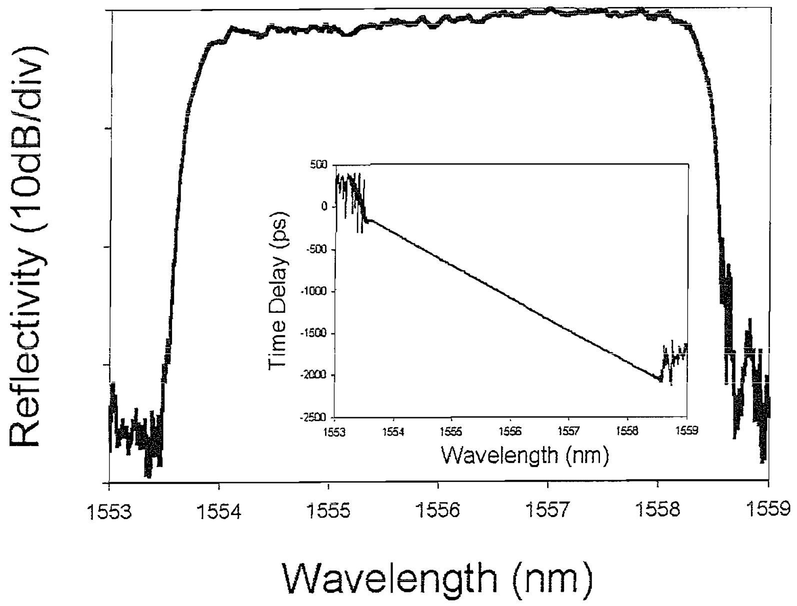

Figure 3.9: Reflectivity spectrum of the dispersion compensating grating. The time delay diagram is shown in the inset.

Figure 3.10 plots the results of 10 Gbit/s BER encoding:decoding experiments using the grating pair M7B-1:M7B-1*. Error free performance and clear eye-diagrams are obtained for the coding:decoding process both with and without the additional 25km transmission distance. No discernable power penalty is observed in both instances relative to the back-to-back transmitter measurements, nor is the appearance of any temporal features away from the chip length long correlation peak. Note that the width of the pattern recognition trace is twice the total code length, i.e. 89.6ps, just less than the bit period of 100ps (corresponding to 10 GHz).

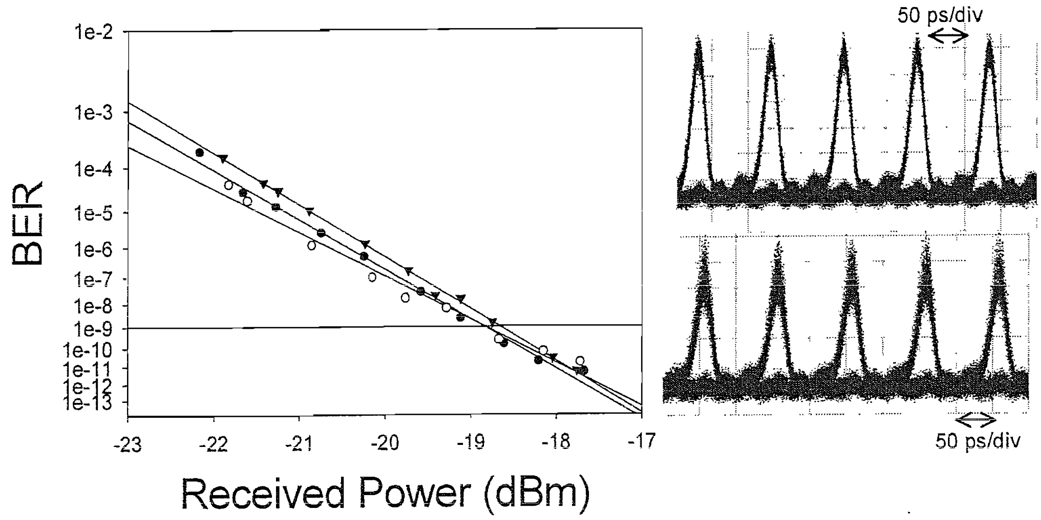

Figure 3.10: BER curves for the M7B-1:M7B-1 combination (open circles: laser back-to-back, closed circles: decoded signal without transmission, triangles: decoded signal after transmission). Inset shows eye diagrams of the decoded signals without (upper trace) and after 25km transmission (lower trace). The data rate was 10 Gbit/s. (Note that the intensity noise observed in the '1' bits in the eye diagram of decoded signals after 25km transmission is due to the drift in the laser pulse source when the measurement was made).*

3.3 Performance of 63-chip bipolar Gold sequence SSFBG

Having experimentally verified the benefits of using bipolar phase coding for OCDMA compared to unipolar codes, this section reports on extending the SSFBG approach to longer code sequences, specifically, 63-chip bipolar Gold code sequences. Such code length allow the possibility of making a more sensible assessment of the achievable minimum levels of code cross-correlation and the system penalties associated with multi-user operation (two-user operation). A two-hop coding:decoding node using SSFBG grating pairs is also demonstrated.

3.3.1 Single channel experiment

The experimental set up used is similar to the earlier 7-chip experiments, except that the gratings used for encoding/decoding are of longer chip length (63-chip compared to the 7-chip used in earlier experiments) (see Figure 3.11). In order to assess the quality of the 63-chip gratings fabricated, the equivalent temporal domain measurements for G63B-1 and G63B-1* were obtained, as plotted in Figure 3.12. In this instance, due to the use of longer code sequences direct electronic measurements are of value since despite the 20 GHz bandwidth limitation, one can still discern features on the waveform associated with the chip structure of the individual codes. Good qualitative agreement between experiment and theory are evident. From the plots it can readily be seen that the impulse response of G63B-1* is close to the time reversed response of G63B-1 as required for good matched filter operation. Importantly, these experiments confirm that good coherence along the gratings with lengths in excess of 40mm can be maintained.

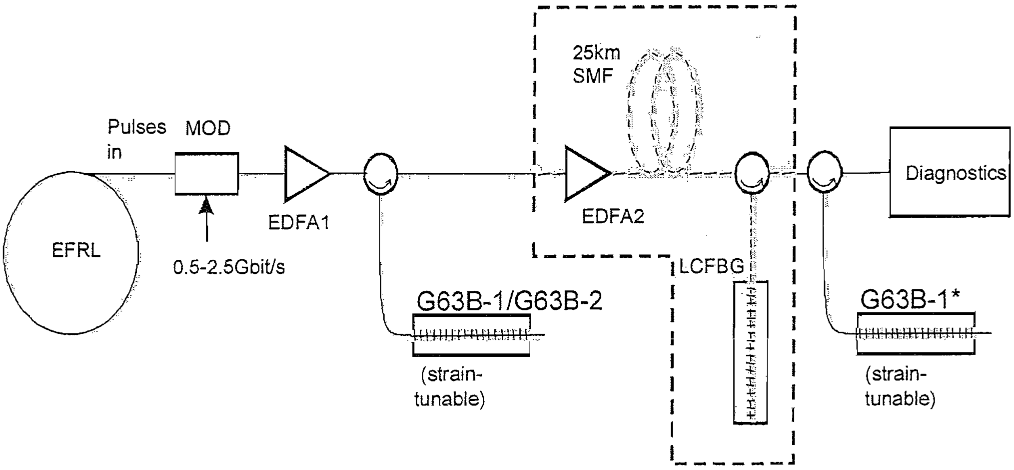

Figure 3.11: Experimental set-up (EDFA: Erbium-doped fibre amplifier, LCFBG: linearly chirped fibre Bragg grating).

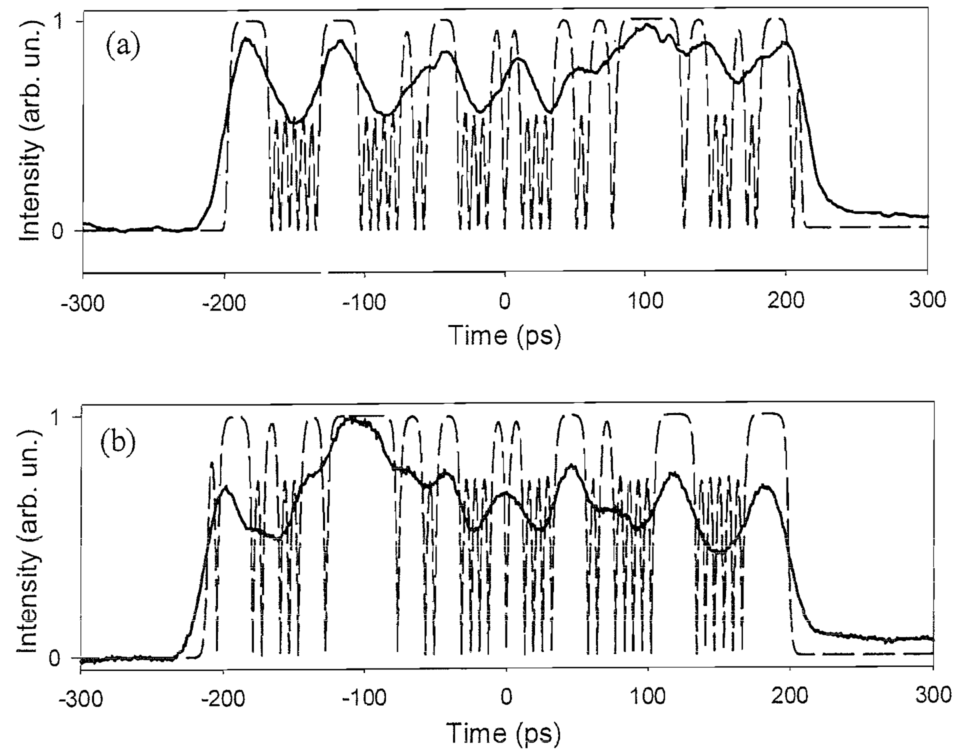

Figure 3.12: Traces of the encoded waveforms for (a) the G63B-1, and (b) the G63B-2 grating, for 2.5ps soliton input pulses (solid lines: experimental measurements, dashed lines: theoretical plots). The detection bandwidth of the experimental measurement (~20GHz) was not taken into account for the theoretical calculation.

The results of the temporal code detection measurements made with the electronic detection system for the 63-bit code grating pairs G63B-1:G63 B-1* and G63B-2:G63B-2* are summarized in Figure 3.13(a) and Figure 3.13(b), where the clarity of the autocorrelation is as expected even more distinct than that of the 7-chip bipolar gratings, due to the larger number of chips used within the code. The height of the autocorrelation spike is predicted to increase as L^2 where L is the code length). Figure 3.13(c) plots the result of the coding:decoding process for two different Gold codes i.e. G63B-1:G63B-2*. No distinct correlation spike is observed as expected for the case of two Gold codes and similar results were also obtained for the G63B-2:G63B-1* case as shown in Figure 3.13(d).

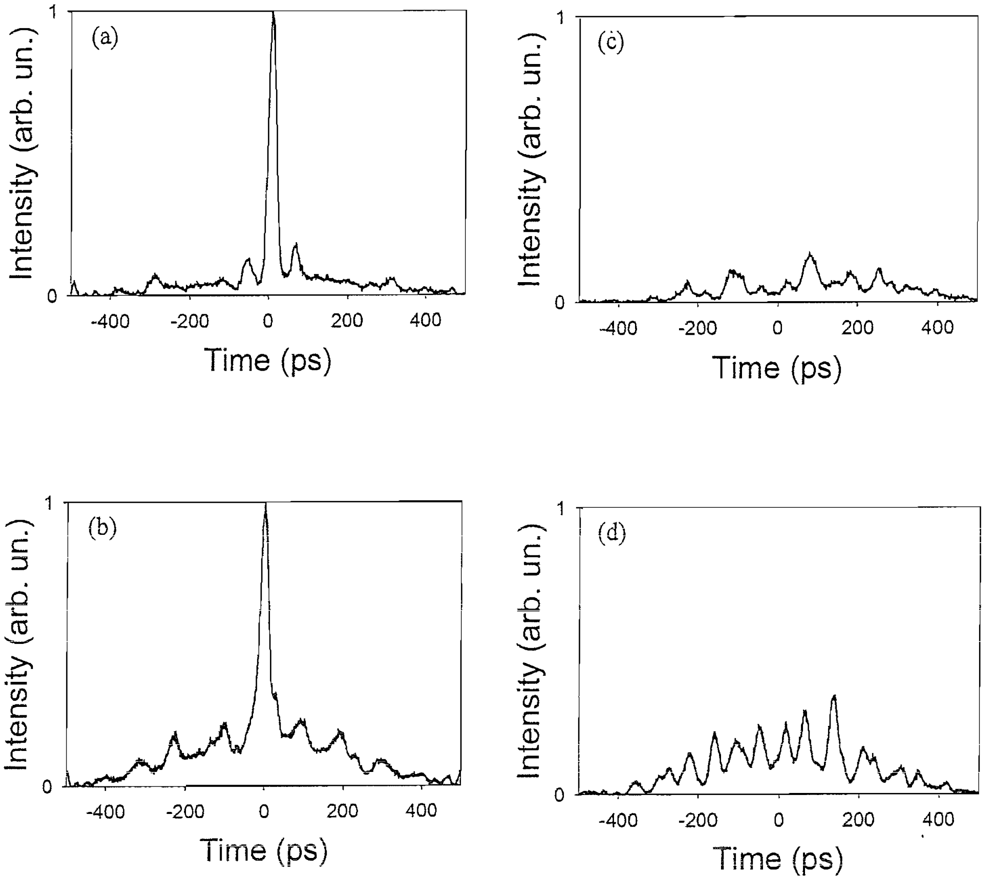

Figure 3.13: Traces of the signals after the code:decode process for 2.5ps soliton input pulses, for the grating combinations: (a) G63B-1:G63B-1, (b) G63B-2:G63B-2*, (c) G63B-2:G63B-1*, and (d) G63B-1:G63B-2*. The detection bandwidth was 20GHz. All the traces were taken at the same received optical power.*

These results are also confirmed from the eye diagrams when modulated at a data rate of 1.25 Gbit/s shown in Figure 3.14 where clear eye openings are seen for the matched case (G63B-1:G63B-1*) while low level noise-like signals are obtained for the unmatched case (G63B-2:G63B-1*).

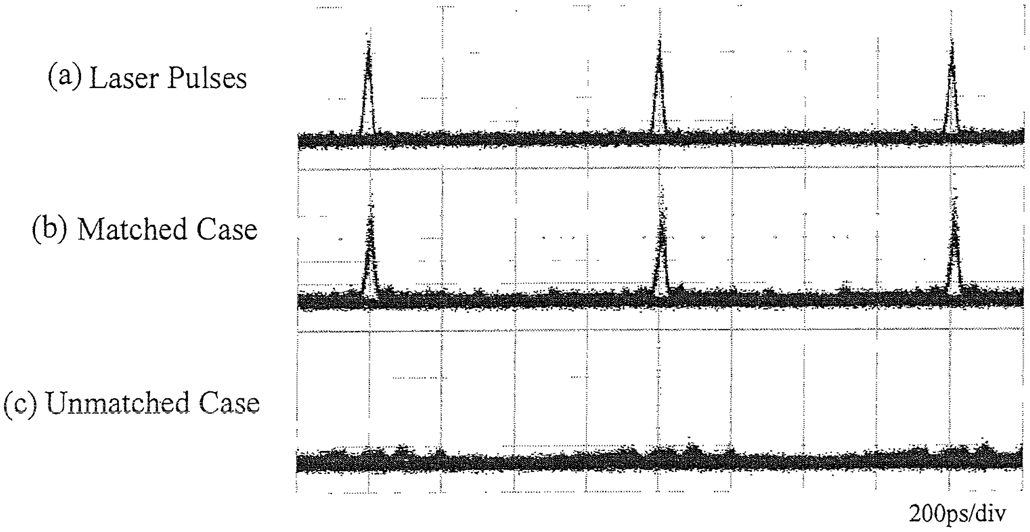

Figure 3.14: Eye diagrams obtained at a data rate of 1.25 Gbit/s. (a) laser back-to-back, (b) matched case (correct code used), (c) unmatched case (incorrect code used).

Figures 3.15(a) and 3.15(b) show the measured SHG autocorrelations of code recognition for G63B-1:G63B-1* and G63B-2:G63B-2* against theoretical calculations. Again, close to theoretical performance can be observed for both cases. The decoded pulse width for G63B-1:G63B-1* is ~6.8ps and G63B-2:G63B-2* is ~8.4ps as calculated from the SHG measurements. The slightly broader decoded pulse width for the G63B-2:G63B-2* gratings combination is due to the choice of the Gold code sequence employed, which exhibits a broader autocorrelation pulse width.

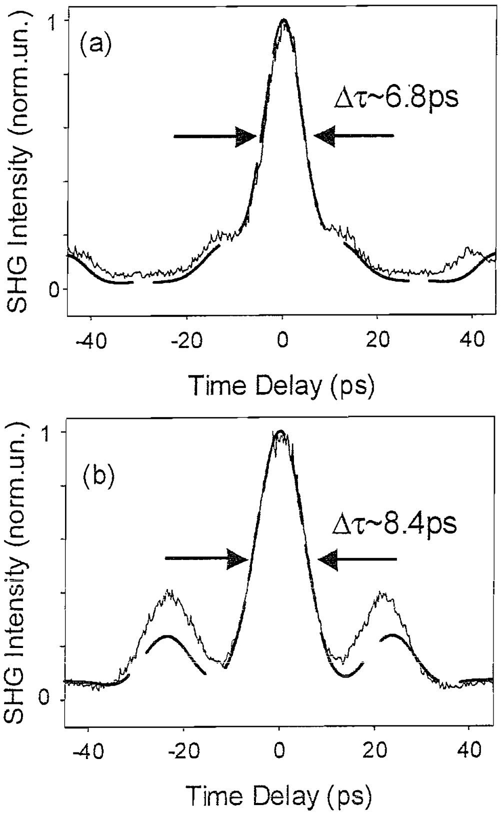

Figure 3.15: Intensity SHG autocorrelation traces of the signals after code:decode process for 2.5ps soliton input pulses for the 63-bit grating combinations: (a) G63B-1:G63B-1 and (b) G63B-2:G63B-2*. (solid lines: experimental measurements, dashed lines: theoretical plots). Δτ is the decoded pulse width obtained from the SHG intensity measurement.*

In Figure 3.16 the BER measurements for the back-to-back G63B-1:G63B-1* grating pair encode:decode process along with results for the associated 25 km transmission are plotted. These measurements were made at a bit rate of 1.25 Gbit/s to ensure no temporal overlap of adjacent decoded correlation pulses as can be seen from the eye diagrams shown earlier in Figure 3.14. Error free performance can be obtained for the encode:decode process both with and without transmission and with minimal power penalty between both cases. However, there is a small power penalty of ~1.5 dB between the code:decode process relative to the laser back-to-back measurement. This small power penalty is due to the use of noisy EDFAs (high value of noise figure) to overcome the insertion loss of both encode and decode gratings.

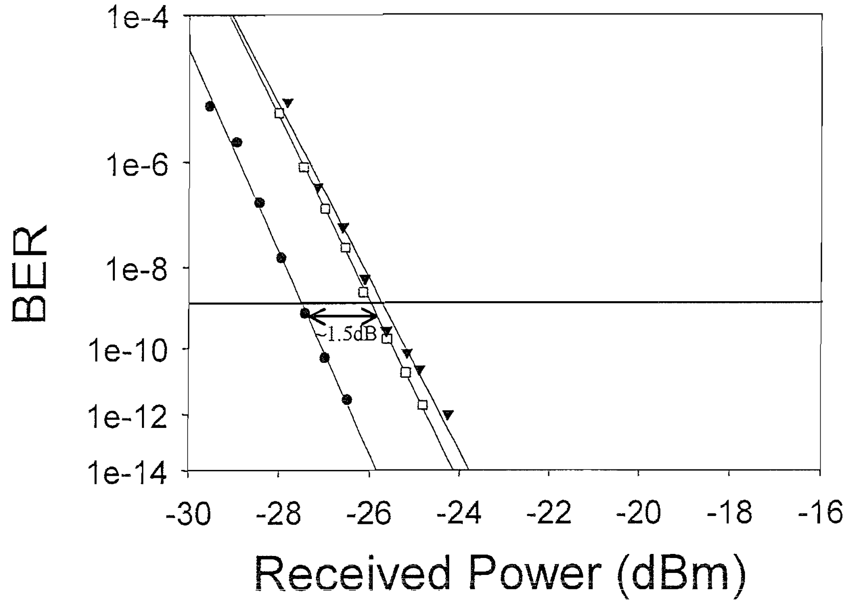

Figure 3.16: BER curves for the G63B-1:G63B-1 combinations (closed circles: laser back to-back, open squares: no transmission, closed triangles: after transmission). The data rate was 1.25 Gbit/s.*

3.3.2 Two-channel experiment (Multi-user operation)

To assess the performance of the multiple user system, the experimental set up is shown as below in Figure 3.17. Pulses of 2.5ps duration generated using a mode-locked soliton fibre ring laser operating at 10 GHz, were first gated down to a lower repetition frequency, and encoded with pseudorandom data at 1.25 Gbit/s. The data pulses were then split using a 3dB coupler and fed onto two separate encoder gratings, denoted G63B-1 and G63B-2 respectively, before being recombined into a single fibre using a 3dB coupler. Once the data pulses are reflected from gratings G63B-1 and G63B-2, they generate two distinct data streams encoded with either one of the two distinct codes. The relative passage time of the two channels could be fine-tuned using the fibre delay lines to allow anywhere between zero and full temporal overlap of the coded bits at the receiver.

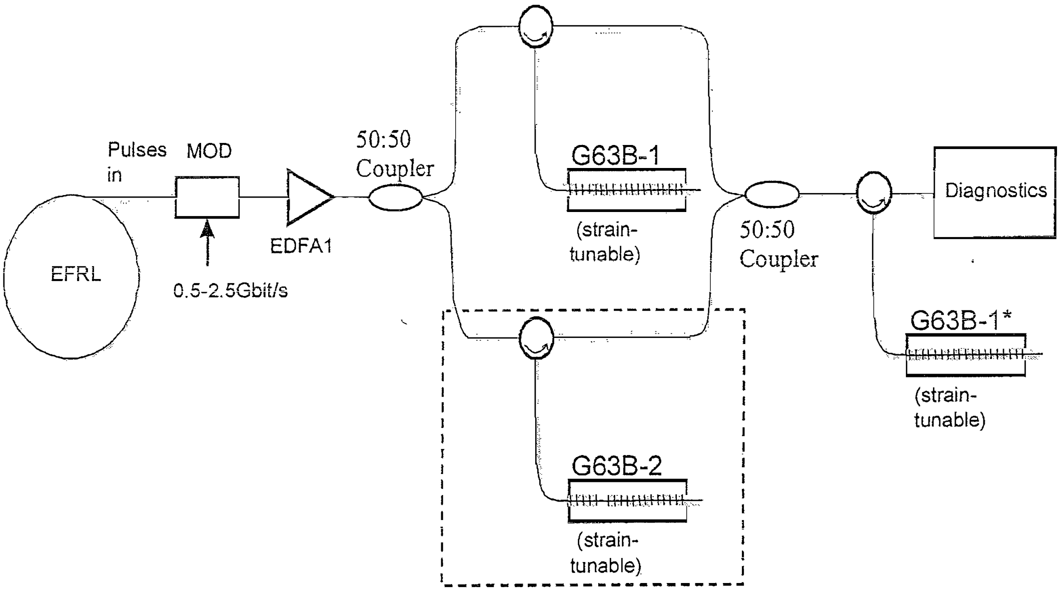

Figure 3.17: Experimental set-up for two-channel experiment (EDFA: Erbium-doped fibre amplifier).

The pulses in each channel were set to fully overlap temporally at the detector so as to maximise the impact of inter-channel interference. The optical power in each individual channel incident at the decoder grating was set to be the same.

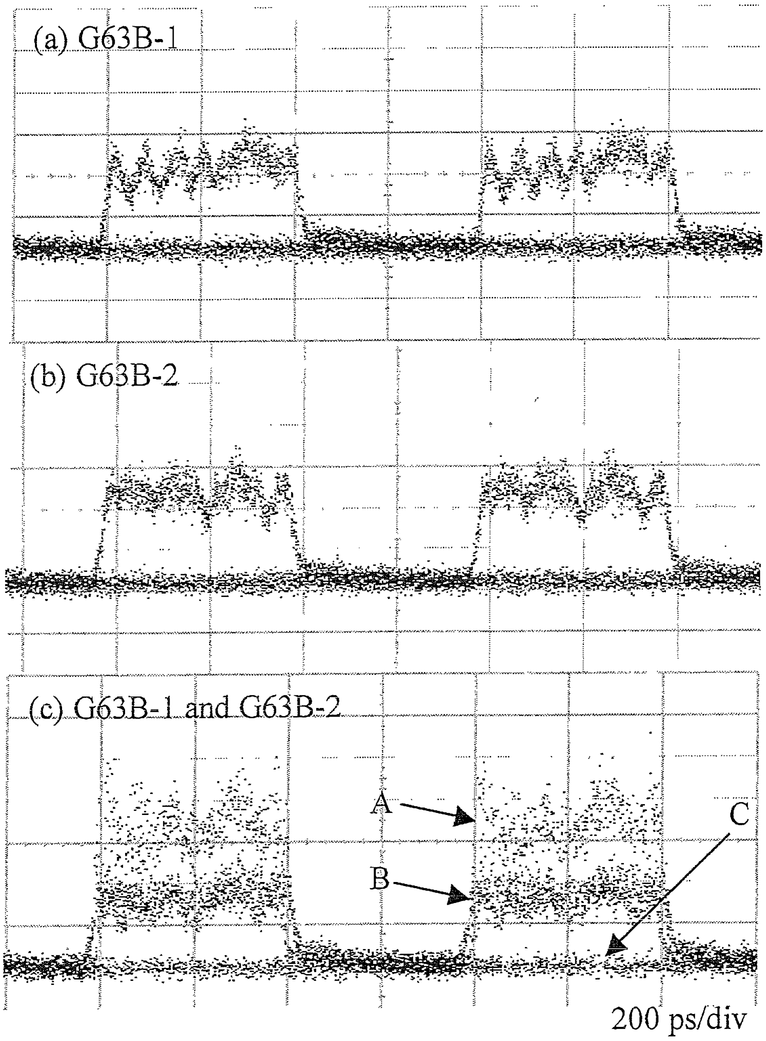

Figure 3.18: Pulseforms at data rate of 1.25 Gbit/s showing the encoding signals after reflection off the gratings: (a) G63B-1, (b) G63B-2 and (c) the combined signals of G63B-1 and G63B-2 with full temporal overlap. A – Combined signal when both channels have '1' data bits, B – Combined signal when only one of the channels has a '1' data bit, while the data bit on the other channel is '0'. C – Combined signal when both channels have '0' data bits.

First, the eye diagrams after reflection off each individual encoding SSFBGs, i.e. G63B-1 and G63B-2, as well as when both the encoding waveforms are combined together were obtained, as shown in Figure 3.18. The combined encoded channels generated after reflection off gratings G63B-1 and G63B-2 allow the investigation of the impact of interchannel crosstalk although it should be appreciated that the codes were generated with pulses derived from the same source and this leads to additional noise due to the coherent interference between the two channels. This noise gives rise to signal 'beating' being observed at the oscilloscope when both the encoded signals overlap. This effect can be reduced by adding additional fibre length to the interfering channel so that the length difference between both channels are more than the coherence length of the pulse source. Furthermore, to avoid coherent interference noise, each coded signal should be generated using an independent pulse source. The two coded channels are then combined into a single fibre before transmission to the decoder grating.

Figure 3.19 shows the BER results and the corresponding eye diagrams after decoding of the above system measurements. Error free performance with minimal power penalty both with and without transmission can be obtained. The apparent noise penalty of ~3.7dB observed when comparing the G63B-1:G63B-1* case with 2-channel case, (G63B-1 and G63B-2):G63B-1* results primarily from the increased average power resulting from the addition of the second interference channel as well as the coherent interference between both channels, thereby demonstrating the excellent code discrimination achieved using the SSFBGs. A more stringent test of the asynchronous cross-talk performance would obviously require the use of an independent pulse generator to generate each of the individual OCDMA coded channels. At the time when these experiments were conducted we did not have the equipment required to make such measurements.

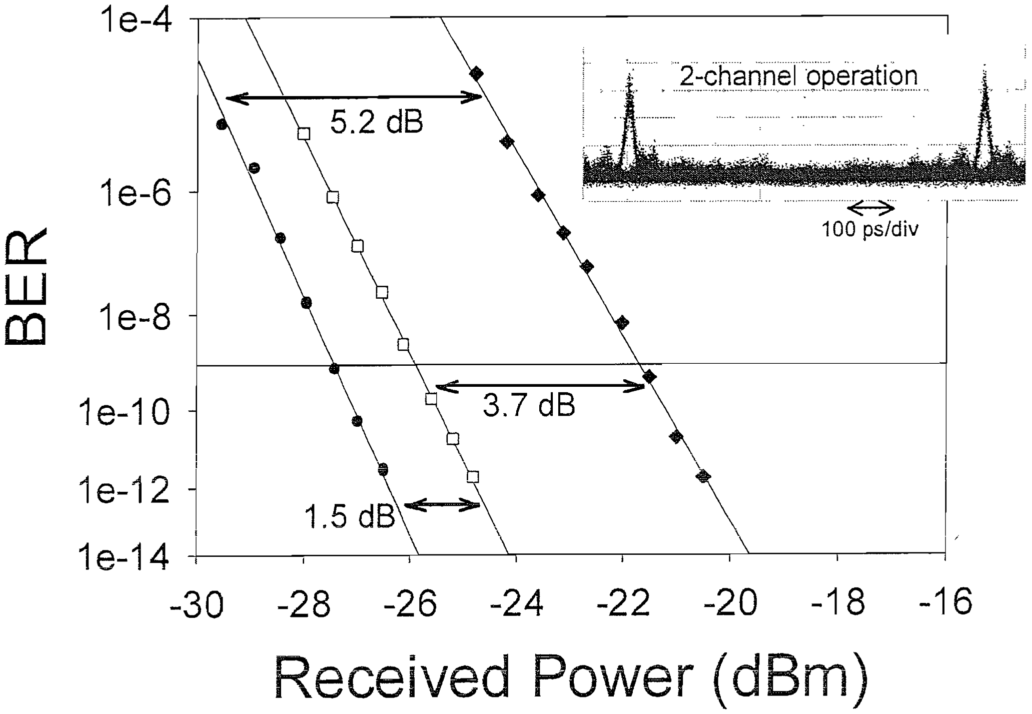

Figure 3.19: BER results for two-channel experiment (closed circles: laser back-to-back, closed diamonds: two-channel operation and open squares: single-channel operation). Inset: Corresponding eye diagram for two-channel experiment. The data rate is 1.25 Gbit/s.

3.3.3 Generation, recognition and re-coding of 63-chip bipolar optical codes sequences

The purpose of this experiment is to show that the SSFBGs fabricated can be applied to the cascading of functions, i.e. generation, recognition and subsequent recoding and decoding. The experimental set up is shown in Figure 3.20 and comprises a similar bit-rate tuneable (0.5 - 10 GHz) erbium fibre ring laser which generates 2ps soliton pulses, and a cascade of two coding:decoding SSFBG pairs that have been used in the earlier experiments. These individual gratings are denoted by G63B-1, G63B-1* and G63B-2, G63B-2*. Grating G63B-1 is used to generate a temporally distributed 63-chip bipolar phase-shift keyed code sequence from an incoming pulse. Grating G63B-1* is then used to decode the resulting code thereby generating a short pulse with a duration of order the chip length. This pulse is then fed onto grating G63B-2 and thereby generates a second bipolar coded sequence. Grating G63B-2* is subsequently used to decode this second code, resulting again in the formation of a further short, distinct correlation peak. In one experiment, we thus demonstrate the key functions of optical pattern generation, recognition and recoding of 63-chip code sequences. Recoding is an important function required, for example, to allow ready switching of data between different optical networks operating with different code allocations, or to enhance a given networks functionality.

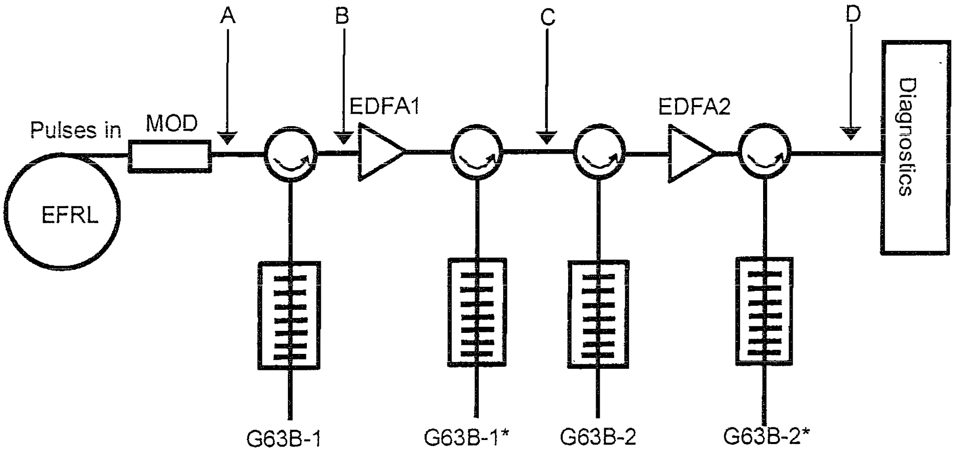

Figure 3.20: Experiment set up for investigation of the cascading of functions.

Figures 3.21(a)-(d) show the temporal pulse forms at corresponding points (A-D) within the experimental set up along with the results of a numerical simulation. These pulse measurements were obtained with a fast diode and scope with ~20 GHz bandwidth, far less than that required to resolve the individual chips, but sufficient to gain a good appreciation of the system's operation. The theoretical plots shown in Figures 3.21(a)-(d) take into account the initial width of the input pulses, but not the electrical bandwidth of the detection system. The high quality of the code generation (Figure 3.21(b)) and pattern recognition (Figure 3.21(c)) obtained is self-evident. Using an SHG autocorrelator (<100fs resolution), the actual width of the peak for the matched filtered process G63B-1:G63B-1* was confirmed to be ~6.8ps, in good agreement with our theoretical calculations. The corresponding SHG autocorrelation plot is shown in Figure 3.21(e). The recoded pulse form (G63B-1:G63B-1*:G63B-2:G63B-2*) appeared to be slightly degraded relative to the single stage (G63B-1:G63B-1*), however a pulse with single, distinct peak was still obtained (Figure 3.21(d)). This was because the pulses input to the second-stage coding process were longer (~6.8ps) as compared to the 2ps pulses input to the first coding stage, and already exhibit additional structure in the wings. As a result, the width of the main peak of the second stage correlation broadened to ~12ps, as confirmed from the SHG autocorrelation measurement (see Figure 3.21(f)). By using a nonlinear element within the system at the receiver, for example: a nonlinear optical loop mirror (NOLM) as described in the next chapter, or two-photon absorption in a semiconductor detector [3], it should be possible to further enhance the correlation contrast, and to reduce the broadening of pulse recognition signature.

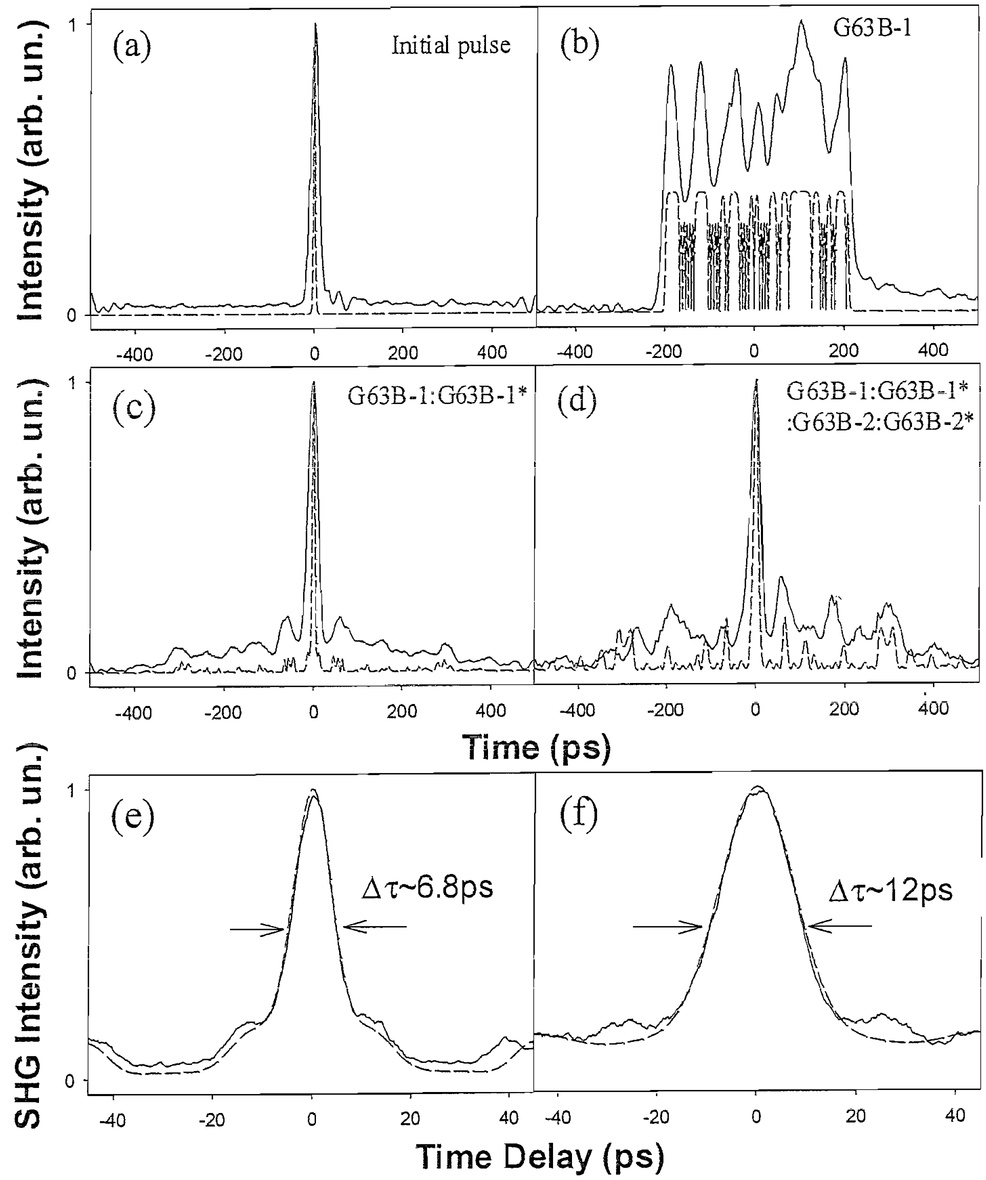

Figure 3.21: The measured (solid) and theoretical (dashed) pulse shapes at points: A - input pulse shape (a), B – G63B-1 code sequences (b), C – G63B-1:G63B-1 correlation (c) and D – G63B-1:G63B-1*:G63B-2:G63B-2* correlation (d) within the system (refer to Figure 20). The theoretical curves are not corrected for the electronic measurement system resolution (20ps), i.e. they represent the true optical signals. The measured (solid) and theoretical (dashed) traces from the SHG intensity autocorrelation measurements for G63B-1:G63B-1* correlation and G63B-1:G63B-1*:G63B-2:G63B-2* correlation are shown in Figures (e) and (f) respectively.*

3.4 Performance of 255-chip quaternary Family A sequence SSFBGs

This section reports on assessing the quality of the 255-chip SSFBGs, which are the longest SSFBG coders/decoders reported to date for DS-OCDMA system. These gratings also have with the highest chip rates and contained up to four discrete phase coding levels. This is followed by a description of the use of these gratings in an elementary 4-channel OCDMA/WDM system incorporating different coding schemes, repetition rates and wavelengths. The experiment shows that the SSFBGs are compatible with WDM techniques.

3.4.1 Assessment of the quality of the 255-chip SSFBGs for coding/decoding operation

A simple back-to-back code:decode measurement similar to the experimental set up shown in Figure 3.11 (without transmission link) is used to assess the performance of the 255-chip gratings (see Figure 3.22). Figures 3.23(b) and 3.23(c) show the calculated encoded response after reflection from grating A255Q-1 and A255Q-2 using a 2.5ps input pulse [Figure 3.23(a)], generated from a mode-locked fibre ring laser. Notice that the both gratings spread the 2.5ps short pulse into an ~800ps encoded waveform. Figure 3.23(d) plots the decoded response of grating A255Q-1* to code sequence A255Q-1, denoted A255Q-1:A255Q-1*, where it is seen that a short chip length pulse on a very low-level pedestal background is obtained, thereby providing a very high-quality pattern recognition signal. Similarly, Figure 3.23(e) shows the theoretical code recognition using gratings A255Q-2:A255Q-2*. However, when incorrect code is sent to the decoder, no discernible recognition signature is observed as expected for two different Family A quaternary codes as shown in Figure 3.23(f). Note that the limited optical detector bandwidth is not taken into account when calculating the above traces.

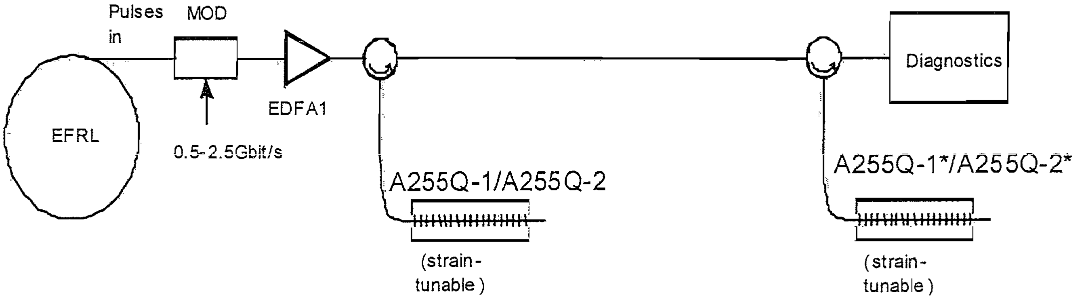

Figure 3.22: Experimental set up to assess the performance of the 255-chip gratings.

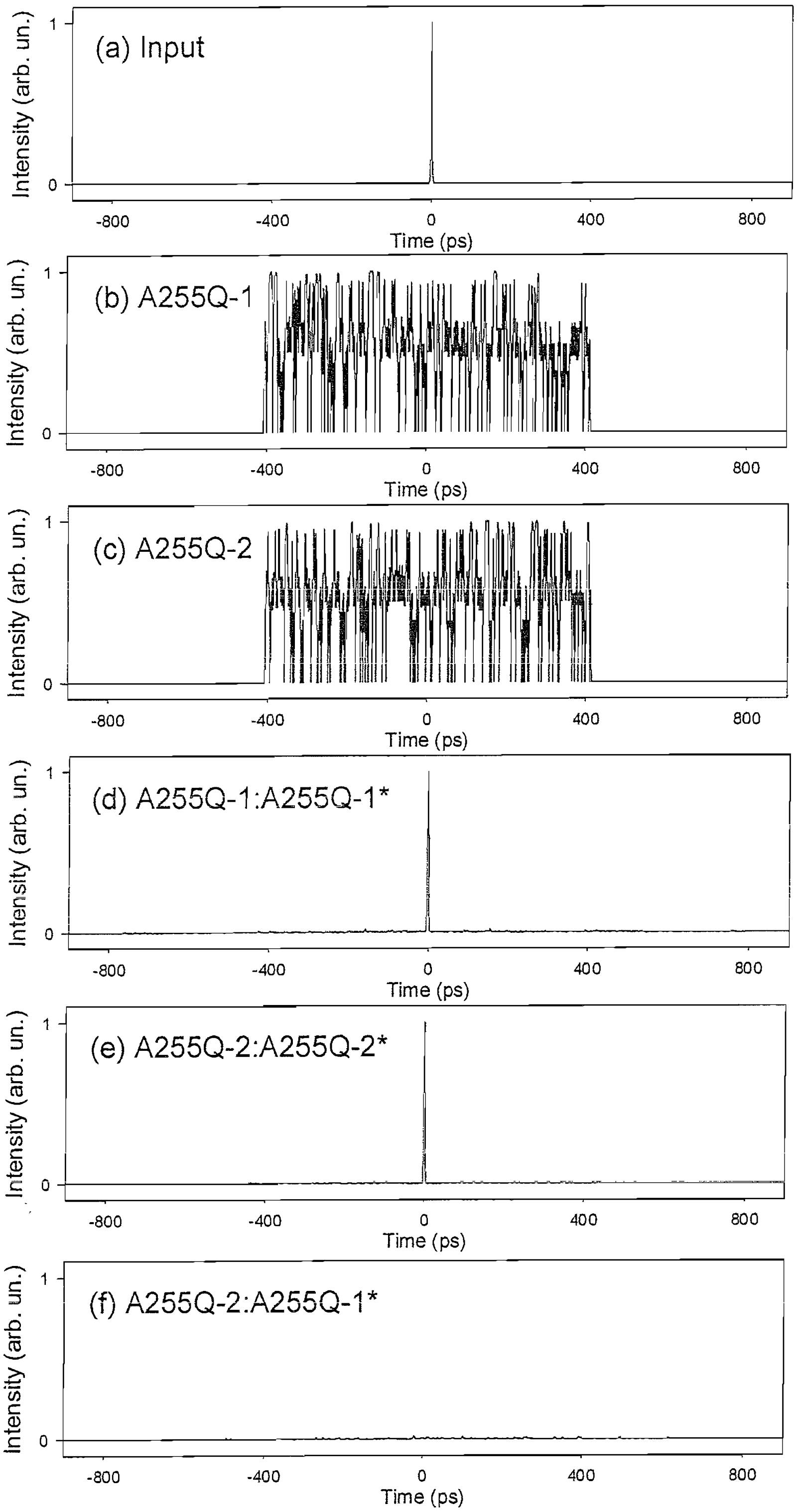

Figure 3.23: Calculated time domain response for (a) 2.5ps transform limited input pulse, (b) encoded waveform from A255Q-1 after convolving with the input response, (c) similar encoded waveform obtained from A255Q-2, (d) autocorrelation signatures using grating combinations A255Q-1:A255Q-1, (e) autocorrelation signatures using grating combinations A255Q-2:A255Q-2*, (f) cross-correlation signatures using grating combinations A255Q-2:A255Q-1*.*

In Figure 3.24(b), the oscilloscope trace of the coded A255Q-1 channel obtained by reflecting 2.5ps short pulses [as shown in Figure 3.24(a)] from grating A255Q-1 are shown. Although the individual features of the coded sequence are too short to be resolved (each chip has a duration of 3.2ps and the detection system has only 20ps resolution), it is clear that the coding grating spreads the incident 2.5ps pulse over a time period of 800ps as expected from our calculations in Figures 3.24(b) and 3.24(c). Figure 3.24(c) shows the corresponding oscilloscope trace when grating A255Q-2 is used for encoding. The bandwidth limited decoded response of grating A255Q-1* to the coded A255Q-1 channel is shown in Figure 3.24(d).

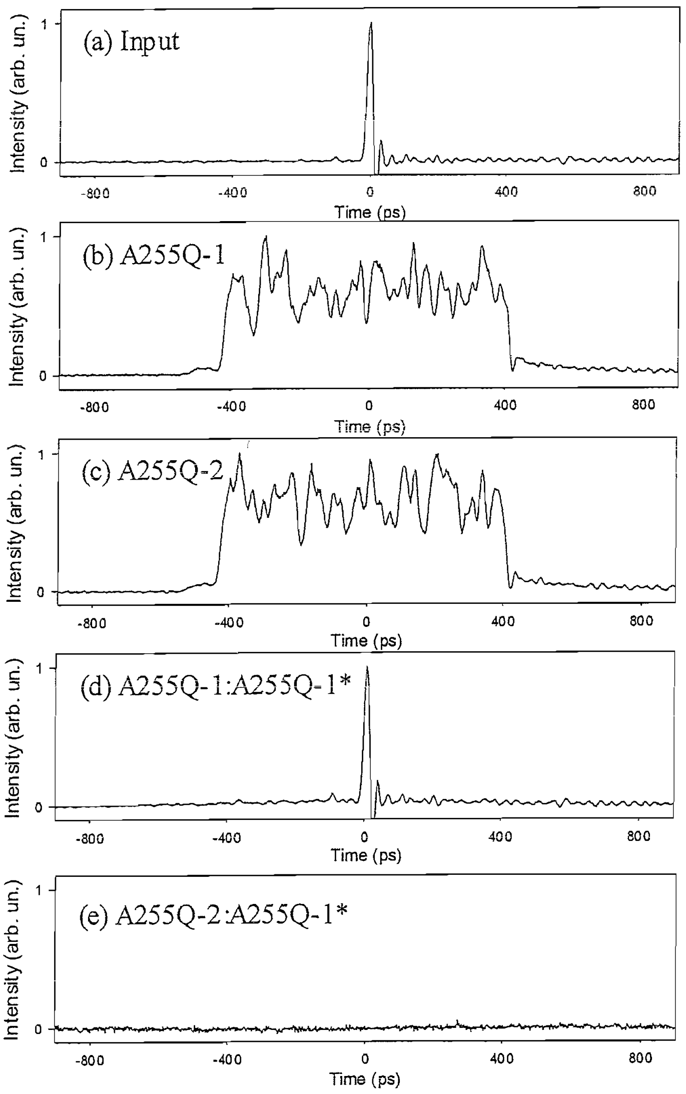

Figure 3.24: Oscilloscope traces of (a) 2.5ps transform limited input pulse, (b) encoded waveform after reflection from SSFBG A255Q-1, (c) encoded waveform after reflection from SSFBG A255Q-2, (d) after matched filtering for the grating combinations A255Q-1:A255Q-1, (e) after matched filtering for the grating combinations A255Q-2:A255Q-1*. The measured resolution was ~20ps. Note that the ringing observed in the traces is due to the effects of the photodiode.*

As expected, a very distinct chip-length pulse with very low-level pedestals at both sides of the pulse is obtained. Figure 3.24(e) shows the crosscorrelation response of A255Q-2:A255Q-1*. No distinct correlation signature can be observed highlighting the excellent quality of the code recognition that can be achieved using such an approach, just as expected from our theoretical calculations.

Next, SHG intensity autocorrelation measurements were taken using an intensity autocorrelator to determine the exact decoded pulse width. The results are plotted in Figure 3.25. SHG intensity measurements showed the recognition signal to have a well-defined peak, having a width of 3.2ps, again in good agreement with the theoretical calculations.

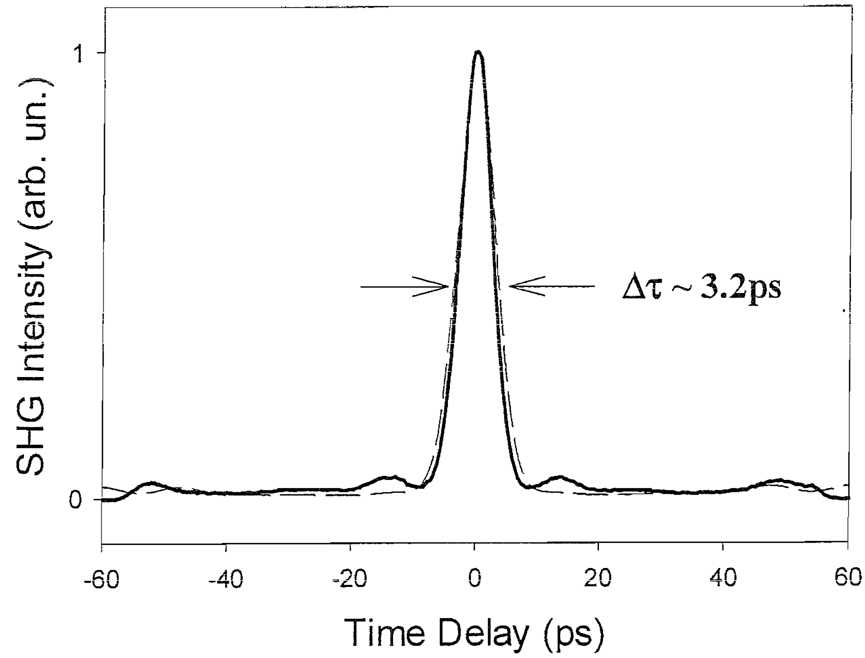

Figure 3.25: Theoretical (dashed line) and experimental (solid line) SHG intensity autocorrelation traces for the Q1:Q1 process. Note that the low level pedestal indicates a high quality code recognition signature. The correctly decoded pulsewidth was ~3.2ps.*

3.4.2 OCDMA/WDM System Experimental Results

The OCDMA/WDM experimental setup is shown in Figure 3.26. Pulses from a 2.5ps, 10GHz, regeneratively mode locked erbium fibre ring laser (EFRL) operating at 1552.5nm were first split using a coupler into two separate fibres. The first of these outputs was modulated to provide a pseudorandom data sequence of 2.5ps pulses at 1.25 Gbit/s. The second output was first amplified and then fed to the control port of a dual-wavelength NOLM operating as a wavelength converter (WC). The NOLM configuration allowed the output of a continuous-wave DFB laser operating at 1556.5nm to be modulated using 1552.5nm control pulses. By appropriately setting the loss and polarisation of light within the WC, a 10 GHz train of high-quality, 3.5ps pulses at 1556.5nm were generated.

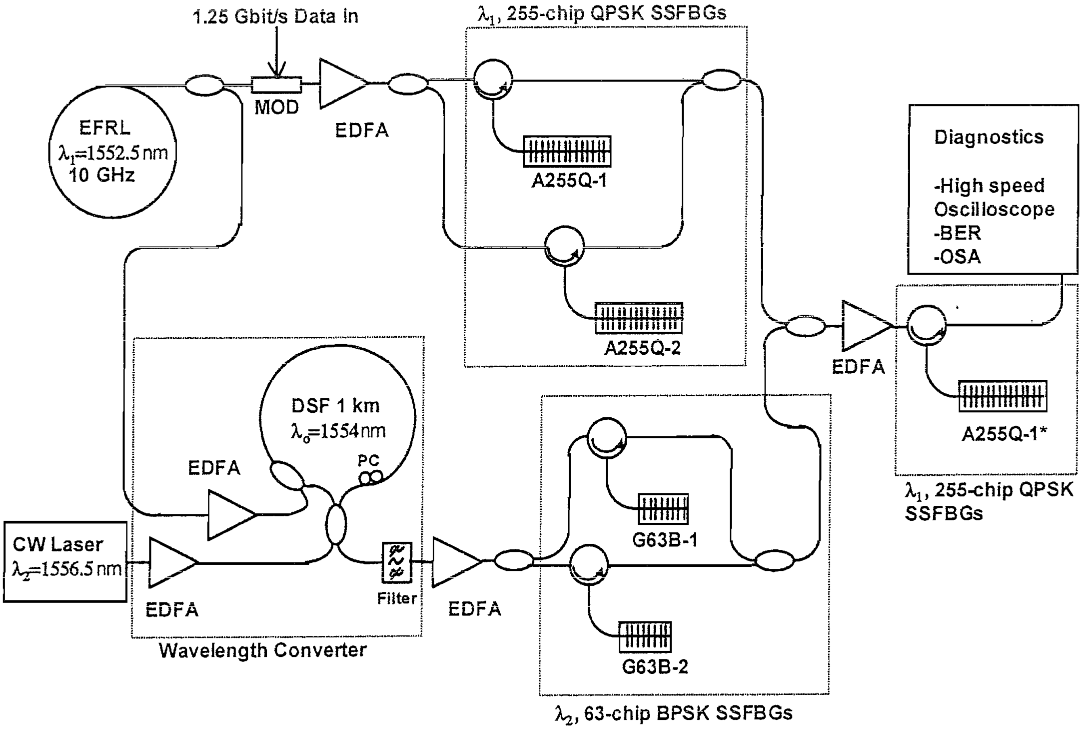

Figure 3.26: Experimental setup to demonstrate the OCDMA/WDM system. QPSK: Quaternary phase shift keying SSFBGs, BPSK: bipolar phase shift keying SSFBGs.

The individual pulse streams at the two wavelengths were then reflected off one of four coding gratings to generate four separate coded data channels. The 1.25 Gbit/s 1552.5nm channels were encoded with either one of two 'orthogonal' 255-chip, 320 Gchip/s, quadrature code sequences (A255Q-1, A255Q-2). The 10 GHz channels at 1556.5nm were encoded with either one of two 63-chip, 160 Gchip/s, bipolar code sequences (G63B-1, G63B-2) corresponding to two 'orthogonal' Gold code-sequences.

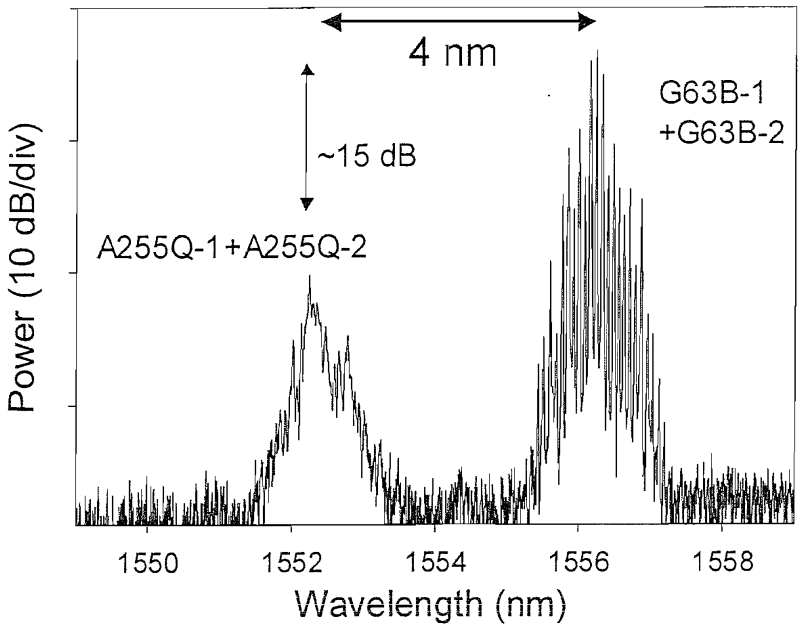

Figure 3.27: Optical spectra for the combined 4-channel (1552nm: A255Q-1, A255Q-2 and 1556.2nm: G63B-1, G63B-2) OCDMA/WDM signals. Note that the different peak power spectrum for both wavelengths is due to the different repetition rates used (1552.5nm: 1.25 Gbit/s and 1556.2nm: 10 GHz). The measured resolution is ~20pm.

All four channels were combined into a single fibre and the resulting signal fed onto an appropriate decode grating matched to the particular channel (These gratings are correspondingly denoted by A255Q-1*, A255Q-2*, G63B-1* or G63B-2*). Figure 3.27 shows the optical spectrum of the combined four-channel OCDMA/WDM signals incident to the decode grating. The channels at 1556.2nm contain ~15 dB more average power than those at 1552.5nm due to the higher 10 GHz repetition rate of the 1556.2nm signals since the average energy per-bit of each channel is kept constant. The optical spectra of the decoded response of gratings A255Q-1* and A255Q-2* to the combined four-channel input (A255Q-1+A255Q-2+G63B-1+G63B-2) are shown in Figure 3.28. The signals at 1556.2nm wavelength (G63B-1+G63B-2) are suppressed by ~15 dB after matched filtering using decode gratings A255Q-1* and A255Q-2* respectively. These plots show that the inherent wavelength selectivity of the decode grating can be used both to provide wavelength channel selection as well as the decoding function for 'in-band' signals, eliminating the requirement for additional wavelength channel filtering elements, in contrast to the experimental demonstration reported in Ref [4].

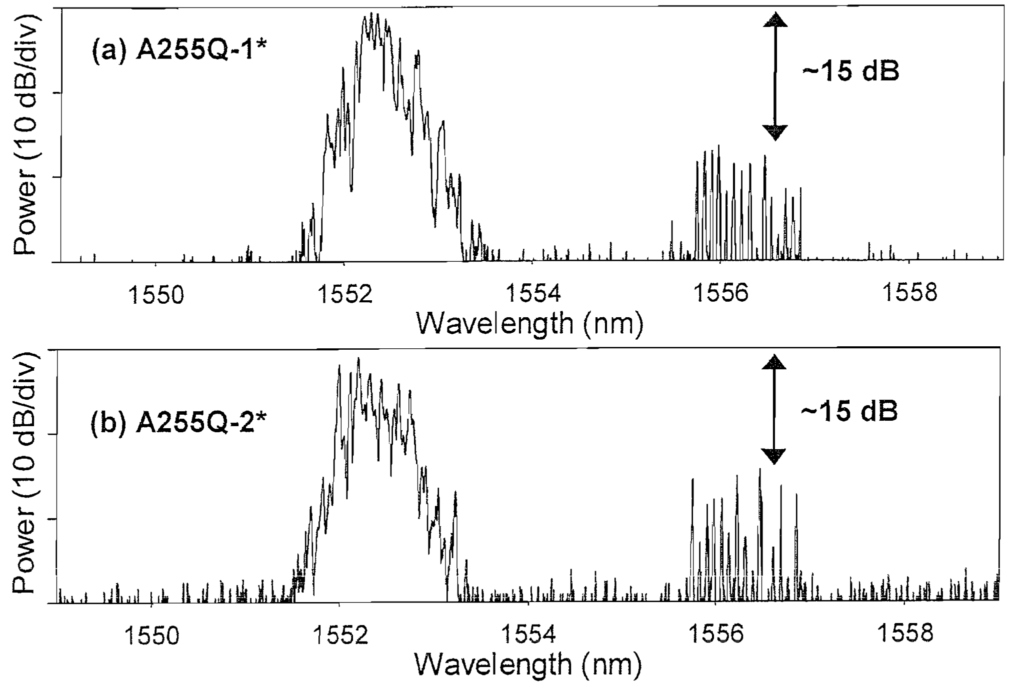

Figure 3.28: Optical spectra after matched filtering with (a) decode grating A255Q-1 and (b) decode grating A255Q-2*. The measured resolution is ~20pm.*

In Figure 3.29 BER measurements made on the individual 255-chip A255Q-1 channel in the presence of various combinations of interfering channels are plotted. A number of features are apparent. Firstly, there is no power penalty observed when additional channels at a second wavelength (1556.5nm) are added, even when these channels operate with different coding schemes and repetition rates. The ~4 dB power penalty observed when comparing the BER cases corresponding to the channel combinations A255Q-1+A255Q-2+G63B-1+G63B-2:A255Q-1* with A255Q-1+G63B-1+G63B-2:A255Q-1* results primarily from the increased average power due to the addition of the second 'in band' channel (A255Q-2), although a contribution from coherent interference noise between the code sequences also arises. Chapter Four describes the use of nonlinear filtering elements after the matched decode grating to enhance the decoded response and reduce this power penalty. Note that the individual pattern recognition signatures each have a total length of 1.6ns. At a data rate of 1.25 Gbit/s the tails of adjacent recognition signatures overlap. This provides an additional element of interference noise which contributes the majority of the ~4 dB power penalty measured when comparing A255Q-1:A255Q-1* relative to the back-to-back measurement. Again, this noise contribution can also be largely eliminated using a nonlinear optical filter at the receiver. When the measurements are performed at 622 Mbit/s (no overlap between adjacent encoded signals), no power penalty is observed for A255Q-1:A255Q-1* measurement relative to the back-to-back measurement (see Figure 3.29).

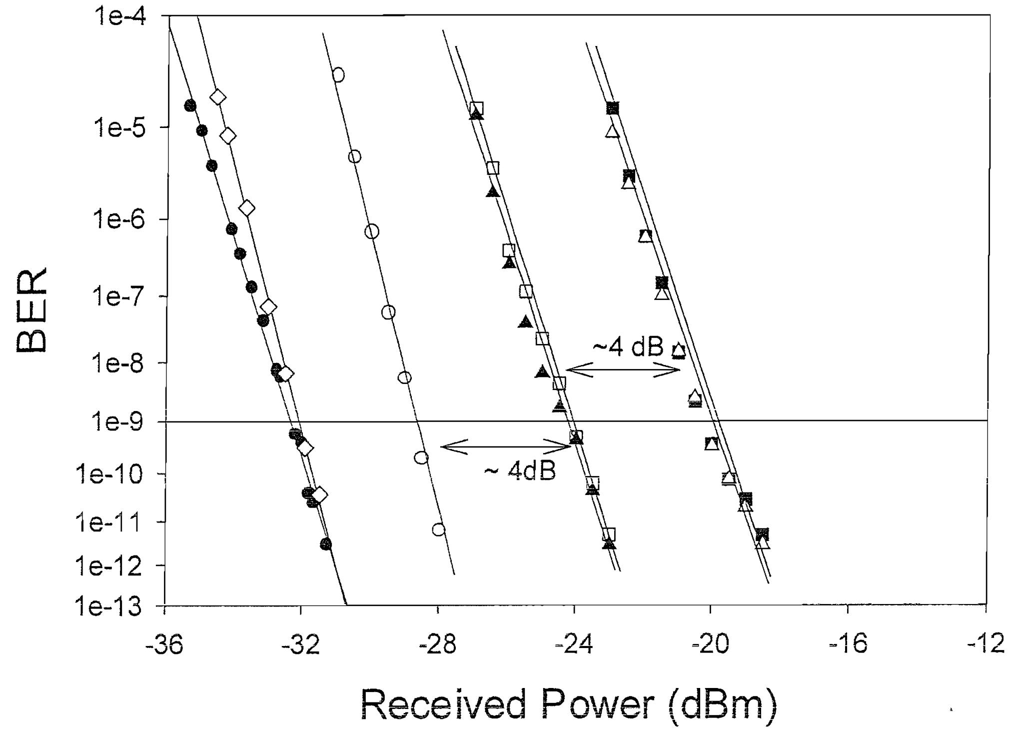

Figure 3.29: BER results for various combinations of interfering channels measured against received power.

At 1.25 Gbit/s

Laser back-to-back (open circles),

A255Q-1:A255Q-1 (closed triangles),*

A255Q-1+A255Q-2:A255Q-1 (open triangles),*

A255Q-1+G63B-1+G63B-2:A255Q-1 (open squares)*

and A255Q-1+A255Q-2+G63B-1+G63B-2:A255Q-1 (closed squares).*

At 622 Mbit/s

Laser back-to-back (closed circles),

and A255Q-1:A255Q-1 (open diamonds)*

3.5 Hybrid combination of fibre delay lines and SSFBG for a 7-chip optical codes generation/recognition

The experiments reported so far have demonstrated the use of SSFBG encoders and decoders to obtain excellent code generation and recognition for use within DS-OCDMA systems. The use of identical technologies for both the encoder and decoder has raised the question as to whether different implementation approaches can be used at the transmitter/receiver ends. Such compatibility will be preferable in practical OCDMA systems to allow coders based on different technological approaches to be used. This section shows that this is possible and demonstrates the use of a hybrid combination of fibre delay lines (encoder) and the SSFBGs (decoder) for a 10 Gbit/s all-optical OCDMA encoder/decoder system.

Figure 3.30 illustrates the experimental set up used to test this hybrid combination. The pulse source used is a 10GHz erbium fibre ring laser (EFRL) producing 2.5ps pulses at 1554nm. Short pulses are multiplexed and delayed in the fibre delay line encoder to generate the desired 7-chip amplitude modulated (unipolar) M-sequence code '1110010'. Four parallel fibre delay arms are used in the delay line encoder configuration as shown in Figure 3.30, where τ corresponds to a delay of 6.4ps, yielding a chip rate of 160 Gchip/s. An unipolar M-sequence code '1110010' is chosen to ensure that the autocorrelation pulseforms upon decoding (with code '0100111') will feature a single dominant, well defined peak, whereas the cross-correlation between this code and other M-sequence codes (for example '0011000') will yield low-level signals. The polarisation controller (PC) in each delay line is used to maintain the same polarisation state for all delayed pulses at the output of the fibre delay line encoder. A single polarisation state of the composite code sequences was further confirmed by launching the code words into a polarising isolator. A 7-chip amplitude modulated (unipolar) SSFBG is used as the decoder. The SSFBG chosen is M7U-1, having the M-sequence code '0100111' imprinted onto the grating during the grating writing process.

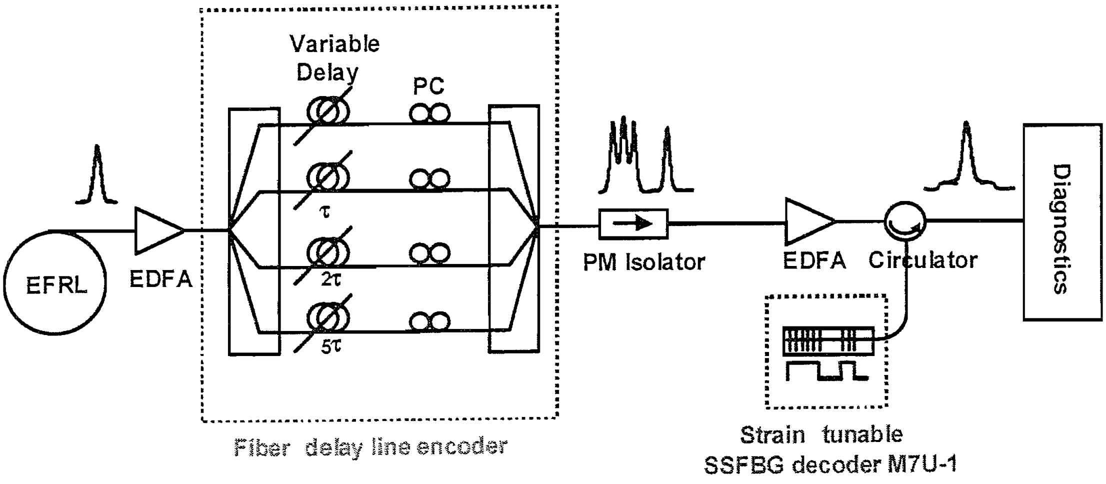

Figure 3.30: Experimental setup and SSFBG decoder reflectivity profile; where EFRL: erbium doped fibre ring laser, PC: polarization controller, PM isolator: polarization maintaining isolator, SSFBG: superstructure fibre Bragg grating.

First, the temporal characteristics of the pattern generated from the delay line encoder were obtained using direct electronic measurement on the oscilloscope (~20 GHz combined electronic bandwidth) and the SHG intensity autocorrelator. From these measurements, the quality of the code words generated from the fibre delay line encoder can be ascertained. The exact delay required from each arm of the fibre delay line encoder is adjusted with the help of the SHG intensity autocorrelator while at the same time, the traces on the oscilloscope are observed to ensure that the correct code sequences are formed (Consider two pulses separated in time by τ, the autocorrelator output will exhibit a three-pulse structure, each separated in time by τ. By measuring the pulse separation, the time delays τ, 2τ and 5τ can be determined accurately). With the delays set correctly, the measured SHG autocorrelation traces and the oscilloscope traces (inset) are found to be in good agreement with the numerical calculations confirming the desired individual chip separation of 6.4ps and the formation of the correct code words as shown in Figure 3.31(a). Note that the theoretical predictions of the traces obtained from the oscilloscope (inset to Figure 3.31(a) and Figure 3.31(b)) take into account the input pulse width and the electrical bandwidth of the combined fast photodiode/scope detection system. These results are then compared to the pulse forms generated on reflection from the SSFBG decoder (in this case used as the encoder), which provide evidence of good qualitative coincidence between theory and experiment. In the case of the fibre delay line encoder, fine control of both the phase and polarisation is required to obtain the optimum results. Since a coherent pulse source is used, each delayed pulse experiences an effectively random phase change, which can affect the formation of the correct output recognition pattern [5].

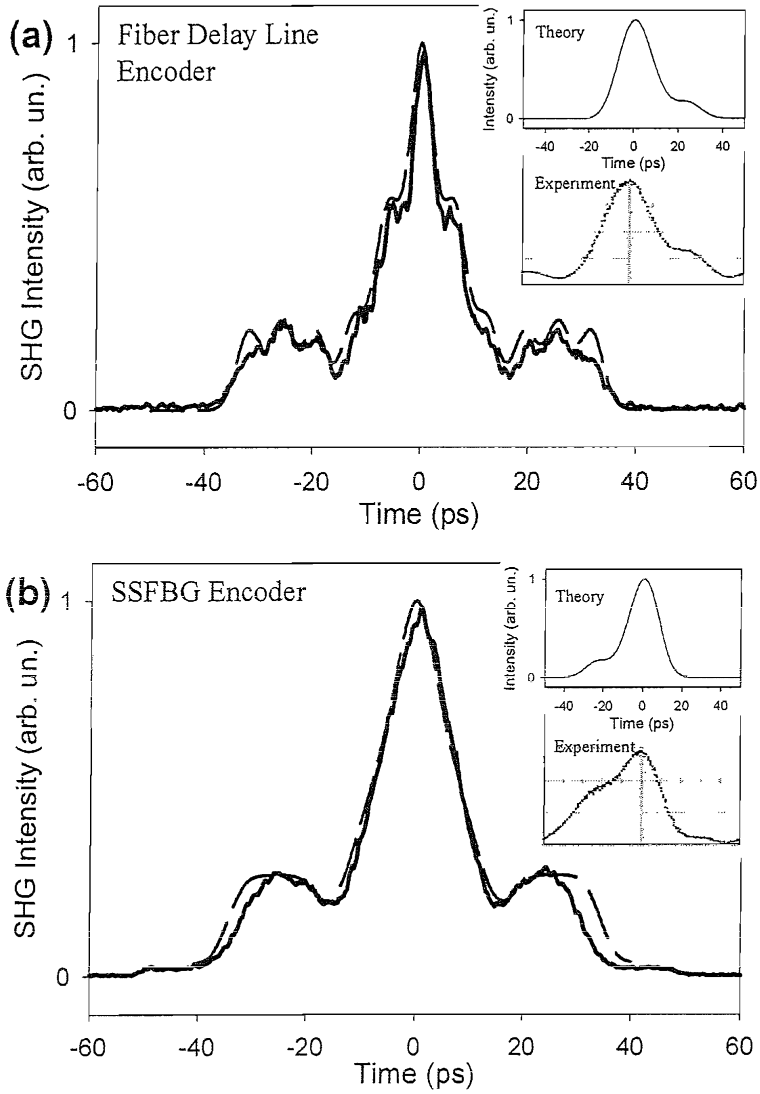

Figure 3.31: (a) Delay line encoder (b) SSFBG encoder M7U-1. Intensity SHG autocorrelation traces of the encoded sequence at the output of the particular encoder (solid line: experiment, dashed line: theory). Inset: Theoretical and experimental traces of the encoded waveform at 10 Gbit/s with 20GHz bandwidth limitation included. (Note: the SSFBG encoder used in (b) is being reflected from the opposite side and hence the time inversed nature of the encoded waveform). The delay line encoder has a chip duration of 2.5ps while the SSFBG encoder has a chip duration of 6.4ps. This explains why the intensity SHG autocorrelation traces for both cases are different.

The two different schemes of encoding/decoding (delay line encoder:SSFBG decoder) were put together to characterize the full hybrid system. The output waveform after the hybrid combination was then analysed. Figure 3.32 shows the SHG autocorrelation of the code recognition signature of the 7-chip unipolar M-sequence code as compared to the theoretical predictions and which highlights the good agreement between them. The decoded pulse form was found to exhibit a pulse width of ~12.4ps. A single peak profile can be obtained for the decoded pulse form at 10 Gbit/s as expected from the theoretical calculations. These results are similar to those obtained using the unipolar SSFBG based encoder and decoder (M7U-1:M7U-1*), shown earlier in Figure 3.8(a).

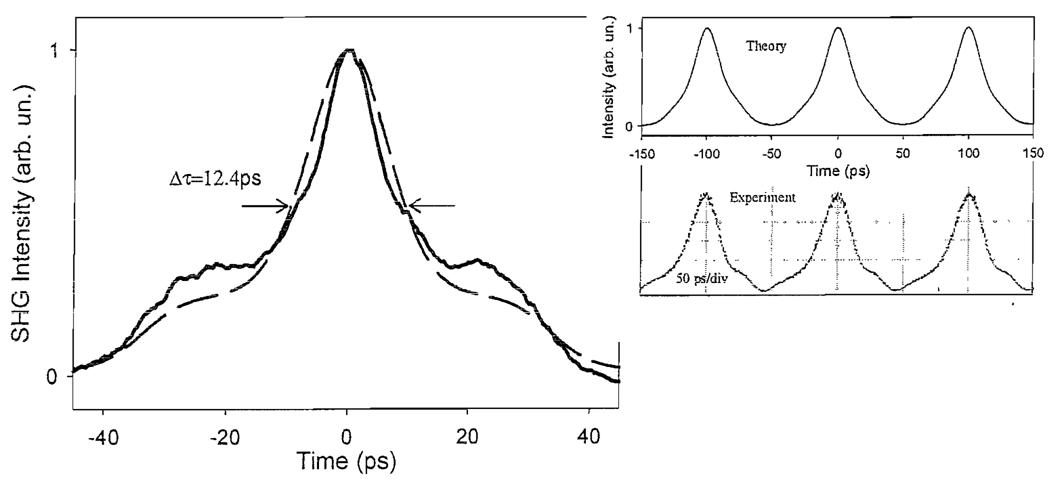

Figure 3.32: A fibre delay line encoder - SSFBG decoder system. Left: Intensity SHG autocorrelation traces of the decoded signal (solid line: experiment, dashed line: theory). Right: Numerically calculated and measured experimental results of the oscilloscope traces of the decoded signal taking into account the 20GHz bandwidth limitation of the detector at 10 Gbit/s.

The above results have demonstrated both theoretically and experimentally that the SSFBG approach is compatible with, and can be used as an alternative technology to recognize codes generated from another pattern generating scheme - in this particular case fibre delay lines. The experiment constitutes the first demonstration of a hybrid all-optical encoder-decoder system, an approach that could prove a suitable solution for many reconfigurable point-to-point optical coding systems.

3.7 Conclusion

In conclusion, a comparative study of the relative merits of bipolar and unipolar coding/decoding schemes based on SSFBG technology has been performed experimentally. The results show that high quality unipolar and bipolar coding can be achieved, with a performance close to that theoretically predicted using the SSFBG approach for coding/decoding in OCDMA. The bipolar phase coding scheme has been found to offer better signal correlation (a distinct, well-defined decoded pulse) compared to unipolar coding (at this relatively short code length) and was used for the design of longer SSFBGs (63-chip).

Using the 63-chip SSFBGs, a number of elementary system measurements of the code sequences, both back-to-back and over a 25km transmission line were performed. The experiments show there to be little, if any, power penalty associated with the coding:decoding and transmission processes for individual codes. Moreover, error free performance under multi-user operation (two simultaneous users) has been demonstrated. In another experiment, the suitability of using the SSFBGs to perform cascaded all-optical coding:decoding function has also been reported.

The SSFBG writing technique was shown to be capable of fabricating longer codes (up to 255-chip), shorter chip duration (3.2ps) and multiple levels of phase shifts (quaternary phase coding). The viability of using 255-chip, 320 Gchip/s quaternary phase coding gratings in OCDMA coding:decoding system was demonstrated. These gratings were incorporated within an elementary four-channel, multi-transmission format OCDMA/WDM system demonstrating the compatibility of SSFBG coding/decoding approach with WDM technique.

This chapter has highlighted the suitability of using the SSFBG coding:decoding approach to perform the required code generation and recognition functions for DS-OCDMA systems. The next chapter describes the use of nonlinear elements to perform ultrafast optical thresholding and which allow for significant improvements to the code recognition contrast such that more coded channels (users) and higher data rates per channel can be accommodated.

References

[1] H. Geiger, A. Fu, P. Petropoulos, M. Ibsen, D. J. Richardson, and R. I. Laming, "Demonstration of a simple CDMA transmitter and receiver using sampled fiber gratings," presented at European Conference on Optical Communication, 1998.

[2] P. Petropoulos, "Novel Techniques and Materials for Optical Telecommunication Systems," in *Optoelectronics Research Centre, Department of Electronics and Computer Science*. Southampton: University of Southampton, 2000, pp. 139.

[3] Z. Zheng, S. Shen, H. P. Sardesai, C.-C. Chang, J. H. Marsh, M. M. Karkhanehchi, and A. M. Weiner, "Ultrafast two-photon absorption optical thresholding of spectrally coded pulses," *Optical Communication*, vol. 167, pp. 225-233, 1999.

[4] K. Kitayama, "OCDM/WDM networks for gigabit access: 1.24 Gbit/s, 2xOCDM by 2xWDM experiment," presented at Europepan Conference on Optical Communication, 1999.

[5] K. P. Jackson, S. A. Newton, B. Moslehi, M. Tur, C. C. Cutler, J. W. Goodman, and H. J. Shaw, "Optical fiber delay-line signal processing," *IEEE Transaction on Microwave Theory and Technique*, vol. MTT-33, pp. 193-209, 1985.

Chapter 4

Multiple Access Interference (MAI) reduction based on nonlinear optical thresholding

Overview

In all of the SSFBG based direct sequence optical code generation and recognition experiments discussed to date, the principle of simple matched filtering, which is based upon purely linear optical effects has been adopted. However one can envisage incorporating additional nonlinear components within SSFBG based processing schemes to either improve the performance by reducing the multiple access interference (MAI) noise, or to extend the functionality, of this technical approach. This chapter describes the use of fast fibre-based nonlinear thresholding devices within OCDMA receivers. These devices are based on either soliton effects in a nonlinear optical loop mirror or filtering of spectrally broadened signal components generated through nonlinear effects in a highly nonlinear holey fibre.

4.1 Multiple Access Interference (MAI) noise reduction

In an OCDMA system, the performance of the system is greatly limited by interference from other coded users transmitting into the network since all users are sharing the same bandwidth [1]. Such interference noise is known as multiple access interference (MAI). MAI is the dominant noise factor compared to other sources of noise in the system like shot noise and thermal noise of the receiver, ASE noise from EDFAs and source fluctuations. MAI is caused by other codes that have pulse overlaps with the desired code at the receiver. This occurs randomly due to the data modulation and the asynchronicity (time offset) of the encoded signals. Consequently, a '1' (high-level) will be detected at the decision circuit of the receiver when no data bit or a '0' is being transmitted to the intended user. In coherent OCDMA systems, MAI noise can be significant due to the coherent addition of electric field of interfering channels, resulting in higher interference noise at the receiver's photodiode, compared to intensity summation of the interfering channels in the incoherent approach. MAI reduction is critical in coherent OCDMA systems since MAI can severely limit the number of users that can be reliably supported within the system, as can be seen from the OCDMA system simulation, described earlier in Chapter Two. Apart from using optimised codes that reduces the MAI noise [2-5], several MAI reduction approaches for use within coherent OCDMA system are summarised below.

The first approach relies on employing a self-homodyne detection at the receiver. This is also known as coherent detection, similar in principle to those used in the wireless domain. It can be implemented in the optical domain using a combination of a local oscillator and a balanced detector. A balanced detection scheme is based on determining the difference signal from two optical detectors. This has the advantage that it cancels out signals that are common to both detectors such as noise and enhances the desired difference signals. In an OCDMA system, such detection schemes that make the noise common to both input ports of the balanced detector can be employed in order to reduce noise arising from multiple user interference (coherent scheme) [6-8]. Huang et. al. recently proposed a coherent detection system that utilised a locally generated optical pulse that is mixed with the decoded signal [6]. Coherent beating between the correlation signal from the optical decoder and the short local oscillator pulse acts as a short time gated amplifier. A balanced detector is then used to measure this signal. This effectively suppresses the residual signals arising from the interfering user codes that fall outside the temporal filtering window determined by the locally generated gating pulse. The disadvantage of this technique is that a local oscillator (normally a pulse laser) is required for each user, thereby increasing the complexity and cost associated with the system. Fast and complicated electronics are also required to ensure that both the locally generated code and the frequency of the carrier are precisely synchronised with the incoming coded signal.

Wada et. al. proposed a detection scheme based on an all-optical nonlinear process, known as the time gating [9]. This time-domain demultiplexer approach is based on a pulse sampling technique centred on the autocorrelation central spike to further improve the pattern recognition contrast for the decoded waveform after matched filtering alone [9, 10]. It uses a second short pulse source (pump), synchronised to the decoded signal and a semiconductor saturable absorber as the switching medium, so that all but that portion of the signal that is input to the optical gate at the same instant as a pump pulse, is absorbed [11]. Thus the time gating effectively suppresses any sidelobes associated with the extended autocorrelation signature of the code and reduces the effect of any interfering channels outside the time frame of the main autocorrelation peak. Such schemes require fast electronics to ensure that the locally generated pulse (time-gating window) is constantly synchronised to the peak of the autocorrelation waveform. Another approach suggested by Zheng et. al. uses two-photon absorption processes in a semiconductor detector to perform optical thresholding on their spectrally coded pulses [12].

The use of fibre based nonlinear thresholding devices for increasing the contrast of the autocorrelation waveform has been previously suggested and demonstrated by a number of research groups [13, 14]. The earliest demonstration was proposed by Chang et. al. and was based on nonlinear spectral broadening filtering in an optical fibre (dispersion shifted fibre) followed by long-pass filtering of the nonlinearly generated spectral components [13]. The discrimination between the correctly and incorrectly decoded waveforms is achieved by exploiting the nonlinear frequency shift effects in optical fibres due to self-phase modulation [15]. When a high peak intensity autocorrelation signal is propagated in the nonlinear fibre thresholder, the output pulse exhibits frequency shifts (hence spectral broadening) while lower peak power incorrectly decoded waveforms do not exhibit any significant changes to their frequency spectrum. A long pass spectral filter is used after the fibre to convert the frequency shifts occurring in the thresholder fibre (Kerr medium) into amplitude variations, which can be detected at the photodetector.

Our particular approach differs substantially in a number of regards from these earlier works. First, fibre-based Kerr nonlinearity is used as the basis of the switch with a completely different physical implementation of the thresholder, i.e. an interferometric nonlinear optical loop mirror (NOLM) device. The NOLM consists of a four-port fibre coupler in which two ports on one side are connected by a loop of fibre (see Figure 4.1). The input optical signal is split into two counterpropagating signals that share the same optical path and interfere at the coupler coherently. The relative phase difference between the counterpropagating signals determines whether an input beam is reflected or transmitted by the NOLM. When a 3 dB (50:50) fibre coupler is used, any input signal is totally reflected, and the NOLM acts as a perfect mirror. By varying the power-splitting ratio of the fibre coupler, high intensity pulse can be switched out of NOLM while low intensity signal will be reflected at the coupler [16].

Secondly, soliton effects are used to enhance the nonlinear discrimination and pulse evolution, which is important because it allows for pulse-shape restoration as well as nonlinear thresholding [17]. It should also be appreciated that this approach in contrast to the previously mentioned fibre-based technique does not result in a wavelength shift of the processed signal. These latter points are extremely important if onward all-optical processing of the coded bit after decoding is required. Such an onward processing function might include recoding, for which a pulse duration substantially shorter than the chip duration is required in order to obtain a sufficiently distinct recoded data bit, and for which wavelength translation is likely to be undesirable. Note that NOLMs have already been adopted for various other optical processing applications, including pulse laser compression [18], extinction ratio improvement of optical time domain multiplexing (OTDM) systems [19], all-optical channel demultiplexing [20] and filtering of amplified spontaneous emission (ASE) noise [21].

The following section reports on the use of a suitably designed NOLM to improve the contrast of a degraded pattern recognition signature due to the imperfect matching of

SSFBG parameters, and demonstrates that such devices can reduce both intrachannel and interchannel interference noise associated with MAI.

Mr. Ju Han Lee, a PhD student, designed and constructed the NOLM for use in the following experiments and worked with me on these experiments.

4.2 High performance 63-chip OCDMA receiver incorporating a nonlinear optical loop mirror

The first experiment demonstrates the enhanced code recognition quality by incorporating this nonlinear loop mirror (NOLM) in a 63-chip, OCDMA code:decode single channel system. The nonlinear response of the NOLM significantly enhances the pattern recognition contrast achievable relative to matched filtering alone. This provides a considerable improvement in the overall system response and allows for error-free, penalty-free performance in BER experiments relative to direct back-to-back measurements on the input laser source itself.

Next, the use of a nonlinear optical switch to suppress the interchannel interference noise generated under multi-user operation of a SSFBG based OCDMA system is demonstrated using the same NOLM. Similar improvements to the code recognition quality is observed in a two–channel 63-chip, bipolar OCDMA code:decode system, and a reduction in the power penalty of the BER measurements is observed. The nonlinear switching response of the NOLM is shown to significantly reject interference noise in regions of temporal overlap of the cross-correlation signatures of the individual coded bits.

4.2.1 Single channel performance

The experimental set up is similar to those illustrated in Figure 3.11 of Chapter Three for the 63-chip SSFBG pairs (G63B-1 and G63B-1*) with the addition of a NOLM before the receiver as illustrated in Figure 4.1. The NOLM incorporated a 70:30 coupler, and contained 6.6km of dispersion shifted fibre, with a dispersion D=1.18ps/nm/km at the system operating wavelength of 1558nm [22].

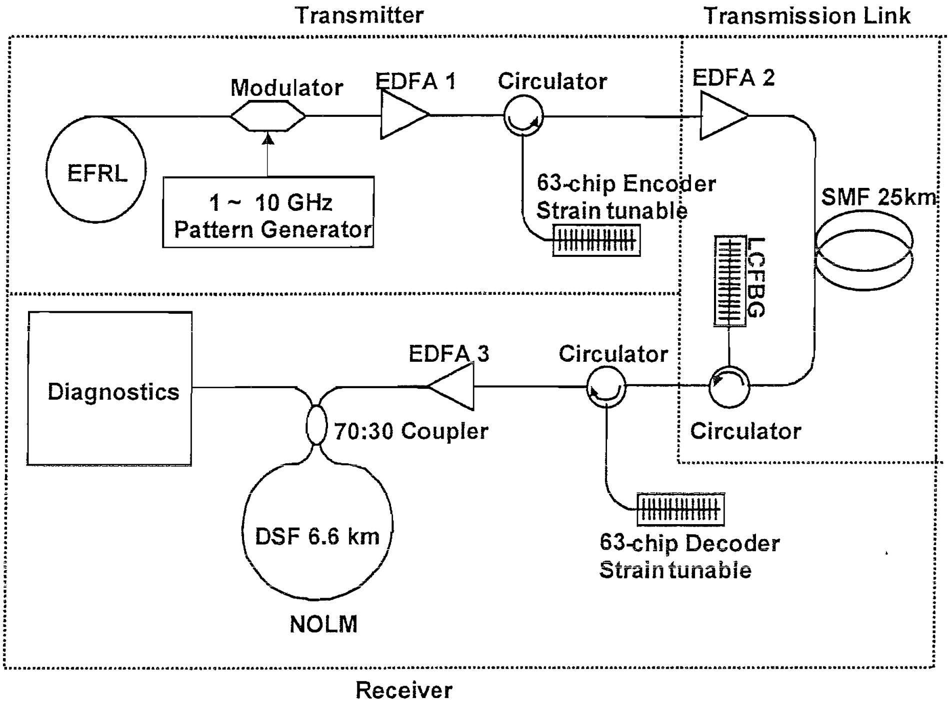

Figure 4.1: Experimental set up (EDFA: Erbium-doped fibre amplifier, LCFBG: linearly chirped fibre Bragg grating).

Initially, experiments were performed at data rates of 1.25 Gbit/s and 2.5 Gbit/s without using the NOLM. The matched filtered pulse forms after the code:decode gratings are shown in Figure 4.2. These code correlation pulses have a full duration of 800ps after reflection from the 63-chip SSFBG. The detailed BER measurements at both data rates show that high quality error free performance can be obtained even in the instance that a 25km dispersion compensated transmission fibre link is inserted between the encoding and decoding stages (see Figure 4.3). However, a power penalty is found to be associated with the process. At a data rate of 1.25 Gbit/s this power penalty is ~1.5dB. The power penalty increases to 4.5dB at 2.5 Gbit/s for which the 800ps long correlation pulses have significant overlap in the pulse tails, as evident from the eye diagrams in Figure 4.5(b). The increased power penalty at 2.5 Gbit/s results from amplitude noise associated with coherent interference between the adjacent '1' data bits. (The correlation pulse tails do not overlap at a data rate of 1.25 Gbit/s)

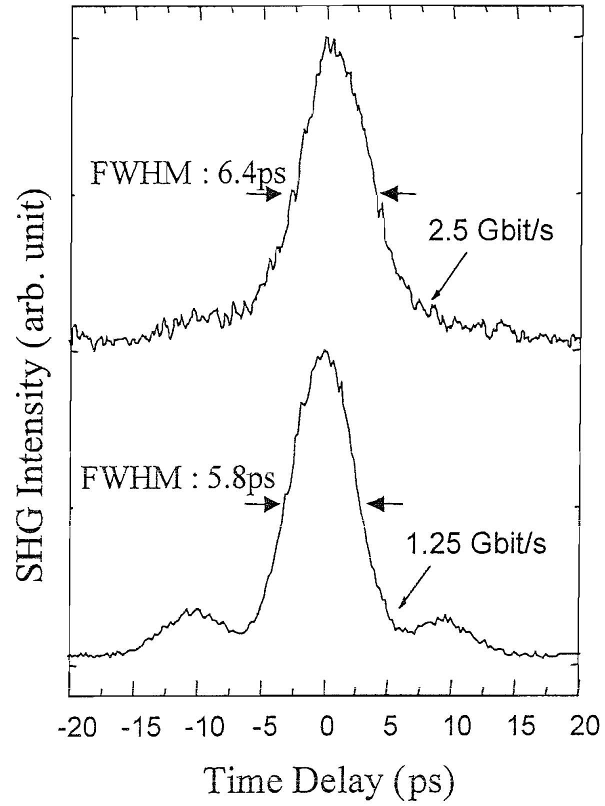

Figure 4.2: SHG intensity autocorrelation traces of the pulse forms after matched filtering at data rates of 1.25 Gbit/s and 2.5 Gbit/s.

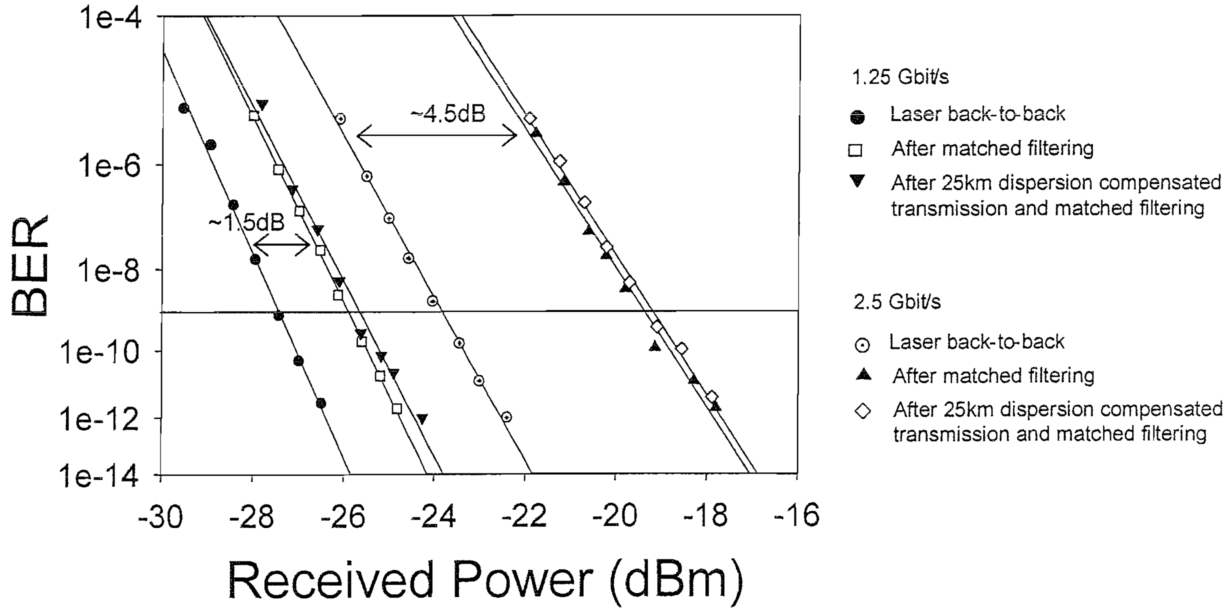

Figure 4.3: BER results without using NOLM at data rates of 1.25 Gbit/s and 2.5 Gbit/s.

Next, the experiments were repeated but with the inclusion of the NOLM. The decoded code-correlation pulse forms were amplified (up to a maximum average power of 15dBm) and fed into the input of the NOLM. The resulting nonlinearly switched waveform was then characterised as previously, and BER measurements performed. The improved pattern recognition contrast is clearly evident by comparing Figure 4.4 and Figure 4.2. From Figure 4.4 it is also seen that the shape and duration of the output pulses were restored to values close to the original input laser pulses due to high-order soliton effects[1] within the NOLM [21].

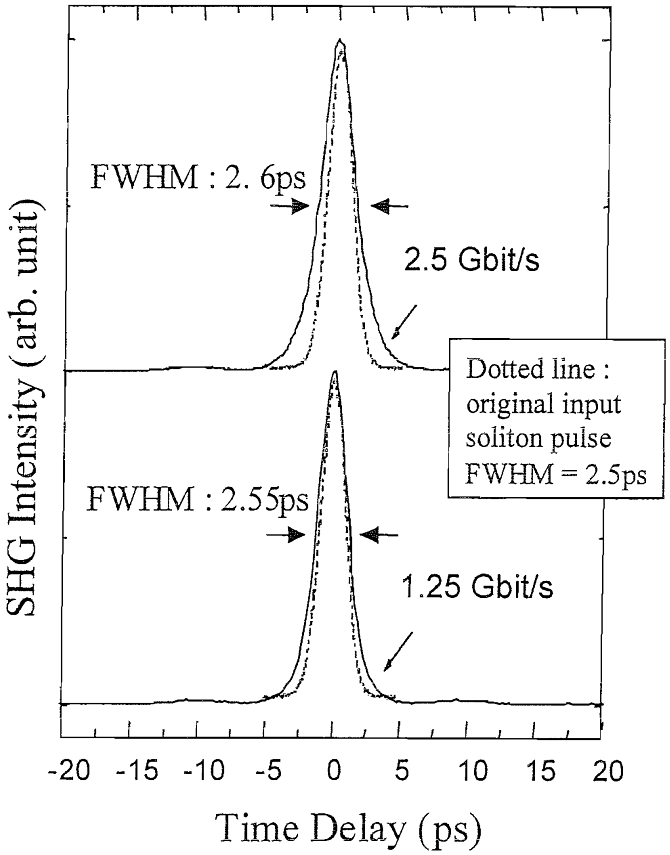

Figure 4.4: SHG intensity autocorrelation traces of the pattern recognition pulse forms after matched filtering and subsequent nonlinear switching by the NOLM at data rates of 1.25 Gbit/s and 2.5 Gbit/s.

---

[1] In the fundamental soliton (N=1), group velocity dispersion (GVD) and self phase modulation (SPM) balance each other such that there is no change to the pulse shape or the spectrum. In the case of **high-order solitons** (N>1), SPM dominates initially but GVD soon catches up and leads to pulse compression. Such effect is used in the above NOLM for pulse compression (see Ref [22] for the detailed analysis of this NOLM).

The low level pedestal obtained with simple matched filtering is almost entirely eliminated by passage through the nonlinear loop mirror as evident in the eye diagrams performed at a data rate of 2.5 Gbit/s in Figure 4.5.

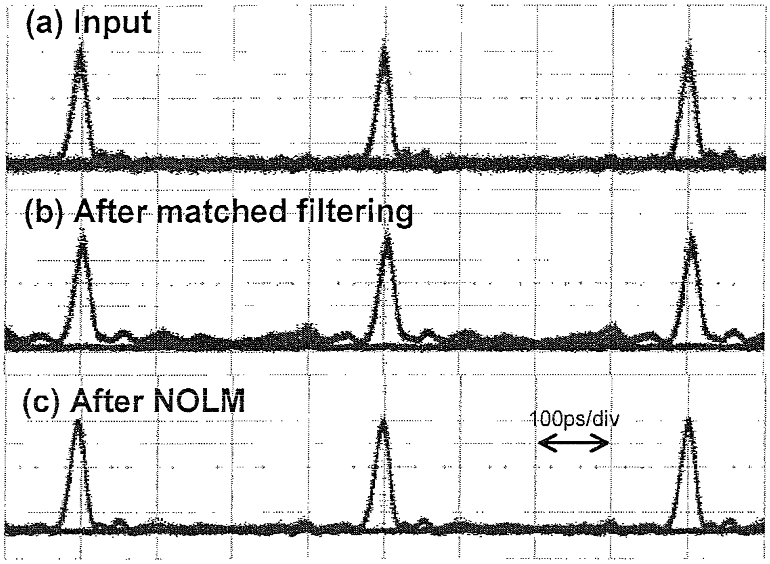

Figure 4.5: Eye diagrams showing (a) laser input 2.5ps pulses (b) the pulses after matched filtering and (c) the correlated pulses after nonlinear switching by the NOLM. The data rate used is 2.5 Gbit/s.

The benefits of the pedestal rejection from a system perspective are shown in the BER measurements in Figure 4.6. The previously observed power penalties associated with simple matched filtering are entirely eliminated even in the presence of considerable autocorrelation tail overlap at the bit-rate of 2.5 Gbit/s. This is significant from a single-channel data rate perspective since it allows for higher bit rates (10 Gbit/s) than possible with simple matched filtering alone.

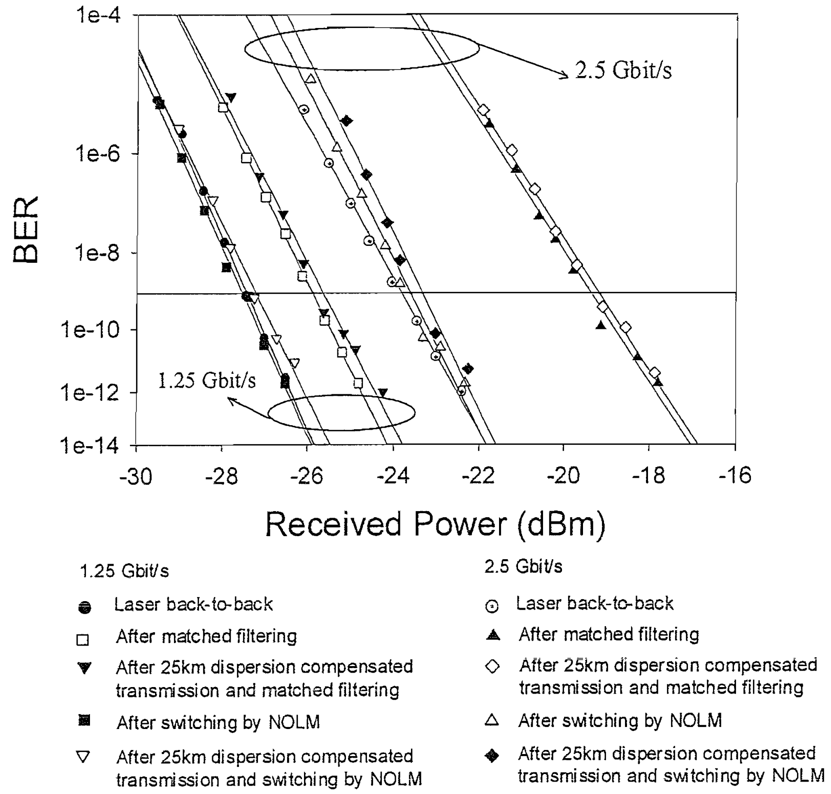

Figure 4.6: BER performances for 1.25 Gbit/s and 2.5 Gbit/s systems.

Next, the performance of the NOLM in this set up when using a higher data bit rate, i.e. 10 Gbit/s was investigated. At this data rate, a given bit-slot receives contributions from as many as 16 neighbouring '1' data bits resulting in significant interference noise (the decoded autocorrelation signal has a full duration of ~800ps). The eye diagram shown in Figure 4.7(a) illustrates the great performance improvements that can be obtained by nonlinear processing of the signal. The eye is completely closed after simple matched filtering alone, however with nonlinear processing, a clear open eye is restored. The performance benefits were confirmed by conducting detailed BER measurements, the results are shown in Figure 4.7(b). Error free performance with a power penalty of only ~2 dB is observed. A similar power penalty is also obtained when the 25 km transmission line is included in the system. However, an error floor can be observed in this instance. This error floor is believe to be caused by the insufficient optical power going into the NOLM after dispersion compensating grating and decoder SSFBG, resulting in the degradation of the decoded autocorrelation contrast after the NOLM. Note that it is impossible to make meaningful BER measurements without incorporating the NOLM due to the high noise level.

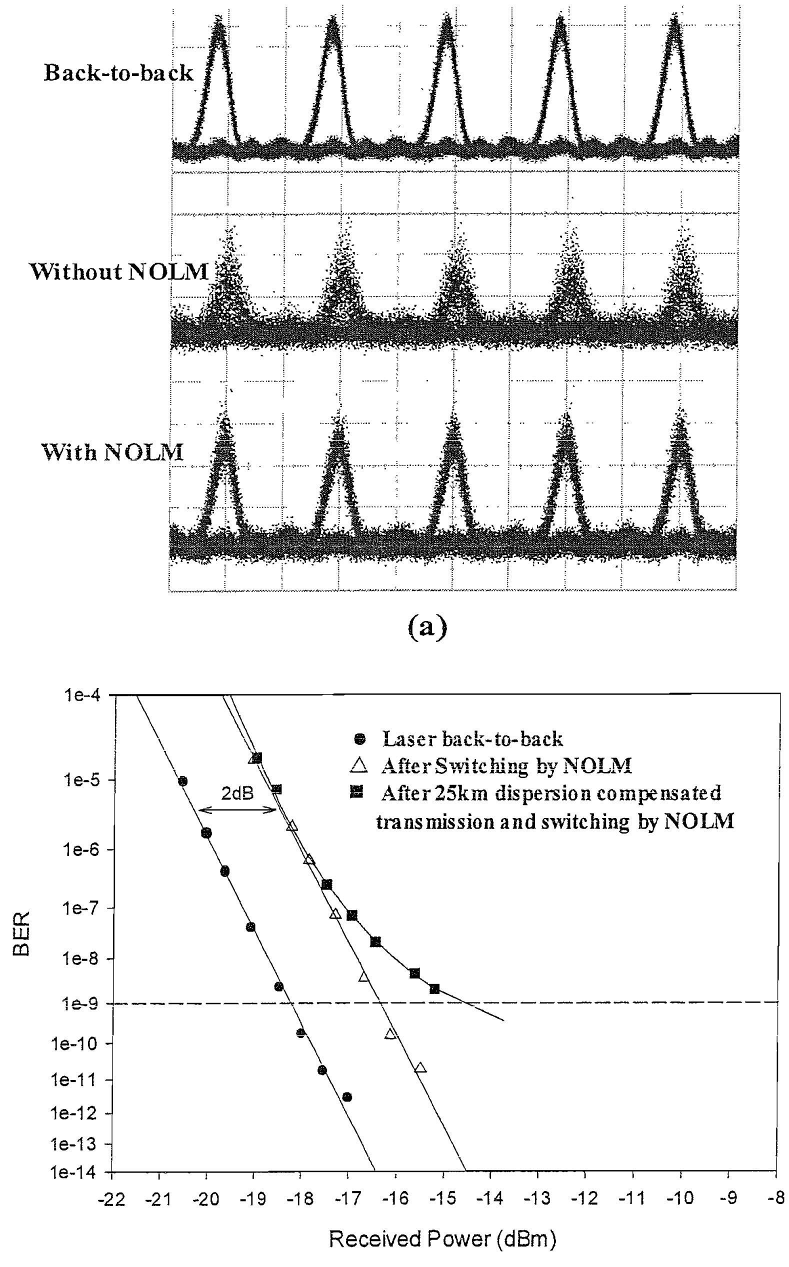

(b)

Figure 4.7: 10 Gbit/s single channel OCDMA operation: (a) eye diagrams (b) BER results.

4.2.2 Two-channel performance

The experimental set up is similar to the previous single channel experiment with the addition of another coded channel at the transmitter as illustrated in Figure 4.8. Similarly, system tests are performed at the data repetition rates of 1.25 Gbit/s and 2.5 Gbit/s. The encoded pulse forms in each channel are set to fully overlap temporally at the detector and with identical power so as to maximise the impact of inter-channel interference.

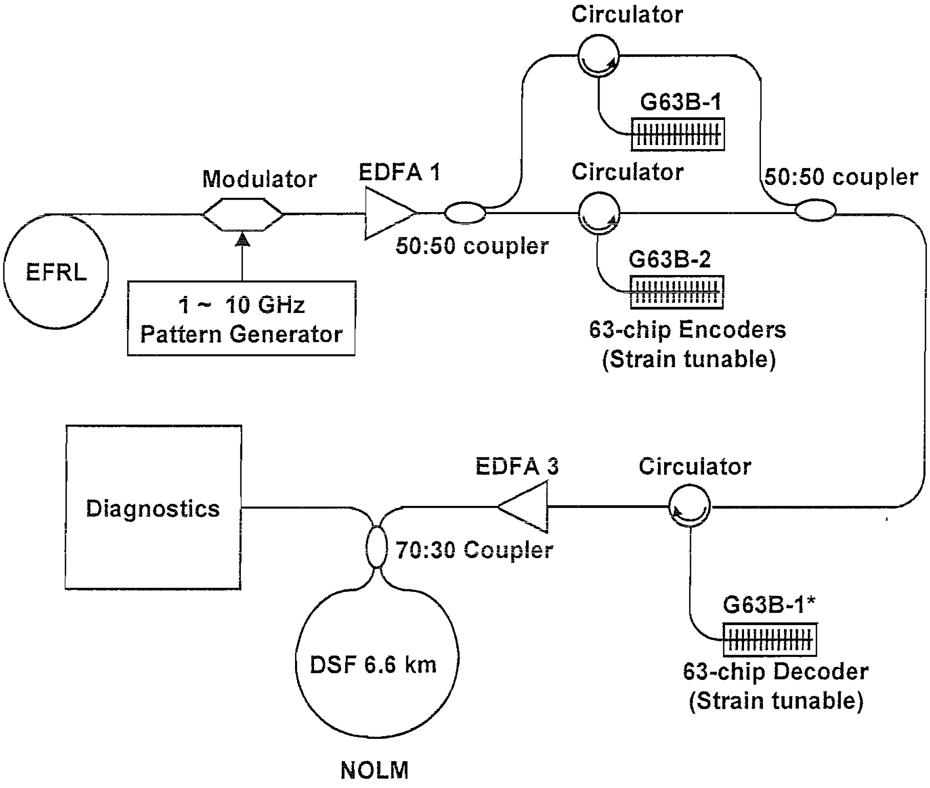

Figure 4.8: Two-channel experimental set up incorporating the NOLM (EDFA: Erbium-doped fibre amplifier).

Firstly, Figure 4.9 compares the results of SHG autocorrelation measurements of the pattern recognition pulse both before and after filtering using the NOLM. The pedestal rejection and pulse reshaping effects are seen to be significant even when two different codes are transmitted simultaneously. The pulse width after the NOLM is about the same as that of the input pulses derived from the laser, which is significant if additional reprocessing of the bit, e.g. recoding as mentioned previously in Chapter Three, is required.

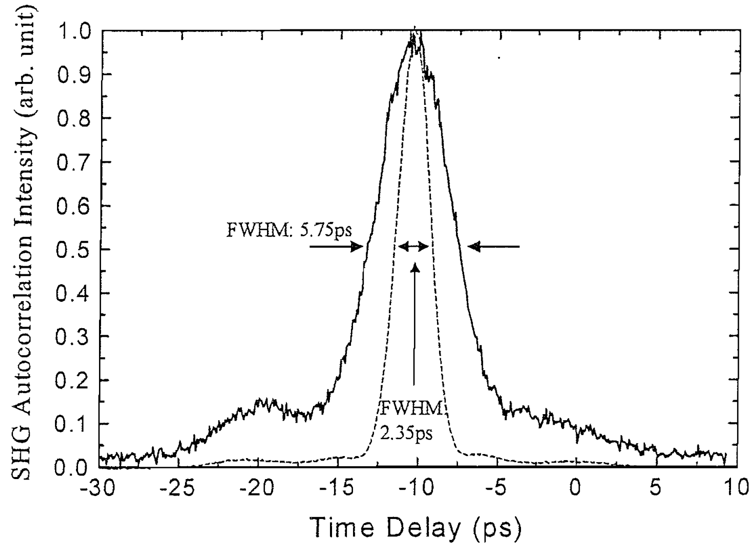

Figure 4.9: SHG intensity autocorrelation traces of the decoded signal central autocorrelation spike (solid line: after matched filtering technique G63B-1:G63B-1 and dashed line: after subsequent nonlinear switching by the NOLM). The data rate is 2.5 Gbit/s.*

As can be seen when comparing the eye diagrams in Figures 4.10(a) and 4.10(b), the temporal overlap of the two orthogonal codes, G63B-1 and G63B-2 results in severe interference noise at the receiver without the NOLM in place. However, as can be seen in Figure 4.10(c) the quality of the eye opening is drastically improved by nonlinear processing of the matched filtered signal, resulting in a substantial improvement in the BER performance of the two-channel coding:decoding process.

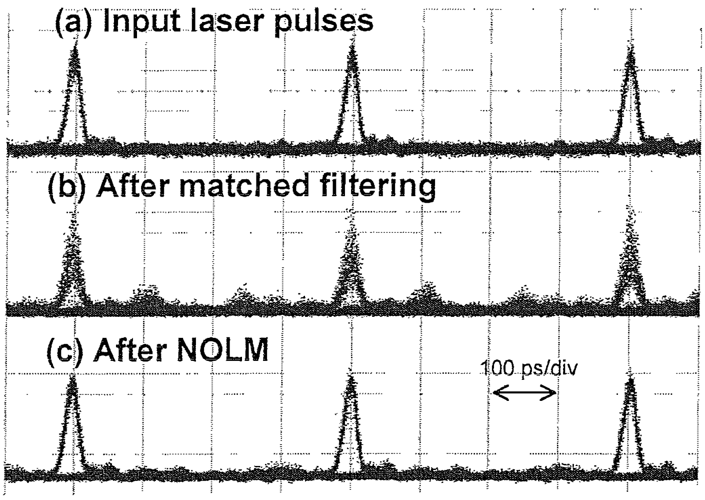

Figure 4.10: Eye diagrams at 2.5 Gbit/s showing (a) laser input pulses (b) after matched filtering alone and (c) after self-switching by the NOLM.

The measured BER plots are summarized in Figure 4.11. For a data rate of 1.25 Gbit/s error-free operation with a ~3.6 dB power penalty reduction relative to simple matched filtering alone is obtained through the use of the NOLM. The residual power penalty of ~1.5 dB is comparable to that achieved for single channel operation without the NOLM. This power penalty in the two-channel experiments is believed to be due primarily to the contribution to the received average power made by the second ('orthogonal') channel due to imperfect filtering. The benefits of using the NOLM at the higher data rate of 2.5 Gbit/s are even more manifest. In this instance it was not possible to get error free operation without the use of the NOLM. The power penalty relative to the back to back in this instance was ~2.8 dB, and which again was similar to that obtained for conventional single channel operation at this data rate. Note that at a data rate of 2.5 Gbit/s the individual pattern recognition signatures which each has a length of 800ps overlap providing an additional element of interference noise. Hence the slightly increased power penalty relative to the 1.25 Gbit/s case in which no such overlap occurs.

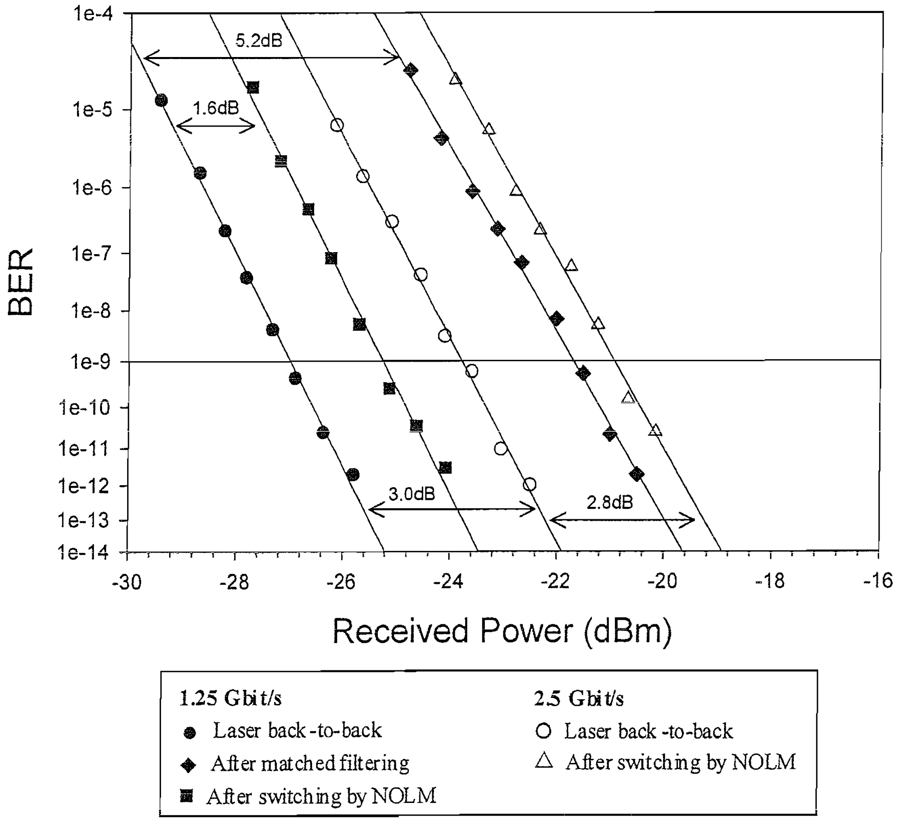

Figure 4.11: BER versus received optical power for two-channel operation at 1.25 Gbit/s and 2.5 Gbit/s.

4.3 Holey fibre based nonlinear optical thresholder

Recently, holey fibre (HF) technology allows the fabrication of fibres with very tightly confined modes, and thus very high optical nonlinearities per unit length. Indeed, a silica holey fibre can have nonlinearity 10-100 times that of a conventional silica fibre. Nonlinear devices based on HF can, thus in principle, be 10–100 times shorter than similar devices based on conventional fibre technology, offering a route to the development of truly practical, ultrafast fibre based nonlinear thresolding devices.

In this section, experimental results concerning the use of a highly nonlinear thresholding device based on HF within an OCDMA receiver are presented. Using only a short (8.7m) length of HF followed by a bandpass filter, enhanced code recognition quality in a 255-chip 320-Gchip/s SSFBG based OCDMA system is demonstrated. Error free penalty free system performance is obtained and the 3-dB power penalty observed for pure matched filtering alone is eliminated.

This work is done in collaboration with Mr. Ju Han Lee and Mr. Zulfadzli Yusoff (both are PhD students). They constructed the HF nonlinear thresholding device for use in this experiment.

4.3.1 Experimental results

The experimental setup is shown in Figure 4.12. The 2.5ps pulses at 10 GHz are first generated using a regeneratively mode-locked erbium fibre ring laser (EFRL) operating at 1553nm. These are then gated down in repetition rate and then modulated to obtain a 1.25 Gbit/s data stream. The 1.25 Gbit/s short pulse data stream was then launched onto an SSFBG encoder (A255Q-1) containing 255-chip 320 Gchip/s quaternary phase code sequence coding information. The chip duration was thus 3.2ps and the coded data pulses had a total duration of 800ps. The characteristics and properties of the gratings have been fully described earlier in Chapter Three. The coded signal was then fed directly to the associated matched decoder grating A255Q-1*. Since the encoder and decoder gratings are matched then, as previously explained, the decoder output should exhibit a short, chip length long autocorrelation spike centered on a relatively broad, (1.6ns) pedestal. The nonlinear HF-based optical thresholder was located after the decoder grating and was preceded by a fibre amplifier.

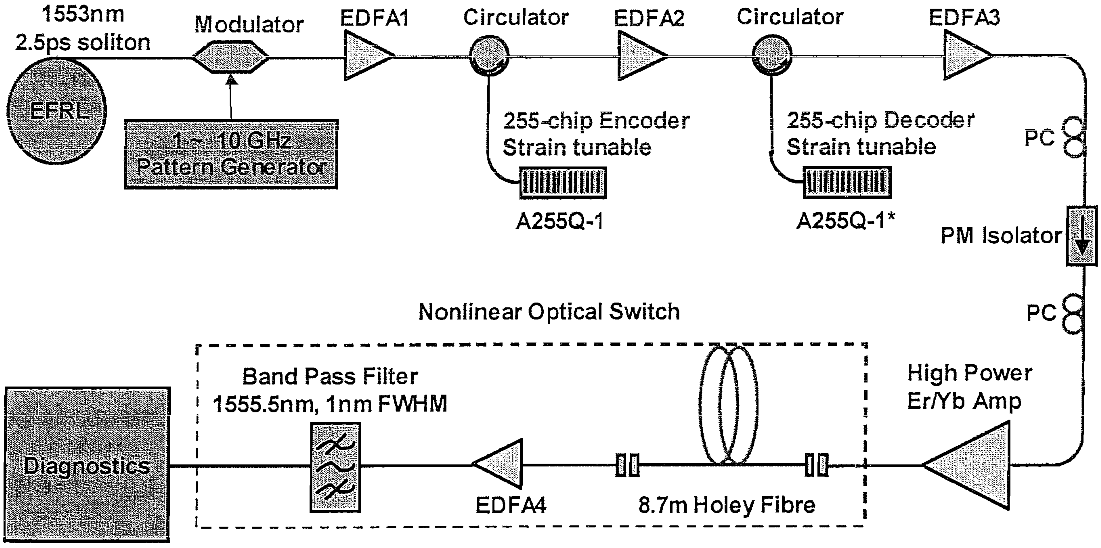

Figure 4.12: Experimental setup to demonstrate the holey fibre nonlinear thresholder.

An SEM of the transverse profile of the highly nonlinear HF is shown inset in Figure 4.13. The core diameter is ~2.0μm and the outer diameter of this fibre is ~125μm. Due to the large air holes and small core size, the fibre is highly nonlinear and the asymmetric arrangement of holes around the core results in a very large linear birefringence. The measured beat length is 0.43mm, which is ~10 times shorter than that of commercially available PM fibre types. This means that fibres with extremely good polarization-maintaining characteristics can be fabricated using HF technology.

From a measurement of the SPM-induced nonlinear phase shift versus launched optical power as shown in Figure 4.13 [23], we obtained a value of $\gamma = 31W^{-1}.km^{-1}$, from which we derive an estimate of Aeff = 2.93(+/-0.3) μm for its effective area. This nonlinearity is ~20 times higher than that of a conventional dispersion shifted fibre.

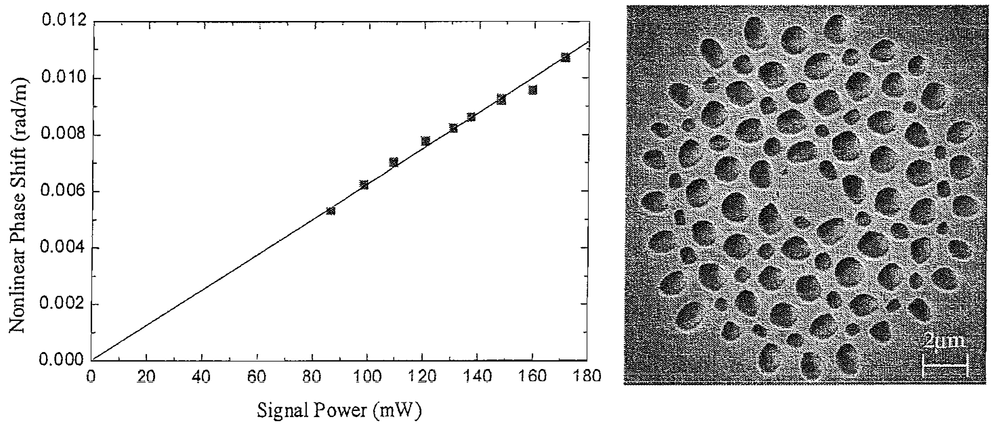

Figure 4.13: Measured SPM-induced nonlinear phase shift versus launched optical power in the HF. Inset: Cross-sectional SEM image of the HF used.

Self-phase modulation (SPM) accompanied by Raman scattering in the highly nonlinear HF due to the intense autocorrelation spike, results in (asymmetric) spectral broadening of correctly decoded bits as shown in Figure 4.14(a). A self-switched signal with a transfer characteristic suitable for intensity thresholding as shown in Figure 4.14(b) was obtained by filtering the resulting spectrally broadened signal with a narrow-band dielectric filter that had its centre wavelength offset by (~2.5nm) relative to the peak wavelength of the incident signal. The power loss of 25 dB between input and output in the nonlinear switch comes from various origins including background HF loss (~0.5 dB), input/output beam coupling (total 8dB loss), and of course the spectral filtering offset. The 3 dB bandwidth of the filter was 1 nm. This value was chosen to ensure that the switched output pulses had roughly the same temporal width as the 2.5ps input pulses. This is confirmed by measuring the pulse width using the SHG intensity measurement. The results are plotted in Figure 4.15.

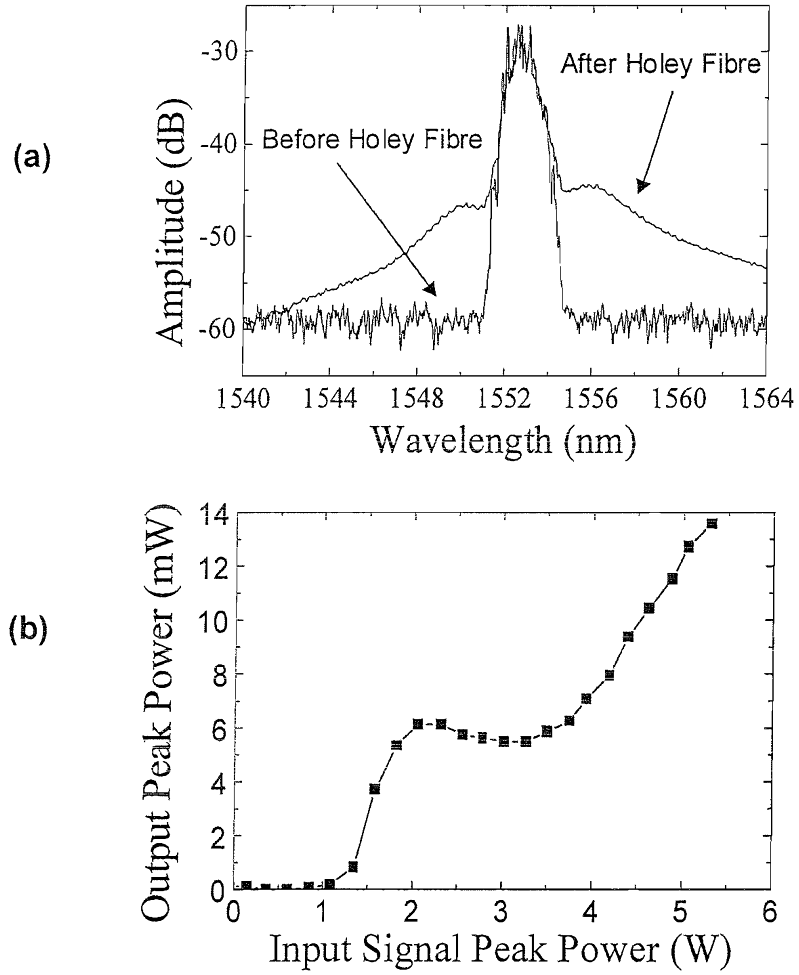

Figure 4.14: (a) Signal spectrum both before and after the HF. (b) Experimentally obtained power transmission characteristic of the HF switch as a function of the input peak power.

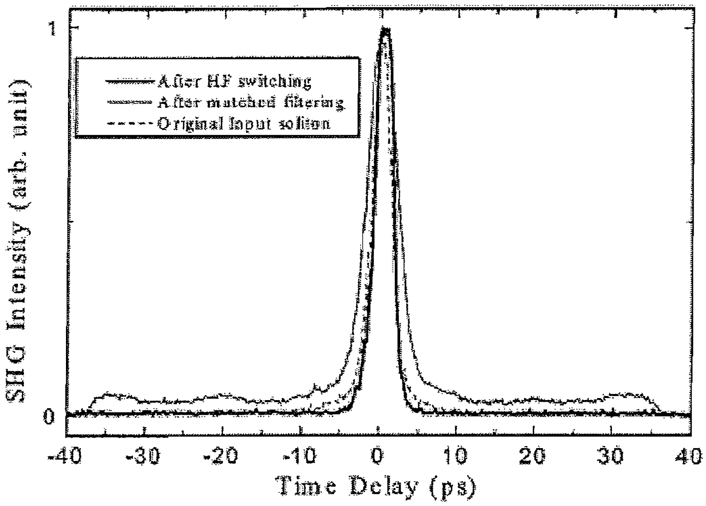

Figure 4.15: SHG intensity auto-correlation traces showing that the switched output pulses had roughly the same temporal width as the 2.5ps input pulses.

In order to assess the impact of using the HF switch as an optical thresholder, the eye diagrams obtained from high-speed sampling oscilloscope were studied. The improved pattern recognition contrast is clearly evident on a 20ps timescale by comparing the eyes and background noise levels in Figure 4.16. The low-level pedestal obtained with simple matched filtering is almost completely eliminated. To quantify the benefits of the pedestal rejection from a system perspective bit error rate (BER) measurements were performed as shown in Figure 4.17. The observed 3 dB power penalty associated with matched filtering alone is totally eliminated.

It should be mentioned that since the fibre has anomalous dispersion (D~100ps/nm km) the resultant filtering process results in additional noise on the '1' bits due to coherence degradation (see Figure 4.16:after HF switch) [24]. Nonlinear pulse propagation in the anomalous dispersion regime tends to generate multiple pulses (higher-order solitons). This generation of multiple pulses leads to coherence degradation caused by the interplay of amplified spontaneous noise and higher-order solitons, resulting in random amplitude fluctuation and increased timing jitter [24, 25]. In contrast, using normal dispersion fibre does not lead to coherent degradation, because no phase-matching condition exists for four-wave mixing between the signal pulse and the noise, hence generating less intensity fluctuation at the output of the nonlinear switch.

However, for this particular application, this does not appear to lead to any penalty. Indeed, an ~1dB penalty improvement relative to the laser back-to-back case was obtained due to the clean up of residual radiation in the zero bit slots due to the poor (~14 dB) extinction ratio of the external data modulator (Figure 4.16: back-to-back trace).

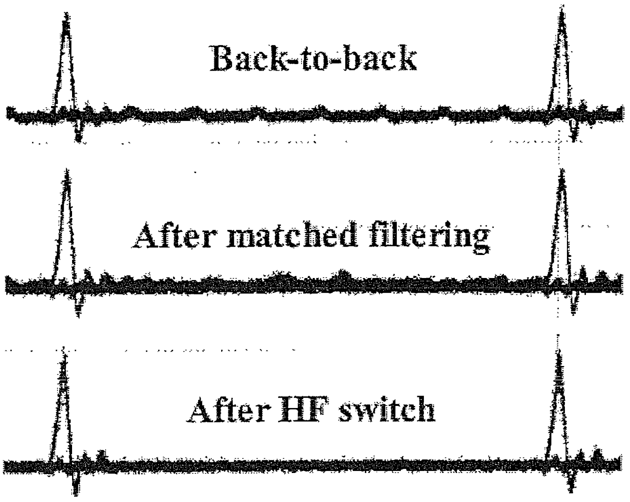

Figure 4.16: Eye diagrams for the 1.25 Gbit/s OCDMA system. The measured resolution is ~20ps.

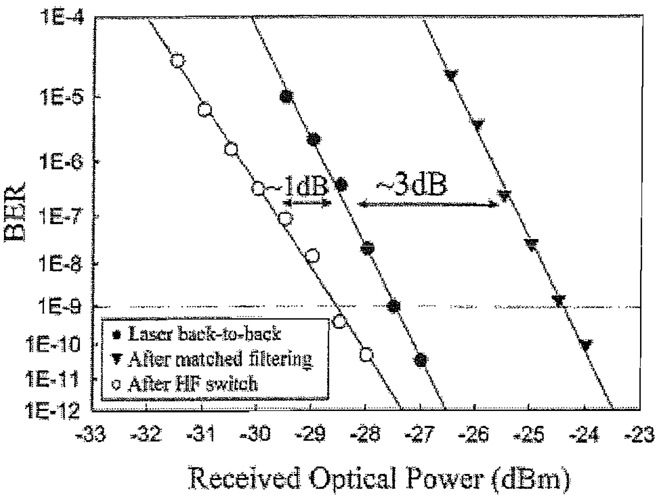

Figure 4.17: Measured BER versus received optical power for the 1.25 Gbit/s OCDMA system.

4.4 Conclusions

The experimental results show that excellent performance improvements can be obtained by incorporating nonlinear elements (NOLMs or HF nonlinear thresholders) within SSFBG based OCDMA and associated all-optical processing schemes. The NOLM experiments show that improved performance can be observed at the repetition rate of 10 Gbit/s, as well as at both 2.5 Gbit/s and 1.25 Gbit/s, offering the possibility of higher capacity data delivery than previously considered viable for coherent DS-OCDMA systems. Moreover, the error-free and penalty-free operation obtained in two-channel multiplexing experiments implies that the approach should give equivalent system benefits when used in OCDMA systems operating under multiuser operation.

The instantaneous nonlinear response of silica fibres (< 10 fs) allows the fibre based NOLM to operate at relatively high bit rates compared to using saturable absorbers which have a limited time response of ~10 ps. However, the main limitation of NOLM stems from the weak fibre nonlinearity. The loop length required to generate sufficient nonlinearity with practical optical power is typically around several km. It lacked the compactness required for use in practical optical systems. By using a semiconductor optical amplifier as a nonlinear element in place of the fibre reduces the loop length of the NOLM to less than 1m. Such configuration is also known as the Terahertz Asymmetric Optical Demultiplexer (TOAD) [26]. TOAD's operation at bit rates as high as 250 Gb/s has been demonstrated [27] and should offer similar system benefits when used in OCDMA system.

Next, a nonlinear optical thresholding device based on a short length of highly nonlinear HF has also been demonstrated for use to enhance code recognition contrast at the OCDMA receiver. Use of such a short length of highly nonlinear fibre is advantageous since small and compact all-fibre nonlinear devices can be constructed based on the holey fibre technology. However, this technology is still in the infancy and further research is required into developing this technology for use in practical systems.

References

[1] D. D. Sampson, M. Calleja, and R. A. Griffin, "Crosstalk performance of coherent time-addressed photonic CDMA networks," *IEEE Transaction on Communications*, vol. 46,.pp. 338-348, 1998.

[2] S. Boztas, R. Hammons, and P. V. Kumar, "4-phase sequences with near-optimum correlation properties," *IEEE Transaction of Information Theory*, vol. 38, pp. 1101-1113, 1992.

[3] E. H. Dinan and B. Jabbari, "Spreading Codes for Direct Sequence CDMA and Wideband CDMA Cellular Networks," *IEEE Communications Magazine*, vol. 36, pp. 48-54, 1998.

[4] P. V. Kumar and O. Moreno, "Polyphase sequences with periodic correlation properties better than binary sequences," *IEEE Transaction of Information Theory*, vol. 37, pp. 603-616, 1991.

[5] J. Zhang, "Design of a special family of optical CDMA address codes for fully asnychronous data communications," *IEEE Transaction on Communications*, vol. 47, pp. 967-973, 1999.

[6] W. Huang and I. Andonovic, "Coherent optical pulse CDMA systems based on coherent correlation detection," *IEEE Transaction on Communications*, vol. 47, pp. 261-271, 1999.

[7] W. Huang, I. Andonovic, and M. Tur, "Decision-directed PLL for coherent optical pulse CDMA systems in the presence of multiuser interference, laser phase noise and shot noise," *IEEE Journal of Lightwave Technology*, vol. 16, pp. 1786-1794, 1998.

[8] N. Wada and K. Kitayama, "A 10Gb/s optical code division multiplexing using 8-chip optical bipolar code and coherent detection," *IEEE Journal of Lightwave Technology*, vol. 17, pp. 1758-1765, 1999.

[9] N. Wada, H. Sotobayashi, and K. Kitayama, "Error-free 100km transmission at 10 Gbit/s in optical code division multiplexing system using BPSK picosecond-pulse code sequence with novel time-gating detection," *IEE Electronics Letters*, vol. 35, pp. 833-834, 1999.

[10] P. Petropoulos, N. Wada, P. C. Teh, M. Ibsen, W. Chujo, K. Kitayama, and D. J. Richardson, "Demonstration of a 64-chip OCDMA system using superstructured fiber gratings and time-gating detection," *IEEE Photonic Technology Letters*, vol. 13, pp. 1239-1241, 2001.

[11] H. Kurita, Y. Hashimoto, I. Ogura, H. Yamda, and H. Yokohama, "All-optical 3R regeneration based in optical clock recovery with mode-locked LD's," presented at European Conference on Optical Communications (ECOC1999), paper PD3-6 (postdeadline), 1999.

[12] Z. Zheng, S. Shen, H. P. Sardesai, C.-C. Chang, J. H. Marsh, M. M. Karkhanehchi, and A. M. Weiner, "Ultrafast two-photon absorption optical thresholding of spectrally coded pulses," *Optical Communication*, vol. 167, pp. 225-233, 1999.

[13] C.-C. Chang, H. P. Sardesai, and A. M. Weiner, "Code-division multiple-access encoding and decoding of femtosecond optical pulses over a 2.5-km fiber link," *IEEE Photonic Technology Letters*, vol. 10, pp. 171-173, 1998.

[14] H. P. Sardesai, C.-C. Chang, and A. M. Weiner, "A femtosecond code-division multiple access communication system test bed," *IEEE Journal of Lightwave Technology*, vol. 16, pp. 1953-1964, 1998.

[15] J. P. Gordon, "Theory of the soliton self-frequency shift," *OSA Optics Letters*, vol. 11, pp. 662-664, 1986.

[16] G. P. Agrawal, *Applications of nonlinear fiber optics*: Academic Press, 2001.

[17] L. Chusseau and E. Delevaque, "250-fs optical pulse generation by simultaneous soliton compression and shaping in a nonlinear optical loop mirror including a weak attenuation," *OSA Optics Letters*, vol. 19, pp. 734-736, 1994.

[18] A. L. Steele, "Pulse compression by an optical fiber loop mirror constructed from two different fibers," *IEE Electronics Letters*, vol. 29, pp. 1972-1974, 1993.

[19] I. Y. Krushchev, I. D. Philips, A. D. Ellis, R. J. Manning, D. Nesset, D. G. Moodie, R. V. Penty, and I. H. White, "OTDM applications of dispersion-imbalanced fiber loop mirror," *IEE Electronics Letters*, vol. 35, pp. 1183-1185, 1999.

[20] D. M. Patrick, A. D. Ellis, and D. M. Spirit, "Bit-rate flexible all-optical demultiplexing using a nonlinear optical loop mirror," *IEE Electronics Letters*, vol. 29, pp. 702-703, 1993.

[21] B.-E. Olsson and P. A. Andrekson, "Noise filtering with the nonlinear optical loop mirror," *IEEE Journal of Lightwave Technology*, vol. 13, pp. 213-215, 1995.

[22] J. H. Lee, P. C. Teh, P.Petropoulos, M. Ibsen, and D. J. Richardson, "A grating-based OCDMA coding-decoding system incorporating a nonlinear optical loop mirror for improved code recognition and noise reduction," *IEEE Journal of Lightwave Technology*, vol. 20, pp. 36-46, 2002.

[23] A. Boskovic, S. V. Chernikov, J. R. Taylor, L. Gruner-Nielsen, and O. A. Levring, "Direct continuous measurement of n2 in various types of telecommunication fibres at 1.55um," *OSA Optics Letters*, vol. 21, pp. 1966-1968, 1996.

[24] M. Nakazawa, H. Kubota, and K. Tamura, "Random evolution and coherence degradation of a high-order optical soliton train in the presence of noise," *OSA Optics Letters*, vol. 24, pp. 318-320, 1999.

[25] M. Nakazawa, K. Tamura, H. Kubota, and E. Yoshida, "Coherence degradation in the process of supercontinuum generation in an optical fiber," *Optical Fiber Technology*, vol. 4, pp. 215-223, 1998.

[26] J. P. Sokoloff, P. R. Prucnal, I. Glesk, and M. Kane, "A terahertz optical asymmetric demultiplexer (TOAD)," *IEEE Photonic Technology Letters*, vol. 5, pp. 787-790, 1993.

[27] I. Glesk, J. P. Sokoloff, and P. R. Prucnal, *IEE Electronics Letters*, vol. 30, pp. 339, 1994.

Chapter 5

16-chip, 50ps, Four-Level Phase Coding Superstructure Fibre Bragg Gratings

Overview

Whilst impressive results on the basic code generation and recognition process have been obtained and reported in the previous chapters, little attention has been paid to the more practical issues of OCDMA system design. In particular, most OCDMA experiments to date have employed expensive and not so commercially available ultrashort pulse seed laser sources [1, 2], complicated detection schemes [3, 4] and have operated only with a limited number of OCDMA channels [5]. This chapter reports on the demonstration of a practical 16-channel OCDMA system based on conventional CW lasers with associated Electro-Absorption (EA) modulators and 16-chip, 20 Gchip/s, quaternary coded SSFBGs encoders/decoders. The system also demonstrates the attraction of incorporating DS-OCDMA coding/decoding approach onto WDM networks to enhance the functionality of the networks and the capability to support a large number of users within a limited wavelength range. Furthermore, the wavelength selectivity of the SSFBG is utilised to simultaneously perform the wavelength 'drop' function and optical decoding function, eliminating the requirements for additional WDM filtering components [6].

5.1 Multi-wavelength pulse generation

The pulse source used in these experiments is based on commercially available CW lasers (for example, tunable external cavity lasers (ECLs) and distributed feedback (DFB) fibre lasers) and Electro-Absorption (EA) modulators. The EA modulator offers the advantages of small chirp values (typically α<0.2), low drive voltage (3V), high stability and easy integration with CW lasers in a small footprint. The device uses a material that under normal conditions has a band gap that is higher than the photon energy of the incident light signal. This allows the light signal to propagate through the device. However, applying an electric field to the modulator results in reduction of the band gap of the material to the extent that incident photons now have energy within the band gap and are hence absorbed by the material. This gives rise to a nonlinear relationship between the reverse bias voltage and the optical transmittance of the device. Thus by applying a sinusoidally-modulated applied voltage and a suitable reverse bias voltage, it is possible to generate a periodic time varying transmission profile that can be used to carve out a sequence of short pulse from an incident CW beams as shown in Figure 5.1 (a) [7].

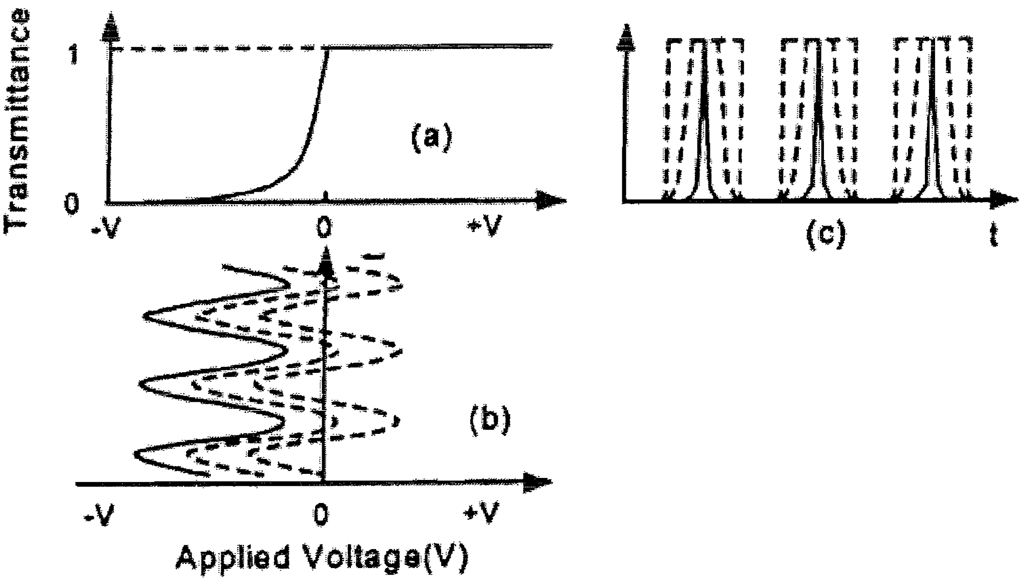

Figure 5.1: Principle of operation of an electro-absorption (EA) modulator. By increasing the reverse bias voltage, shorter duration pulse trains (solid lines) can be obtained.

Our EA modulator allows the generation of high quality 20ps pulse trains at a repetition rate of 10 GHz. Multiple-wavelength (WDM) pulse generation can be obtained by feeding an array of semiconductor CW lasers/distributed feedback DFB [8] fibre lasers into a single EA modulator, as illustrated in the schematic shown in Figure 5.2 below. Furthermore, CW lasers based on DFB fibre lasers offer several advantages compared to conventional semiconductor based lasers, these include excellent optical signal to noise ratio (>60dB), low relative intensity noise (RIN) (<-160 dB/Hz), ultra-narrow linewidth (~18 kHz). Moreover, these devices can be packaged to be passively athermal and are fibre compatible, making them ideal for optical communication system applications [9]. Figure 5.3 shows a typical configuration of a DFB fibre laser.

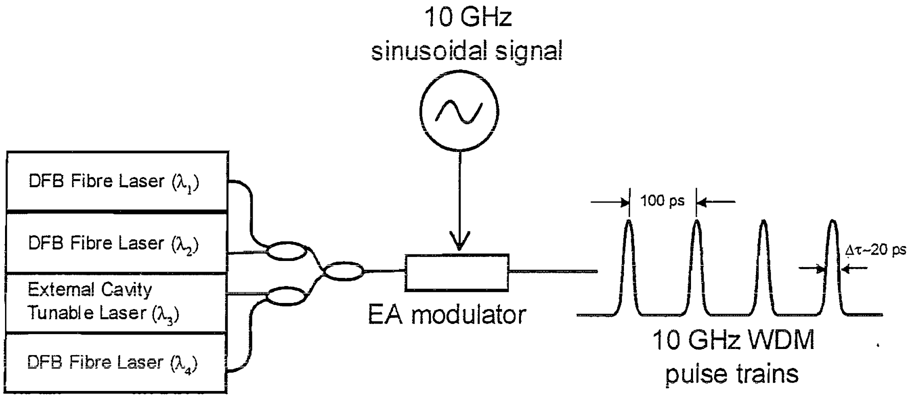

Figure 5.2: Multi-wavelength pulse generation using EA modulator.

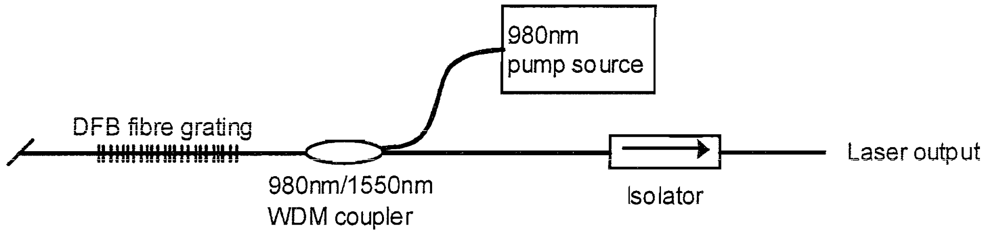

Figure 5.3: Typical configuration of a distributed feedback (DFB) fibre laser. The 980nm pump is absorbed by the ytterbium ions (Yb^{3+}) in the fibre grating. The absorbed power is transferred from the Yb^{3+} ions to nearby erbium (Er^{3+}) ions. The Er^{3+} ions undergo a non-radiative decay to an upper laser level. The lasing action starts with spontaneous emission from the upper laser level within the grating such that only a specific wavelength is reflected by the grating structure. The presence of a phase shift in the grating defines a resonant cavity, which enables laser emission as the level of stimulated emission and gain increases and the threshold conditions are met.

5.2 16-chip, 50ps quaternary SSFBGs

Firstly, a theoretical assessment is performed to determine whether the pulses generated from the combination of the array of CW lasers and an EA modulator have sufficiently short duration (similarly bandwidth) to obtain good contrast code recognition profile from the SSFBG coders. Since the optical pulses generated from the semiconductor CW lasers/distributed feedback DFB fibre lasers using EA modulator have duration of 20ps, the chip duration of the SSFBG gratings are chosen to be 50ps. This will ensure that the optical bandwidth of the source is sufficiently large when compared to the bandwidth of the SSFBG encoders/decoders (see calculated optical spectra in Figures 5.4(a) and 5.4(b)). A 16-chip quaternary phase code derived from Family A [10] is used in this calculation. It is also apparent from Figure 5.4(c) that the calculated temporal features of the encoded waveforms are not as well-defined/sharp as compared to when ultrashort pulses (pulsewidth ~2ps) are used (see Figure 5.5(c)). The full duration of the encoded sequence is 800ps.

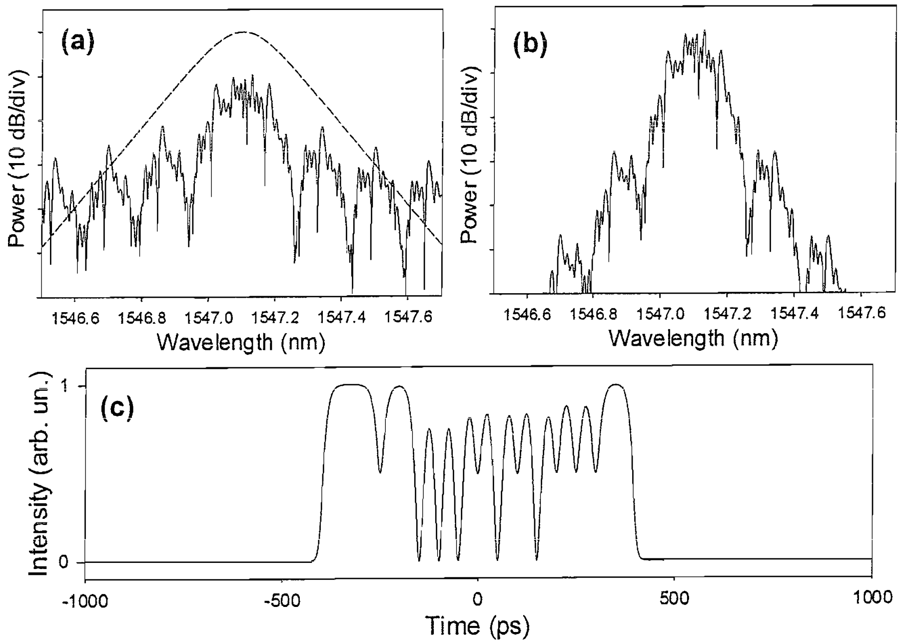

Figure 5.4: (a) Calculated optical spectra of the 20ps pulse source (dashed lines) and the reflectivity spectrum of the 16-chip, quaternary phase coding grating (solid lines). (b) Calculated resulting reflected optical power spectrum after excitation with 20ps pulses. (c) Calculated temporal response after reflection from the SSFBG when 20ps pulses were launched into the grating (less defined chip-transition). The 16-chip code used is 'π, π, π, 0.5π, 0.5π, 1.5π, 0.5π, 1.5π, π, 0, 0.5π, 1.5π, π, 1.5π, 0, 0'.

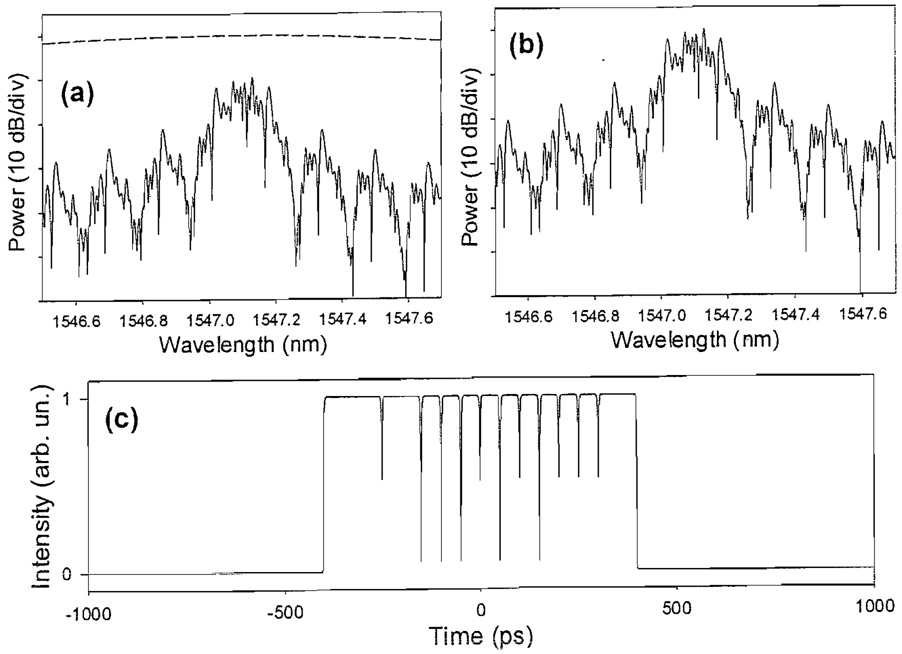

Figure 5.5: Calculated optical spectra of the (a) 2ps pulse source (dashed lines) and the reflectivity spectrum of the 16-chip, quaternary phase coding grating (solid lines). (b) Calculated resulting reflected optical power spectrum after excitation with 2ps pulses. (c) Calculated temporal response after reflection from the SSFBG when ultrashort 2ps pulses were launched into the grating (sharp chip-transition).

Figure 5.6 shows the calculated decoded trace after matched filtering the encoded signal with another SSFBG decoder having an inverse spatial response to the encoder SSFBG.

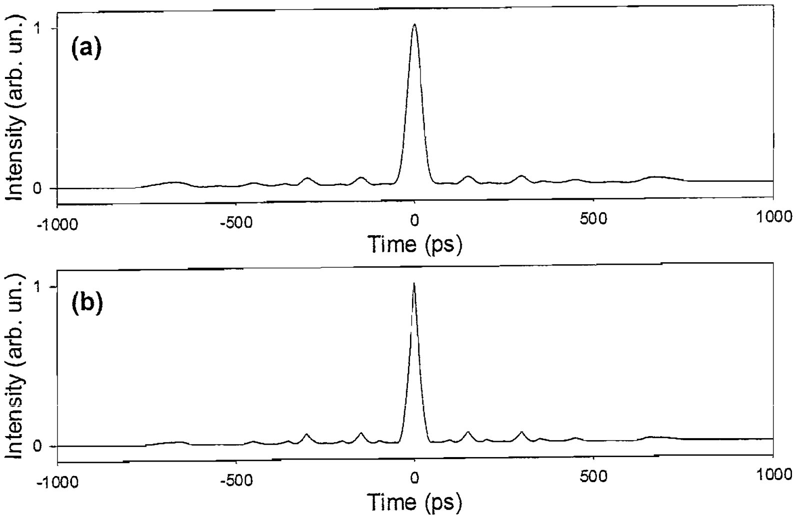

Figure 5.6: Calculated decoded autocorrelation traces when input pulse duration used to excite the gratings is (a) 20ps and (b) 2ps.

Observing Figures 5.6(a) and 5.6(b), it is worth noting that the autocorrelation signatures is almost identical for both cases, with a slight broadening of the decoded pulsewidth when 20ps input pulses are used to perform the encoding/decoding functions.

Four different quaternary phase shift keyed OCDMA codes, labelled as Q1, Q2, Q3 and Q4 are selected from the 16-chip Family A code sequences and are imprinted into the SSFBGs using the continuous grating writing technique. These codes are selected to provide the best autocorrelation and crosscorrelation properties among the 18 distinct code combinations that are available in the 16-chip Family A code sequences [10]. It is to be appreciated that although only 16-chip codes are used within the experiments (in order to limit the total grating length to be fabricated to about 8cm with chip duration of 50ps), the use of longer phase code sequences and shorter chip duration would allow a large number of simultaneous users to be supported within the system [11].

The quaternary code was implemented by introducing the required distinct phase shifts at the interface of the localized regions within the grating as defined by the code sequences. A total of 20 quaternary phase coding SSFBGs (corresponding to four different OCDMA codes, denoted by Q1, Q2, Q3 and Q4, centred on four different ITU wavelengths and four different OCDMA decode gratings, denoted by Q1*, Q2*, Q3* and Q4*) were fabricated.

Figure 5.7 shows the phase modulation profile of four different 16-chip quaternary codes imposed upon the gratings during the writing process together with the corresponding measured and calculated plots of the reflectivity spectrum of the gratings. Good agreement is achieved between the measured and calculated results, which show the precision, repeatability and quality of the gratings produced.

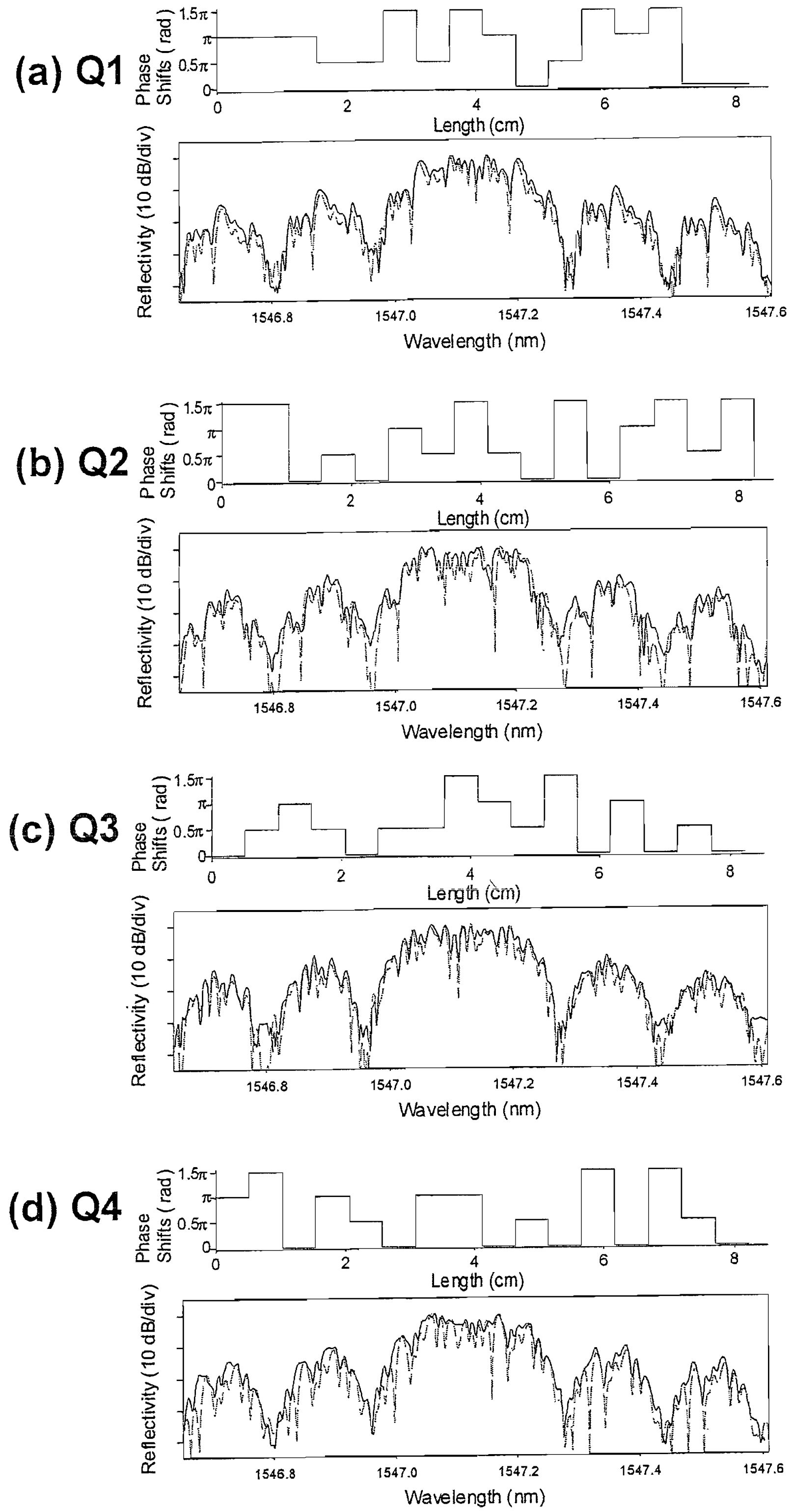

Figure 5.7: (a)-(d) Phase modulation profile of the four 16-chip quaternary codes and the respective measured (solid line) and calculated (dashed line) reflectivity spectra of the gratings fabricated using the continuous grating writing technique. These gratings have a peak reflectivity of ~25% and are 8.22cm long.

The measured and calculated time domain responses for the four different OCDMA codes after reflection from their respective gratings are shown in Figure 5.8. It can be seen that the coding gratings spread the incident 20ps input pulse over a time period of ~800ps as expected. Again, excellent agreement can be observed when comparing the experimental data with the theoretical calculations.

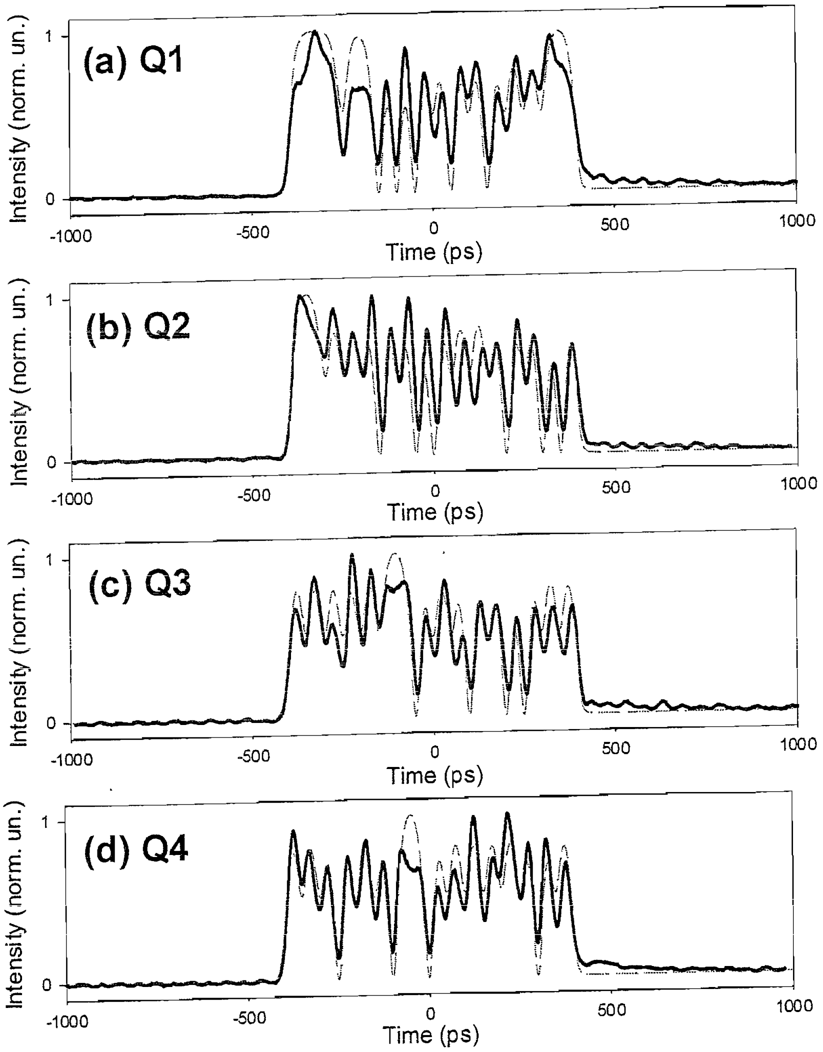

Figure 5.8: (a)-(d) Oscilloscope traces (measured – solid line and theory – dashed line) after reflection off the respective gratings. These measurements have a resolution of ~20ps.

All-optical code recognition is performed by the matched filtering process using a decoder SSFBG having the spatially reversed form of the encoder (i.e. an identical SSFBG to the encoder but reflected from the opposite end). Figure 5.9 illustrates the auto- and cross-correlation outputs from decoder grating Q1* when different encoder gratings (Q1, Q2, Q3 and Q4) are used. As expected, the autocorrelation output (Q1:Q1*) exhibits a dominant, sharp peak signature while low level, noise-like signals are obtained for all crosscorrelation output combinations (Q2:Q1*, Q3:Q1* and Q4:Q1*). The average extinction ratio between the peak of the correctly decoded pulse (Figure 5.9(a)) to the incorrectly decoded low-level signals (Figures 5.9(b) to 5.9(d)) is ~ 8dB.

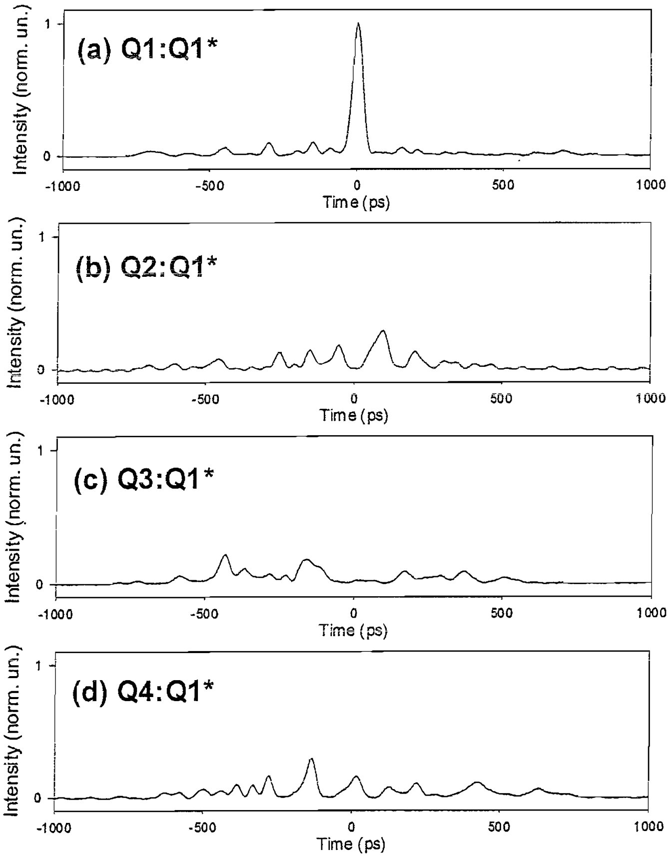

Figure 5.9: (a) Measured decoded autocorrelation signature after reflecting encoded signal Q1 off the decoder grating Q1. (b)-(d): Measured crosscorrelation signatures obtained after reflecting encoded signal Q2, Q3 and Q4 respectively off the decoder grating Q1*. The extinction between auto-correlation signature and cross-correlation waveforms is ~ 8dB. All the decoded output signals have a full duration of 1.6ns corresponding to twice the encoded duration as a result of the matched filtering process.*

Figure 5.10 shows the correctly decoded autocorrelation output for all the four different OCDMA codes. All the four code:decode pairs exhibit a sharp and distinct pulse-like features at the centre of the autocorrelation output waveforms with good agreements between the theoretical and experimental plots.

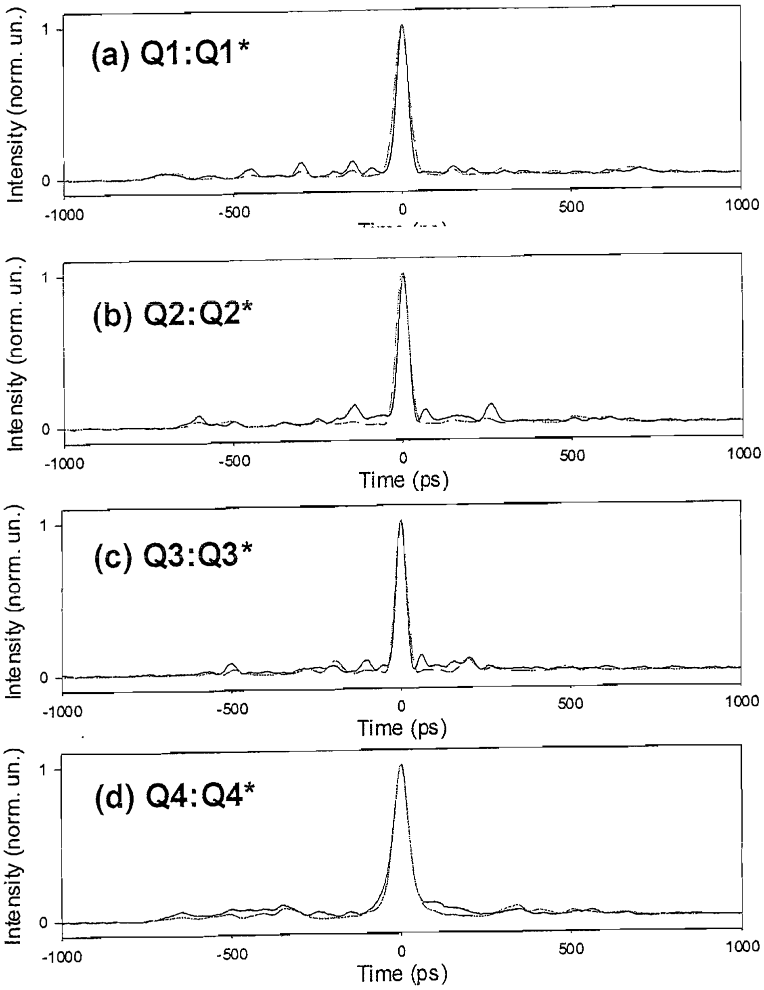

Figure 5.10: (a)-(d) Measured (solid lines) and calculated (dashed lines) of the correctly decoded autocorrelation traces for all four different quaternary codes to be used in the experiment. The decoded pulsewidths are ~50ps.

Having successfully characterised the quality and the coding/decoding performance of the 16-chip SSFBGs, we then incorporated the gratings into a 16-channel OCDMA/DWDM system comprising four OCDMA codes centred on each DWDM wavelength.

5.3 16-channel OCDMA/DWDM experimental results

The experimental set up used to study the performance of the 16-channel OCDMA/DWDM system is shown in Figure 5.11. Four transmitters comprising three single-polarization asymmetric distributed feedback (DFB) fibre lasers [12] and a tunable external cavity semiconductor laser, all separated in frequency by 100 GHz were used. The output from these lasers was first multiplexed together and fed into an Electro-Absorption (EA) modulator. The EA modulator was used to generate 10 GHz, 20ps DWDM pulse trains. The pulse trains were then amplified and gated down to a repetition rate of 311 MHz using an intensity modulator and were simultaneously modulated to obtain a 2^7-1 pseudorandom data sequence pulses at a data rate of 311 Mbit/s. These modulated pulses were then reflected from an array of 16 coding SSFBGs (four different OCDMA codes per wavelength) to generate 16 simultaneous coded data channels. All of the 16 quaternary coded channels were combined together and transmitted over a distance of 50km of standard single mode fibre having a total dispersion of 812ps/nm. The transmitted data streams were then split and reflected off four separate decode gratings matched to the particular OCDMA codes and wavelength channels. In this configuration, all four different OCDMA code channels located on the same wavelength (or different wavelengths) can be decoded simultaneously and the bit error rate (BER) of each individual channel can be measured.

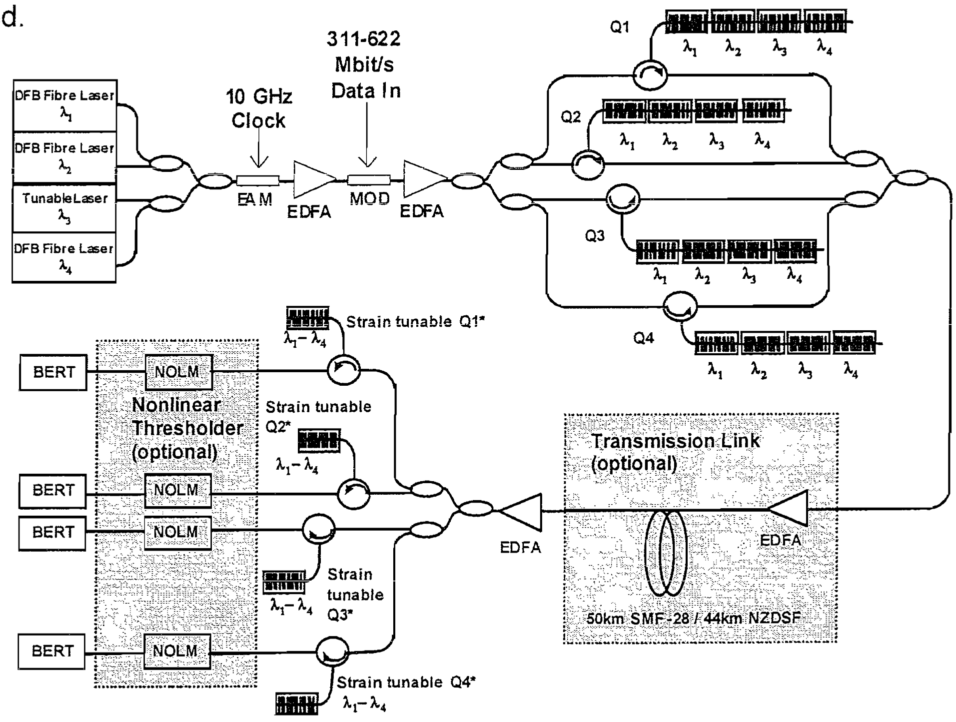

Figure 5.11: Schematic diagram of the OCDMA/DWDM experimental set up.

Figure 5.12(a) shows the optical spectrum of the combined DWDM laser sources. The optical spectrum of the 16-coded channels OCDMA/DWDM combined after reflection from the individual coding gratings is shown in Figure 5.12(b) while Figure 5.12(c) shows the optical spectrum of the decoded response of grating Q1* to the combined 16-channel input. Figure 5.12(c) shows that by using just a single decode SSFBG we can simultaneously perform both the wavelength 'drop' function (~25 dB of extinction between adjacent 100 GHz channels), and the channel decode function in the time domain.

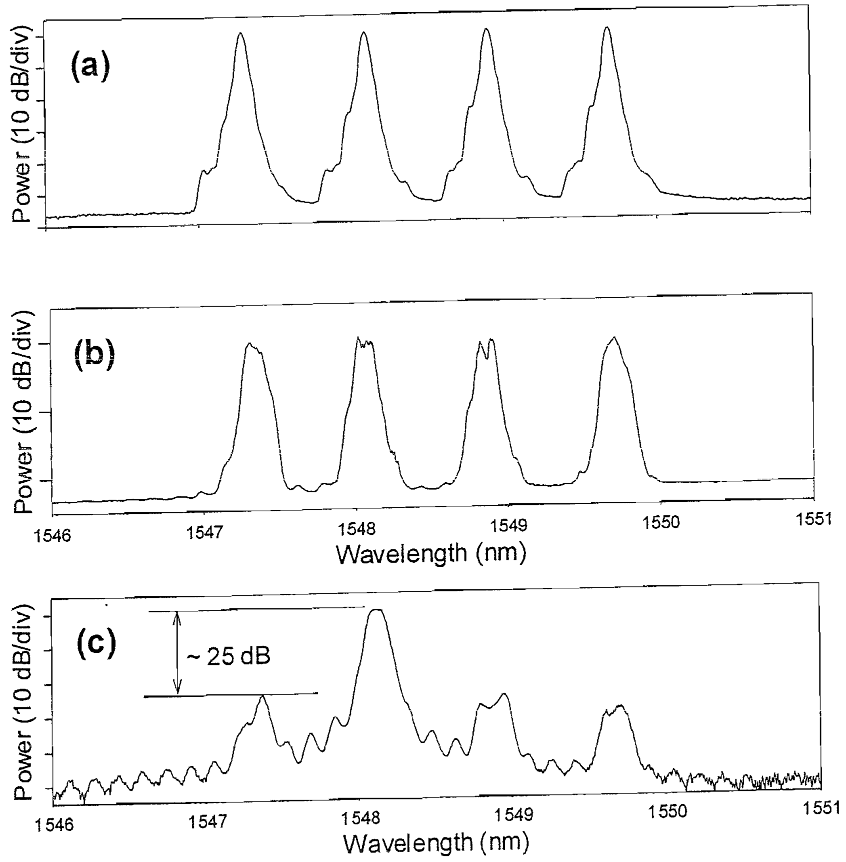

Figure 5.12: Optical spectra obtained at various points along the system: (a) The multiplexed four WDM sources, separated in frequency by 100 GHz. (b) Encoded 16-channel OCDMA/DWDM. (c) After matched filtering using decoder grating Q1 centred at* λ_2 *= 1548.11nm. The measured resolution is 60pm.*

Next, in Figure 5.13 the degradation to the decoded eye diagrams as the number of active 'in-band' OCDMA channels is added into the system is illustrated. Clean, open eyes are observed confirming that good code recognition quality can be obtained even in the instance when all four OCDMA coded channels are transmitting simultaneously.

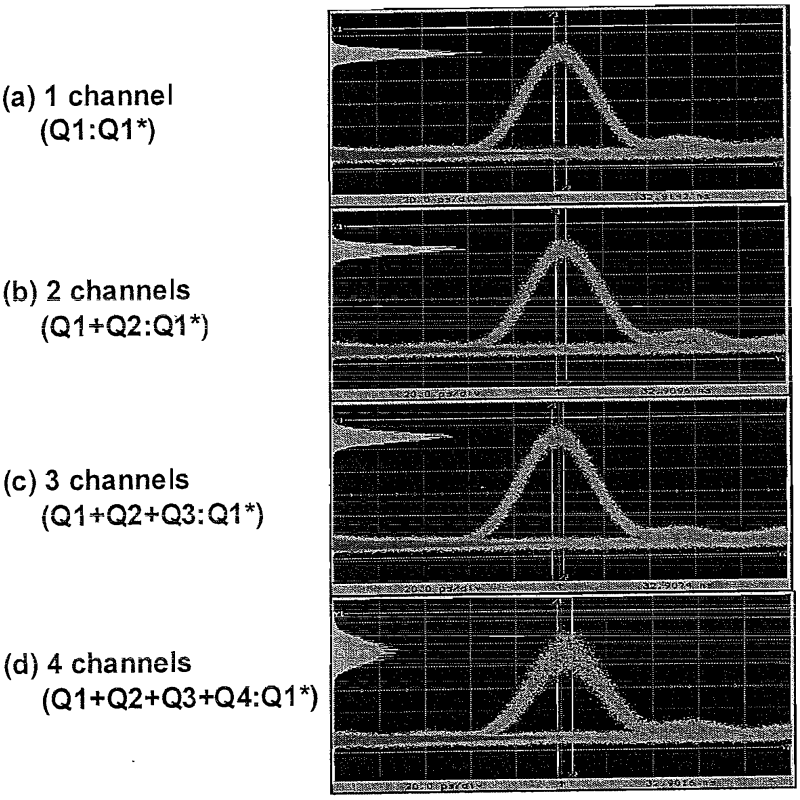
(a) 1 channel (Q1:Q1*)

(b) 2 channels (Q1+Q2:Q1*)

(c) 3 channels (Q1+Q2+Q3:Q1*)

(d) 4 channels (Q1+Q2+Q3+Q4:Q1*)

Figure 5.13: Eye diagrams and the histogram data showing the distribution of zeros and ones of the decoded signals after reflection from decode grating Q1 when all four OCDMA coded channels (Q1, Q2, Q3 and Q4) are active in the system. The measurements were taken using a 10 GHz detector.*

In Figure 5.14 the eye diagrams obtained after matched filtering at a data rate of 311 Mbit/s for the full 16-channel system are shown. Clean eyes are observed confirming that good code recognition quality can be obtained when all 16 OCDMA channels are active even in the instance of transmission over 50km of standard fibre with uncompensated dispersion. The performance of the 16-channel system was characterised by measuring the bit error rate (BER) against the total received power for each OCDMA channel in the presence of the other 15 interfering channels. The results are plotted in Figure 5.15. Error free performance is obtained for all the 16 channels. Note that a large proportion of the apparent ~ 5dB power penalty when compared to the laser back-to-back case results simply from the increased incident average power due to the additional 4 'in-band' OCDMA channels. A further ~ 2dB of power penalty is observed for all the channels when the 16-coded channels are transmitted through 50km of standard fibre. However, error free operation can still be obtained in this case without the need for dispersion compensation. This penalty can certainly be reduced with the incorporation of dispersion compensating elements, albeit with an increase in system complexity.

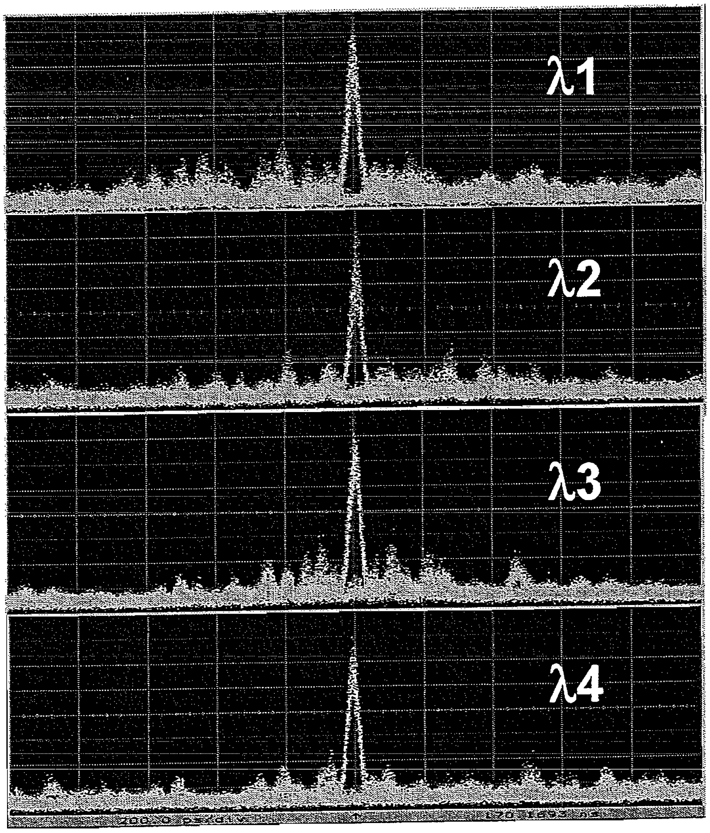

Figure 5.14: Eye diagrams obtained after matched filtering process using decode grating Q2 for all four wavelengths in the presence of all 16 coded channels at data rate of 311 Mbit/s.*

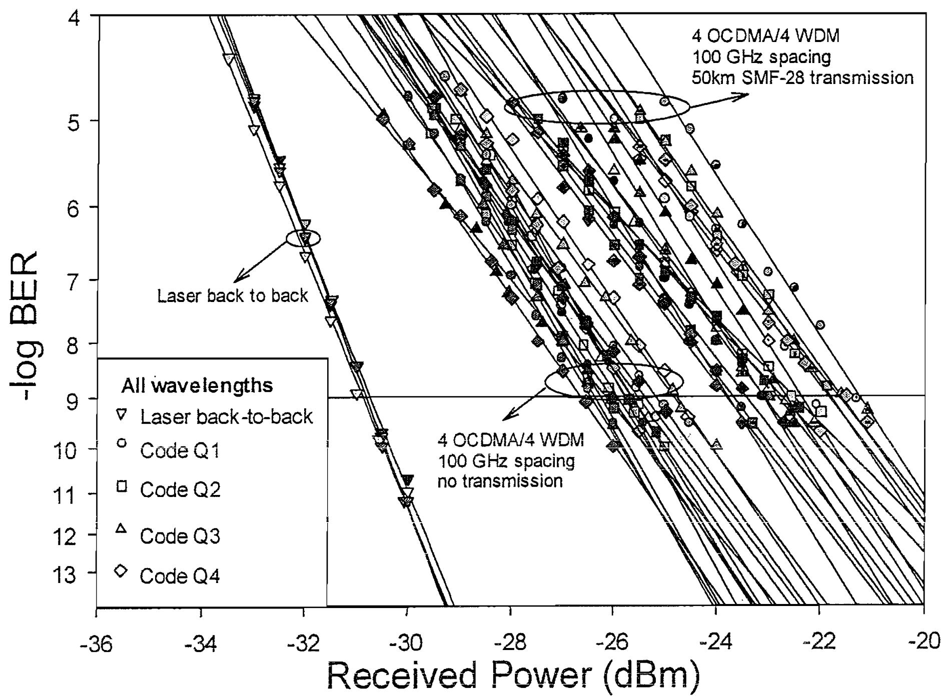

Figure 5.15: BER measurements obtained against received optical power for all 311 Mbit/s, 16-coded channels including after transmission over 50km of SMF-28.

Next, the frequency spacing between the adjacent DWDM lasers was reduced to 50 GHz. The transmission fibre was also replaced with 44km of non-zero dispersion shifted fibre (NZDSF) with a total dispersion of 118.8 ps/nm. Note that at such tight frequency spacing, it was not possible to obtain BER measurements when 50km of SMF-28 was used as the transmission link without dispersion compensation. This is because the crosstalks from adjacent 50GHz WDM channels are introducing significant interference noise to the already degraded decoded autocorrelation signal after transmission over 50km of uncompensated dispersion.

Figure 5.16(a) shows the multilplexed 16-coded channels optical spectrum before decoding, while Figure 5.16(b) illustrates the optical spectrum obtained after the code recognition process. An ~18 dB of extinction between adjacent 50 GHz DWDM channels was obtained.

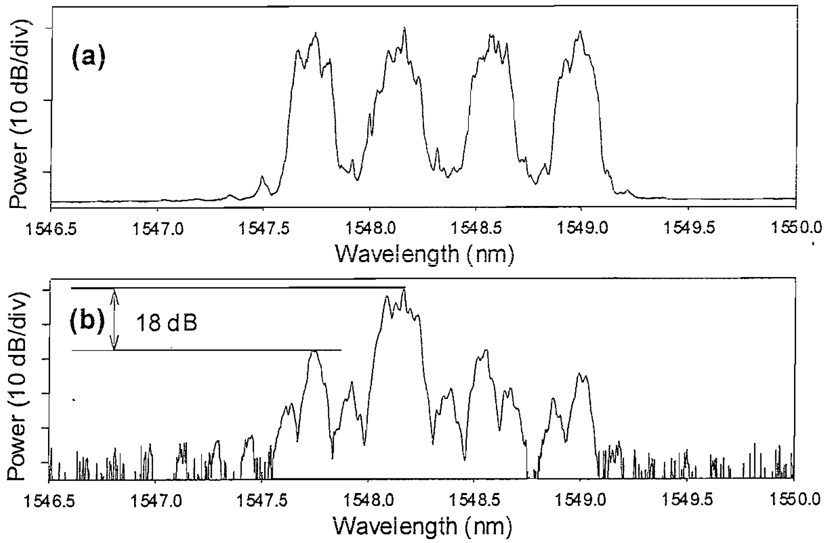

Figure 5.16: (a) Optical spectrum showing the multiplexed 16-channel OCDMA/DWDM when the WDM laser sources have their frequency spacing reduced to 50 GHz. (b) After matched filtering using decode grating Q1. The measured resolution is 10pm.*

Eye diagrams and BER measurements were taken for a selection of OCDMA channels when all 16 channels were transmitting in the system. The results are illustrated in Figure 5.17 and Figure 5.18 respectively. Error free performance is obtained at data rate of 311 Mbit/s for the case corresponding to coded channels Q1 λ_1, Q2 λ_2, Q3 λ_3 and Q4 λ_4 after transmission through the 44km of NZDSF (in fact, it is anticipated that error free performance can be obtained for the rest of the coded channels). An ~6 dB power penalty is observed when compared to the laser back-to-back measurements. In order to improve the system performance at such close channel spacings, it is necessary to either improve the spectral filtering or to apply some form of nonlinear processing at the receiver [13, 14]. This later approach should also allow for increases in terms of simultaneous users per wavelength and data rate per OCDMA channel. A nonlinear thresholder based on a nonlinear optical loop mirror (NOLM) was implemented in the 50 GHz OCDMA/DWDM experiment as described in the following section.

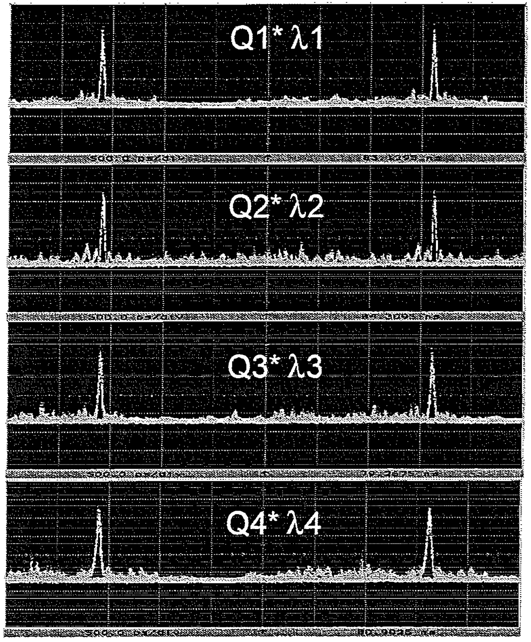

Figure 5.17: Eye diagrams of the decoded signals after reflection from the decode gratings Q1 λ_1, Q2* λ_2, Q3* λ_3 and Q4* λ_4 respectively at data rate of 311 Mbit/s.*

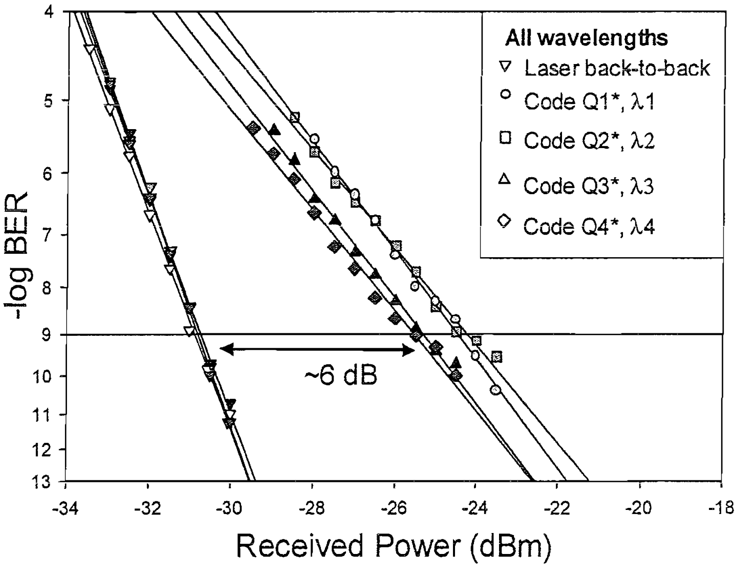

Figure 5.18: BER measurements made against received optical power at data rate of 311 Mbit/s using decode gratings Q1 λ_1, Q2* λ_2, Q3* λ_3 and Q4* λ_4 in the presence other 15 interfering channels after transmission through the 44km of NZDSF.*

5.4 Performance Enhancement using NOLM

As has been demonstrated previously in Chapter Four, a nonlinear optical loop mirror (NOLM) can be inserted after the decode gratings to improve the code recognition contrast. A similar NOLM, incorporated a 70:30 coupler, and contained 6.6km of dispersion shifted fibre, with a dispersion D=1.18ps/nm/km at the system operating wavelength of 1558nm was used in the experiment.

Figure 5.19 shows the eye diagrams obtained when the 16-coded channels (4 OCDMA x 4 DWDM with 50 GHz frequency spacing) and higher channel data rate of 622 Mbit/s are used in conjunction with the NOLM. Note that at this higher data rate, there is a significant autocorrelation tail overlap between adjacent bits, which leads to increased interference noise. The improved pattern recognition contrast is clearly evident when comparing Figures 5.19(b) and 5.19(c). The low-level pedestal obtained after simple matched filtering is almost entirely eliminated after passing through the NOLM. Note that although the NOLM used in this experiment was not optimised for broad decoded pulsewidth (~50ps compared to only 6.4ps in Chapter Four), good code recognition performance and pedestal removal could still be obtained, further improved performance is to be anticipated with an improved and optimised NOLM design.

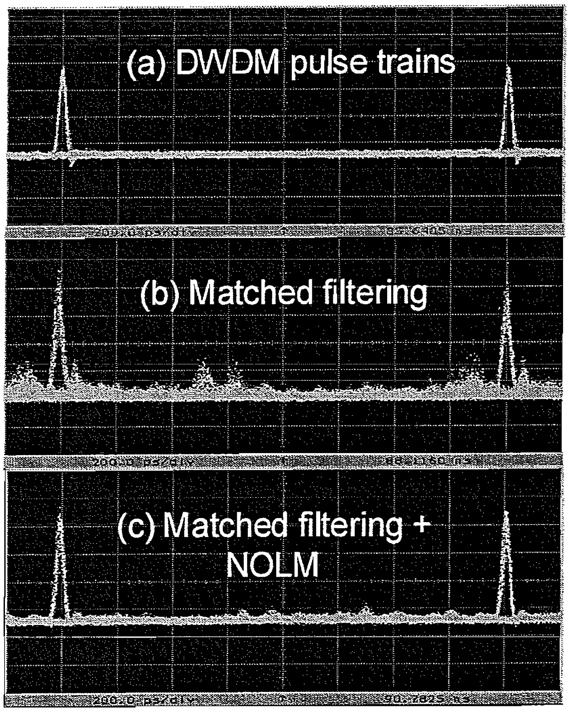

Figure 5.19: Eye diagrams obtained at data rate of 622 Mbit/s for the (a) 20ps DWDM input pulse trains (b) after matched filtering using the decode gratings Q1 (c) improved eye diagrams after NOLM.*

The benefits of the pedestal rejection from a system perspective are highlighted in the BER measurements plotted in Figure 5.20. There is only a ~3.5 dB power penalty observed for all the measured channels when compared to the laser back-to-back case at a data rate of 622 Mbit/s using the NOLM after the decode gratings. These results show that the use of nonlinear thresholding can allow for higher channel data rates than possible with simple matched filtering alone as well as increasing the number of simultaneous users per wavelength. Note that without the NOLM, no discernible BER measurements can be obtained at such tight frequency spacing and high data rates.

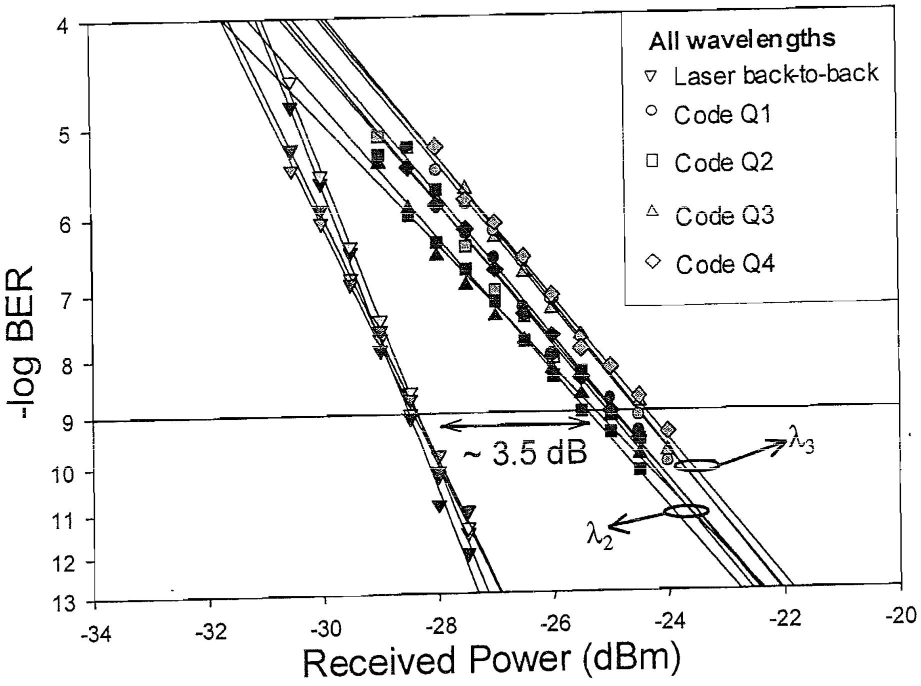

Figure 5.20: BER measurements obtained at data rate of 622 Mbit/s after nonlinear thresholding using the NOLM for all four decode gratings (Q1, Q2*, Q3* and Q4*) strain-tuned to λ_2, λ_3 in the presence of other 15 interfering OCDMA/DWDM channels.*

5.5 Conclusions

In conclusion, the above results have experimentally demonstrated that the SSFBGs coding/decoding approach can be implemented using practical all-fibre sources in a 16-channel OCDMA/DWDM system with adjacent wavelength spacing as close as 50 GHz. These experiments have also demonstrated that error free performance can be obtained even in the instance when the coded channels are transmitted over some distance of uncompensated dispersion. Though both encoder/decoder SSFBGs used in the experiments were based on fixed phase-code predetermined during the writing process, the use of code-tunable encoder/decoder would be preferable since it would enhance the flexibility and reconfigurability of the OCDMA network. Chapter Six reports on the development and demonstration of phase code-tunable devices based on uniform fibre Bragg grating and wire heaters.

References

[1] J. A. Salehi, A. M. Weiner, and J. P. Heritage, "Coherent ultrashort pight pulse code-division multiple access communication systems," *IEEE Journal of Lightwave Technology*, vol. 8, pp. 478-491, 1990.

[2] H. P. Sardesai, C.-C. Chang, and A. M. Weiner, "A femtosecond code-division multiple access communication system test bed," *IEEE Journal of Lightwave Technology*, vol. 16, pp. 1953-1964, 1998.

[3] W. Huang and I. Andonovic, "Coherent optical pulse CDMA systems based on coherent correlation detection," *IEEE Transaction on Communications*, vol. 47, pp. 261-271, 1999.

[4] W. Huang, I. Andonovic, and M. Tur, "Decision-directed PLL for coherent optical pulse CDMA systems in the presence of multiuser interference, laser phase noise and shot noise," *IEEE Journal of Lightwave Technology*, vol. 16, pp. 1786-1794, 1998.

[5] K. Takiguchi, T. Shibata, and M. Itoh, "Encoder/decoder on planar lightwave circuit for time-spreading/wavelength-hopping optical CDMA," presented at Optical Fiber Communications Conference (OFC2002), paper TuK8, 2002.

[6] K. Kitayama, "OCDM/WDM networks for gigabit access: 1.24 Gbit/s, 2xOCDM by 2xWDM experiment," presented at Europepan Conference on Optical Communication, 1999.

[7] H. Tanaka, T. Otani, M. Hayashi, and M. Suzuki, "Optical signal processing with electro-absorption modulators," *Proceeding of Optical Fiber Communication Conference (OFC 2002)*, vol. WM3 (Invited), pp. 262-264, 2002.

[8] M. Ibsen, S. Alam, M. N. Zervas, A. B. Grudinin, and D. N. Payne, "8- and 16-channel all-fiber DFB laser WDM transmitters with integrated pump redundancy," *IEEE Photonic Technology Letters*, vol. 11, pp. 1114-1116, 1999.

[9] W. H. Loh, B. N. Samson, L. Dong, G. J. Cowle, and K. Hsu, "High performance single frequency fiber grating-based erbium:ytterbium-codoped fiber lasers," *IEEE Journal of Lightwave Technology*, vol. 16, pp. 114-118, 1998.

[10] S. Boztas, R. Hammons, and P. V. Kumar, "4-phase sequences with near-optimum correlation properties," *IEEE Transaction of Information Theory*, vol. 38, pp. 1101-1113, 1992.

[11] W. Ma, C. Zuo, H. Pu, and J. Lin, "Performance Analysis on Phase-Encoded OCDMA Communication System," *IEEE Journal of Lightwave Technology*, vol. 20, pp. 798-803, 2002.

[12] M. Ibsen, A. Fu, H. Geiger, and R. I. Laming, "All-fibre 4x10 Gbit/s WDM link with DFB fibre laser transmitters and single sinc-sampled fibre grating dispersion compensator," *IEE Electronics Letters*, vol. 35, pp. 982-983, 1999.

[13] Y. J. Chai, I. Y. Khrushchev, and I. H. White, "Nonlinear suppression of interferometric noise using dispersion-imbalanced loop mirror," *IEE Electronics Letters*, vol. 36, pp. 1565-1566, 2000.

[14] N. Wada, H. Sotobayashi, and K. Kitayama, "Error-free 100km transmission at 10 Gbit/s in optical code division multiplexing system using BPSK picosecond-pulse code sequence with novel time-gating detection," *IEE Electronics Letters*, vol. 35, pp. 833-834, 1999.

Chapter 6

Reconfigurable OCDMA Phase Coders

Overview

The development of the phase code tunable encoders/decoders based on uniform fibre Bragg gratings is described. A phase shift can be obtained in a uniform grating by locally increasing the background effective refractive index of the fibre through controlled localised heating using thin resistive wires placed at the physical points of chip-transition. 8-chip and 16-chip reconfigurable coders have been demonstrated in a range of OCDMA coding/decoding experiments.

6.1 Introduction

The results reported in the previous Chapters Three, Four and Five have all used phase coders with fixed superstructure profiles imposed upon the photosensitive fibres during the grating writing process. Dynamically code-tunable devices will be required in many instances to allow for maximum network flexibility, code provisioning and control. The use of such reconfigurable devices simplifies the transmitter and receiver architectures by reducing the number of individual coding elements and allowing a single laser transmitter/receiver to transmit/receive on multiple, different codes. This chapter reports on the demonstration of a simple reconfigurable code generator for phase encoding/decoding applications in OCDMA systems based on fibre Bragg gratings.

A number of technological approaches to demonstrate code tunability in DS-OCDMA have been reported to date. The earliest implementation is based on arrays of discrete fibre delay lines with tunable delays [1]. These tunable delays were simply fibre stretchers; hence they lacked the fine-tuning resolution required and were impractical to be scaled to encompass a long code sequence. Implementation in optical waveguide technology has also been reported using planar lightwave circuits (PLCs) [2]. In these PLCs, microheaters incorporated into the substrate allow both the delays and phase shifts to be reconfigured. However the PLC approach has the disadvantages of high fabrication complexity and cost. A more recent technique based on cascading arrays of fibre Bragg gratings, has also been demonstrated by several research groups [3-5]. Nevertheless, the lack of compactness, relatively short code lengths and the associated high cost of fabricating such devices lead to limited practical value.

The proposed approach, however, is based on the use of a single-structure grating, i.e. a uniform fibre Bragg grating. The device uses thin resistive wires at the chip-transitions to control the phase through controlled heating at these points. This approach allows accurate phase codes to be obtained, in fact levels of phase shifts definitions as high as quaternary have been achieved. The compatibility of this approach with fixed code SSFBG is also demonstrated in this chapter.

The principle of this reconfigurable OCDMA phase coder is proposed by Mr. Morten Ibsen, who also fabricated the gratings used in these experiments. This work is also performed in collaboration with Mr. Mohd. Ridzuan Mokhtar, a PhD student from the Fibre Bragg Grating group.

6.2 Principle of Operation

A typical phase-shifted grating can be produced, by shifting the phase of the rapidly varying refractive index during the grating writing process (please refer to SSFBG fabrication in Chapter Two). Alternatively, a phase shift can be imposed within an otherwise uniform pitch grating by locally increasing the background effective refractive index of the fibre. The refractive index of the grating is sensitive to slight variations in both temperature and strain [6]. This condition is dictated by the following equation:

$$\Delta n_{eff} = \frac{\partial n_{eff}}{\partial T}.\Delta T + \frac{\partial n_{eff}}{\partial \sigma}.\Delta\sigma \qquad (6.1)$$

where $\partial n_{eff}/\partial T$ is the temperature coefficient of the refractive index, ΔT is the change in temperature, $\partial n_{eff}/\partial\sigma$ is the longitudinal stress optic coefficient, and $\Delta\sigma$ is the applied longitudinal stress. The stress however, needs to be cautiously applied to the fragile grating and is difficult to adjust and to localise. On the other hand, heating can easily be controlled and spatially confined. Heating can produce stress as a result of thermal expansion, however the thermal expansion coefficient of silica is approximately 5.2×10^{-7}, whereas thermo-optic effect ($\partial n_{eff}/\partial T$) is about 1.1×10^{-5} $^{\circ}C^{-1}$. Therefore, the contribution of the thermo-optic effect should be far greater than the thermo-elastic effect. Moreover, the temperature-induced index variation is not permanent, as long as the temperature does not exceed the grating erasure temperature (~150 °C). Applying adjustable localised heating should thus be an effective method to control the amount of phase shift imposed to the propagating mode.

The variation in the effective refractive index obtained due to the localised heating will appear as a modulation of the local Bragg wavelength $\Delta\lambda_B$, and can be expressed by the following equation

$$\Delta\lambda_B = 2(\Lambda\frac{\partial n_{eff}}{\partial T}.+n_{eff}\frac{\partial\Lambda}{\partial T})\Delta T + 2(\Lambda\frac{\partial n_{eff}}{\partial\sigma}+n_{eff}\frac{\partial\Lambda}{\partial\sigma})\Delta\sigma \qquad (6.2)$$

To obtain the phase shift, first consider the phase of a propagating signal along a distance *z* is given by $\phi = 2\beta z$ where $\beta=2\pi n_{eff}/\lambda_B$, n_{eff} is the effective refractive index of the fibre core and λ_B is the grating initial Bragg wavelength. The small variation of the phase can be expressed as

$$\Delta\phi = 2\Delta\beta\Delta z = \frac{4\pi\Delta n_{eff}\Delta z}{\lambda_B} \tag{6.3}$$

where $\Delta\beta=2\pi\Delta n_{eff}/\lambda_B$. The period of the grating can is given by $\Lambda=\lambda_B/2n_{eff}$. Assumming that $\lambda_B>>\Delta\lambda_B$, $\Delta n_{eff}=\Delta\lambda_B/2\Lambda=$. $\Delta\lambda_B n_{eff}/\lambda_B$. Substituting into Equation (6.3),

$$\Delta\phi = \frac{4\pi n_{eff}\Delta\lambda_B\Delta z}{\lambda_B{}^2} \tag{6.4}$$

The corresponding accumulated phase shift ϕ_{total} associated with the Bragg wavelength variation at the chip boundary, can then be determined from the equation below:

$$\phi_{total} \approx \frac{4\pi n_{eff}}{\lambda_B^2}\int_{-\Delta z/2}^{\Delta z/2}\Delta\lambda_B(T(z))dz \tag{6.5}$$

where Δz is the width of the heated segment and *T(z)* is the temperature shift at position *z* relative to the overall temperature of the uniform grating. This distributed temperature varies over a short length scale and the phase shift is defined over this length scale. This length scale (~ wire thickness but many grating planes) is much shorter when compared to the chip length. The localized temperature at the chip boundary of the uniform grating is varied by controlling the temperature of a particular heating element. A controllable phase shift can be obtained at that point in the grating due to the shift of the local Bragg wavelength. In the proposed approach, the heating element can be constructed using very thin resistive wire in series with a variable resistor. The variable resistor controls the amount of current flowing in the wire and hence controlling the amount of local temperature induced at a particular point along the grating length.

Using this effect, a phase code-tunable device can be constructed for use in DS-OCDMA systems by deploying several thin resistive wires in series with a variable resistor at equal intervals along a uniform fibre Bragg grating. The spatial phase profile of the device can be altered to generate a desired optical phase code by simply adjusting the temperature at the required chip boundaries. A short input signal pulse can thus be directly transformed into a coded pulse sequence upon reflection from the device.

In reality it will not be possible to fully localise a change in temperature at the chip boundary and there will be a modified temperature over a short physical length of the grating and there is a need to understand how this distributed temperature variation will affect the ability to define a localised phase shift.

6.3 Device Description

The uniform fibre Bragg gratings used for the experimental demonstrations (8-chip and 16-chip) are 4cm and 8cm long and are written in a standard telecom compatible photosensitive fibre with an NA ≈ 0.12. The uniform coupling coefficients in the gratings are ~33m^{-1} and ~12m^{-1} respectively (These correspond to a peak reflectivity of ~75% and ~55%). A lower coupling coefficient is required for the longer uniform fibre Bragg grating to ensure that every element along the grating structure contributes more or less equally to the overall reflected response. The gratings are written using the continuous grating writing technique similar to the one used to fabricate the SSFBGs.

To implement the heating elements along the grating, thin tungsten wires (18μm in diameter) are wrapped around or laid on top of the grating to ensure a firm contact within a small confined area. A single N-chip code generator with a chip-duration of T_c (in seconds) is constructed by positioning N-1 parallel tungsten wires L_c (in metres) apart along the fibre grating with the first wire being placed L_c into the grating, where

$$T_c \approx \frac{2n_{eff}L_c}{c} \qquad (6.6)$$

where c is the speed of light in free space. The amount of temperature rise is controlled independently by varying the current flow using a variable potentiometer inserted in each parallel circuit. In addition, the fibre grating is mounted on a fibre stretcher to allow flexible tuning of the grating central wavelength. The structure of the reconfigurable device is illustrated in Figure 6.1. Figure 6.2 shows the measured and calculated spectral profile of the 4cm long uniform fibre Bragg grating.

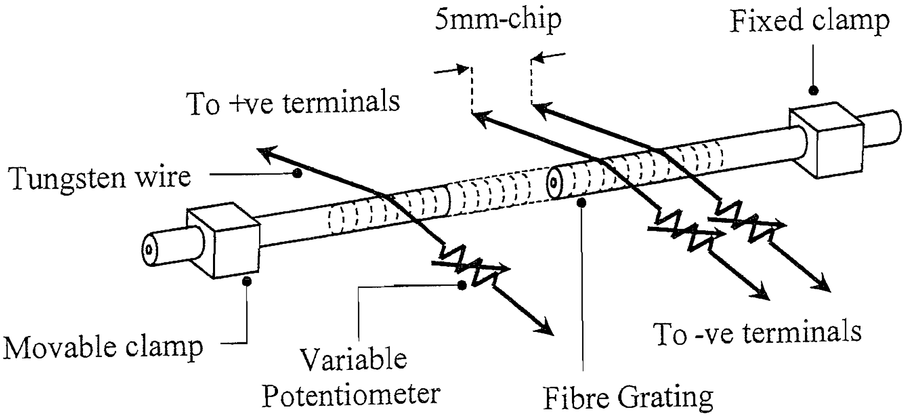

Figure 6.1: Schematic structure of the reconfigurable encoder/decoder. The grating is mounted on a fibre stretcher to allow flexible tuning of the overall grating central wavelength.

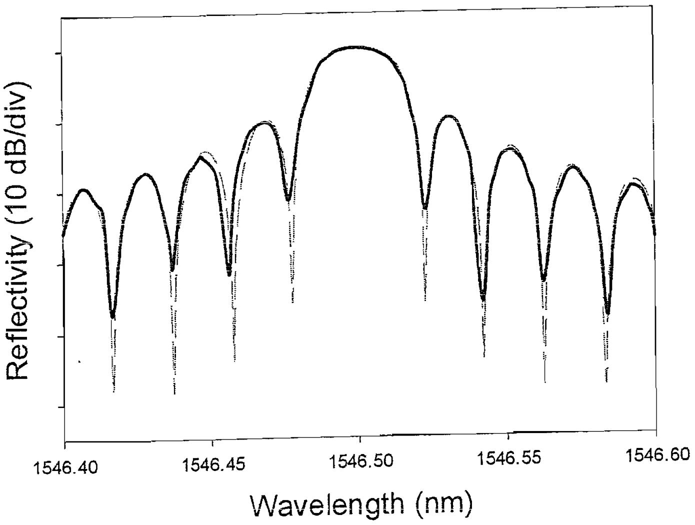

Figure 6.2: 4cm Uniform fibre Bragg grating spectral reflectivity profile. (measured – solid line and calculated – dashed line). The peak reflectivity of the grating, R is ~75%.

Initially a single wire is placed as close as possible to the centre of the 4cm uniform fibre Bragg grating to allow for the determination of the magnitude of the induced single phase-shift against the applied current. By increasing the current applied to the wire, the localised temperature at that point will increase and hence a phase-shift can be obtained in accordance with Equation 6.2. The magnitude of the phase-shift is determined by comparing the measured spectral response of the central phase-shifted fibre Bragg grating with theoretical predictions such that a predetermined phase-shift can be set with sufficient accuracy, simply by applying the correct current to a particular wire. The result of this phase-shift determination is shown in Figure 6.3. Subsequently, similar characterisation is performed on the 8cm grating. The plot of the induced phase shift against the applied current is shown in Figure 6.4.

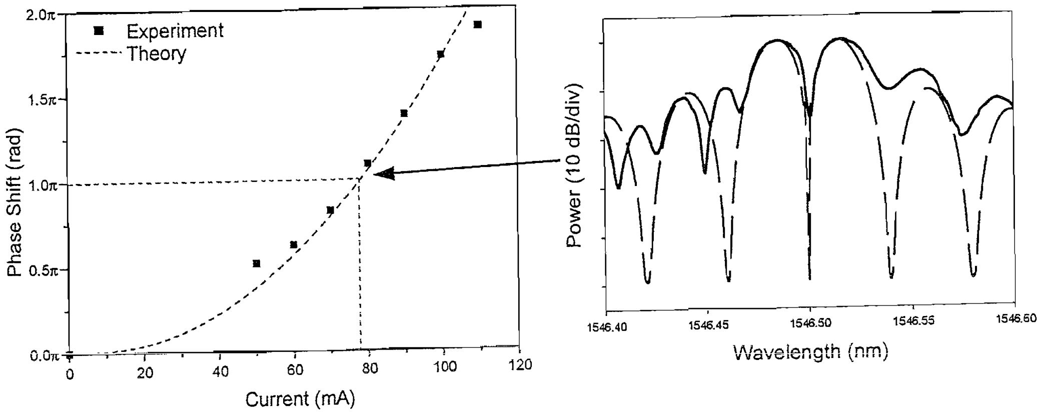

Figure 6.3: Phase shift obtained when various amounts of electrical current are applied to the thin heating wire placed at the centre of the 4cm uniform grating. Inset shows the spectral reflectivity response obtained when a π–phase shift is induced at the centre of the uniform fibre Bragg grating.

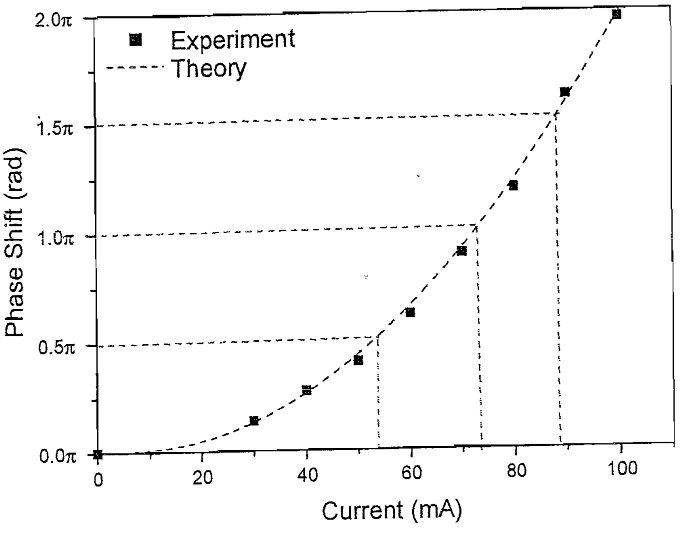

Figure 6.4: Induced phase shift as a function of the applied current obtained for 8cm uniform fibre Bragg grating. The dotted lines show the required amount of current to induce the four different phase shifts.

The overall Bragg wavelength of the fibre grating is expected to rise due to the increase in temperature of the surrounding air. Both the operating and environment conditions must be left stable before measuring in order to obtain consistent results. This Bragg wavelength shift due to environment is taken into account in determining the amount of phase shift for a particular electrical current. Error due to the resolution of the optical spectrum analyser and the ammeter are also considered. However, effects due to small misplacement of the wires from the appropriate positions along the fibre grating can be considered negligible, since their spectral profiles remain essentially the same for misplacement of up to 0.2mm.

6.4 8-chip bipolar code-tunable OCDMA encoders/decoders

A pair of 8-chip code-tunable encoder/decoder were constructed using 4cm long uniform fibre Bragg gratings. Seven tungsten wires with 25μm in diameter were wrapped firmly along each grating length at equal distance of 0.5cm apart from the start of the grating to obtain an 8-chip having chip duration of 50ps.

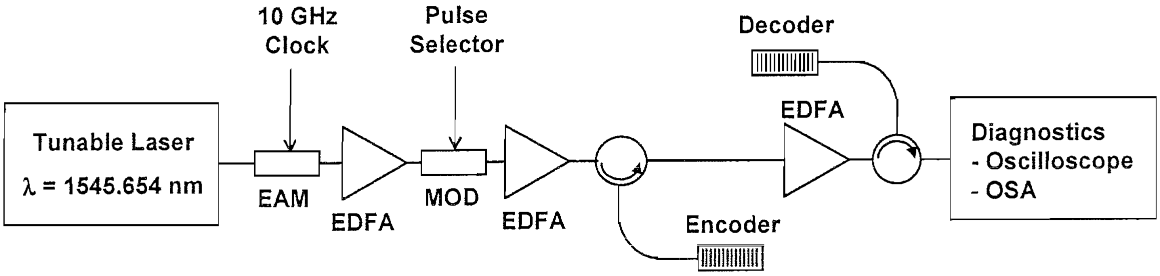

Figure 6.5: Experimental set up using 8-chip code-tunable encoder and decoder. EAM – Electro-Absorption modulator, MOD – Electro-optic modulator.

To demonstrate the potential of using this code-tunable device in a systems context, a simple encoder/decoder experiment was set up as shown in Figure 6.5. CW signals from a tunable laser source were fed through an electro-absorption (EA) modulator to generate a 10 GHz pulse train of 20 ps pulse duration before being amplified and passed through an electro-optic (EO) modulator which functioned as a 'pulse picker' to allow for the generation of 20 ps pulses at a repetition rate of 622 MHz. These pulses were reflected off the first code tunable encoder grating. Temporal profiles corresponding to an 8-chip bipolar code (0π00πππ0) were obtained by heating the appropriate wires along the uniform fibre grating in accordance with the phase shift vs. current tuning characteristics shown earlier in Figure 6.3. The figure shows that a π-phase shift could be obtained at a current value of 78 mA. The oscilloscope trace of the encoded waveform after reflecting the 20ps input pulses off the encoder is shown in Figure 6.6(a). At the receiving end, an identical 4cm code-tunable decoder was tuned to the inverse bipolar code (0πππ 00π0) so as to perform the decoding function via matched filtering process. Figure 6.6(b) shows the time response of the decoder when a short 20ps pulse is reflected off the decoder grating.

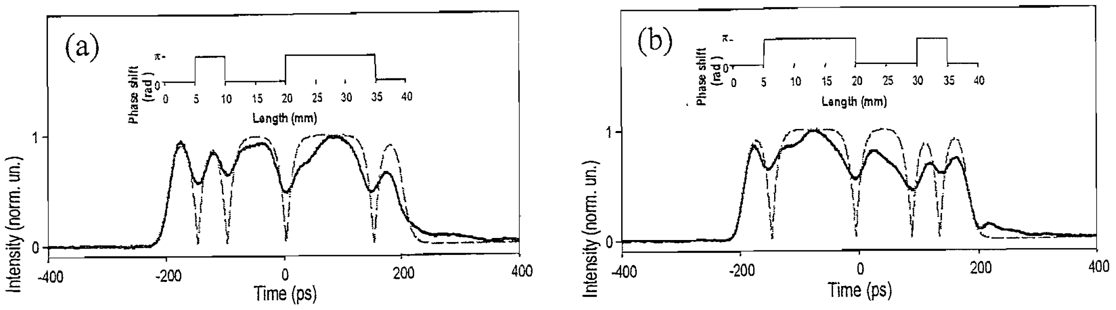

Figure 6.6: Oscilloscope traces (measured: solid line and calculated: dashed line) after reflection off the code tunable grating, (a) encoder (b) decoder, when configured to the bipolar phase code shown in the inset.

When the encoded waveform generated from the first code-tunable encoder grating is reflected off the code-tunable decoder grating with an inverse code to that of the encoder, the autocorrelation (code recognition) output is obtained. Figure 6.7(a) shows the decoded signal obtained using a photodetector and sampling oscilloscope (~20 GHz combined bandwidth). Slight broadening of the decoded pulsewidth can be observed when compared to the theoretically expected decoded pulseform (the theoretical calculations were computed by assuming discrete phase shifts at the boundary of the chip transition compared to the not totally discrete phase shifts generated from the code-tunable grating encoder/decoder and minor uncertainties/variations in the electrical current values applied to the tungsten wires in the experiment).

When the decoder grating is reconfigured to the almost 'orthogonal' code (00ππ 00ππ), the quality of the crosscorrelation could be assessed as well. The result is shown in Figure 6.7(b), again confirming only a slight broadening of the decoded pulseforms compared to the theoretical calculations.

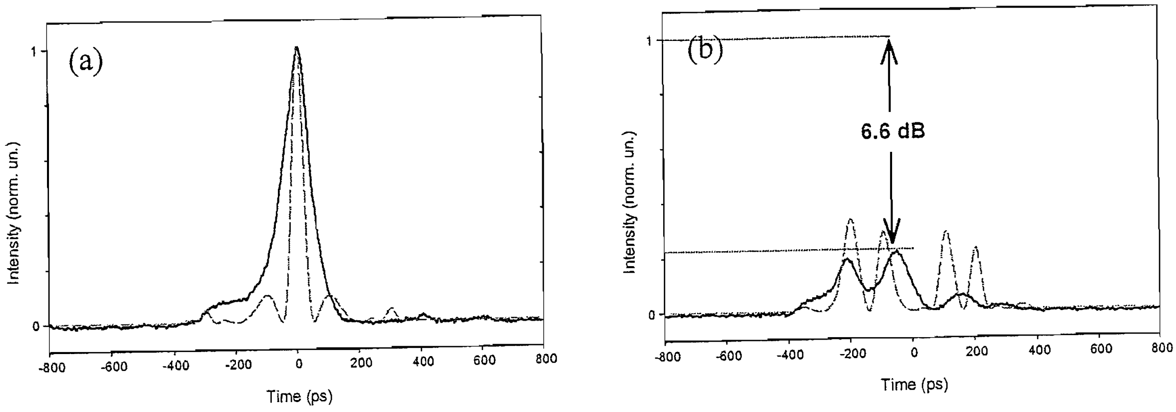

Figure 6.7: Measured (solid lines) and calculated (dashed lines) oscilloscope traces of the matched filtered output after encoding:decoding process for (a) correctly matched code (0π00πππ0:0πππ00π0) (b) incorrectly matched code (00ππ00ππ:0πππ00π0). The measured extinction between the peak autocorrelation pulse with the crosscorrelation sidelobes is 6.6 dB.

The bipolar code-tunable encoder/decoder grating pair was found to be slightly polarisation sensitive. This effect might arise from the fact that the heating wires were not tightly wrapped around the uniform fibre Bragg grating. Consequently, this would cause a radially asymmetric heating at the corresponding chip-transitions.

The above results prove the viability of the proposed approach for the implementation of reconfigurable phase encoders/decoders for DS-OCDMA system. The subsequent section describes an extension of this approach to construct a 16-chip device based on an 8cm uniform fibre Bragg grating that is capable to reconfigure quaternary phase codes. In the experiment, the compatibility of using this code-tunable device together with the decoder based on fixed-code SSFBGs is investigated.

6.5 16-chip multi-level reconfigurable OCDMA phase encoder

The extended 16-chip code-tunable encoder consists of an 8cm uniform fibre Bragg grating having 15 parallel tungsten wires (18μm in diameter) positioned 0.5cm apart along the fibre grating with the first wire being placed 0.5cm from the start of the grating. A 16-chip phase code-tunable device with a chip duration of 50ps is obtained. For this experiment, the phase code-tunable encoder is required to generate 16-chip code sequences containing up to four distinct phase shifts, according to the quaternary phase coding descried earlier in Chapter Three. The value of the electrical current required to induce the various phase shifts in the back-reflected light is predetermined through measurements of the dynamic spectral behaviour of the grating when heated in the centre of the grating (see Figure 6.4). From these measurements, the electrical currents required to generate 0.5π, π and 1.5π are 30mA, 60mA and 90mA respectively.

The code-tunable device is use as the encoder in an optical code generation and recognition set up shown in Figure 6.8, while the decoders consist of fixed-code SSFBGs (denoted by Q1* and Q2*), used earlier in experiments described in Chapter Five. A 10 GHz pulse train (pulse duration 20ps) was generated using an electro-absorption modulator (EAM) fed by a CW laser operating at 1548nm. This pulse train was then gated down and simultaneously modulated with 2^7-1 pseudorandom electrical data generated from a pseudorandom pattern generator (PPG), with a mark space ratio of 8:1 (622 Mbit/s) using an electro-optic modulator (EOM). By independently controlling the electrical current flow at each wire heater within the code-tunable encoder, four–level phase shift keyed (quaternary) code can be obtained and can be encoded onto the input pulse stream by reflecting it from the grating via a circulator. The encoded waveform has duration of ~800ps, and contains the temporal profile of the 16-chip quaternary phase code. At the receiving end, the encoded signal is split into two channels using a 3 dB coupler, with each channel containing a fixed superstructure grating with a 16-chip quaternary phase-code profile written into it. The phase modulation profiles used to write the two 16-chip SSFBG decoders, Q1* and Q2* are shown in Figure 6.9.

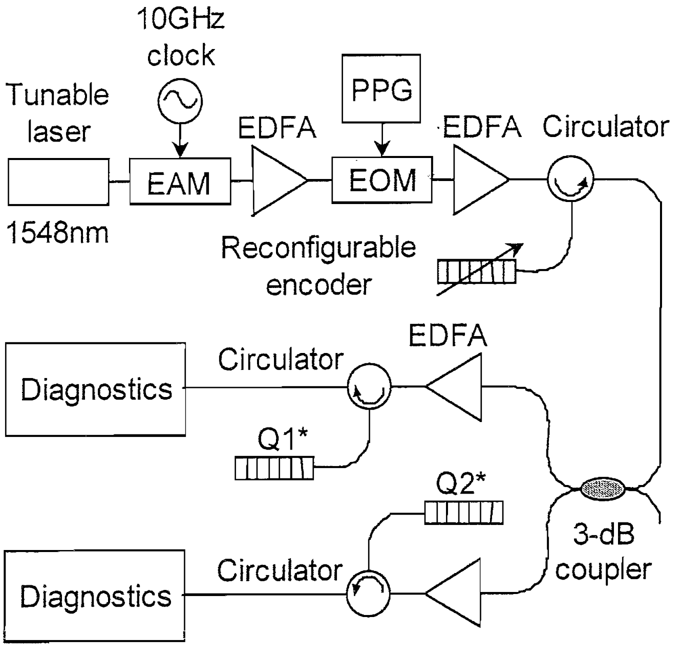

Figure 6.8: Experimental set up. Q1 and Q2* are fixed-code SSFBGs.*

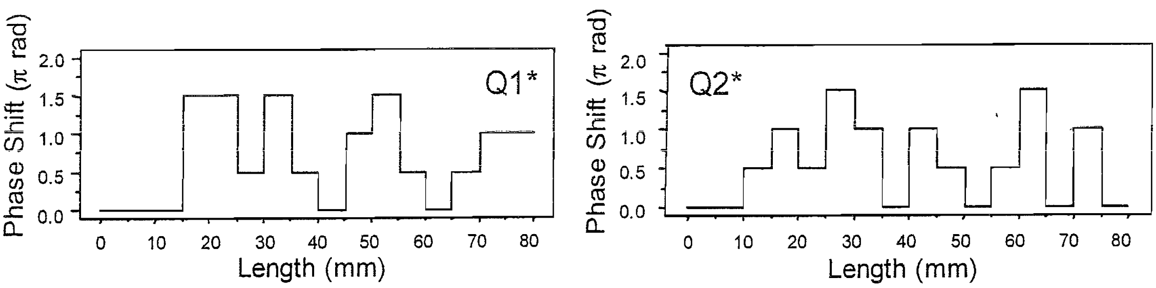

Figure 6.9: Phase modulation profile imprinted onto the fixed-code SSFBG during the writing process for decoders Q1 and Q2*.*

In this experimental setup, the code-tunable encoder can be programmed to produce an encoded code that matches either one of the fixed gratings. The autocorrelation signatures (correctly matched code) and the cross-correlation signatures (incorrectly matched code) of the decoded output signal after reflection from the decoder grating in both channels can be measured simultaneously. The results are shown in Figure 6.10 (using decode grating Q1*) and Figure 6.11 (using decode grating Q2*). Both figures also show the measured extinction between peak autocorrelation pulse and peak crosscorrelation sidelobes.

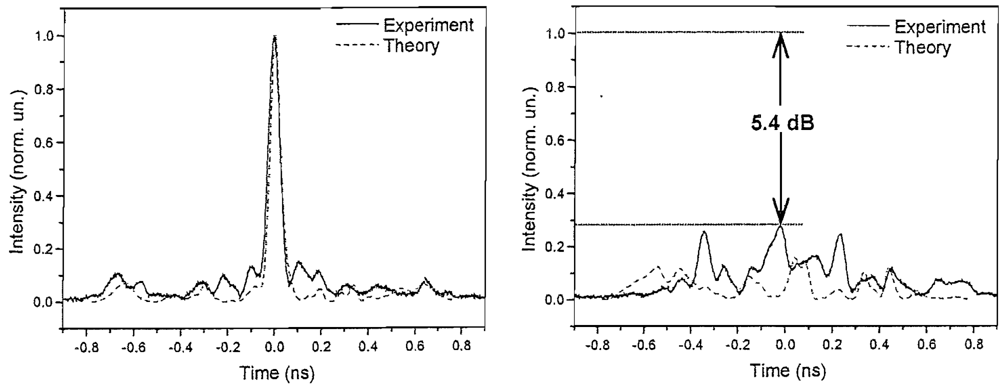

Figure 6.10: Oscilloscope traces of the decoded autocorrelation (left) and the crosscorrelation (right) outputs when the quaternary phase code-tunable encoder is programmed to generate Code Q1 (0, 0, 0, 1.5π, 1.5π, 0.5π, 1.5π, 0.5π, 0, π, 1.5π, 0.5π, 0, 0.5π, π, π). Code Q1 is the matched filtered code to Q1. The measured extinction between the peak autocorrelation pulse with the crosscorrelation sidelobes is 5.4 dB.*

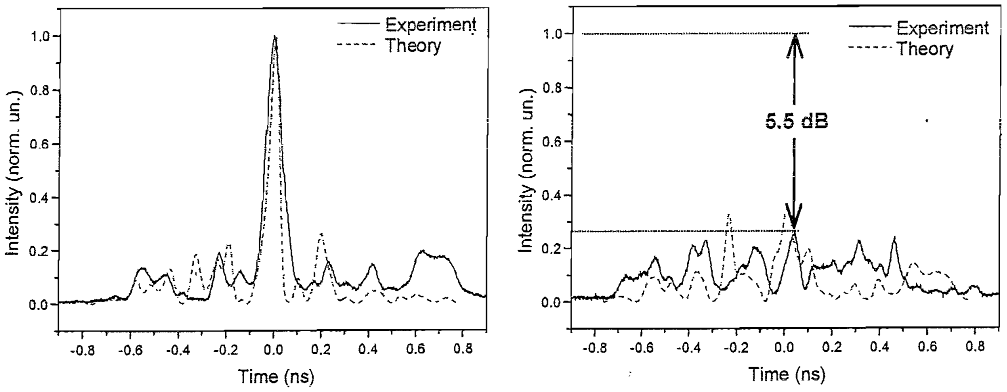

Figure 6.11: Oscilloscope traces of the decoded autocorrelation (left) and the crosscorrelation (right) outputs when the quaternary phase code-tunable encoder is programmed to generate Code Q2 (0, 0, 0.5π, π, 0.5π, 1.5π, π, 0, π, 0.5π, 0, 0.5π, 1.5π, 0, π, 0). Code Q2 is the matched filtered code to Q2. The measured extinction between the peak autocorrelation pulse with the crosscorrelation sidelobes is 5.5 dB.*

Figure 6.12 shows the correctly decoded eye diagrams obtained when the code-tunable encoder is reconfigured for both cases: Reconfigurable Q1: Q1* and Reconfigurable Q2:Q2*. Open eyes can be seen for both cases highlighting the excellent code recognition obtained when using the reconfigurable device to generate optical codes that can be recognised using the fixed code SSFBGs.

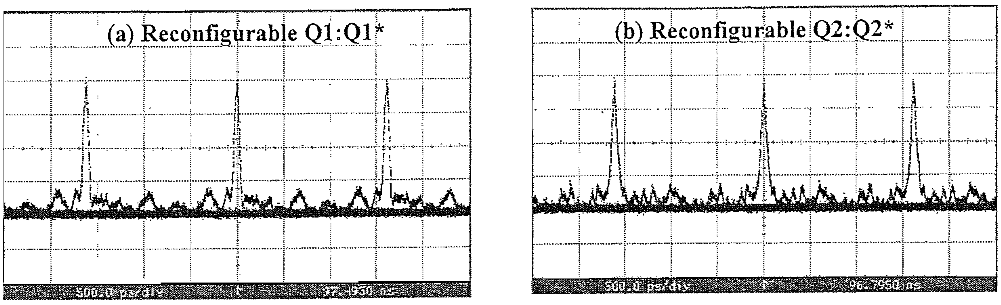

Figure 6.12: Eye diagrams obtained at a data rate of 622 Mbit/s when the code-tunable encoder is set to match the SSFBG decoder (a) Q1 and (b) Q2*.*

Bit-error-rate (BER) measurements were made for the two different quaternary phase codes to assess the performance of the code-tunable encoder as well as its compatibility with decoder SSFBGs. The results are plotted in Figure 6.13. The BER measurements reveal a power penalty of only 2.5dB when compared to the laser back-to-back response and when both the encoder and decoder use fixed-code SSFBGs. This power penalty may stem from the fact that the phase shift induced by the code-tunable encoder is not totally discrete along the grating and minor uncertainties/variations in the electrical current values applied to the wire heaters.

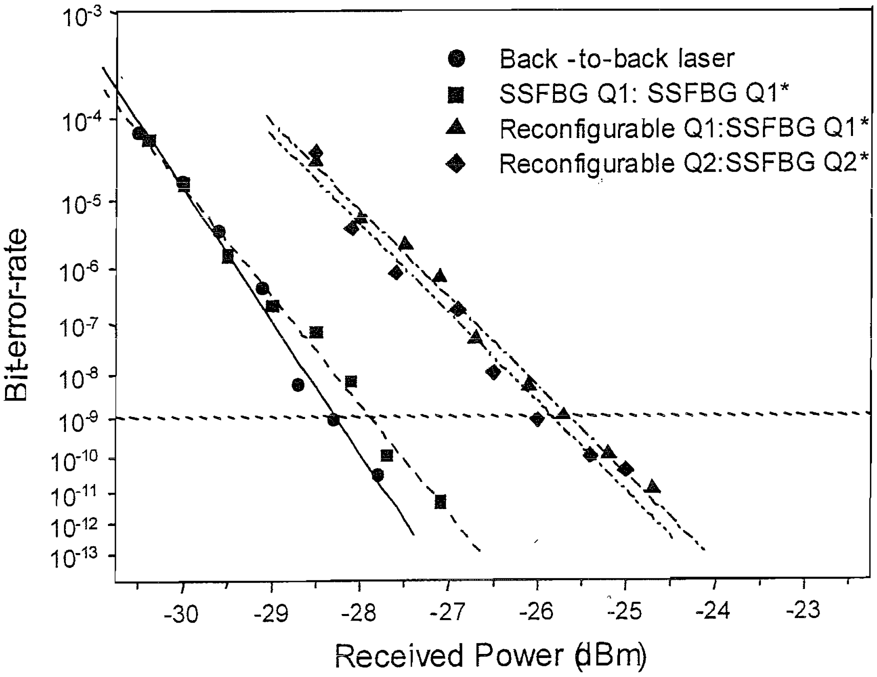

Figure 6.13: Bit-error-rate measurements under the influence of the reconfigurable encoder in comparison to that using a fixed-code SSFBG encoder and also for the back-to-back laser.

6.6 Summary

A relatively simple reconfigurable OCDMA phase encoder/decoder can be constructed from a uniform fibre Bragg grating having fine heating elements deployed at equal intervals along the fibre grating. Such devices offer the advantages of compactness, low cost, fibre-compatible and low fabrication complexity. An initial demonstration to investigate the viability of the reconfigurable device in an 8-chip, 20 Gchip/s bipolar configuration has been presented. This is followed by an extension to the proposed technique using a longer uniform fibre Bragg grating to construct a 16-chip code tunable encoder capable of reconfiguring quaternary phase codes. The reconfigurable device is used in an optical code generation and recognition experiment based on a combination of code-tunable encoders based on a uniform fibre Bragg grating and fixed-code decoders based on SSFBGs. Excellent code recognition results have been obtained and error free operation can be achieved in the BER measurements. Furthermore, such a device can also be strain-tuned over a number of wavelength channels (<2nm to avoid breaking the fibre) making the device useful in an OCDMA/WDM system that is wavelength multiplexed together. Compressive bending [7] of the FBG, which shifts the Bragg wavelength, can be used for tuning of the operating wavelength over a wide range.

The subsequent chapter describes two initial demonstrations of advanced OCDMA architectures that can be used to simplify the network topology and thereby reducing the number of expensive components (for example laser transmitters and fibre links) while allowing the system to be scalable to higher levels of connectivity.

References

[1] P. R. Prucnal, M. A. Santoro, and T. R. Fan, "Spread spectrum fiber-optic local area network using optical processing," *IEEE Journal of Lightwave Technology*, vol. 4, pp. 547-554, 1986.

[2] N. Wada and K. Kitayama, "A 10Gb/s optical code division multiplexing using 8-chip optical bipolar code and coherent detection," *IEEE Journal of Lightwave Technology*, vol. 17, pp. 1758-1765, 1999.

[3] P. Boffi, D. Piccinin, P. Parolari, R. Aldeghi, and M. Martinelli, "Programmable fiber Bragg gratings for spectral CDMA," presented at Conference on Laser and Electro-Optics (CLEO2000), 2000.

[4] L. R. Chen, "Flexible fiber Bragg grating encoder/decoder for hybrid wavelength-time optical CDMA," *IEEE Photonic Technology Letters*, vol. 13, pp. 1233-1235, 2001.

[5] H. Fathallah, L. A. Rusch, and S. LaRochelle, "Passive Optical Fast Frequency-Hop CDMA Communications System," *IEEE Journal of Lightwave Technology*, vol. 17, pp. 397-405, 1999.

[6] A. Othonos and K. Kalli, *Fiber Bragg Gratings: Funcamentals and Applications in Telecommunications and Sensing*: Artech House Inc, 1999.

[7] C. S. Goh, M. R. Mokhtar, S. A. Butler, S. Y. Set, K. Kikuchi, and M. Ibsen, "Over 70nm wideband tuning of fibre Bragg gratings using a compressive bending technique," presented at Optoelectronics and Communications Conference (OECC2002), paper PD-2-1 (postdeadline), 2002.

Chapter 7

OCDMA Architectures

Overview

The thesis have so far described the coding/decoding process using fixed-code SSFBGs encoders/decoders, the use of nonlinearity of the optical fibre to provide an improved code recognition contrast after the simple matched filtering decoding process and the application of code-tunable encoders/decoders based on simple uniform fibre Bragg gratings. This chapter will instead focus on the development of two novel DS-OCDMA architectures that offer increased network capability and functionality, while at the same time reducing costs associated with installing additional equipment. In the bi-directional OCDMA networks, both downstream and upstream[1] coded data channels are transmitted using the same fibre link so that the cost of installing additional and separate fibres for both data streams can be eliminated. In the clock distribution OCDMA architectures, the downstream signals consist of coded channels as well as optical pulse trains. These clock pulses will be used at the receiving end for upstream transmission. Such implementations do not require expensive laser transmitters to be installed at the users' end.

---

[1] **Downstream** data refers to information data that is being transmitted to the user from the central broadcast station while **Upstream** data refers to information transmitted from the user back to the central broadcast station.

7.1 Bi-directional Spectrally Interleaved OCDMA/WDM

In general, uplink and downlink data channels are transmitted using separate optical fibre links. However, as the transmission spans approaching several kilometres in a typical access network, the costs of installing additional fibres become significant. It is highly desirable to use as few existing fibres on the ground as possible and it would be advantageous to minimize the requirement for additional fibre links by adopting a bi-directional configuration to carry both uplink and downlink data channels on the same fibre.

7.1.1 Proposed bi-directional architecture

Such bi-directional configurations can be applied in an OCDMA system. Figure 7.1 shows a block diagram of the proposed implementation. Data communications between the subscriber (user) and the central broadcast station is achieved by just using a single fibre link. In our proposed architecture, the upstream OCDMA channels are spectrally interleaved between adjacent downstream OCDMA channels in order to make efficient use of the fibre bandwidth and also to eliminate the need to allocate separate fibres for uplink and downlink channels. This spectrally interleaved bi-directional configuration can also be integrated into the OCDMA on WDM approach to further increase the functionality and capacity of the system.

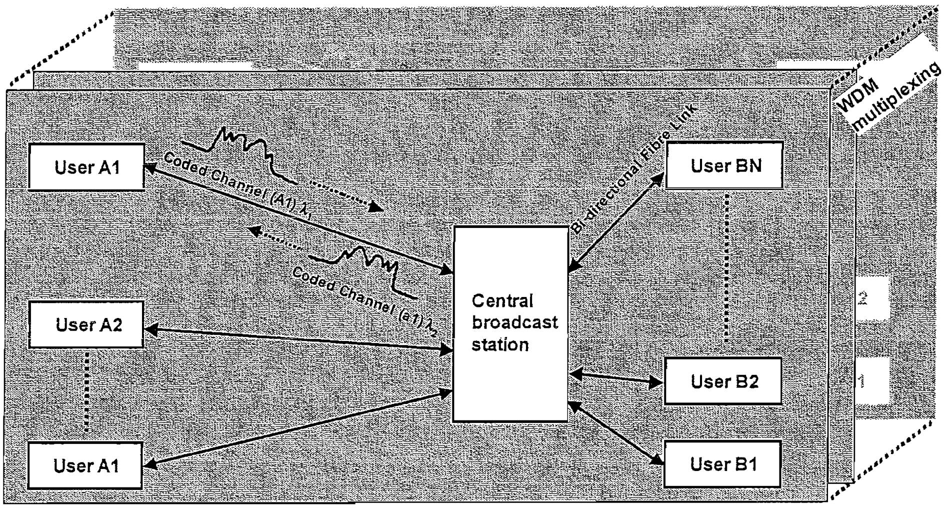

Figure 7.1: Block diagram showing the bi-directional spectrally interleaved OCDMA system on WDM architecture.

To investigate the viability of the proposed architecture, a test bed consisting of an eight-channel full-duplex bi-directional spectrally interleaved OCDMA/DWDM access network based on four-level phase encoded SSFBGs coders/decoders was constructed. Each link (upstream or downstream) comprised four wavelengths containing two OCDMA coded channels on each wavelength (4 WDM x 2 OCDMA giving a total of eight coded channels on each link). Most importantly, the application of the inherent wavelength selectivity of the coding SSFBGs to perform DWDM filtering at both OCDMA encoders and decoders was used to eliminate the need for additional wavelength filtering components (such as AWGs [1], Fabry-Perot filters [2, 3] or interleavers based on fibre gratings [4, 5]) that are generally required to separate the multiplexed DWDM data signals.

7.1.2 Experimental Results

The experimental set-up used to demonstrate the bi-directional OCDMA/DWDM network is shown in Figure 7.2. Eight continuous-wave (CW) lasers, separated in frequency by 50 GHz are used to generate eight DWDM channels (denoted by λ_1 - λ_8). The combined DWDM channels are directed into an Electro-Absorption (EA) modulator that was driven with a 10 GHz sinusoidal signal in order to produce 10 GHz, 20 ps DWDM pulse trains. These pulse trains were then split using a fibre coupler to generate the upstream and downstream links. The downstream DWDM pulse trains were gated down to 622 MHz and modulated with a 2^7-1 pseudorandom data sequence using a $LiNbO_3$ intensity modulator so as to generate 20 ps, 622 Mbit/s data streams. These modulated pulse trains were reflected from an array of eight 16-chip, 50 ps quaternary phase coding gratings: two different OCDM codes (Q1 and Q2) centred on odd wavelengths, denoted by λ_1, λ_3, λ_5 and λ_7 so as to generate eight separate coded data channels (2 OCDM x 4 DWDM on a 100 GHz grid). The profiles of these SSFBGs have been discussed earlier in Chapter 5. Note that no additional wavelength filtering components are required to separate the individual 50 GHz DWDM signals before encoding since each SSFBG simultaneously performs code generation and DWDM wavelength selection with ~ 18 dB of extinction between adjacent 50 GHz DWDM wavelengths (see Figure 7.2). All the eight coded channels generated from the array of SSFBGs were combined and then transmitted over a distance of 44km in non-zero dispersion shifted fibre (NZDSF) having a total dispersion of 118.8 ps/nm. The transmitted data streams were then split using another fibre coupler and fed onto two decode gratings matched to the particular codes and wavelengths of interest.

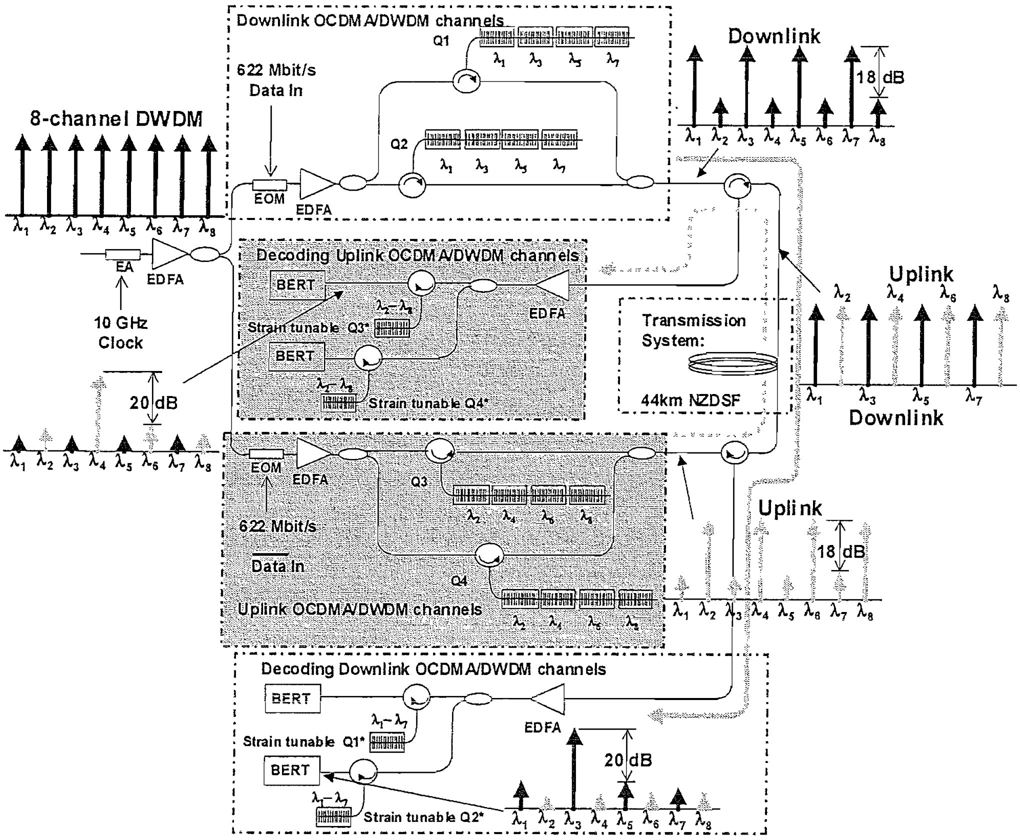

Figure 7.2: Full-duplex bi-directional spectrally interleaved OCDMA/DWDM experimental set-up. Q1-Q4: SSFBGs matched to the DWDM wavelengths. The schematics show the DWDM wavelength filtering using SSFBGs at various points along the system.

Similarly, the other output (upstream) was gated and modulated with the complementary data at the same data rate before being reflected from another array of eight coding gratings comprising two OCDM codes (Q3 and Q4) centred on even wavelengths, denoted by λ_2, λ_4, λ_6 and λ_8 for upstream link. All the eight coded upstream signals were then combined and transmitted from the opposite end of the same NZDSF. Again, two decode gratings were included at the receiving end, matched to the particular codes and wavelengths of interest. In this implementation, the upstream coded channels are spectrally interleaved between the adjacent 100 GHz downstream coded channels as illustrated in Figure 7.2. The performance of both upstream and downstream pairs of OCDM coded channels can be simultaneously analysed by measuring the bit-error-rate performance of both the upstream and downstream coded channels.

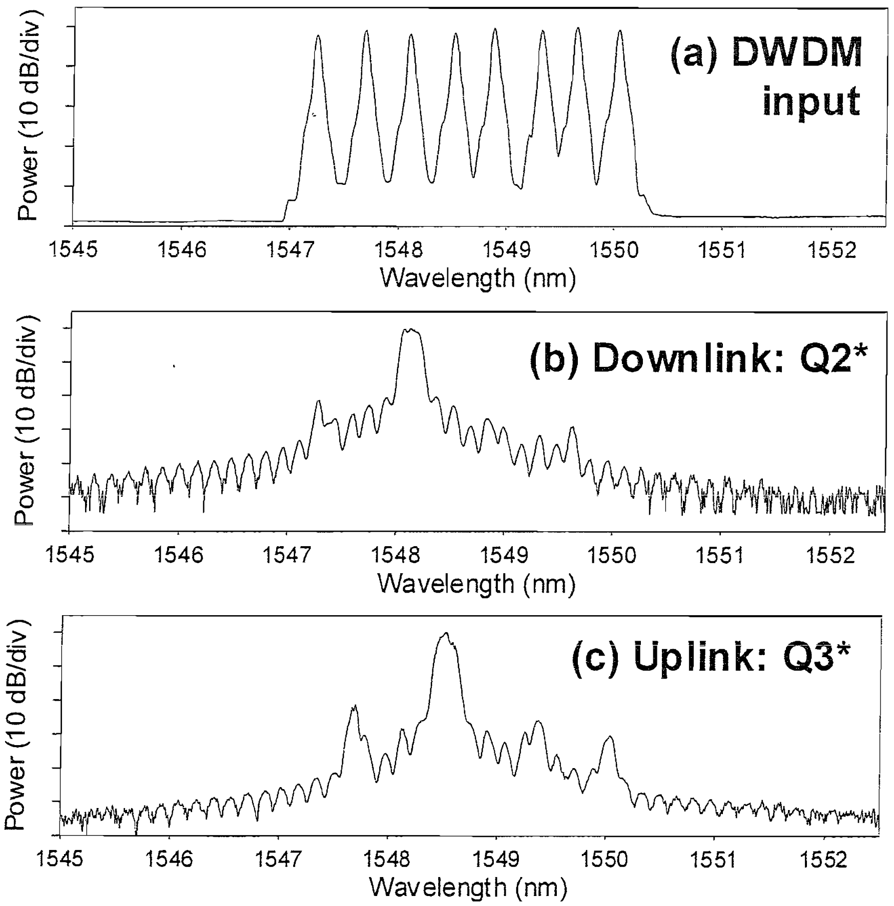

Figure 7.3: (a) Combined eight DWDM wavelengths separated in frequency by 50 GHz. (b) Downstream optical spectra obtained after matched filtering with decode grating Q2. (c) Similar upstream results after matched filtering with grating Q3*.*

The optical spectrum of the eight DWDM wavelengths separated in frequency by 50 GHz is shown in Figure 7.3(a). Figure 7.3(b) shows the optical spectrum of the downstream decoded response after matched filtering using grating Q2*. An extinction ratio of ~ 20 dB between adjacent 100 GHz OCDMA wavelength channels is obtained. Similar extinction ratios are observed for the upstream decoded response after matched filtering using grating Q3* as shown in Figure 7.3(c). The above optical spectra show that the inherent wavelength selectivity of the SSFBG can be used both to provide DWDM wavelength 'drop' function as well as the OCDMA decoding function for the 'in-band' signals, eliminating the requirement for additional wavelength channel filtering elements at the receiver. Clean eye diagrams were obtained at the data rate of 622 Mbit/s for the downstream link in the presence of eight active coded channels as illustrated in Figure 7.4(a). Figure 7.4(b) shows the similar eye diagram obtained for the upstream direction. (Note that the low level pedestal observed on both sides of the decode pulseforms after simple matched filtering alone could easily be eliminated by incorporating a nonlinear thresholding device after each decode grating [6]).

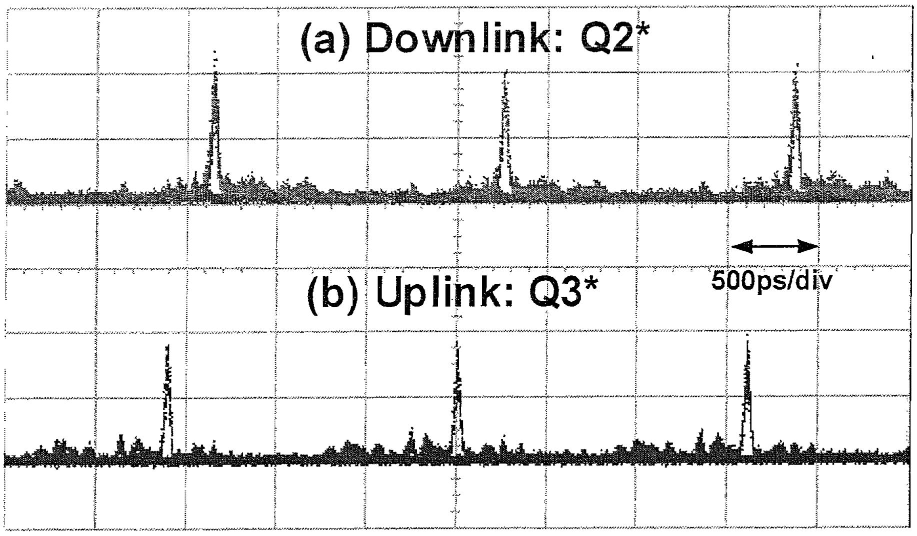

Figure 7.4: (a) Downstream decoded eye diagram after matched filtering with grating Q2 at the data rate of 622 Mbit/s. (c) Similar upstream eye diagram after matched filtering with grating Q3*. The correctly decoded pulseforms have duration of 50ps.*

The performance of the full-duplex OCDMA/DWDM bi-directional system was characterized by measuring the bit error rate (BER) of both upstream and downstream channels versus the total optical power at the receiver. These results are plotted in Figure 7.5. Error free performance is obtained for all the measured channels with ~ 3 dB power penalty when compared to the laser back-to-back measurement for both upstream and downstream transmissions. The main contribution of this power penalty comes from the multiple access interference of the remaining other coded channel on the same wavelength. Most importantly, no power penalty is observed when comparing both upstream and downstream channel performances. If some sort of nonlinear thresholding is introduced at the receiver, significant improvements in both system performance and capacity both in terms of number of simultaneous users per wavelength and data rate per OCDMA channel can be obtained [7, 8]. Again though, there would be a cost in terms of system complexity and practicality.

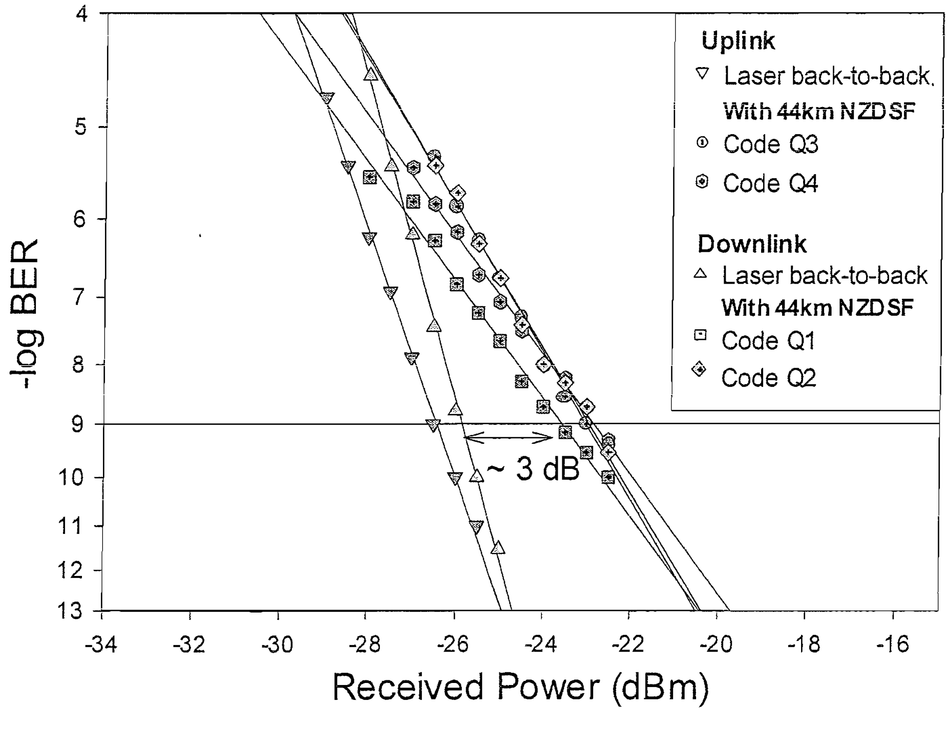

Figure 7.5: BER measurements for bi-directional OCDMA/DWDM experiment at a data rate of 622 Mbit/s.

7.2 Clock Distribution OCDMA Architecture

This section describes another novel OCDMA architecture that eliminates the requirement for expensive laser transmitters to be installed at the users' end by simultaneously transmitting both OCDMA coded signals and clock pulses from the central broadcast station to the users (subscribers). These clock pulses will be used at the users' end to generate a coded data streams for uplink transmission. Furthermore this architecture also utilises the bi-directional configuration to further reduce costs associated with installing additional fibre links.

7.2.1 Proposed clock distribution architecture

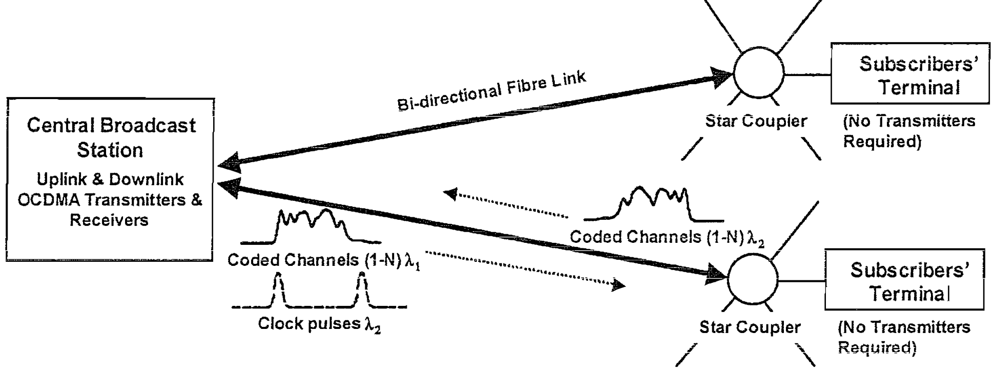

Figure 7.6: Schematic showing the proposed clock distribution OCDMA architecture.

Figure 7.6 shows a schematic of the proposed architecture. The optical pulse sources for both downlink and uplink transmission are located at the central broadcast station. Coded OCDMA channels and uncoded clock pulses on a separate wavelength are wavelength division multiplexed and transmitted down the fibre link. Each coded channel comprises coded data bits that can only be received by users with a decoder grating with a matched filter response corresponding to that of the coded data bits and will not be received by other users. At the receiving end matched filtering is used to decode the desired channel. Users transmitting information back to the broadcast station modulate their data onto the clock pulses and then optically encode the bits to generate a coded upstream channel. The coded channels are transmitted back to the broadcast station using the same fibre link. This architecture has the advantage that all the optical transmitters are located in the broadcast station facilitating the maintenance and repair of the system and reducing the overall cost of equipment at the user end.

An initial experiment to demonstrate this architecture is described below. The demonstration also includes the use of a code-tunable encoder based on a simple uniform fibre Bragg grating with thin wire heaters to demonstrate the added reconfigurable functionality that can be obtained when using a code-tunable device in such architecture.

7.2.2 Experimental Results

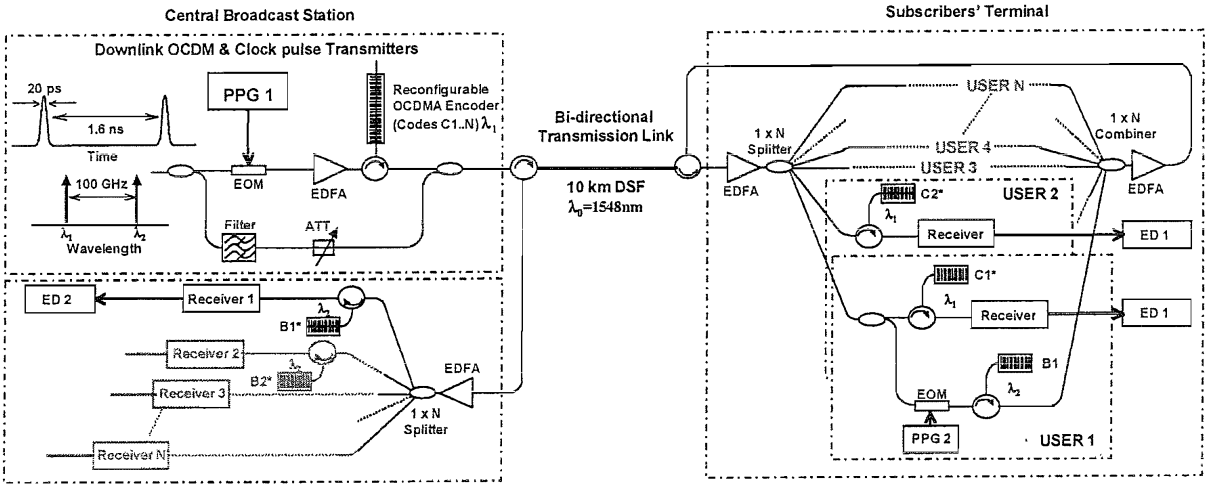

Figure 7.7: Experimental setup to demonstrate the bi-directional, clock distributed OCDMA architecture. PPG – Pseudorandom Pattern Generator, ED – Error Detector, EOM – Electro-optic Modulator, ATT – optical attenuator.

Figure 7.7 shows the experimental setup used to demonstrate the proposed bi-directional, clock distributed architecture. Two WDM channels (denoted by λ_1 - 1547.8nm and λ_2 – 1548.6nm, separated in frequency by 100GHz) comprising 622MHz, 20ps pulse trains were first split using a fibre coupler. In one path the pulse trains were modulated with a 2^7-1 pseudorandom data sequence using an electro-optic modulator to generate 20ps, 622 Mbit/s data streams. These data streams were then reflected from a 16-chip, 20Gchip/s 4-level phase code-tunable device based on a uniform fibre Bragg grating, centred on λ_1. The device has a total length of 80mm with 15 parallel tungsten wires (18um diameter) positioned 5mm apart along the fibre grating. Each of these wires was supplied with a predetermined electrical current to generate the required 4-level phase shifts that define the particular code. The details of this code-tunable encoder have been discussed earlier in Chapter Six. The code-tunable device is capable of generating 800ps coded data streams comprising 16-chip quaternary phase shift keyed code sequences from the 20ps input pulses. The other wavelength channel (λ_2) is not reflected due to the inherent wavelength selectivity of the code-tunable grating (3 dB spectral width of the grating reflectivitiy spectrum is ~0.32nm) and is rejected from this part of the system.

On the other path, the pulse trains at λ_1 were filtered out using a 0.3nm bandpass filter centred at λ_2. The 622 Mbit/s coded data streams at λ_1 and the 622 MHz clock pulses at λ_2 were then combined into a single fibre using another fibre coupler. The average energy-per-bit for both channels was kept constant by adjusting the optical attenuation experienced by the clock pulses. Figure 7.8(a) shows the optical spectrum of the multiplexed 622 Mbit/s coded OCDMA channel and the 622MHz clock pulse channel. The signals were then transmitted over the bi-directional link, which comprises a 10km DSF with a zero dispersion wavelength at 1548nm, before being split and broadcast to all users at the receiving end.

At each user's terminal, the signal was first split using a fibre coupler. One path is used to decode the coded OCDMA channel at λ_1 using a matched-filter decoder SSFBG. For example, when the code-tunable device is programmed to generate a coded signal C1, the output after reflection from the decoder SSFBG C1* at the User 1 terminal exhibits a sharp, dominant pulse-like feature (see Figure 7.9(a)). The decoder SSFBG has a fixed superstructure profile of code C1* written into it during the grating writing process [3]. (Note that the notation Cn* indicates that the code is a matched response to the code Cn generated from the reconfigurable encoder). For all the other users in the network, only low-level unmatched signals are obtained at this receiver. Figure 7.8(b) shows the optical spectrum of the decoded signal after matched filtering using decode grating C1* centred at λ_1. No additional filters are required to reject the clock pulses at λ_2 since the decode SSFBG is also wavelength selective and exhibits an extinction ratio of ~40 dB. On the other path, the 622 MHz clock pulses (λ_2) are modulated with a 2^7-1 pseudorandom data sequence using an electro-optic modulator so as to generate the uplink data streams destined for the central broadcast station. The modulated data streams at 622 Mbit/s were then optically encoded by reflection from another 16-chip quaternary phase coding SSFBG B1 centred at λ_2 so as to obtain 800ps OCDMA coded signals. In this instance, the coded downlink OCDMA data stream at λ_1 was rejected after reflection from the encoder grating B1. The uplink coded data streams at λ_2 from all other users in the terminal were combined and transmitted back to the central broadcast station using the same fibre link. These coded channels were split and decoded at the broadcast station using similar 16-chip decoder SSFBGs B1* - Bn* centred at λ_2, matched accordingly to the encoder SSFBGs B1 - Bn. Figure 7.8(c) shows the optical spectrum obtained after matched filtering using decode grating B1* at the broadcast station. Optical circulators were used in the transmission link to enable a full-duplex bi-directional link between the broadcast station and the subscribers' terminal.

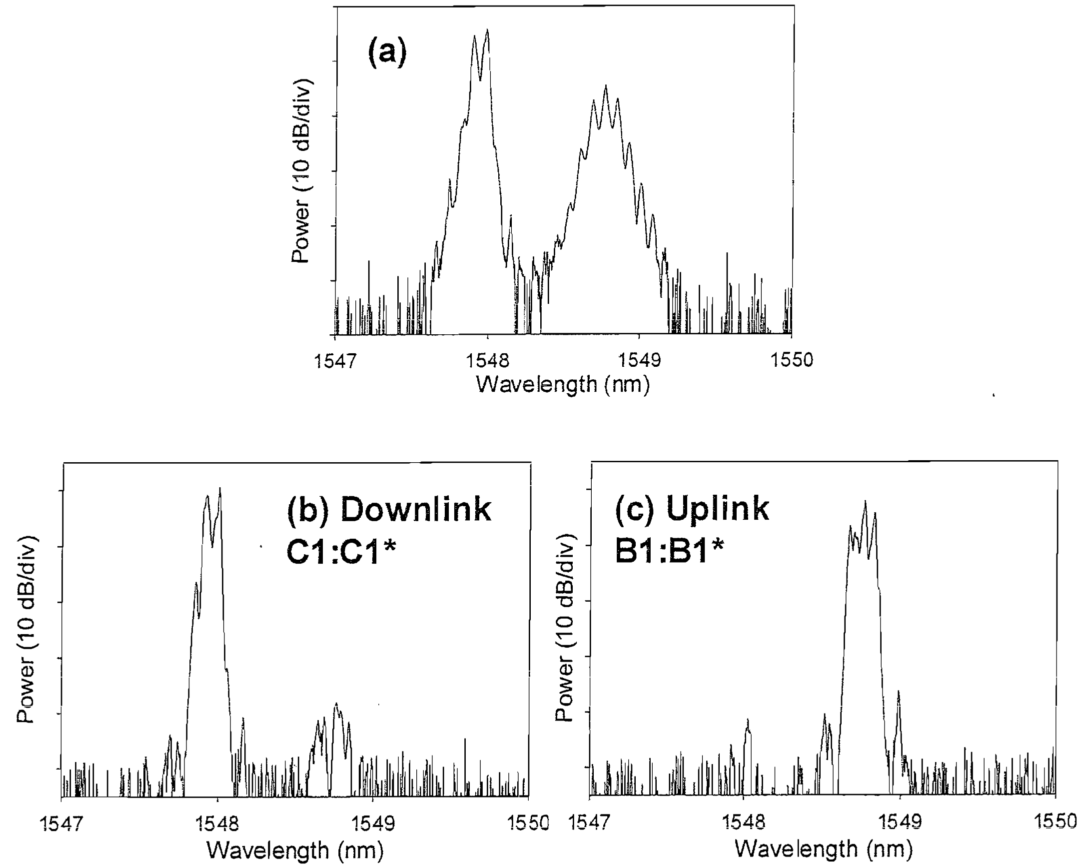

Figure 7.8: Optical spectra showing (a) the combined 622 Mbit/s OCDMA coded channel and 622 MHz clock pulses, (b) the downlink decoded response using decoder SSFBG C1, (c) the uplink decoded response using SSFBG B1*.*

Figures 7.9(a) and 7.9(b) show the downlink autocorrelation signatures obtained after matched filtering using SSFBG C1* λ_1 and C2* λ_1. Note that the decoded pulsewidths have slightly broader durations due to the fact that the phase-shift induced by the reconfigurable encoder is not totally discrete along the grating and minor uncertainties/variations in the electrical current values applied to the tungsten wires. Figure 7.9(c) shows the uplink autocorrelation signature obtained after matched filtering using SSFBG B1* at λ_2.

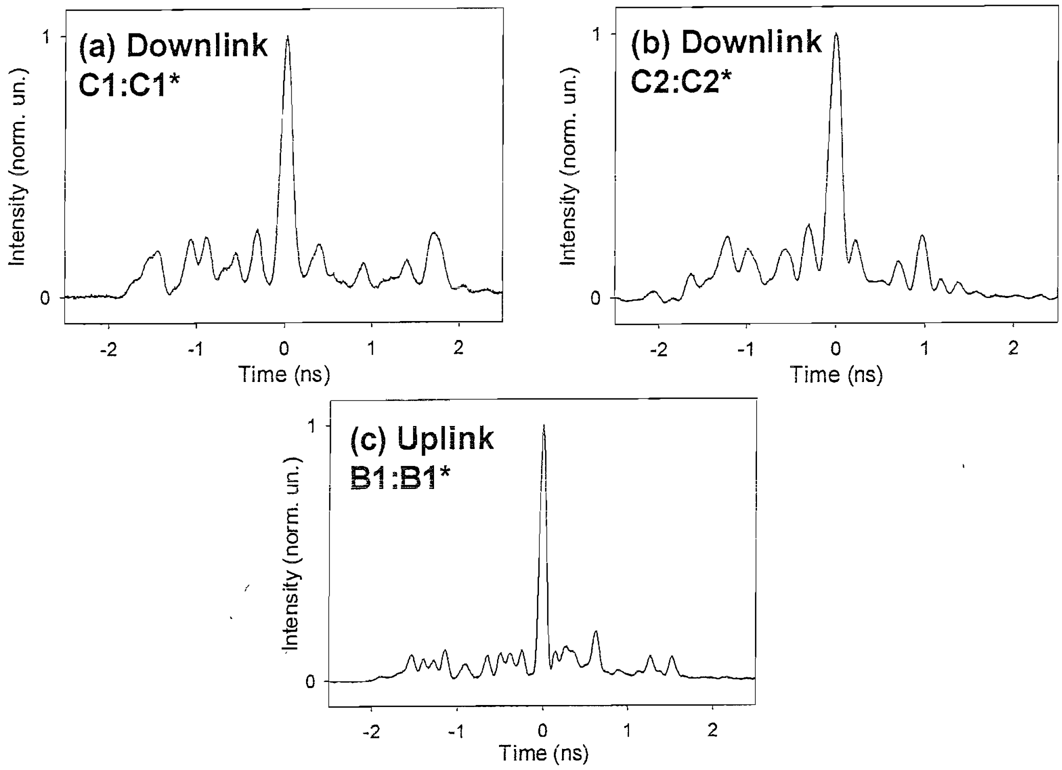

Figure 7.9: Oscilloscope traces after matched filtering for (a) code-tunable C1:SSFBG C1, (b) code-tunable C2:SSFBG C2* and (c) SSFBGs B1:B1*. The measured resolution is 20ps for all three cases.*

Next, the eye diagrams for both downlink and uplink channels after decoding using SSFBGs C1*, C2* and B1* respectively are obtained and shown in Figure 7.10. Clean, open eyes can be seen for all three cases.

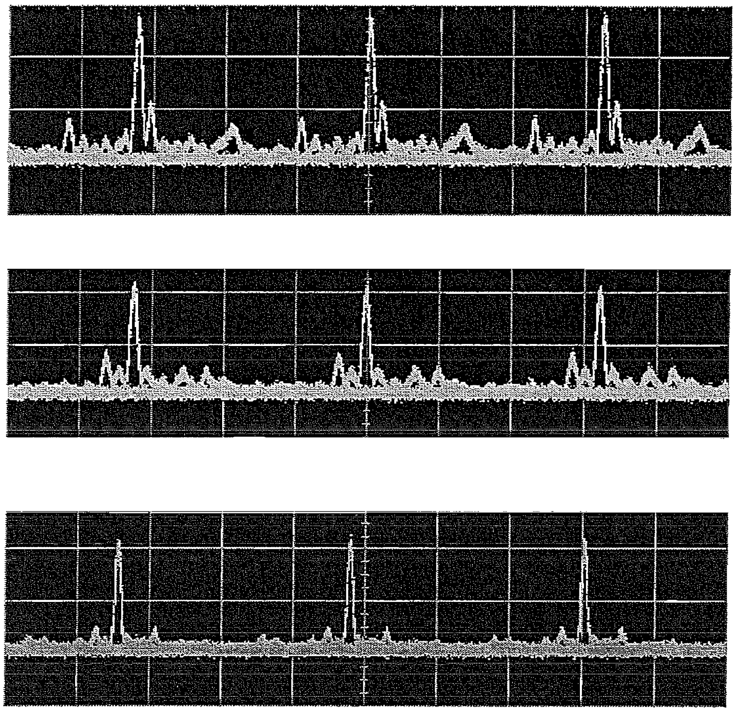

(a) Downlink C1:C1*

(b) Downlink C2:C2*

(c) Uplink B1:B1*

Figure 7.10: 622 Mbit/s decoded eye diagrams for both downlink and uplink OCDMA channels.

The performance of both upstream and downstream OCDMA coded channels can be simultaneously analysed by measuring the bit-error-rate (BER) performance. Figure 7.11 plots the various BER measurements made against the received optical power. Error free operation with ~2.5 dB of power penalty can be obtained for downlink channels C1:C1* and C2:C2* when compared to the λ_1 laser back-to-back measurements after transmission over 10km of DSF. No power penalty was observed for the uplink channel B1:B1* when compared to the λ_2 laser back–to-back measured at the user's terminal.

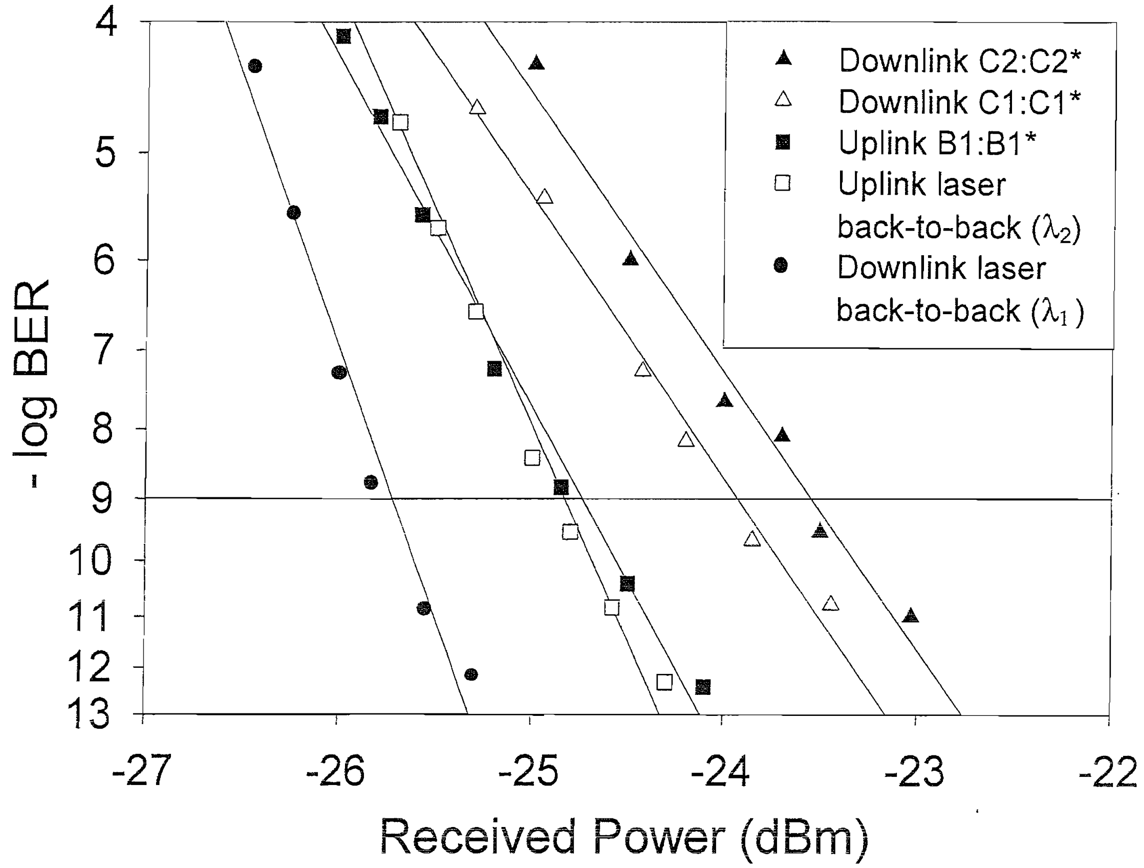

Figure 7.11: BER results when both uplink and downlink channels are transmitting simultaneously at a data rate of 622 Mbit/s.

7.3 Summary

Two novel DS-OCDMA architectures have been proposed and initial experiments to demonstrate these architectures have been carried out. In the bi-directional spectrally interleaved configuration, no additional wavelength filtering components are required to separate the multiplexed WDM signals before OCDMA encoding and decoding since the SSFBGs encoders/decoders were wavelength selective. Error free performance and no power penalty were observed when comparing between upstream and downstream BER measurements, indicating the suitability of using the SSFBG coders/decoders in a bi-directional configuration. The subsequent clock distribution experiment showed that optical clock pulses could be delivered together with the downstream OCDMA coded signals to the receiving users from the central broadcast station. These clock pulses could then be used for uplink OCDMA coded communications eliminating the need for expensive laser transmitters to be installed at the users' end.

The two architectures described here have the potential for implementation within the fibre to the home (FTTH) access systems. In FTTH, a central broadcasting station is connected to all the users via a passive optical network (PON) (the network comprises of some form of passive component, such as an optical star coupler as a remote node). OCDMA implementation has the advantage that asynchronous operation can be supported (eliminating the need for clock synchronisation across the network and timing jitter that exists within the network). New connection to the network can be performed by simply assigning an additional code to the network.

An attractive OCDMA access system should be capable of supporting up to 32 asynchronous subscribers with an operating bandwidth as high as 1 Gbit/s per user for both upstream and downstream links over a distance of several tens of km. This requirement can be readily achieved by using a code length of 1023-chip with a chip duration of T_{chip}~1ps (see Chapter Two Figure 2.9). Note that the current TDM based PON architecture standard specifies a total downstream bandwidth of up to 622 Mb/s and an upstream bandwidth of up to 155 Mb/s having up to 32 users, covering a distance of 20km [9].

References

[1] H. Takahashi, I. Nishi, and Y. Hibino, "10 GHz spacing optical frequency division multiplexer based on arrayed-waveguide grating," *IEE Electronics Letters*, vol. 28, pp. 380-381, 1992.

[2] G. E. Town, K. Sugden, J. A. R. Williams, I. Bennion, and S. B. Poole, "Wide-band Fabry-Perot-like filters in optical fiber," *IEEE Photonic Technology Letters*, vol. 7, pp. 78-80, 1995.

[3] S. Doucet, R. Slavik, and S. LaRochelle, "High-finesse large band Fabry-Perot fiber filter with superimposed chirped Bragg gratings," *IEE Electronics Letters*, vol. 38, pp. 402-403, 2002.

[4] M. Ibsen, P. Petropoulos, R. Feced, P. C. Teh, M. K. Durkin, M. N. Zervas, D. J. Richardson, D. N. Payne, and R. I. Laming, "System applications of fibre Bragg grating technology," presented at Optoelectronics and Communication Conference (OECC2001), paper TUA (Invited), 2001.

[5] M. Ibsen, P. Petropoulos, M. N. Zervas, and R. Feced, "Dispersion -free fibre Bragg gratings," presented at Optical Fiber Communications Conference (OFC2001), paper MC1 (Invited), 2001.

[6] H. P. Sardesai, C.-C. Chang, and A. M. Weiner, "A femtosecond code-division multiple access communication system test bed," *IEEE Journal of Lightwave Technology*, vol. 16, pp. 1953-1964, 1998.

[7] J. A. Salehi and C. A. Brackett, "Code Division Multiple-Access techniques in optical fiber networks-Part II: Systems performance analysis," *IEEE Transaction on Communications*, vol. 37, pp. 834-842, 1989.

[8] J. A. Salehi, A. M. Weiner, and J. P. Heritage, "Coherent ultrashort pight pulse code-division multiple access communication systems," *IEEE Journal of Lightwave Technology*, vol. 8, pp. 478-491, 1990.

[9] ITU-T. *Recommendation G. 983*: Broadband Optical Access Systems based on Passive Optical Networks, 1998.

Chapter 8

Header Generation and Recognition for Optical Packet Switched Networks

Overview

Though the previous chapters have largely focused on the use of SSFBG technology for OCDMA applications, it is to be appreciated that the technology should also find use in a whole range of other network and transport applications in which optical pattern/code generation and recognition are required. In particular, the SSFBG technology is relevant to optical packet-switched network applications for generating and processing optical headers that contain key routing information associated with the data payload. First, a multi-hop optical packet switched system using 255-chip SSFBG coders/decoders is described. Header re-use functionality is also incorporated within the node. A 400 Gbit/s multi-wavelength optical packet switched network node based on header generation and recognition using 16-chip, quaternary phase encoded SSFBGs and switching using fast electro-optic switches is reported next. The multi-wavelength node allows packet processing rates of up to 4 Gigapackets per second (4 Gpps) to be achieved. Finally, a novel self-routing approach to optical packet switched system is proposed and experimentally demonstrated. The self-routing architecture moves the routing decisions to the edge of the network, reducing the optical processing elements that are required within the optical core of the network.

8.1 Introduction to Optical Packet Switching

The topic of optical packet switching has recently received greater attention due to the rapid growth of Internet IP traffic and the need for next-generation Internet router technologies capable of handling data rates of the order of Tbit/s. Optical packet switched networks have the potential to provide these networks with a high bandwidth, flexible core that is well suited to the bursty nature of IP traffic while providing the Quality of Service (QoS)[1] required for supporting both voice and high-definition video transmissions [1-3]. Packet based systems can also be designed to run under a variety of protocols and formats including both Internet Protocol (IP) and Asynchronous Transfer Mode (ATM) protocol. The technology is also capable of supporting a mixture of protocols on one network. Most importantly, optical packet switched systems have the advantage of overcoming the bottleneck associated with the limited processing speed in current electronic based packet routers. Higher processing speed (up to 10 Gigapackets per second (Gpps) and beyond) and network throughput up to 1 Petabit/s[2] [3] should be achievable with optical packet switched systems.

In optical packet switched systems, individual blocks of data, known as ‘payload’ is generally preceded by an optical header that defines its destination. Both the payload and the header combined to make an optical packet. Several configurations for tagging the optical header to the data payload have been proposed and demonstrated. One method is to transmit the optical header in parallel with the data payload, either via subcarrier multiplexing[3] on the same optical channel as the data [2, 4], or on a separate optical channel using wavelength-division multiplexing [5, 6] (see Figure 8.1(a)). The major drawback of adopting subcarrier multiplexing approach is that the required subcarrier frequency is often much higher that the data bit rate, hence higher frequency modulators and receivers are required for supporting data packet rates beyond 10 Gbit/s. The method of assigning a separate wavelength to define the optical header makes an inefficient use of the available fibre bandwidth

---

[1] **Quality of Service (QoS)** refers to certain guarantees on the maximum packet delay as well as the variation in the delay, and guarantees on providing a minimum average bandwidth for each connection.

[2] **Petabit/s** refers to 10^{15} data bits transmitted in a second.

[3] In **subcarrier multiplexing** technique, the optical header is first modulated onto a microwave subcarrier and then onto the same wavelength as the data payload. To recover the optical header, the signal is converted into electrical domain and then high pass filtered to remove the data leaving only the header on the microwave carrier frequency for processing.

since a dedicated wavelength is always required to transmit the header. Alternatively, an optical header can be tagged in serial to the data payload as shown in Figure 8.1(b). A short time-interval, known as the guard band, separates the optical header from the data payload, providing time for the system to start processing the header information before a routing decision is made on the data payload. This method has the advantage that both header and data payload are located on the same wavelength, allowing higher capacities to be achieved when combined with the WDM header multiplexing technique. The rest of this chapter will focus on optical packet switched systems based on this approach (i.e. optical header tagged in serial with the data payload to create an optical packet).

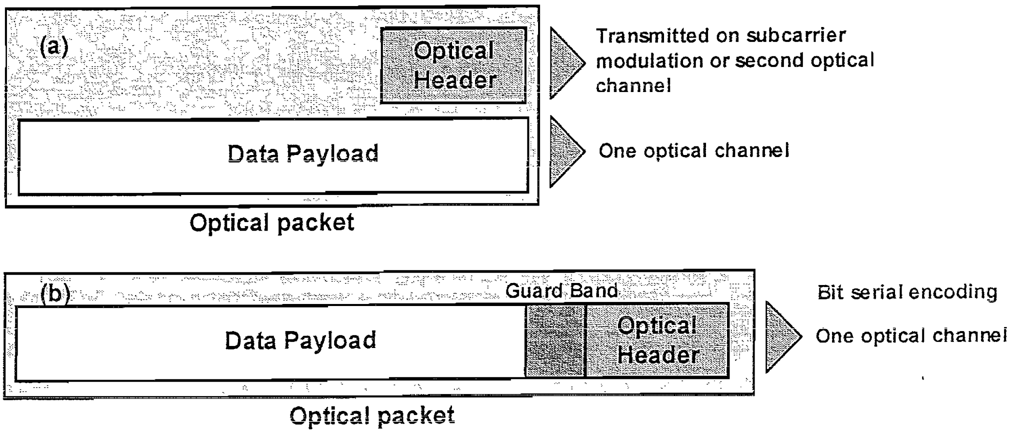

Figure 8.1: An optical packet structure, including both payload and header. (a) The optical header is transmitted in parallel by subcarrier multiplexing or on another optical channel. (b) The optical header is tagged in series with the data payload, separated by a guard band.

An optical packet generally passes through a series of packet routers (nodes) on its way to its destination. Each router reads the header, interprets the destination address, then directs the data packet via a suitable output port towards its intended final destination. Figure 8.2 shows a typical architecture of an optical packet switched router. An incoming data stream made up of a series of data packets is received at the input of the router. A portion of the signal is tapped and enters the header processing section. In the header processor, optical correlation based on matched filtering is performed on all the destination entries in the look-up table, in a parallel fashion. An autocorrelation peak emerges in the bit time duration only where the header codes match, while on the contrary all the other correlations will exhibit crosscorrelation outputs. This relatively intense pulse is supplied to a node controller, which controls the optical switching of the incoming packets. In the other path, the signal passes through an actively controlled optical fibre delay line (for example by stretching a fibre spool with a piezoelectric actuator) to synchronise between the incoming packets with the switching decisions made after processing the header of each packet. Additional functionalities such as header re-labelling and packet add/drop can be included in the router as shown in Figure 8.2

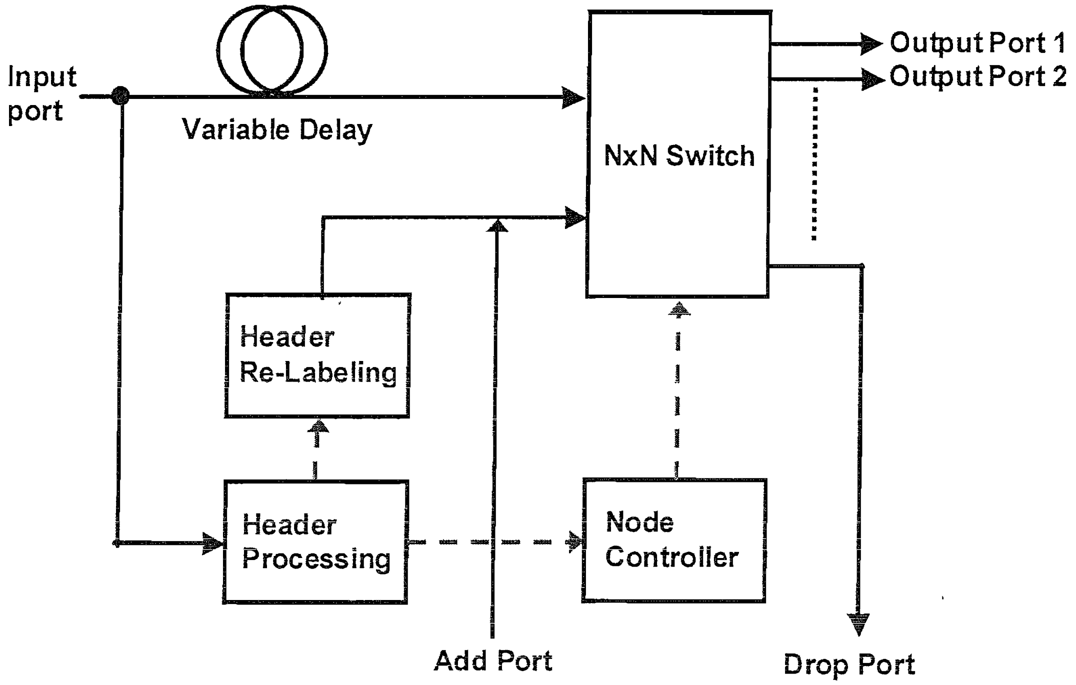

Figure 8.2: Architecture of an optical packet routing node. Dashed lines show electrical connections. Add (drop) ports allow packets to be added into (removed from) the optical networks.

To date, a number of techniques have been proposed to implement the serial optical header generation and recognition based on matched filtering in packet switched networks. One such approach is based on implementing the tapped delay lines and tunable phase shifters monolithically into silicon-on-silicon substrates by using planar lightwave circuit (PLC) technology [3]. The authors have demonstrated the use of such devices to generate an eight-chip bipolar code header for use in a 1x2 photonic label processing demonstration. The PLC approach has the advantage that a single device can be used to generate different headers by adjusting both the delay and the optical phase of the light. However, PLC components are difficult to fabricate and lack the resolution required to support a long coding length (>32 bits). More recently optical headers comprising multiple-wavelength codes generated from arrays of fibre

Bragg grating (FBG) centred of different wavelengths has been demonstrated [7, 8]. ITU-grid wavelength bands were used to generate multi-wavelength headers while the data payload was located on a different wavelength band. Multiple wavelengths based optical labels require a number of wavelengths to generate the optical label (in this demonstration the authors used a supercontinuum (SC) generated pulse source). Such an approach degrades the data to waveband transmission rate ratio and is likely to suffer from scalability and cost issues when more wavelength channels are required. The cost of extending the wavelength channels to the S- and L-band are exceedingly high at the moment.

In view of this, an optical packet switching system based on phase coded SSFBGs (developed for use within coherent direct sequence OCDMA systems) to generate and recognize optical headers that are used to label the packets has been proposed and demonstrated. Phase coded encoders/decoders gratings offer several advantages. They are readily scaled to longer code sequences (255-chip OCDMA codes previously demonstrated in the laboratory) than currently possible using PLCs, low cost, compact and integrate easily with other fiberised network components. Optical packet switching systems based on SSFBGs also make an efficient use of the available bandwidth since both the optical header and data payload are located on the same wavelength and can share the same pulse source for generating both header and data payload. Moreover, due to the inherent wavelength selectivity of the SSFBGs, the technology will allow significant WDM or DWDM multiplexing of optical channels.

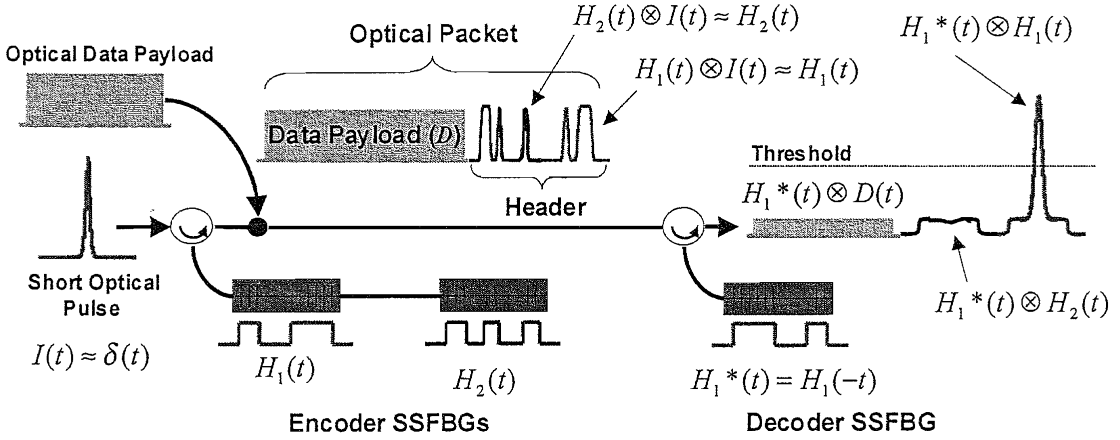

Figure 8.3: Schematic showing the principle of optical header generation and recognition using SSFBGs.

Figure 8.3 shows the outline of the principle of header generation and recognition using SSFBGs. The optically coded header is created by reflecting a short optical pulse ($I(t)$) off the encoder grating. The encoder grating contains the coding information which is written into its spatial refractive index profile during fabrication. The reflected signal is effectively the impulse response of the encoder grating and contains the code. In this illustration two coded headers are generated denoted by $H_1(t)\otimes I(t)\approx H_1(t)$ and $H_2(t)\otimes I(t)\approx H_2(t)$.

Code recognition at the decoder is obtained by matched filtering of the coded signal, using a decoder grating with the time reversed (conjugate) impulse response to that of the encoder grating. In this illustration the coded optical pulse is reflected off a decoding grating containing the code $H_1(t)^*$ that is matched to the coded grating $H_1(t)$. The reflected signal from the decoder grating shows a strong correlation peak when the incoming header code is matched to a decoding grating ($H_1(t)^*\otimes H_1(t)$). When the decoding grating is not matched to the incoming signal the cross-correlation results in a low-level background as is observed for the gratings combination $H_1(t)^*\otimes H_2(t)$. The cross-correlation with the data payload ($H_1(t)^*\otimes D(t)$) also results in a low-level background. An electrical or optical thresholder is used to reject the low-level background terms.

A parallel optical look-up table (similar to the electronic look-up table that exists within standard electrical packet router) can be configured using multiple decoder SSFBGs as shown in Figure 8.4. The optical implementation of the look-up table has the advantage of fast processing speed, hence eliminating the electrical bottlenecks that exist within the electronics router due to the slow electronic processing of the headers. Each decoder grating is designed to provide a matched filtered response to a particular optical header. When correct matched filtering is obtained, (i.e. the incoming header matches one of the decoder SSFBGs), a relatively intense autocorrelation signature is generated by the decoder grating which is then supplied to an optoelectronic converter, for example, a fast-response photodetector, or optionally, through a nonlinear element for pulse shaping [9-12] in order to obtain enhanced header recognition contrast. An electrical square signal is generated in response to the sharp autocorrelation pulse by the square window generator that gates the optical switch for sufficient time to allow the passage of the original data packet (and generally, but not necessarily also the header into the output line). Packet collision control circuit is used to avoid multiple packets on the same wavelength being switched to the same output destination at the same time and preventing more than one output port to be switched due to autocorrelation signals generated from multiple decoders.

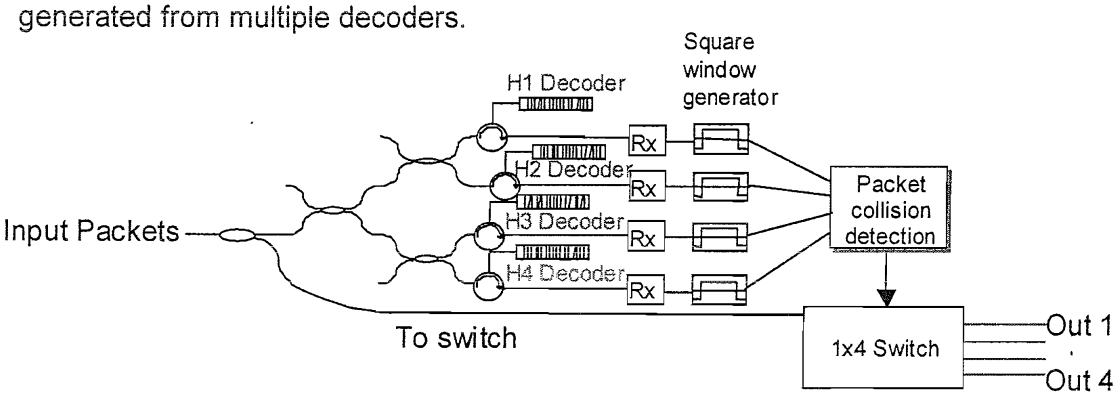

Figure 8.4: Parallel decoder SSFBGs configuration.

The rest of the chapter describes a range of experiments that demonstrates the suitability of using the SSFBG approach to perform the required key task of header generation, recognition and processing in the optical domain for applications in optical packet switched networks.

8.2 255-chip Multi-hop Experiment

This section describes an optical packet switching experiment based on all-optical header generation and recognition using 255-chip, 320 Gchip/s superstructured fibre Bragg gratings and fast switching using lithium niobate ($LiNbO_3$) electro-optic modulators. The experiment also demonstrates a two-hop operation, with header reuse, of a packet add/drop node that may be configured for the packet re-labelling function.

The functionality of the packet switching system, which incorporates a packet transmitter and two switching nodes, is first shown in Figure 8.5. Figure 8.6 shows the experimental configuration used to demonstrate the principle of optical packet switching based on SSFBGs.

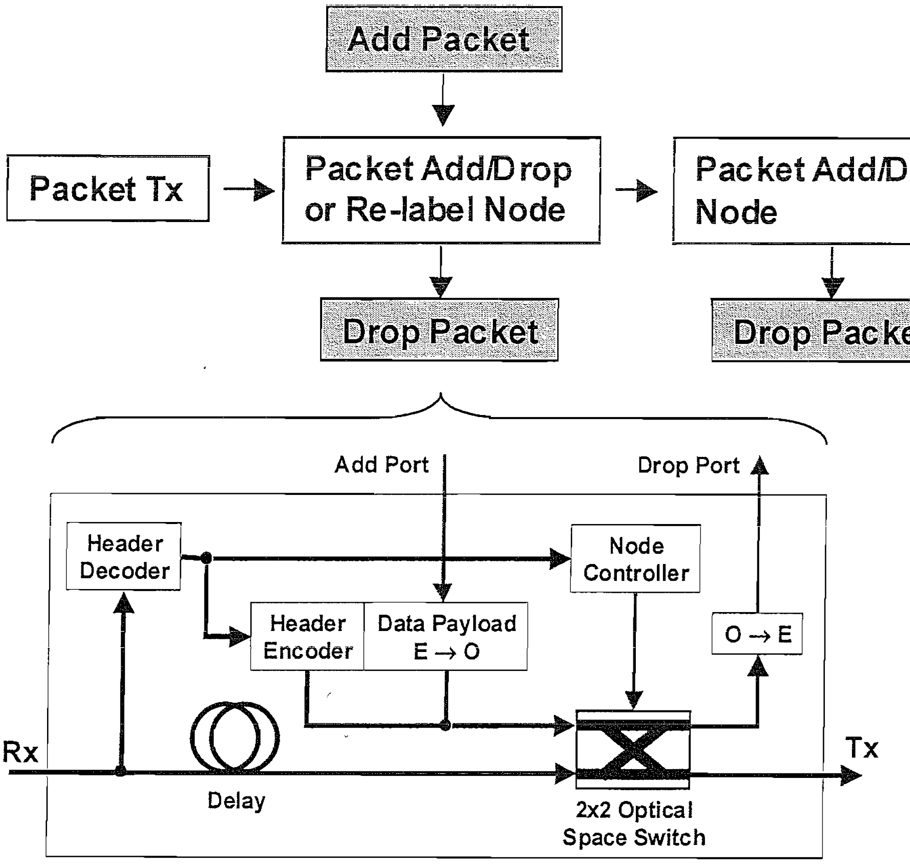

Figure 8.5: Block diagrams showing the optical packet switching experiment. The architecture of the packet add/drop and re-label node is shown inset. Input packets enter the node at Rx and appropriate packets are switched out at Tx.

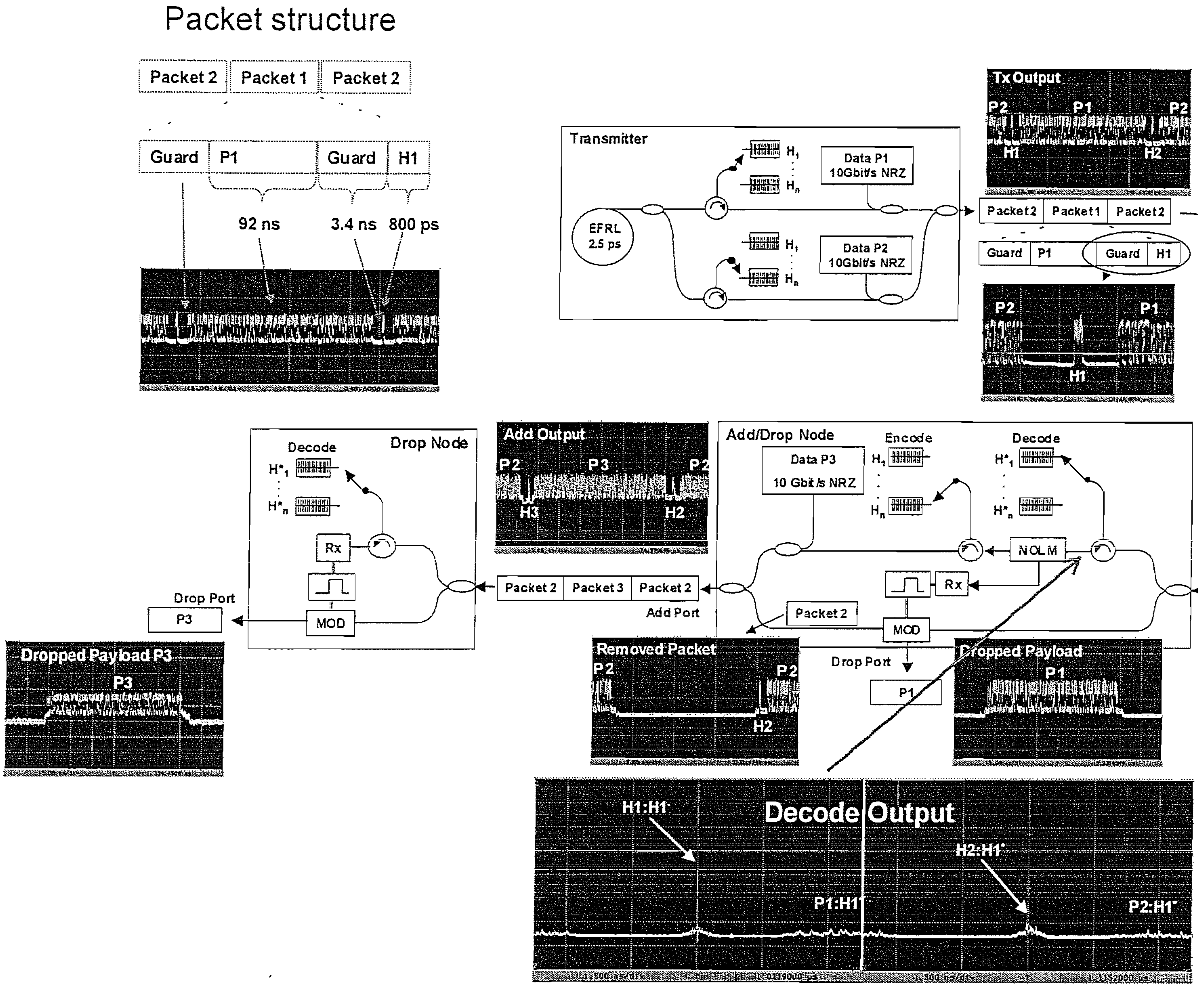

Figure 8.6: Experimental optical packet switching system configuration and associated optical outputs. The packet structure is shown inset.

The packet transmitter generates optically coded header pulses that are inserted in front of the data payload to create an optical packet. The header pulses are generated by a regeneratively mode locked erbium doped fibre ring laser (EFRL) that produces short pulses of 2.5ps duration. These pulses are then optically encoded by reflection from an SSFBG. The SSFBGs used within this experiment contain coding information within their spatial refractive index profile that allow for the generation of 255-chip, 320 Gchip/s quaternary phase coded waveforms. Figure 8.7 shows the phase modulation profile and the measured and calculated spectral reflectivity plots of two SSFBGs (denoted by H1 and H2) used within the experiment. These quaternary codes, obtained from Family A code family have distinct well defined autocorrelation peaks, very low autocorrelation sidelobes and mutually low crosscorrelation properties allowing at least 255 distinct headers to be used for the given code length [13].

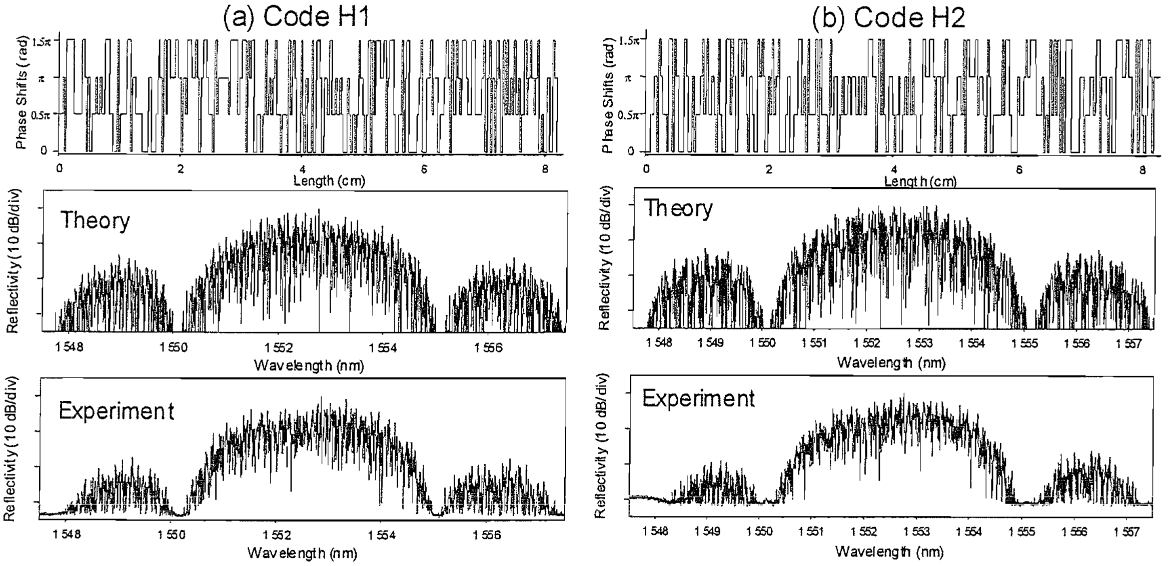

Figure 8.7: Phase modulation profile, measured and calculated spectral reflectivity plots of SSFBG (a) H1 and (b) H2.

The packet structure shown inset in Figure 8.6 consists of the coded header followed by the data payload. The packet switching is transparent to the bit-rate and format of the data payload employed. In this experiment a 10 Gbit/s, PRBS 2^{31}-1, non-return-to-zero (NRZ) data payload that is 924 bits long is used (total payload duration 92.4ns). The header and the data payload are located at the same wavelength, which allows for increased network capacity if WDM techniques are to be additionally employed (the experiment demonstrating this is described in the next section). The packet switching transmitter presented here utilises two distinct data payloads, labelled as P1 and P2, each preceded by a unique header labelled as H1 and H2 as shown at the packet transmitter output in Figure 8.6.

At the add/drop node optical header recognition is performed in order to control the switching of the data. Part of the incoming packet stream is sent to the header decoder that consists of an array of SSFBGs (H1* - Hn*) whose codes are matched to the coding gratings in the transmitter. In this experiment the decoding grating H1* is chosen in order to recognize the incoming Packet 1. Header recognition is carried out by reflecting the incoming packets off the decoding grating H1* which results in a strong correlation peak arising from header H1 (H1:H1*), with some residual background from the crosscorrelation between header H2 and the decoding grating H1* (H2:H1*) and a contribution from the reflected data payloads. Figure 8.6 (Decode Output) illustrates these correlation results.

In order to improve the extinction of the header recognition and to allow for the reuse of the header pulses, all-optical regeneration of the decoded header pulse is carried out using a nonlinear optical loop mirror (NOLM) [10]. Regeneration in the NOLM improved the header extinction to 18 dB. The SHG intensity autocorrelation measurement shown in Figure 8.8 shows that the decoded header pulse is reshaped back to a pulse with the same pulsewidth as the original 2.5ps input pulses.

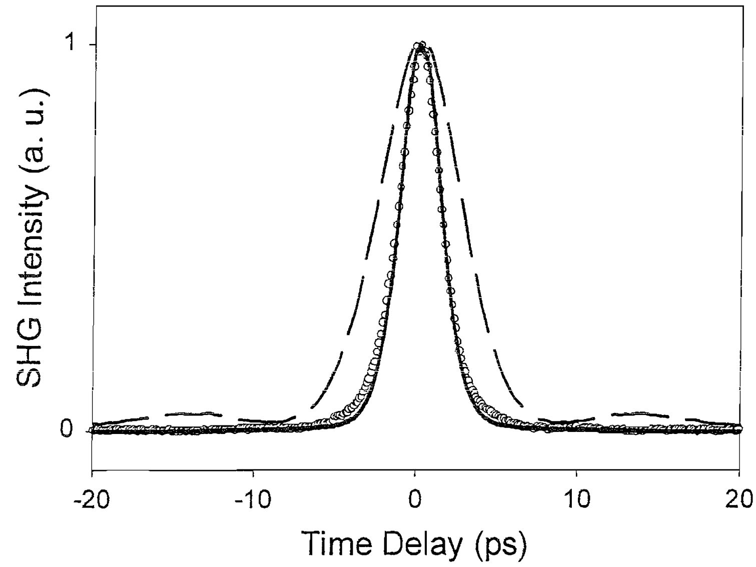

Figure 8.8: SHG Intensity autocorrelation measurements of the header pulse before encoding (solid line), after matched filtering (dashed line) and after reshaping in the NOLM (circles).

Figure 8.6 (Dropped Payload) shows the data payload dropped at the first node when the packet labelled by header H1 is recognized. The data payload P1 is clearly switched out as is shown by observing the signal before and after the switch in Figure 8.6 (Removed Packet). Once the payload P1 is removed, a new packet can be added. A new header H3 is obtained at the 'add' section of the node by reflecting the reshaped 2.5ps pulses after the NOLM from another SSFBG H3. A new data payload P3 is inserted after the generated header H3 to form a new packet. This packet is then inserted into the space vacated by the dropped packet as shown in Figure 8.6 (Add Output). The add/drop node can also be configured to be used for packet re-labelling. In this application only the header corresponding to the recognized packet is dropped, and a new re-encoded header is then inserted in its place at the add port of the node.

A further packet drop operation at a second add/drop node is used to test the quality of the 'add' and header re-encoding operations. At this node the decoded signal after reflection from the decoder grating H3*, is used to control the switch in order to drop the data payload P3 as shown in Figure 8.6 (Dropped Payload P3). Note that in this instance, there is no requirement to use a NOLM to enhance the pattern recognition signature H3:H3* if no further processing other than electrical detection of the header is required. Figure 8.9 presents the BER measurements performed on the dropped data, which shows that there is no significant power penalty when the switch is controlled by the decoded header H3* in the instance when the packet P3 is injected into the data stream and removed after one hop within the optical packet node.

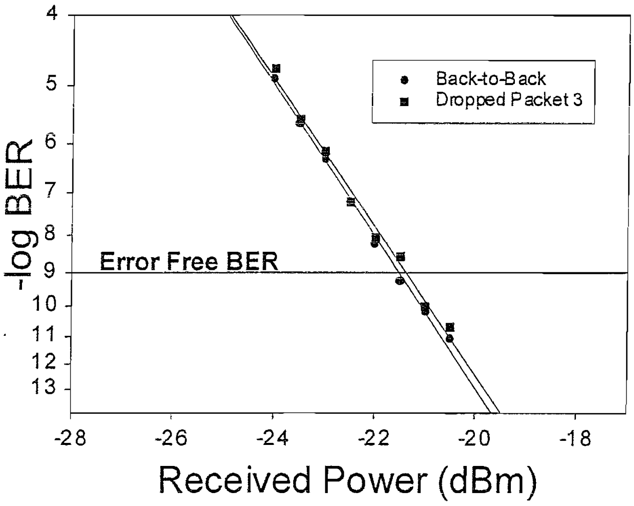

Figure 8.9: BER measurements on dropped Packet 3 after one-hop operation.

This experiment has demonstrated an optical packet switching system based on optical header encoding and decoding using SSFBGs. Error-free operation of multiple cascaded add/drop nodes that utilise a recoded header pulse has been experimentally verified with no observed penalty. The reuse of the decoded header pulse after reshaping in the NOLM removes the need for an additional ultrashort pulse source at each node, hence reducing the high cost associated with expensive short pulse lasers. The next section reports on a WDM add-drop packet switch experiment, which uses conventional externally modulated CW lasers as pulse sources.

8.3 Multi-wavelength add/drop node

In this section an experimental demonstration of a 400Gbit/s throughput, multiwavelength (40 WDM x 10 Gbit/s) optical packet switched network node based on all-optical header recognition and generation using 16-bit phase-coded superstructured fibre Bragg gratings (SSFBGs), and switching using fast electro-optic switches is described. The routing look-up table is implemented in parallel all optically, using an array of SSFBGs header processors. All-optical header processing is completed in 1.6ns, allowing packet processing rates of up to 4 Gigapackets/s (4 Gpps) to be achieved within the node. This routing approach demonstrates the compatibility with existing WDM technologies and networks and, since both the header and payload use the same wavelength, it is spectrally more efficient than techniques that place the header and payload on separate wavelengths [14].

8.3.1 Proposed multi-wavelength packet switched architecture

In the multi-wavelength (WDM) based optical packet switched network each WDM channel carries data within optically labelled packets that can be independently routed through the network by packet switching nodes (see Figure 8.10).

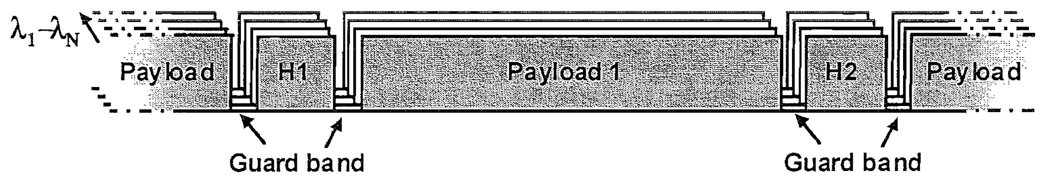

Figure 8.10: Multi-wavelength optical packet structure based on serial encoding.

The functionality of the multi-wavelength optically packet switched node is illustrated in Figure 8.11. The incoming WDM channels, containing the packet streams, are first wavelength demultiplexed using an arrayed waveguide grating (AWG). The individual wavelength channels are then sent to an array of optical packet routers. At the packet router part of the signal is picked off in an optical coupler and sent to the optical label decoder, whilst the remaining signal is sent to the optical switch via an appropriate optical delay to compensate for the header processing time. The optical header decoder uses a parallel array of decoders (based on SSFBGs) in order to recognise the optical header. The signal from the correctly recognised header (an intense autocorrelation spike) is used to control the optical space switch so that the original optical packet is routed to the switch output determined by the header. The routed packets are then recombined in an AWG before continuing through the network.

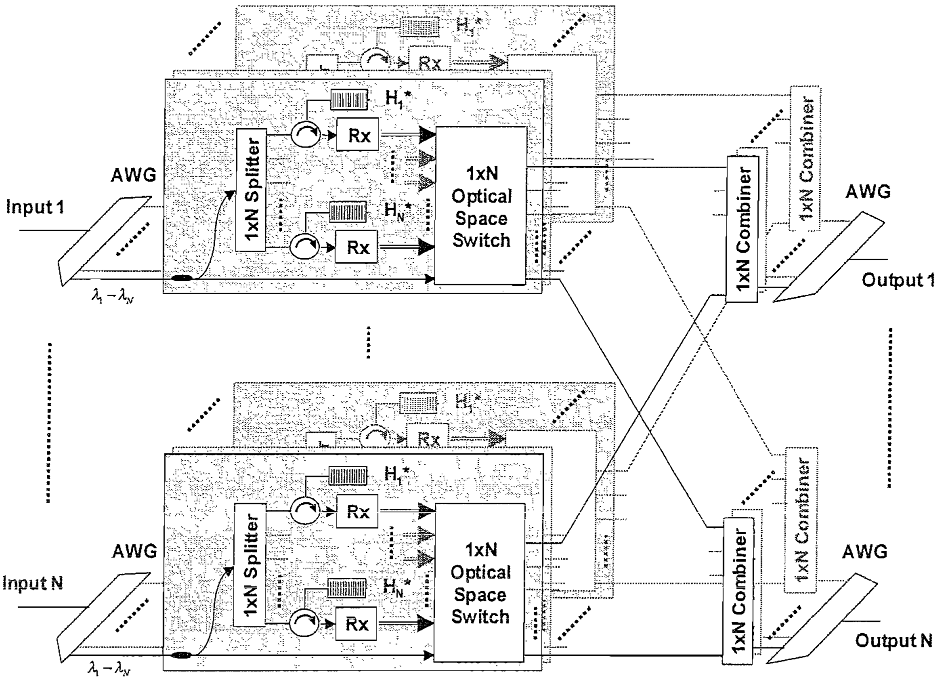

Figure 8.11: An NxN multi-wavelength optical packet routing node.

8.3.2 Multi-wavelength packet transmitter

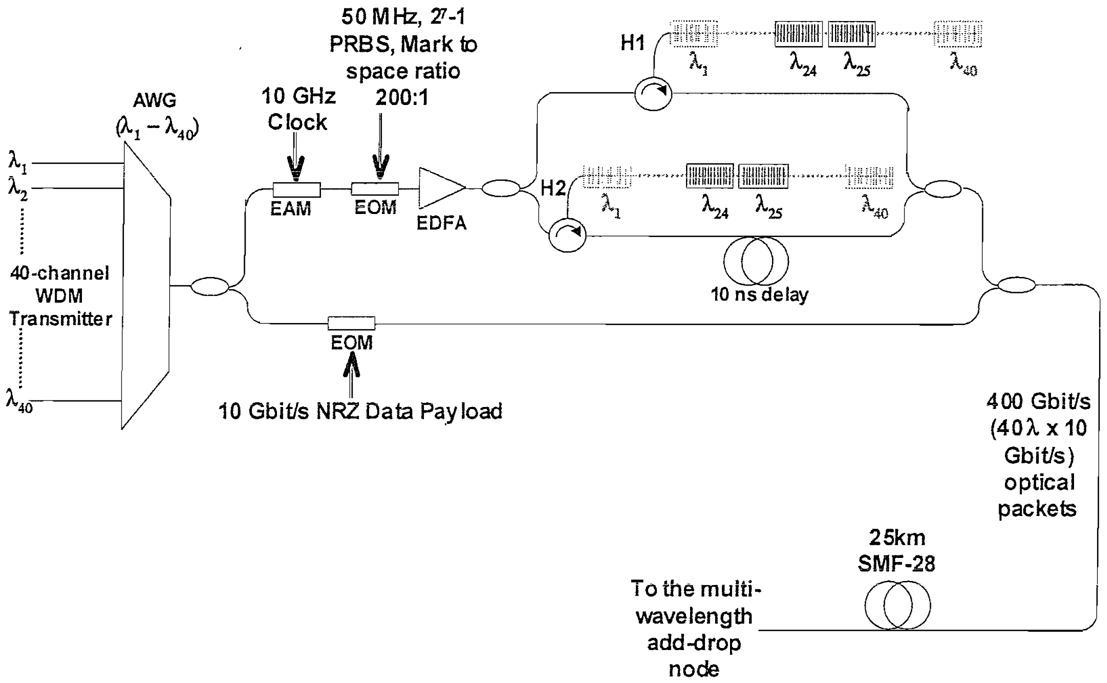

Figure 8.12: Experimental configuration of the multi-wavelength packet transmitter.

The schematic of the experimental multi-wavelength packet transmitter is shown in Figure 8.12. The packet transmitter generates optically coded header pulses, containing the switching codes, which are appended to the front of the data payload to create labelled packets (containing header+data payload) on each of 40 optical wavelengths. Firstly 20 ps duration optical pulses are generated by external modulation of the multiplexed WDM CW laser sources (separated in frequency by 100 GHz) using an electro absorption modulator (EAM) driven with a 10 GHz sinusoidal signal. This is then followed by another modulator acting as a pulse picker to gate the pulses down to the packet rate of 100 Mpps. These pulses are then optically encoded, to produce the optical headers, after reflection off the SSFBG encoders. For convenience a 10 Gbit/s (PRBS 2^7-1) NRZ modulated data payload was used. It should be noted that the packet switching is completely transparent to the bit-rate and the modulation format of the data payload, thus the system will readily support data payloads with higher bit rates. The resulting packets are 10 ns long corresponding to a packet rate of 100 Mpacket/s. The optically coded header is 800 ps in duration, and is separated from the payload by 800 ps guard bands. The label thus occupies 16% of the total packet duration in this implementation (see Figure 8.13). In this experiment two distinct coded header pulses, denoted by H1 and H2 are used at each wavelength to reduce the complexity of the set up. The SSFBGs used within this experiment allow for the generation of 16-bit, 20 Gbit/s quaternary phase coded pulse sequences. The characteristics of the gratings have been described in Chapter Five. These codes have distinct well-defined autocorrelation properties, and mutually low cross correlation properties allowing for a maximum of 4^{15}–1 distinct address labels to be used per wavelength. These header pulses were also modulated with a 2^7-1 pseudorandom bit pattern in order to produce randomly labelled packets with either label H1, H2 or no label.

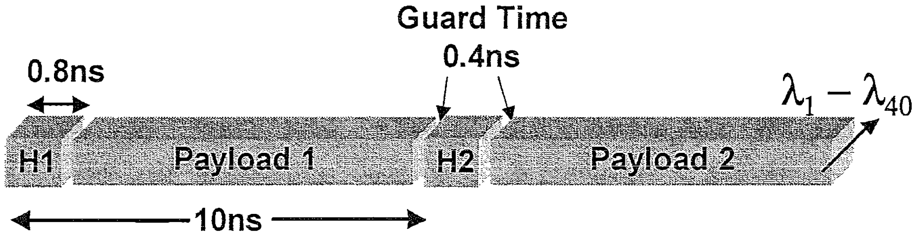

Figure 8.13: Multi-wavelength packet structure used in the experiment. H1 and H2 are the coded pulse sequences generated by reflection from the SSFBGs.

The 400 Gbit/s packet stream was transmitted over a distance of 25km of standard single mode fibre before entering the multi-wavelength packet switching node.

8.3.3 Multi-wavelength packet switching node

The packet switching node performs header recognition on the incoming packets in order to determine the correct switching output for each packet. Parallel arrays of decoder gratings (H1* and H2*) are used on each wavelength input of the node to optically decode the header via the matched filtering process. The correctly decoded output is then used to control an electro-optic switch so that the incoming packet is correctly routed. Figure 8.14 shows the set-up of the experimental multi-wavelength packet switching node.

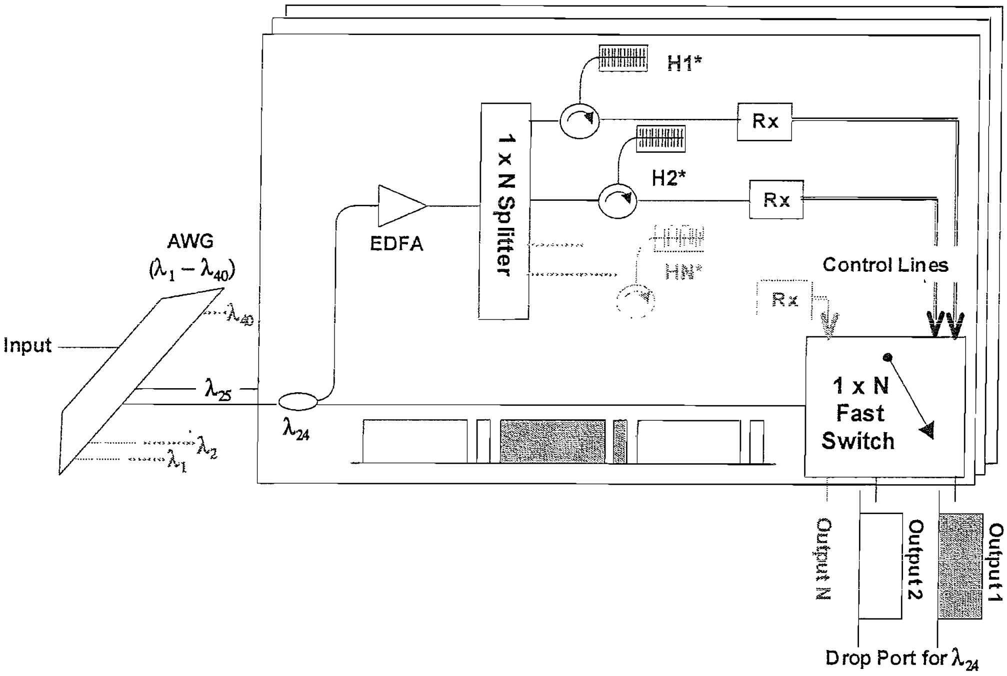

Figure 8.14: Experimental configuration of the multi-wavelength optical packet router.

Figure 8.15(a) shows the optical spectrum of 40 WDM optical packet channels upon entering the add/drop node. Wavelength demultiplexing is first performed using the AWG. An extinction ratio of ~30 dB is obtained as shown in Figure 8.15(b).

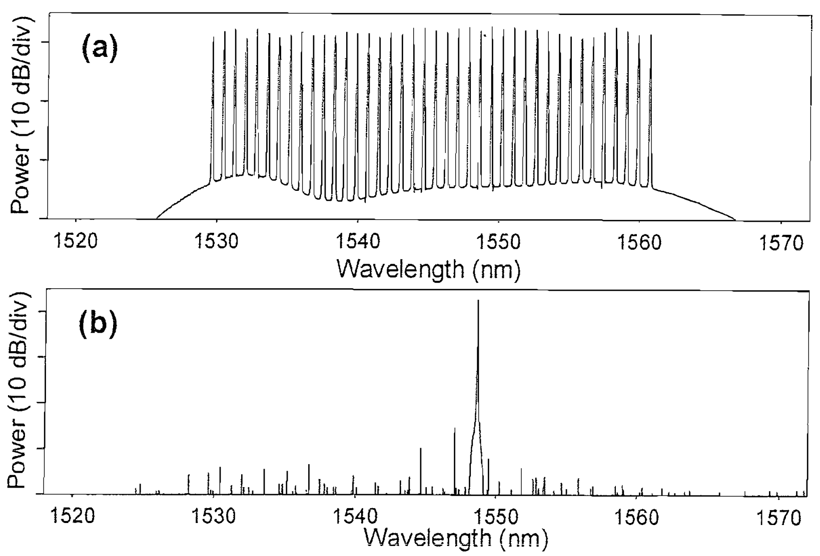

Figure 8.15: (a) Optical spectrum incident to the demultiplexing AWG. (b) Optical spectrum of a dropped wavelength channel. The measured resolution was 10pm.

Optical header recognition is performed independently for each wavelength channel in order to control the switching of the data. Part of the incoming packet stream is sent to the header-decoder which consists of an array of fibre gratings H1* and H2* whose codes are matched to the encoding gratings in the transmitter (H1 and H2). For example, if header recognition is carried out by reflecting the packets (shown in Figure 8.16(a)) off decoding grating H1* a strong correlation peak H1:H1* arises from label H1 as shown in Figure 8.16(b). There is also some residual background arising from the cross-correlation between label H2 and the decoding grating H1*, and a contribution from the reflected data payloads is also shown in Figure 8.16(b). The detected signal is then electrically thresholded and used to control the electro-optic switch. In this experiment the detection of labels H1 or H2 sets the switch so that the packet is routed out of ports 1 or 2 respectively. The correctly routed packets at output ports 1 and 2 are shown in Figures 8.16(c) and 8.16(d) respectively.

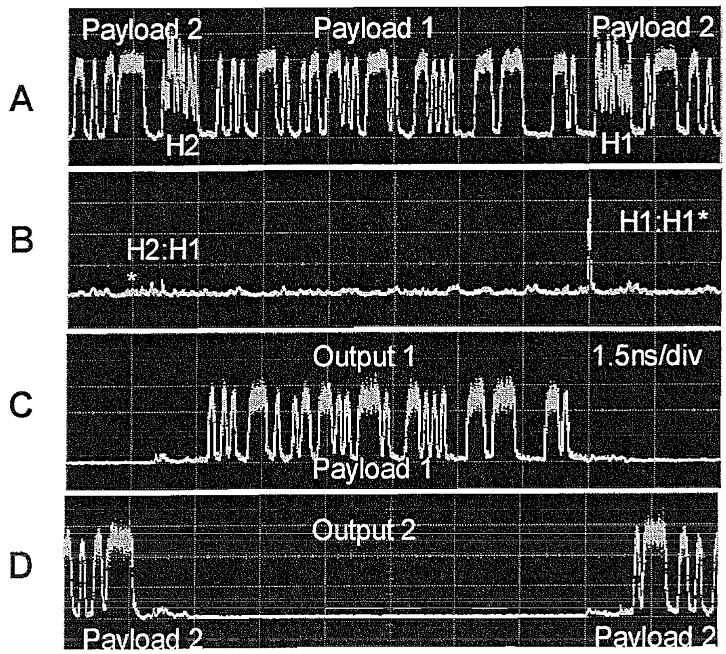

Figure 8.16: *A:* *Packet structure at a particular wavelength showing two headers and the associated packets.*
B: *Corresponding decode signal after matched filtering using decoder grating H1*.*
C&D: *Dropped packets at output ports 1 and 2 respectively.*

The quality of the header recognition is characterised by measuring the bit error rate (BER) of the header recognition process. The results are plotted in Figure 8.17(a) and show that no power penalty can be observed when comparing with laser back-to-back measurements. Figure 8.17(b) shows the BER measurements made on the routed packets in the presence of multiple WDM wavelengths. Again, error free performance is obtained for all of the measured channels, even in the instance that all 40 channels are transmitting simultaneously.

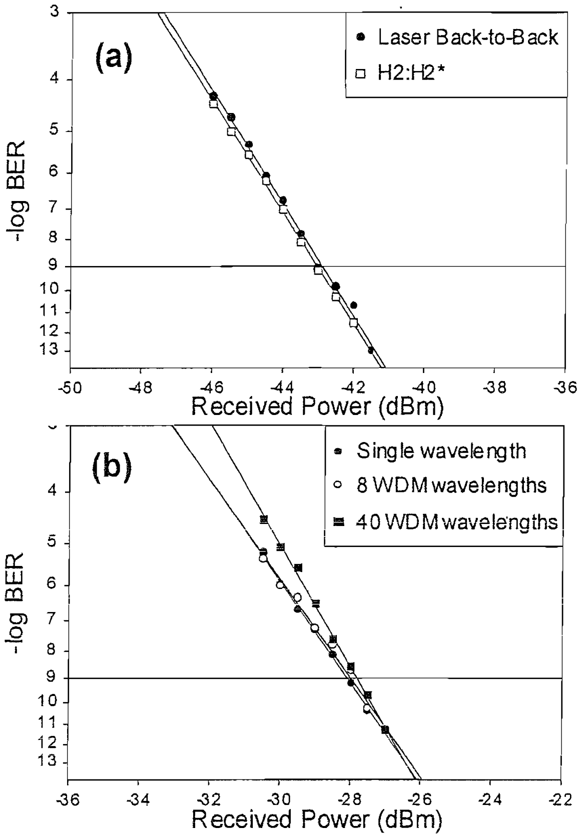

Figure 8.17: (a) BER of header recognition (H2:H2*) in the absence of the attached payloads and WDM MUX:DEMUX. (b) BER of the dropped payload 2 (with H2 as the header) for the full system in the presence of multiple WDM wavelengths.

The experiment has demonstrated the suitability of implementing the optical packet switched systems based on SSFBGs coders into WDM networks. The next section describes a self-routed optical packet switched network based on cascaded headers.

8.4 Self Routed Edge-to-Edge Packet Switched Network

This section describes a self-routed optical packet switched network architecture that moves the routing intelligence to the edge of the network, simplifying the optical packet processing that is required within the optical core of the network.

8.4.1 Proposed self-routing architecture

The proposed self-routed optically packet switched network is based on a slotted[4] mesh topology[5] where incoming data packets to the network are aligned according to fixed time slots. The network consists of a number of optical packet switching nodes (OPSN) interconnected as illustrated in Figure 8.18. This system is based on an optical packet, created at the source edge of the network, consisting of an optically coded header followed by a data payload. The optical header describes the route for each packet from the source edge to the destination edge of the network via several OPSNs.

The packet header is made up of a number of unique optically coded waveforms, one for each OPSN in the network path to produce a cascaded header. The cascaded header is used at each OPSN in the network to determine the routing of the data packets through the network. Note that no packet contention has been considered at this stage but various solutions to packet contentions have been reported [15].

At each OPSN only the part of the header that controls the switching for that particular node is correctly decoded (this will generate an appropriate autocorrelation pulse). The decoded signal is then used to control the switching of the packet through the switch to the desired output. Superstructured fibre Bragg gratings (SSFBG) are used to carry out the encoding and decoding of the optical header pulses. Figure 8.18 shows the routing and switching decisions made for a single packet entering the mesh network at $OPSN_1$ and being routed to its destination at $OPSN_5$.

---

[4] In a **slotted** network, the size of the packets and their timing slots are fixed. Before the packets enter each routing node, they must be aligned so that packet switching happens only at the slot boundaries. Synchronisation stages are therefore required for this type of network for aligning the packets. See ref[15] for more detailed information.

[5] A **mesh topology** refers to a network topology in which there are at least two nodes with two or more paths connected between them as shown in Figure 8.18.

Self-routing of optical packets in a two node optically packet switched mesh network consisting of two 1x2 OPSNs is demonstrated and error free decoding of a four node cascaded header will be shown subsequently.

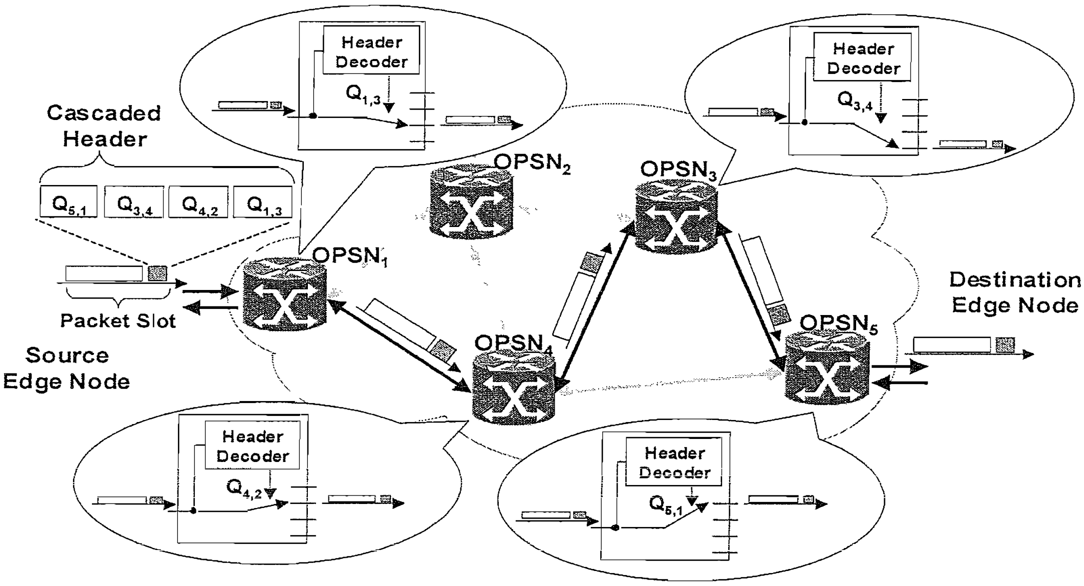

Figure 8.18: Self-routing optically packet switched mesh network architecture. The packet structure and self-routing principle is illustrated. Matched filtering of the cascaded header using an array of decoder gratings allows self-routing of the packet at each node. The schematic shows a cascaded header and payload being self-routed across the core network from the source edge node to the destination edge node.

8.4.2 Experimental demonstration and results

The two node self-routing demonstration uses an edge source node that generates a series of packets that have three different possible destinations. Each optical packet consists of a cascaded header containing two optically coded pulses (one specific to a particular switching decision for each node in the system) followed by a data payload. Figure 8.19 schematics show the series of optical packets, denoted by P1, P2 and P3 containing optically coded cascaded headers, denoted by $Q_{1,1}$ $Q_{2,1}$, $Q_{1,2}$ $Q_{2,2}$ and $Q_{1,1}$ $Q_{2,2}$ respectively that were generated from the edge source node. The routes taken by each optical packet is also illustrated.

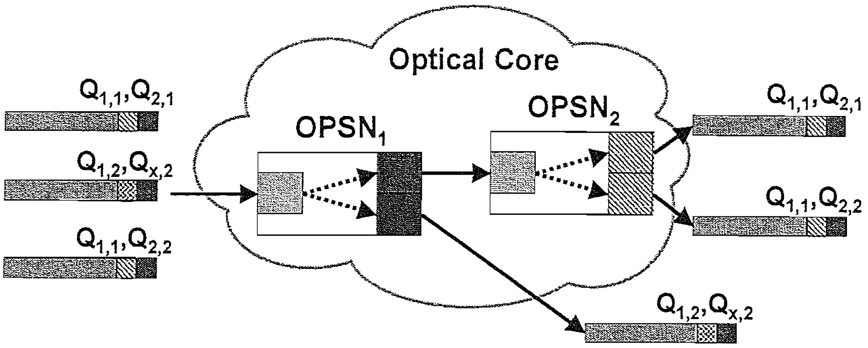

Figure 8.19: Schematics showing the two-node self-routing demonstration. The notation $Q_{1,2}$ refers to optical header that will be decoded at $OPSN_1$ and will exit the node at output 2.

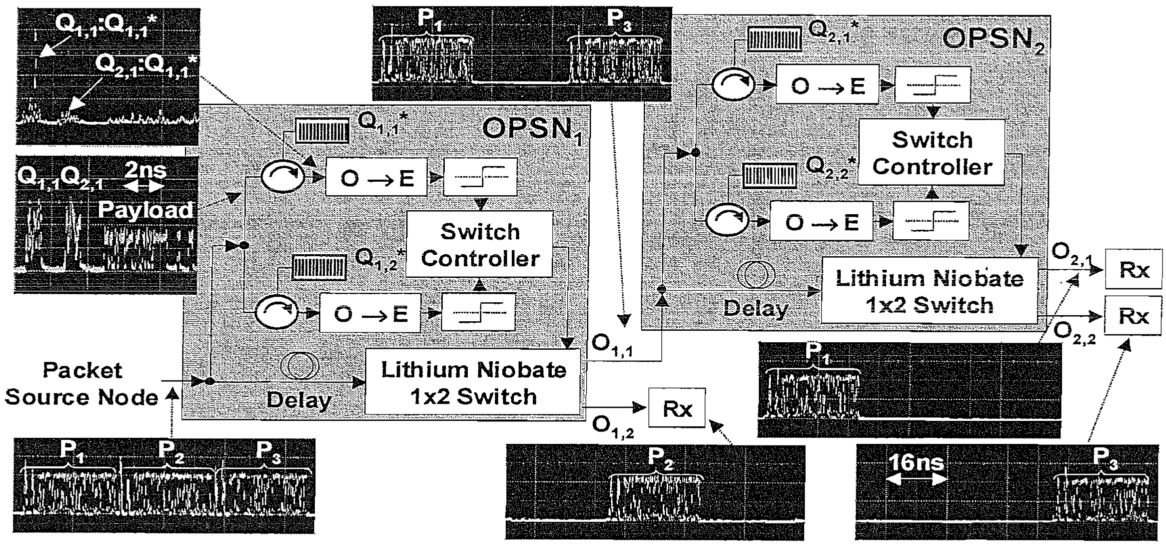

Figure 8.20: Self-routing optical packet switching experimental setup. The packet routes and associated outputs are shown. The packets P1, P2 and P3 were labelled with optically coded cascaded headers denoted by $Q_{1,1}$ $Q_{2,1}$, $Q_{1,2}$ $Q_{2,2}$ and $Q_{1,1}$ $Q_{2,2}$ respectively.

Figure 8.20 shows the experimental configuration used to demonstrate the two-node self-routing optical packet switching system. The cascaded header is optically encoded by reflecting 20ps optical pulses off a cascaded SSFBG. The 20ps pulses were generated using a combination of semiconductor CW lasers and an electro-absorption modulator. The cascaded SSFBG comprises of multiple individual coding SSFBG spliced together with the appropriate time delay between each SSFBG. All the SSFBGs used within this experiment contain the coding information within their spatial refractive index profile that allows for the generation of 16-chip, 20 Gchip/s quaternary phase coded pulse sequences. The two optically coded pulses and their guard bands occupy 20% of the total packet duration of 25ns. Note that the packet switching is transparent to the bit-rate and format of the data payload employed. In this experiment it was convenient to use 10 Gbit/s, PRBS 2^{31}-1, NRZ data as the data payload.

The packets (P1, P2 and P3) are sent to the first packet switching node ($OPSN_1$) where they are switched to either output $O_{1,1}$ or $O_{1,2}$ of this switch depending on the first code ($Q_{1,1}$ or $Q_{1,2}$ respectively) in the packet header. Packets exiting output $O_{1,1}$ of the first switch are sent on to the second $OPSN_2$ whilst packets exiting output $O_{1,2}$ are measured. The second switching node similarly directs the incoming packets according to the second code ($Q_{2,1}$ or $Q_{2,2}$) in the packet header.

Part of the incoming optical packet stream is tapped off using an optical coupler and sent to the header decoder section while the remaining signal is routed to the optical switch, which controls the packet routing. The tapped optical signal in the header decoder section is split between the parallel array of header SSFBG decoders whose codes, $Q_{n,1}*$ and $Q_{n,2}*$ correspond to the switch outputs $O_{n,1}$ or $O_{n,2}$. The decoding process is based on matched filtering and is carried out using SSFBGs that have the complementary header code imprinted in the SSFBGs spatial refractive index profile. When the incident optical header pulse code corresponds to that of the decoder, i.e. $Q_{n,1}$:$Q_{n,1}*$, then the reflected signal has a distinct autocorrelation peak, otherwise only a low-level crosscorrelation signal is reflected as illustrated in the oscilloscope traces in Figure 8.20. The autocorrelation signal from the SSFBG decoder ($Q_{n,1}*$ or $Q_{n,2}*$) is used to control the 1x2 lithium niobate switch so that the packet is routed to the output $O_{n,1}$ or $O_{n,2}$ respectively. Figure 8.20 also shows the packets at the outputs of the two OPSNs (OPSN1 and OPSN2) indicating that the correct packet routing has occurred.

Next, a packet labelled with a cascaded header containing four unique routing codes was constructed as shown in Figure 8.21, to further demonstrate the potential of the cascaded header for self-routing. This cascaded header is capable of routing a packet through four core switches in the network as illustrated.

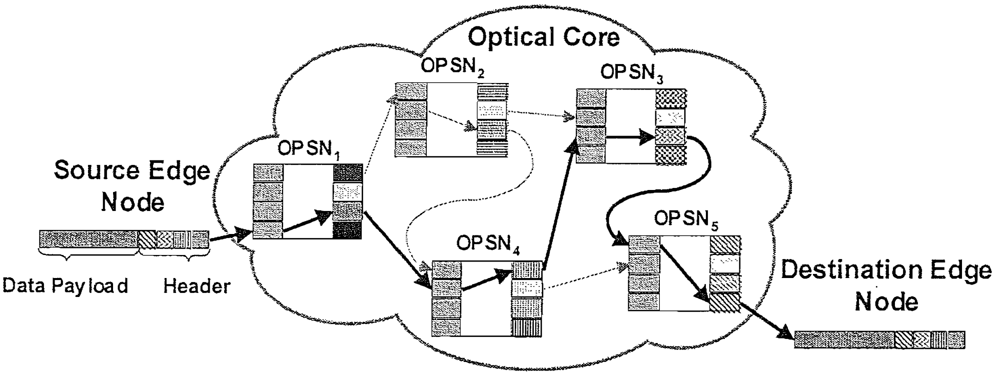

Figure 8.21: Schematics showing a packet labelled containing four unique routing codes being routed through four OPSNs before arriving at its destination.

Figure 8.22(a) shows the oscilloscope traces of the cascaded header comprising four routing codes. Figures 8.22(b)-(e) illustrates the code recognition (autocorrelation and crosscorrelation) features after the matched filtered decoding process when using one of the decoder gratings: Q_1*, Q_2*, Q_3* and Q_4* respectively.

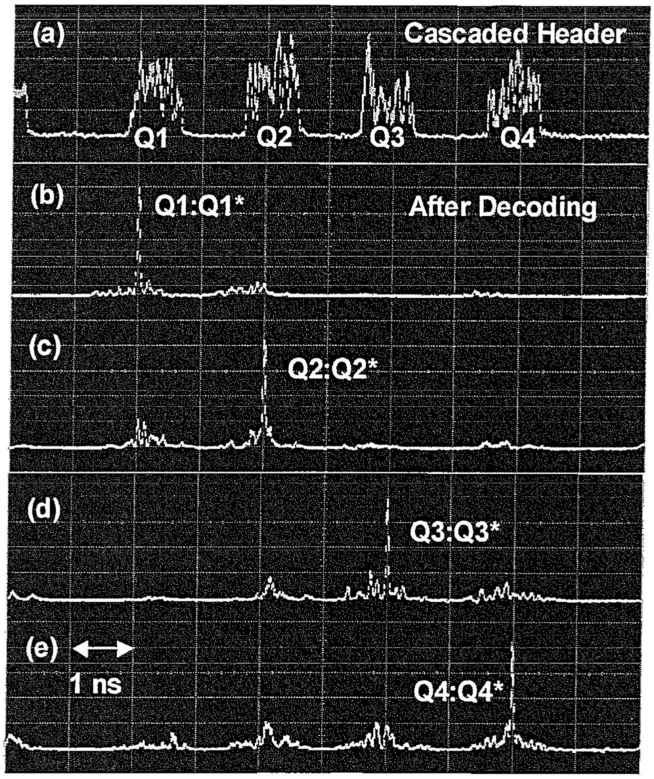

Figure 8.22(a)-(e): Oscilloscope traces showing the cascaded header before and after the decoding operation on each of the four codes.

Figure 8.23 shows the BER measurements on the header decoding process indicating that error free operation is obtained for all four codes with a 3 dB power penalty observed over the back-to-back measurement.

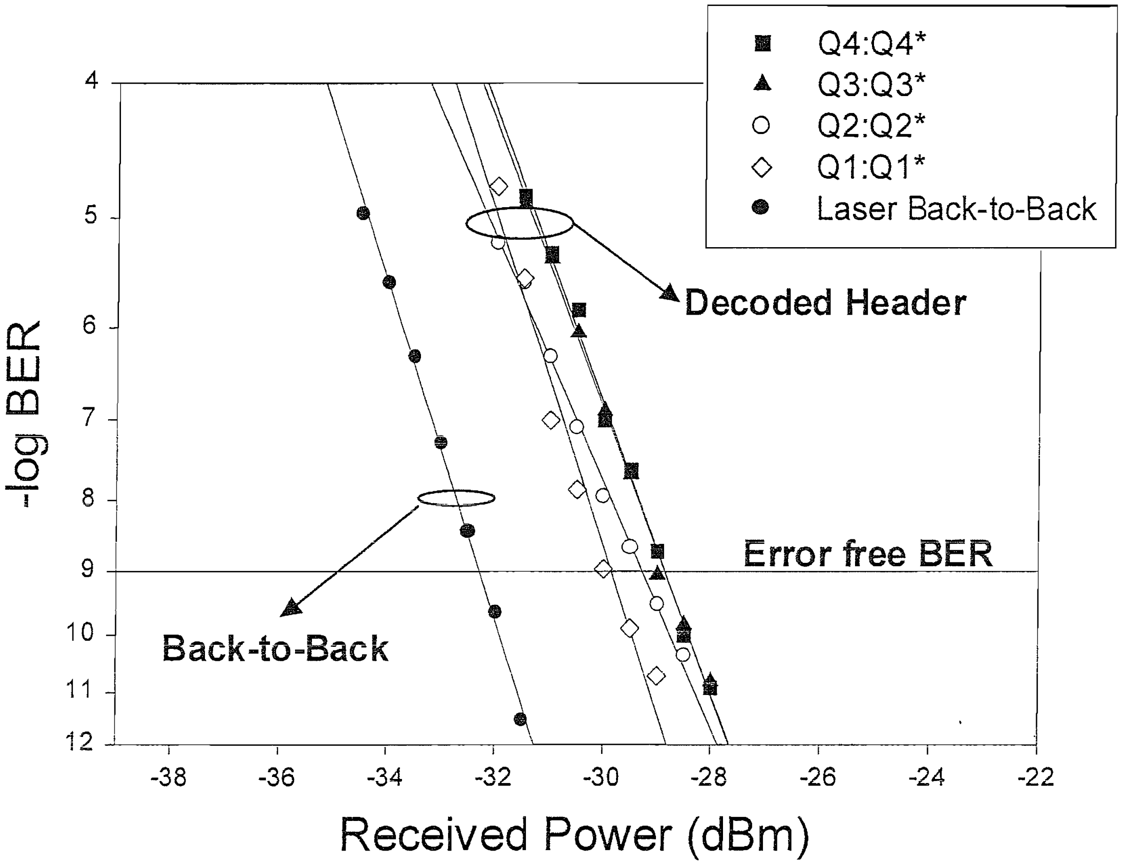

Figure 8.23: BER measurements obtained for each of the four codes in the cascaded header after the decoding operation.

8.5 Summary

This chapter has reported on a range of experimental demonstrations on the use of the SSFBG encoders/decoders developed for OCDMA systems to perform all-optical header generation and recognition in a packet switched network.

In the first packet switching experiment using 255-chip, 320 Gchip/s encoders/decoders based on SSFBG, error-free operation of multiple cascaded add/drop nodes that utilise a recoded header pulse has been experimentally verified with no observed penalty. The re-use of the decoded header pulse after reshaping in the NOLM removes the need for an additional pulse source at each node.

Next, a multi-wavelength packet switching node capable of high packet processing capacity (> 4 Gpps) and aggregate data capacity (currently 0.4 Tbit/s but readily upgradable to the multi Tbit/s level) have been demonstrated based on 16-chip, 50ps quaternary phase coded SSFBGs. These results further demonstrate that the optical packet switched system based on SSFBG approach can be combined with WDM multiplexing to provide a high throughput system. The functionality and reconfigurability of the system can be further improved by using a multi-level phase code-tunable device based on a uniform fiber Bragg grating (the descriptions on the principle of tunable multi-level phase code-tunable coders are described in Chapter Six).

Finally, the operation of a self-routing optical packet switched mesh network has been proposed. A two-node self-routing experiment has been successfully demonstrated. An optical packet containing four unique routing headers has been constructed and error free performance is obtained with only 3 dB of power penalty is observed for BER measurements when comparing with laser back-to-back measurements. The above results show that this optical packet switching architecture is readily scalable and can form the basis of larger switches and that the appraoch is also commensurate with existing WDM technology.

All these experiments have demonstrated that the SSFBG approach provides an extremely powerful and flexible technology that is well-suited to performing the optical processing functions required within all-optical packet switched networks.

References

[1] D. J. Blumenthal, "Photonic packet and all-optical label switching technologies and techniques," presented at Optical Fiber Communications Conference (OFC2002), paper WO3 (Invited), 2002.

[2] D. J. Blumenthal, B. Olsson, G. Rossi, T. E. Dimmick, L. Rau, M. Masanovic, O. Lavrova, R. Doshi, O. Jerphagnon, J. E. Bowers, V. Kaman, L. A. Coldren, and J. Barton, "All-optical label swapping networks and technologies," *IEEE Journal of Lightwave Technology*, vol. 18, pp. 2058-2075, 2000.

[3] K. Kitayama, N. Wada, and H. Sotobayashi, "Architectural considerations for Photonic IP Router based upon optical code correlaiton," *IEEE Journal of Lightwave Technology*, vol. 18, pp. 1834-1844, 2000.

[4] Y. M. Lin, W. I. Way, and G. K. Chang, "A novel optical label swapping techniques using erasable optical single sideband subcarrier label," *IEEE Photonic Technology Letters*, vol. 12, pp. 1088-1090, 2000.

[5] S. J. B. Yoo, "All-Optical Label Switching: Architecture, Protocol, and Systems Demonstration," presented at Optoelectronics and Communications Conference, Japan, 2002.

[6] S. J. B. Yoo, Y. Bansal, Z. Pan, J. Cao, V. K. Tsui, S. K. H. fong, Y. Zhang, J. Taylor, H. J. Lee, M. Jeon, and V. Akella, "Optical label based packet routing system with contention resolution in wavelenth, time and space domains," presented at Optical Fiber Communications Conference (OFC2002), paper WO2, 2002.

[7] N. Wada, H. Harai, W. Chujo, and F. Kubota, "80G to 10G bit/s variable rate photonic packet routing based on multi-wavelength label switch," presented at European Conference on Optical Communications (ECOC2001), 2001.

[8] N. Wada, H. Harai, W. Chujo, and F. Kubota, "Multi-hop, 40 Gbit/s variable length photonic packet routing based on multi-wavelength label switching, waveband routing and label swapping," presented at Optical Fiber Communications Conference (OFC2002), paper WG3, 2002.

[9] Z. Zheng, S. Shen, H. P. Sardesai, C.-C. Chang, J. H. Marsh, M. M. Karkhanehchi, and A. M. Weiner, "Ultrafast two-photon absorption optical thresholding of spectrally coded pulses," *Optical Communication*, vol. 167, pp. 225-233, 1999.

[10] J. H. Lee, P. C. Teh, P.Petropoulos, M. Ibsen, and D. J. Richardson, "A grating-based OCDMA coding-decoding system incorporating a nonlinear

optical loop mirror for improved code recognition and noise reduction," *IEEE Journal of Lightwave Technology*, vol. 20, pp. 36-46, 2002.

[11] I. Y. Krushchev, I. D. Philips, A. D. Ellis, R. J. Manning, D. Nesset, D. G. Moodie, R. V. Penty, and I. H. White, "OTDM applications of dispersion-imbalanced fiber loop mirror," *IEE Electronics Letters*, vol. 35, pp. 1183-1185, 1999.

[12] Y. J. Chai, I. Y. Khrushchev, and I. H. White, "Nonlinear suppression of interferometric noise using dispersion-imbalanced loop mirror," *IEE Electronics Letters*, vol. 36, pp. 1565-1566, 2000.

[13] S. Boztas, R. Hammons, and P. V. Kumar, "4-phase sequences with near-optimum correlation properties," *IEEE Transaction of Information Theory*, vol. 38, pp. 1101-1113, 1992.

[14] L. Rau, S. Rangarajan, D. J. Blumenthal, H.-F. Chou, Y.-J. Chiu, and J. E. Bowers, "Two-Hop All-Optical Label Swapping with Variable Length 80 Gb/s Packets and 10 Gb/s Labels using Nonlinear Fiber Wavelength Converters, Unicast/Multicast Output and a Single EAM for 80- to 10 Gb/s Packet Demultiplexing," presented at Optical Fiber Communication Conference, USA, 2002.

[15] S. Yao, B. Mukherjee, and S. Dixit, "Advances in photonic packet swithching: an overview," IEEE Communications Magazine, vol. 2, pp. 84-94, 2000.

Conclusions and Future Directions

This thesis has discussed a range of activities that focused on the investigation of the suitability of using SSFBG technology to perform optical code generation and recognition functions as required within both OCDMA systems and optical packet switched networks.

The continuous grating writing technique has shown to have the precision and flexibility required to fabricate SSFBG based encoders/decoders containing up to 255-chip code sequences with relatively short chip duration (3.2ps). Such long code sequences provide distinct autocorrelation spikes and very low-level crosscorrelation backgrounds. The SSFBG approach also allows for significant WDM multiplexing (and subsequently demultiplexing) due to the inherent wavelength selectivity of the gratings. Optical nonlinear thresholders have been constructed (based on NOLMs or holey fibre based optical thresholders) and were used to demonstrate the enhanced code recognition performance relative to the simple matched filtering only. In another novel approach, commercially available CW lasers and an Electro-Absorption modulator were used to generate WDM pulse trains. These pulses were then used to generate 16 OCDMA encoded channels (4 OCDMA channels centred on 4 wavelengths) after reflection from 16 SSFBG encoders. While these SSFBGs have fixed code profiles created during the grating writing process, reconfigurable code-tunable devices based on uniform fibre Bragg gratings and thin heated wires have been proposed and experimentally demonstrated. Optical code sequences generated from the reconfigurable encoder can be recognised using a fixed-code SSFBG decoder. Two novel DS-OCDMA network architectures had been proposed and initial experiments were carried out to test the viability of the proposal. Both bi-directional spectrally interleaved OCDMA architectures and the bi-directional clock distributed OCDMA architectures promise improved functionality and simpler OCDMA topologies. In the area of optical packet switching, several early experiments have shown that the SSFBG approach provides a highly flexible and effective approach to perform the required optical header generation and processing (decoding and header re-labelling if required) functions.

However, it should be appreciated that the OCDMA experiments (and the associated use of SSFBG coders in optical packet switched systems) reported herein are still relatively elementary and that further research work is required to establish the commercial viability/practicality of the approach. Some future research possibilities are suggested below:

High reflectivity SSFBG

While the current SSFBG based OCDMA encoders/decoders were designed within the weak grating limit such that the reflectivity of the grating R<20%, higher reflectivity coded SSFBGs (with peak reflectivity as high as 90% is possible) and can be designed using inverse scattering design algorithms [1]. These algorithms are based on the layer-peeling technique whereby the grating is synthesized layer-by-layer to meet the desired performance characteristics. High reflectivity SSFBGs will have less optical insertion loss and should reduce the requirement for additional costly optical amplifiers within the system at the encoder/decoder nodes.

Combined functionality

Moreover, the SSFBG technology also has the capability to enable the combination of both dispersion compensation and coding functionality into a single grating structure. High reflectivity OCDMA encoders and decoders that incorporate dispersion compensation will eliminate the needs for separate dispersion compensation modules in an OCDMA access network, allowing the network to cover a large geographical area. Again, the development of these complex-profile grating designs will be based on the inverse scattering design.

OCDMA codes

There are many available techniques for designing optimal codes suitable for fibre Bragg grating implementations. In the past most of these techniques have been based on existing approaches adopted from wireless communications. New code designs, which focus on increasing the potential number of users whilst maintaining error free operation, can be investigated. One such approach is to investigate the use of higher order phase levels (8- and 16-phase level) that will provide excellent autocorrelation contrast and reduce the deleterious multiple access interference (MAI) when transmitted simultaneously with other interfering channels. It is also possible to expand the current one-dimensional codes (phase coding only) into higher dimensions codes using suitable mapping algorithms. For example, two-dimensional codes where both the amplitude and the phase of the grating are changed according to the two dimensional (2D) codes suggested in Ref [2] can be investigated. Furthermore, three-dimensional codes (amplitude, phase and wavelength) can also be designed and fabricated using the SSFBG technology.

The simulations presented in Chapter Two show that the use of longer code sequences will allow for more users to be accommodated. The flexibility of the SSFBG grating writing technique should enable code sequences up to 1023-chip, 1.6ps chip duration and higher phase levels (8 and 16 distinct phase shifts) to be fabricated.

Asynchronous OCDMA test bed

The improved SSFBG gratings (incorporating higher reflectivity, advanced codes and additional functionality) can be configured in an asynchronous OCDMA test bed where each user in the system has their individual pulse source as shown in the figure below. In our current experiments the system operation has been synchronous since the same pulse source has been used for all channels. Ultimately, the performance of this asynchronous test bed can be compared with the simulated model so that more accurate predictions can be obtained for an OCDMA system that encompasses large number of users (up to several tens of active users per wavelength).

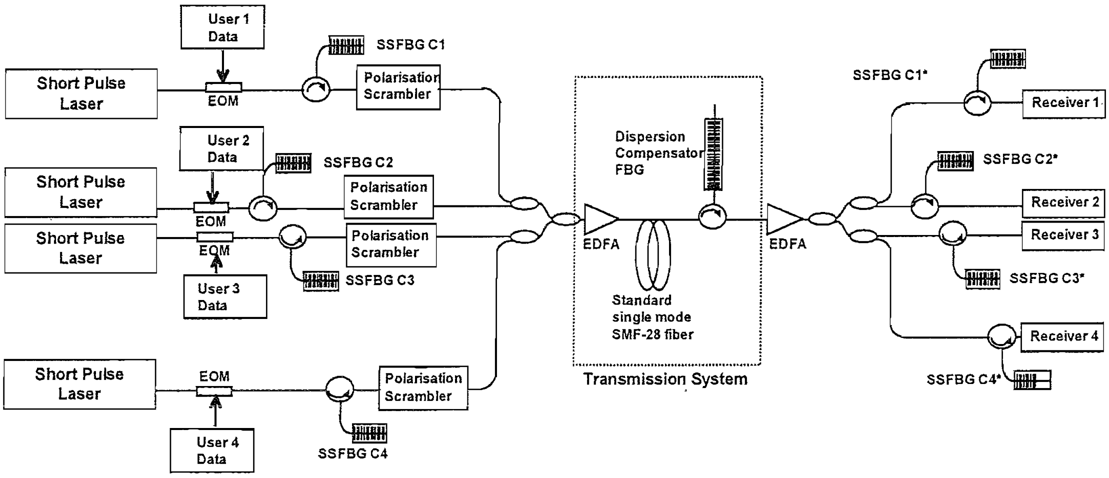

Figure 1: Proposed asynchronous DS-OCDMA test bed.

Optical Packet Switched networks

While impressive results have been obtained on the basic header generation and recognition using SSFBG coders, further work is required to investigate the performance of the optical packet as it is being switched through multiple SSFBG based optical packet routers in the network. A re-circulating loop can be constructed to investigate the performance of the optical packet system under multiple hops (several tens of hops instead of just the two hops described earlier in Chapter Eight). Additional functionality such as header regeneration/packet re-labelling can be included in the loop.

It is also interesting to note that the code-tunable encoder/decoder described earlier in Chapter Six can be used to implement a dynamically reconfigurable optical packet switched system. Such a system can have the advantages of rapid network provisioning and intelligent control over the routing of the packets. In this proposed system, the reconfigurable decoder will be used at the packet router to decipher the incoming optical header and routes the optical packet to its suitable outputs, according to the code programmed into the reconfigurable decoder.

References

[1] R. Feced, M. N. Zervas, and M. A. Muriel, "An efficient inverse scattering algorithm for the design of nonuniform fiber Bragg gratings," *IEEE Journal of Quantum Electronics*, vol. 35, pp. 1105-1115, 1999.

[2] E. Park, A. J. Mendez, and E. M. Garmire, "Temporal/Spatial Optical CDMA Networks-Design, Demonstration, and Comparison with Temporal Networks," *IEEE Photonic Technology Letters*, vol. 4, pp. 1160-1162, 1992.

Appendix A

Code Sequences

This appendix describes the main characteristics and the methods used to generate the M-sequence (unipolar and bipolar), bipolar Gold code and Family A quaternary sequences reported in this thesis.

1. M-sequence Codes

M-sequence (also known as maximal length sequence) codes are codes with lengths of 2^L-1 where L is the number of shift registers used to generate the sequence [1]. A simple linear feedback shift register (LFSR) generator has all the feedback signals returned to a single input of the first shift register and the feedback function can be expressed as a modulo-2 sum (EX-OR). Figure 1 below shows a simple example of a LFSR.

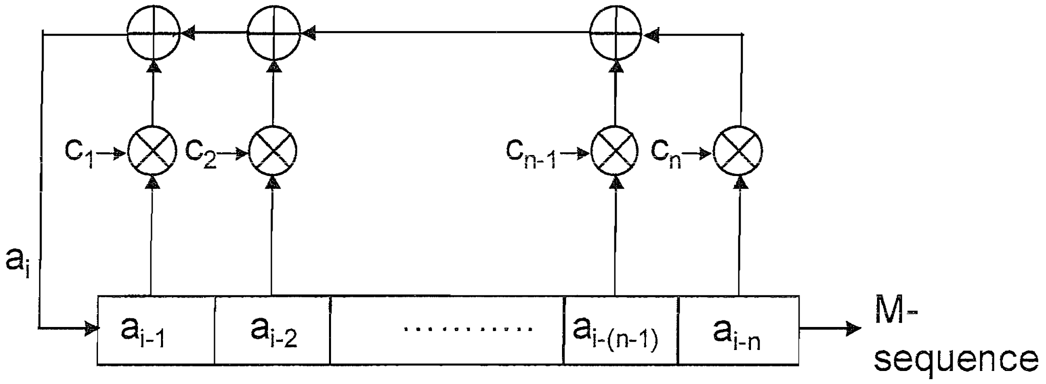

Figure 1: A typical LFSR generator with feedback.

The feedback function a_i is generated according to the recursive formula

$$a_i=c_1a_{i-1}+c_2a_{i-2}+\ldots\ldots+c_na_{i-n} \qquad (A.1)$$

where $a_{i-1},a_{i-2},\ldots a_{i-n}$ being the contents of the shift register cells and c_i being the feedback connection coefficients (c_i=0 or 1, where i ranges from 1 to L). The characteristic polynomial of the LFSR sequence generator is given by *f(D)* and depends solely on the connection vector c_1, c_2, ...c_n as well as determining the main characteristics of the generated sequence.

Figure 2 below shows an example of a 7-chip M-sequence LFSR generator of $f(D)=1+D^2+D^3$ where the notation [3,2] refers to the position of the feedback taps. Only two M-sequence codes can be generated from this LFSR. A 7-chip M-sequence code will be generated after 7 clock cycles.

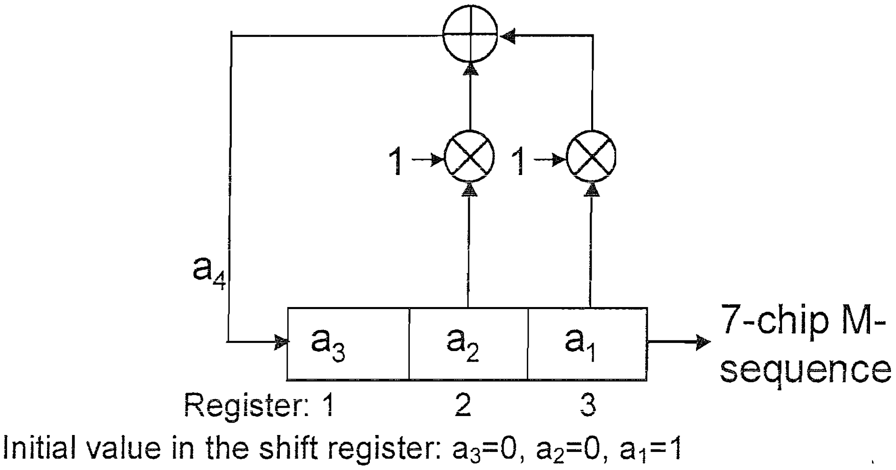

Figure 2: 7-chip M-sequence generator. The feedback taps for M-sequence is given by [3,2] where the notation [A,B,C ...N] refers to the location of the feedback taps. The characteristic polynomial equation is $f(D)=1+D^2+D^3$.

The above LFSR and other LFSR configurations described later to generate M-sequence, Gold code and Family A quaternary codes can be easily implemented using computer programming such as 'C' or Matlab.

The following Table 1 lists the feedback connections for M-sequence codes generated using the LFSR generator, together with the number of M-sequence code combinations available for a given code length.

Number of shift registers, L	Code length, $N_c=2^L-1$	Feedback Taps for M-sequence	No. of M-sequence codes
2	3	[2,1]	1
3	7	[3,2]	2
4	15	[4,1]	2
5	31	[5,3], [5,4,3,2], [5,4,2,1]	6
6	63	[6,1], [6,5,2,1], [6,5,3,2]	6
7	127	[7,1], [7,3], [7,3,2,1], [7,4,3,2], [7,6,4,2], [7,6,3,1], [7,6,5,2], [7,6,5,4,2,1], [7,5,4,3,2,1]	18
8	255	[8,4,3,2], [8,6,5,3], [8,6,5,2], [8,5,3,1], [8,6,5,1], [8,7,6,1], [8,7,6,5,2,1], [8,6,4,3,2,1]	16
9	511	[9,4], [9,6,4,3], [9,8,5,4], [9,8,4,1], [9,5,3,2], [9,8,6,5], [9,8,7,2], [9,6,5,4,2,1], [9,7,6,5,3,1], [9,8,7,6,5,3]	48
10	1023	[10,3], [10,8,3,2], [10,4,3,1], [10,8,5,1], [10,8,5,4], [10,9,4,1], [10,8,4,3], [10,5,3,2], [10,5,2,1], [10,9,4,2], [10,6,5,3,2,1], [10,9,8,6,3,2], [10,9,8,7,6,5,4,3], [10,8,7,6,5,4,3,1]	176

Table 1: M-sequence feedback connections generated using LFSR generator.

For an M-sequence there is one more 'one' than 'zero' in a full period of the sequence. Since all states but the 'all-zero' state are reached in an M-sequence, there must be 2^{L-1} 'ones' and 2^{L-1}-1 'zeroes'. For every M-sequence period, half the runs (of all 'one's or all 'zero's) have length 1, one-fourth have length 2, one-eight have length 3, etc. For each of the runs there are equally many runs of 'one's and 'zero's. Autocorrelation refers to the degree of correspondence between a sequence and a time-delayed replica of itself. In a bipolar M-sequence (containing '–1' and '1' bits), the peak autocorrelation has a value of N_c when the sequence and the time-delayed replica are exactly time-aligned, otherwise a value of −1 will be obtained for all other time-delays (Note that in intensity detection at the photodiode, the peak autocorrelation scales with N_c^2 and all the autocorrelation sidelobes has a value of 1). However, in unipolar M-sequence, the peak autocorrelation only is given by the total number of '1's in the code, i.e. $\sim N_c/2$. The cross-correlation is a measure of agreement between two different codes. For M-sequence, the cross-correlation is relatively poor and have large values. Welch obtained the lower bound on the crosscorrelation between any pair of binary sequences of period N_c in a set of M sequences [2]:

$$\text{Welch lower bound} \geq N_c\sqrt{\frac{M-1}{MN_c-1}} \cong \sqrt{N_c} \tag{A.2}$$

2. Gold Codes

In a multi-user environment (such as in CDMA and OCDMA), there is a requirement for a large number of codes and good crosscorrelation properties. Gold code sequences are useful because a large number of codes (with the same length and with controlled crosscorrelation) can be generated, although they require only one 'pair' of feedback tap sets [1]. Gold codes are product codes achieved by the exclusive OR (EX-OR) or modulo-2 adding of two M-sequence codes with the same length. The code sequences are added chip-by-chip by synchronous clocking. Because the M-sequences are of the same length, the two code generators maintain the same phase relationship, and the codes generated are of the same length as the two base codes which are added together, but are non-maximal (so the autocorrelation function will be worse than that of M-sequences). Every change in phase position between the two generated M-sequences causes a new sequence to be generated. Figure 3 below shows a typical Gold code generator comprising of two M-sequence LFSR generators. Any two-register Gold code generator of length L can generate 2^L-1 sequences plus the two base M-sequences, giving a total of 2^L+1 code combinations.

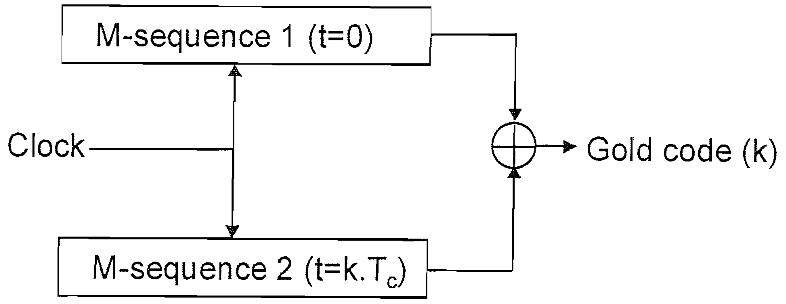

Figure 3: A typical illustration of a Gold code generator.

In addition to their advantage in generating large numbers of codes, the Gold codes may be chosen so that over a set of codes available from a given generator the autocorrelation and the crosscorrelation between the codes is uniform and bounded. When specially selected M-sequences, called preferred M-sequences, are used the generated Gold codes have a three-valued crosscorrelation. For large N_c, the Welch bound is lower by $\sqrt{2}$ for L odd and by 2 for L even. Table 2 below shows the preferred pairs of M-sequence required to generate the optimum Gold codes.

Number of shift registers, L	Code length $N_c=2^L-1$	Preferred pairs of M-sequences	Peak auto-correlation value	Average 3-value Crosscorrelation		
5	31	[5,2], [5,4,3,2]	31	7	-1	-9
6	63	[6,1], [6,5,2,1]	63	15	-1	-17
7	127	[7,3], [7,3,2,1] [7,3,2,1], [7,5,4,3,2,1]	127	31	-1	-17
*8	255	[8,7,6,5,2,1], [8,7,6,1]	255	31	-1	-17
9	511	[9,4], [9,6,4,3] [9,6,4,3], [9,8,4,1]	511	63	-1	-33
10	1023	[10,9,8,7,6,5,4,3],[10,9,7,6,4,1] [10,8,5,1], [10,7,6,4,2,1] [10,8,7,6,5,4,3,1],[10,9,7,6,4,1]	1023	63	-1	-65

Table 2: Preferred pairs of M-sequences used to generate Gold codes and their corresponding crosscorrelation values.

For the 63-chip Gold codes, they can be generated using the following feedback tap sequences as shown in Figure 4 below.

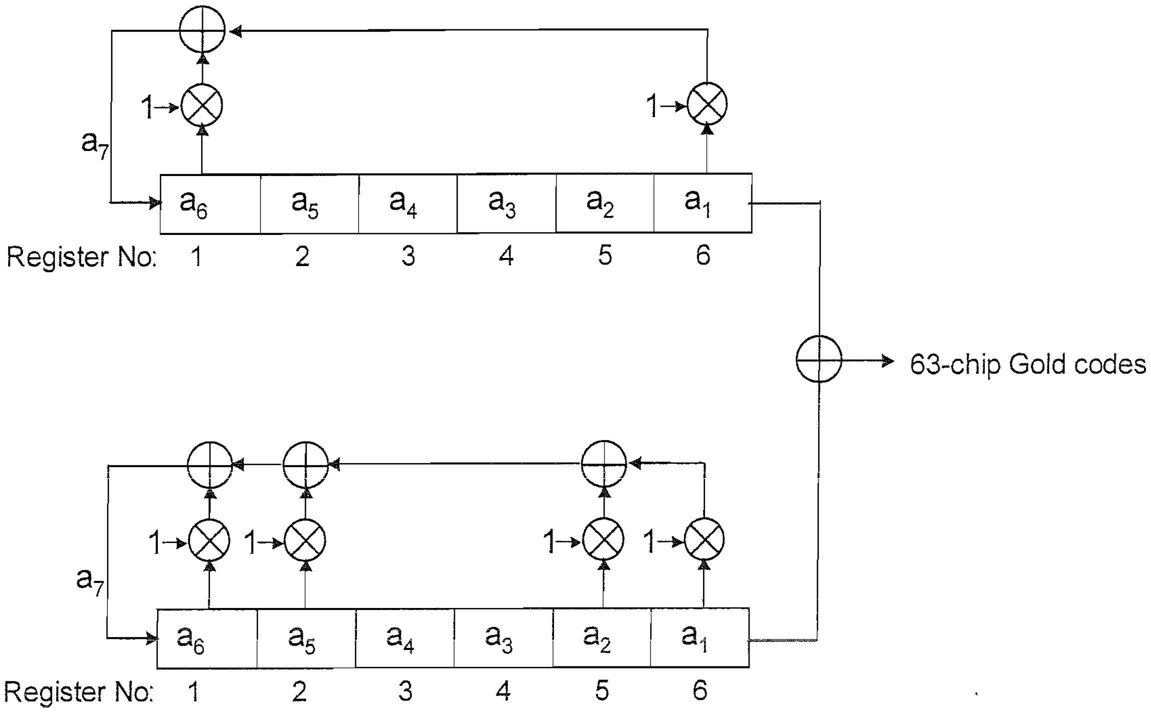

Figure 4: 63-chip Gold codes LFSR generator. The preferred pairs of M-sequences used are [6,1] and [6,5,2,1].

3. Family A Quaternary Codes

In quaternary codes, c_i has value from 0 to 3 representing the four phase levels in the codes (0, π /2, π, 3π/2). Different sequences in Family A may be generated by loading the shift register with any set of initial conditions not identically zero and cycling the shift register through a full period. Table 3 below gives the characteristic polynomials *f(D)* defining the Family A quaternary codes [3]. In this case the position of the feedback taps sequence can be determined from the following expression (note that a '0' on the polynomials is represented by c_i=4):

$$a_i=(4-c_1)a_{i-1}+(4-c_2)a_{i-2}+\ldots\ldots+(4-c_n)a_{i-n} \qquad (A.3)$$

For example, the characteristic polynomial equation, $f(D)=D^3+2D^2+D+3$, has the position of the feedback taps sequence given by $a_4=2a_3+3a_2+a_1$.

Number of shift registers, L	Code length, N_c	Characteristic Polynomials
3	7	1213 1323
4	15	10231 13201
5	31	100323 113013 113123 121003 123133
6	63	1002031 1110231 1211031 1301121 1302001
7	127	10020013 10030203 10201003 10221133 10233123
8	255	**100103121** 100301231 102231321 111002031 111021311 111310321
9	511	1000030203 1001011333 1001233203 1002231013 1020100003 1020332213 1021123003 1021301133
10	1023	10000203001 10002102111 10002123121 10020213031 10030023231 10030200001

Table 3: Characteristic polynomials for Family A code for L=3 to 10. For example, L=3, the entry 1213 represents the polynomial $f(D)=1D^3+2D^2+1D+3$.

For example, in the 255-chip quaternary codes, the characteristic polynomial equation, $f(D)=D^8+D^5+3D^3+D^2+2D^1+1$ (highlighted in bold in Table 3) can be implemented using the following LFSR with the following feedback tap expression $a_9=3a_6+a_4+3a_3+2a_2+3a_1$. The LFSR implementation is shown in Figure 5 below.

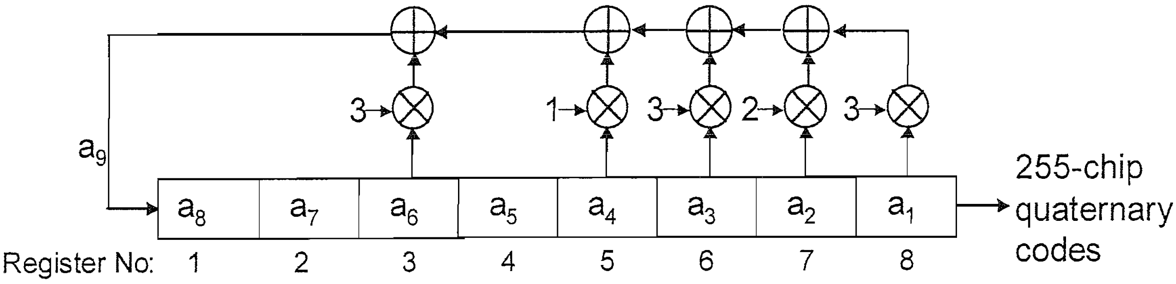

Figure 5: 255-chip Family A quaternary code generator implemented using LFSR.

Although Family A quaternary phase sequences only have as many codes as the bipolar Gold code, they provide codes with more desirable cross-correlation characteristics (for the same code length) than can be achieved with lower level coding such as unipolar and bipolar. In fact several literatures have reported that these codes provide up to 3 dB of improvement in terms of the extinction between the peak autocorrelation spike and the low-level crosscorrelation traces compared to when using randomly generated quaternary-phase sequences.

References

[1] E. H. Dinan and B. Jabbari, "Spreading Codes for Direct Sequence CDMA and Wideband CDMA Cellular Networks," IEEE Communications Magazine, vol. 36, pp. 48-54, 1998.

[2] L. R. Welch, "Lower bounds on the maximum crosscorrelation of signals," IEEE Transaction of Information Theory, vol. IT-20, pp. 397-399, 1974.

[3] S. Boztas, R. Hammons, and P. V. Kumar, "4-phase sequences with near-optimum correlation properties," IEEE Transaction of Information Theory, vol. 38, pp. 1101-1113, 1992.

Appendix B

Regeneratively Mode-Locked Erbium Fibre Ring Laser

This appendix describes the principle and operation of the 10GHz, 2.5ps transform limited pulse laser source based on polarisation maintaining (PM), actively and harmonically mode-locked erbium fibre ring laser (EFRL), obtained from Ref [1]. Dr. Periklis Petropoulos constructed this EFRL.

The EFRL design is based on an all polarisation maintaining ring design using active amplitude modulation with intracavity soliton compression and filtering to obtain ultrashort operation and a phase locked loop (PLL) to ensure good long-term stability. The principle of mode-locking is well known [2] and can be explained as follows: when several longitudinal modes are made to lase together with a (forced) phase coherence between them, pulsed outputs can be obtained. Active mode-locking offers the advantage of being a reliable pulse source and is based on the modulation of the amplitude/phase of the optical field in the cavity applied at a frequency equal to or a multiple of the mode spacing. This frequency corresponds to the cavity round trip time. Short optical pulses experience minimum loss in such cavities and this fact provides the mechanism by which the pulses form. $LiNbO_3$ electro-optic modulators are usually used in the cavity for modulating the optical field, due to their high speed, compactness and low loss [3].

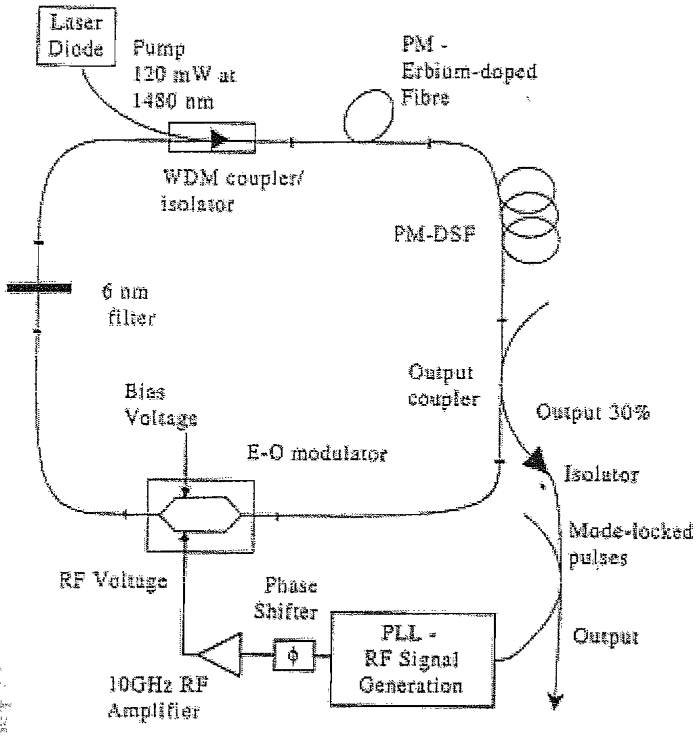

Figure 1: The all polarisation-maintaining Er-doped fibre ring laser.

Figure 1 shows the cavity layout of the laser. The $LiNbO_3$ Mach-Zender electro-optic modulator has a 10 GHz electrical bandwidth. The active element in the laser is a 19m erbium-doped fibre, pumped at 1480nm by a 120mW pump laser diode. The PM-WDM coupler used also incorporated an isolator to ensure unidirectional operation of the cavity. The in-line filter has a 6nm bandwidth with both input and output comprising PM fibre pigtails. Light was coupled out of the cavity using a 30% PM coupler. An isolator at the output port of the coupler prevented any stray light from coming back into the EFRL.

The main part of the cavity is the polarisation maintaining dispersion-shifted fibre (PM-DSF). The use of such fibre is necessary to generate nonlinear soliton compression in the pulses. In order to achieve ultrastable operation in the cavity, amplitude noise suppression would have to be achieved, by a combination of a long cavity and a narrowband filtering to achieve a reduction in pulse width and noise [4]. The concept behind this is that self-phase modulation (SPM) due to a strong optical pulse propagating in the long cavity results in the generation of new frequency components in the wings of the pulse. These new frequency components (pulse chirp) are then removed through the optical filter, resulting in a fast intensity-dependent loss, which increases with increasing pulse intensity. This intensity-dependent loss thus provides a means for pulse amplitude stabilisation.

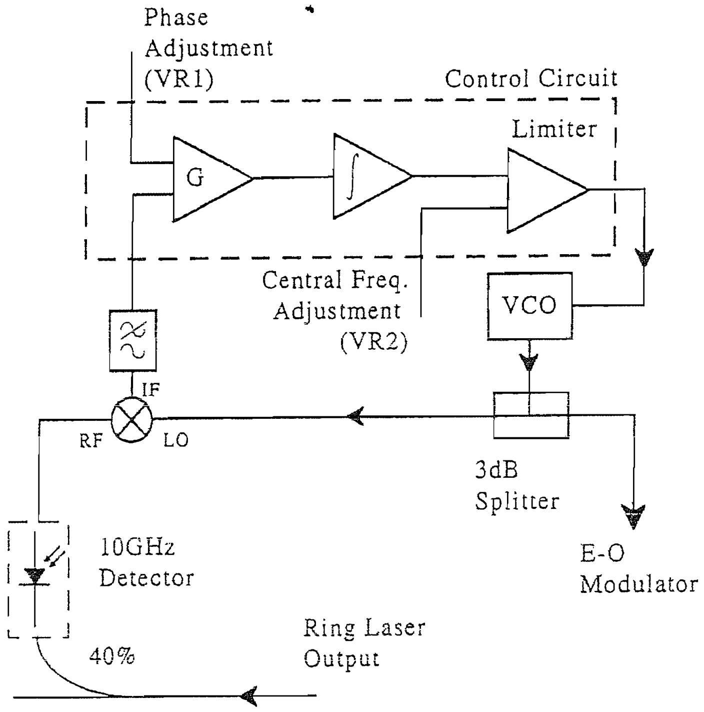

Figure 2: Block diagram of the Phase Lock Loop (PLL).

The PLL consists of an electronic control circuit responsible for driving a 10GHz voltage controlled oscillator (VCO) and is used to provide a modulating signal to the $LiNbO_3$ modulator at exactly the mode-locking frequency of the EFRL. A block diagram of the PLL is shown in Figure 2. A 10GHZ photodiode detector is used to detect a portion of the laser output and the electrical signal is fed to the RF input port of a high frequency mixer. Part of the signal generated by the VCO is fed to the LO port of the mixer. The two signals are mixed and the sum and difference frequency signals are generated. A low-pass filter is used to reject the sum frequency signal, leaving the difference frequency signal as a measure of the disagreement in phase between the signal generated by the oscillator and the exact mode-locking frequency. The further away the VCO frequency from one of the mode-locking harmonics, the higher the frequency of the difference signal. This signal vanishes once the PLL is locked. Any small perturbation from the locking frequency generates a slowly alternating signal, the phase of which indicates the direction in frequency towards which the VCO signal should shift. By using a simple PLL control circuit, the difference frequency signal can be minimised by constantly adjusting the VCO driving frequency to match the frequency of the mode-locking harmonics.

The PLL control circuit can be divided into three parts: The first stage is a non-inverting comparator serving to provide a low noise amplification of the input signal received at the filtered output of the mixer. At this stage, an externally adjusted voltage, VR1 is added in the amplification process to finely adjust the phase of the generated signal. Even when the PLL is locked, the phases of the two input signals to the RF mixer are not necessarily the same, as phase matching of the generated RF signal to the actual mode-locked signal has to be achieved at the $LiNbO_3$ modulator. This implies that phase-locking can be represented by a constant dc signal at the output of the mixer. Because of the integrating nature of the second stage of the control circuit, the output of the amplification stage for the phase-lcoking condition has to be zero, and VR1 along with a direct phase adjustment of the VCO signal at the output of the PLL, are used to ensure this.

The second stage is an integrator circuit which functions to lock the VCO signal onto the incoming RF signal. This is achieved by charging its feedback capacitor to a value dependant on the signal level at its input. While the capacitor is charging, the PLL sought to lock onto the incoming RF signal fed to the mixer. Once this is achieved the input to this stage is zero giving a constant level output. The PLL has a fast dynamic response due to the time constant of the integrator, measured to be ~0.1ms. A switch is included in this stage to reset the integrator by discharging the capacitor and restart the tracking procedure. The final part of the control circuit is a limiter stage, which provides the driving voltage for the VCO and protects it from overdriving. a second input voltage VR2 is introduced at this stage to adjust the central frequency of the VCO around the frequencies of interest.

The laser operates at 10.055 GHz producing around 2.5ps transform limited soliton pulses with an average output power of 3dBm. Stable operation of the laser could be maintained for hours without significant degradation of the laser performance. The operating wavelength could be tuned between 1546nm and 1557nm. The RF spectrum around the mode-locking frequency show supermode suppression of

~58dB. The pulse jitter is also greatly minimised. Figure 3 shows the typical laser characteristics of the EFRL.

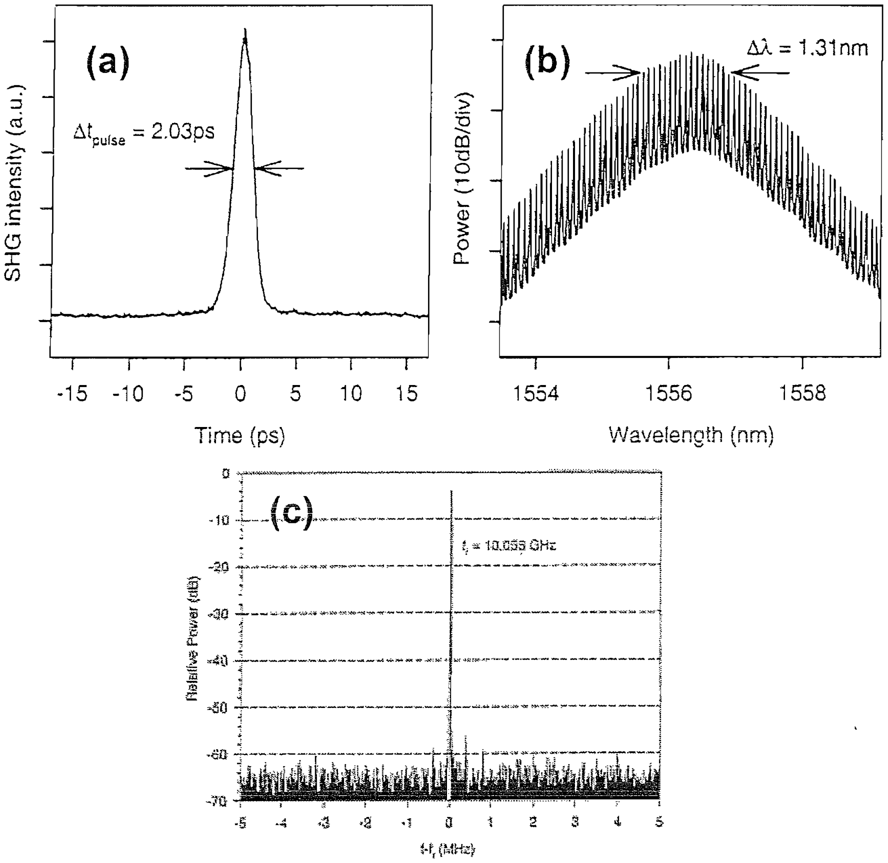

Figure 3: (a) Typical SHG intensity autocorrelation trace of the pulses, (b) the corresponding optical spectrum (resolution 10pm) and (c) RF spectrum around the mode-locking frequency.

References

[1] P. Petropoulos, "Novel Techniques and Materials for Optical Telecommunication Systems," in *Optoelectronics Research Centre, Department of Electronics and Computer Science*. Southampton: University of Southampton, 2000, pp. 139.

[2] A. E. Siegman, *Lasers*. California: University Science Books, 1986.

[3] G. P. Agrawal, *Nonlinear fiber optics*, 2nd ed: Academic Press Inc, 1995.

[4] M. Nakazawa, K. Tamura, and E. Yosida, "Supermode noise suppression in a harmonically modelocked fibre laser by selfphase modulation and spectral filtering," *IEE Electronics Letters*, vol. 32, pp. 461-463, 1996.

List of Publications

Invited Papers

1. M.Ibsen, R.Feced, P.C.Teh, J.H.Lee, M.R.Mokhtar, P.Petropoulos, M.N.Zervas, D.J.Richardson, D.N.Payne
   Advanced fibre Bragg gratings and where they are going
   Australian Institute of Physics Congress 2002 - Australian Conference on Fibre Optic Technology Program (AIP-ACOFT 2002), Sydney 8-11 Jul 2002 (Invited).

2. P.C.Teh, M.Ibsen, L.B.Fu, J.H.Lee, Z.Yusoff, D.J.Richardson
   A 16-channel OCDMA system (4 OCDMA x 4 WDM) based on 16-chip, 20 Gchip/s superstructure fibre Bragg gratings and DFB fibre laser transmitters
   Optical Fiber Communication Conference (OFC 2002), Anaheim USA, March 2002, Paper ThEE1 (Invited).

3. M.Ibsen, P.Petropoulos, R. Feced, P.C.Teh, M.K.Durkin, M.N.Zervas, D.J.Richardson, D.N.Payne, R.I.Laming
   Systems applications of fibre Bragg grating technology
   Optoelectronics and Communications Conference (OECC/IOOC 2001), Sydney Australia, July 2001 (Invited).

Postdeadline Papers

4. B.C. Thomsen, P.C. Teh, M. Ibsen, D.J. Richardson
   Self-Routing Edge-to-edge Optical Packet Switched Network Based on Superstructure Fiber Bragg gratings
   European Conference on Optical Communication (ECOC 2002), Copenhagen, Denmark, September 2002, Paper PD.2.3 (Postdeadline).

5. M.R. Mokhtar, M. Ibsen, P.C. Teh, D.J. Richardson
   16-bit multilevel reconfigurable phase encoder for all optical header generation/recognition based on a uniform fibre Bragg grating
   Optoelectronics and Communications Conference (OECC 2002), Yokohama, Japan, July 2002, Paper PD2-2 (Postdeadline).

6. P.C. Teh, B.C. Thomsen, M. Ibsen, D.J. Richardson
   400 G/bits 4 Gigapckets/s multiwavelength optical packet router based on superstructure fibre Bragg gratings
   Optoelectronics and Communications Conference (OECC 2002), Yokohama, Japan, July 2002, Paper PD1-1 (Postdeadline).

7. J.H. Lee, Z. Yusoff, W. Belardi, T.M. Monro, P.C. Teh, D.J. Richardson
   A Holey Fibre Raman Amplifier and All-Optical Modulator
   European Conference on Optical Communication (ECOC 2001), Amsterdam Holland, September 2001, Paper PD.A.1.1 (Postdeadline).

8. J.H. Lee, P.C. Teh, Z. Yusoff, M. Ibsen, W. Belardi, T.M. Monro, D.J. Richardson
   An OCDMA Receiver Incorporating a Holey Fibre Nonlinear Thresholder
   European Conference on Optical Communication (ECOC 2001), Amsterdam Holland, September 2001, Paper PD.B.1.2 (Postdeadline).

9. P.C.Teh, M.Ibsen, J.H.Lee, P.Petropoulos, D.J.Richardson
   A 4-channel WDM/OCDMA system incorporating 255-chip 320 Gchip/s quaternary phase coding and decoding gratings
   Optical Fiber Communication (OFC 2001), Anaheim USA, March 2001, Paper PD37-1 (Postdeadline).

10. J.H.Lee, P.C.Teh, P.Petropoulos, M.Ibsen, D.J.Richardson
    Timing jitter tolerant all-optical modulator and demultiplexing systems incorporating pulse-shaping fiber Bragg gratings
    Optical Fiber Communication (OFC 2001), Anaheim USA, March 2001, Paper PD30-1 (Postdeadline).

11. P.C.Teh, P.Petropoulos, M.Ibsen, D.J.Richardson
The generation recognition and re-coding of 64-bit 160 Gbit/s optical code sequences using superstructured fiber Bragg gratings
Optoelectronics and Communications Conference (OECC 2000), Japan, July 2000, Paper PD1-3 (Postdeadline).

12. P.C.Teh, P.Petropoulos, M.Ibsen, D.J.Richardson
A 10 Gbit/s 160Gchip/s coding:decoding system based on superstructured fiber gratings
Optical Fiber Communication (OFC 2000), Baltimore USA, March 2000, Paper PD9-1 (Postdeadline).

Conferences

13. Z.Yusoff, P.C.Teh, P.Petropulos, K.Furusawa, W.Belardi, T.M.Monro, D.J.Richardson
24 channels x 10 GHz multiwavelength pulse source based on supercontinuum generation in highly nonlinear holey fiber
Optical Fiber Communication (OFC 2003), Atlanta USA, 23-28 Mar 2003.

14. P.C.Teh, M.R. Mokhtar, M. Ibsen, D.J.Richardson
A novel distributed bidirectional OCDMA architecture based on simultaneous transmission of 16-chip OCDMA signals and clock pulses
Optical Fiber Communication (OFC 2003), Atlanta USA, 23-28 Mar 2003.

15. B.C.Thomsen, P.C.Teh, M.Ibsen, J.H.Lee, D.J.Richardson
A multi-hop optical packet switching demonstration employing all-optical grating based header generation and recognition
European Conference on Optical Communication (ECOC 2002), Copenhagen, Denmark, September 2002, paper 5.5.3.

16. P.C.Teh, M.Ibsen, D.J.Richardson
8-channel Bi-directional Spectrally Interleaved OCDMA/DWDM experiment employing 16-chip four-level phase coding gratings
Optoelectronics and Communications Conference (OECC 2002), Yokohama Japan, July 2002, Paper 11A1-1.

17. M.R.Mokhtar, M.Ibsen, D.J.Richardson
Simple dynamically reconfigurable OCDMA encoder/decoder based on a uniform fiber Bragg grating
Optical Fiber Communication (OFC 2002), Anaheim USA, Mar 2002, Paper ThGG54.

18. J H.Lee, P.C.Teh, P.Petropoulos, M.Ibsen, D.J.Richardson
All-optical TDM demultiplexing systems with significant timing jitter tolerance through incorporation of square pulse generating fiber Bragg gratings
IOP meeting on - In-fibre Bragg Gratings and Speciality Fibres, Coventry UK, Oct 2001.

19. P.C.Teh, P.Petropoulos, M.Ibsen, D.J.Richardson
Optical code division multiple access encoders and decoders based on superstructured fiber Bragg gratings
Rank Prize Fund Mini-Symposium: Terabit Optical Networks, Grasmere UK, April 2001.

20. J.H.Lee, P.C.Teh, P.Petropoulos, M.Ibsen, D.J.Richardson
The use of nonlinear element for signal enhancement in a grating based all-optical pattern recognition system
Rank Prize Fund Mini-Symposium: Terabit Optical Networks, Grasmere UK, April 2001.

21. J.H.Lee, P.C.Teh, P.Petropoulos, M.Ibsen, D.J.Richardson
High performance 64-chip 160 Gchip/s fiber grating based OCDMA receiver incorporating a nonlinear optical loop mirror
Optical Fiber Communication (OFC 2001), Anaheim USA, March 2001, Paper ThH4.

22. P.C.Teh, J.H.Lee, M.Ibsen, P.Petropoulos, D.J.Richardson
A 10-Gbit/s all-optical code generation and recognition system based on a hybrid approach of optical fiber delay line and superstructure fiber Bragg grating technologies
Optical Fiber Communication (OFC 2001), Anaheim USA, March 2001, Poster session 2.

23. P.C.Teh, P.Petropoulos, M.Ibsen, D.J.Richardson
160 Gbit/s, 64-bit all-optical code generation and recognition using superstructured fibre Bragg gratings
European Conference on Optical Communication (ECOC 2000), Munich Germany, September 2000, Paper 1.1.2.

24. P.C.Teh, P.Petropoulos, M.Ibsen, D.J.Richardson
A 10 Gbit/s 160 Gchip/s superstructured fibre Bragg gratings for OCDMA coding:decoding system
Applied Optics & Opto-electronics Conference on In-fibre Bragg Gratings and Special Fibres, Loughborough UK, September 2000.

25. P.Petropoulos, P.C.Teh, M.Ibsen, M.N.Zervas, D.J.Richardson
Pulse shaping and pattern generation/recognition using fibre Bragg gratings
CSNDSP 2000, Bournemouth UK, 18-20 July 2000.

26. P.Petropoulos, P.C.Teh, M.Ibsen, M.N.Zervas, D.J.Richardson
The use of fibre Bragg gratings for advanced optical signal processing
Rank Prize Fund Mini Symposium: Microwave Photonics, Grasmere UK, April 2000.

Journals and Letters

27. P.C. Teh, B.C. Thomsen, M. Ibsen, D.J. Richardson
Multi-wavelength (40 WDM x 10 Gbit/s) optical packet router based on superstructure fibre Bragg gratings
Submitted to IEICE Transaction/Joint Special Issue on Recent Progress in Optoelectronics and Communication (Invited Paper).

28. P.C. Teh, M. Ibsen, D.J. Richardson
Demonstration of a Full-Duplex Bi-directional Spectrally Interleaved OCDMA/DWDM system using 16-bit, four-level phase coding superstructure fiber Bragg gratings
Submitted to IEEE Photonics Technology Letters.

29. M.R. Mokhtar, M. Ibsen, P.C. Teh, D.J. Richardson
Reconfigurable multi-level phase shift keying encoder/decoder all-optical networks
Submitted to IEEE Photonics Technology Letters.

30. J.H.Lee, P.C.Teh, Z.Yusoff, M.Ibsen, W.Belardi, T.M.Monro, D.J.Richardson
A holey fiber-based nonlinear thresholding device for optical CDMA receiver performance enhancement
IEEE Photonics Technology Letters 2002, Vol.14(6), pp. 876-878.

31. Z.Yusoff, J.H.Lee, W.Belardi, T.M.Monro, P.C.Teh, D.J.Richardson
Raman effects in a highly nonlinear holey fiber: amplification and modulation
OSA Optics Letters 2002, Vol.27(6).

32. J H.Lee, P.C.Teh, P.Petropoulos, M.Ibsen, D.J.Richardson
All optical modulation and demultiplexing systems with significant timing jitter tolelrance through incorporation of pulse-shaping fiber Bragg gratings
IEEE Photonics Technology Letters 2002, Vol.14(2), pp. 203-205.

33. P.C.Teh, M.Ibsen, J.H.Lee, P.Petropoulos, D.J.Richardson
Simultaneous optical decoding and wavelength channel selection using 255-chip, 320 Gchip/s quarternary phase coding gratings in a four-channel WDM/OCDMA system
IEEE Photonics Technology Letters 2002, Vol.14(2), pp. 227-229.

34. P. Petropoulos, N. Wada, P.C.Teh, M.Ibsen, W.Chujo, K.-I. Kitayama, D.J. Richardson
Demonstration of a 64-chip OCDMA system using superstructured fiber gratings and time-gating detection
IEEE Photonics Technology Letters 2001, Vol.13(11), pp. 1239-1241.

35. D.J.Richardson, P.C.Teh, M.Ibsen, P.Petropoulos, J.H.Lee
Superstructured gratings enable OCDMA/WDM
WDM Solutions 2001, pp. 57-64, Also on wdm-solutions.com.

36. P.C. Teh, P. Petropoulos, M. Ibsen, D.J. Richardson
A comparative study of the performance of seven-and 63-chip optical code-division multiple-access encoders and decoders based on superstructured fiber Bragg gratings
IEEE Journal of Lightwave Technology 2001, Vol.19(9), pp. 1352-1365.

37. J.H.Lee, P.C.Teh, P.Petropoulos, M.Ibsen, D.J.Richardson
Reduction of interchannel interference noise in a two-channel grating based OCDMA system using a nonlinear optical loop mrror
IEEE Photonics Technology Letters 2001, Vol.13(5), pp. 529-531.

38. P.C.Teh, P.Petropoulos, M.Ibsen, D.J.Richardson
Generation recognition and recoding of 64-chip bipolar optical code sequences using superstructured fibre Bragg gratings
IEE Electronics Letters 2001, Vol.37(3), pp. 190-191.

39. P.C.Teh, P.Petropoulos, M.Ibsen, D.J.Richardson
Phase encoding and decoding of short pulses at 10Gbit/s using superstructured fiber Bragg gratings
IEEE Photonics Technology Letters 2001, Vol.13(2), pp. 154-156.

40. J.H.Lee, P.C.Teh, P.Petropoulos, M.Ibsen, D.J.Richardson
A grating based OCDMA coding:decoding system incorporating a nonlinear optical loop mirror for improved code recognition and noise reduction
IEEE Journal of Lightwave Technology 2002, Vol.20(1), pp. 36-46.